



THE UNIVERSITY OF
WAIKATO
Te Whare Wānanga o Waikato

Research Commons

<http://researchcommons.waikato.ac.nz/>

Research Commons at the University of Waikato

Copyright Statement:

The digital copy of this thesis is protected by the Copyright Act 1994 (New Zealand).

The thesis may be consulted by you, provided you comply with the provisions of the Act and the following conditions of use:

- Any use you make of these documents or images must be for research or private study purposes only, and you may not make them available to any other person.
- Authors control the copyright of their thesis. You will recognise the author's right to be identified as the author of the thesis, and due acknowledgement will be made to the author where appropriate.
- You will obtain the author's permission before publishing any material from the thesis.

**The Effect of Powder Characteristics and Processing Conditions
on the Microstructure and Mechanical Properties of Titanium
Alloys Made by Powder Forging**

A thesis
submitted in fulfilment
of the requirements for the degree

of

Doctor of Philosophy

at

The University of Waikato

by

MINGTU JIA



THE UNIVERSITY OF
WAIKATO
Tē Whare Wānanga o Waikato

2013

Abstract

Powder compact forging was used to produce Ti and Ti-6Al-4V rocker arms using pre-alloyed and blended elemental powders. Green powder compacts with high relative density were manufactured by warm compaction. Due to the characteristics of raw powders, interlocking and cold welding are the main mechanisms for HDH powder compaction, while warm welding is the main mechanism for GA powder compaction. During induction heating of the powder compact, it was found that necks formed extensively in as-sintered HDH Ti powder compact, leading to an average elongation to fracture of 7.5%, whereas necks did not form so extensively in as-sintered HDH Ti-6Al-4V and GA Ti-6Al-4V powder compacts, which make them brittle due to their low relative density.

As a rapid consolidation process, the densification rate was enhanced by powder compact forging due to pore collapsing caused by material flow driven by a large amount of localized plastic deformation. The degree of powder consolidation of powder compact forging using HDH Ti, HDH and GA Ti-6Al-4V powders were studied by characterising their porosity distributions, microstructure, mechanical properties and fracture behaviour. Due to the positive effect of shear deformation on the powder consolidation of powder compact forging, the powder compact in the centre of forged parts were consolidated completely with full density and had better mechanical properties than those from ingot metallurgy.

The effects of heat treatments on microstructure and mechanical properties of as-forged HDH Ti part, HDH and GA Ti-6Al-4V parts were investigated, and the ductility of forged HDH Ti part was improved significantly by annealing treatment. Recrystallization annealing was regarded as one of the best heat

treatments to achieve the high ductility of as-forged HDH and GA Ti-6Al-4V parts, which can open the applications of forged HDH Ti-6Al-4V part with high oxygen content (~0.5%). The mechanical properties of forged HDH and GA Ti-6Al-4V parts after solution and aging treatment and recrystallization annealing were much better than those from both the ones from reported pre-alloyed approaches and wrought parts, which were caused by the enhancement of powder consolidation during recrystallization process.

Blended elemental approach and mechanical alloying method were applied to produce Ti-6Al-4V rocker arm by powder compact forging at 1350 °C. The effect of holding time at forging temperature on the samples produced by forging the compact of HDH Ti/Al-V master alloy powder mixture was studied, and it was found that a holding time of 5-10 minutes at forging temperature is required to get the as-forged part with good mechanical properties and homogeneous microstructure of free undissolved master alloy powders. Also, in order to reduce the holding time for achieving composition homogeneity, the powder mixture of Ti and Al-V master alloy powders was milled to produce Ti/Al-40wt%V composite powder. With such composite powder, the master alloy layers/particles were dissolved rapidly into Ti matrix, but the oxygen pick up during milling and powder passivation make the mechanical properties of the forged samples inferior to those of the parts made by powder compact forging of the powder mixture or pre-alloyed powder.

List of Publications

Journals

1. Comparison of blended elemental (BE) and mechanical alloyed (MA) powder compact forging into Ti-6Al-4V rocker arms
Author/s: M. Jia, D. Zhang, B. Gabbitas
Key Engineering Materials, 520 (2012) pp.82

Conference Proceedings

1. The use of Titanium and Titanium Alloy Powder Compact Forging to Produce Near-Net Shaped Rocker Arms and The Influence of Processing Conditions
Author/s: M. Jia, D. Zhang, B. Gabbitas
Proceedings of the 12th World Conference on Titanium, 19-24 June 2011, Beijing, China.

Acknowledgements

I would like to express my immense gratitude to my chief supervisor A/Prof. Brian Gabbitas and Prof. Deliang Zhang, without whose guidance, help, patience and encouragement, the completion of this thesis would not have been possible. I would also like to extend my gratitude to my associate supervisor Prof. Ilanko Sinniah, whose assistance and recommendations are of major importance.

I would like to appreciate the assistance and help of the administrative staff and technicians working in the school of Engineering at the University of Waikato. Especially I want to thank Mary Dalbeth for her administrative support, and also I am obliged to Helen Turner, Yuanji Zhang and Chris Wang for their technical assistance.

I am highly indebted to my many colleagues in the metallic materials research group, Dr. Fantao Kong, Stella Raynova, Paul Ewart, Zhibo Zhang, Dengshan Zhou, Qian Xu, and Huiyang Lu, who supported and helped me during experiments.

Finally, I would like to express my gratitude towards my parents and my partner Weidong Wang for their kind co-operation and encouragement which helped me in the completion of this PhD thesis. I would also like to thank the Foundation for Research, Science and Technology (Later Ministry of Science and Innovation and Ministry of Business, Innovation and Employment), New Zealand for the financial support to the project.

Table of contents

<i>Abstract</i>	<i>ii</i>
<i>List of Publications</i>	<i>iv</i>
<i>Acknowledgements</i>	<i>v</i>
<i>Table of contents</i>	<i>vi</i>
<i>List of Figures</i>	<i>x</i>
<i>List of Tables</i>	<i>xvi</i>
<i>Abbreviations</i>	<i>xviii</i>
Chapter 1: Introduction and Literature Review	1
1.1 Introduction	1
1.2 Literature Review	3
1.2.1 Powder Metallurgy in General	3
1.2.1.1 Compaction	5
1.2.1.2 Sintering	6
1.2.1.3 Powder Forging	8
1.2.2 Titanium and Its Alloys	13
1.2.2.1 Classification of Titanium Alloys	13
1.2.2.2 Commercially Pure (CP) Ti	15
1.2.2.3 Ti-6Al-4V Alloy	15
1.2.2.4 Thermomechanical Processing and Heat Treatment of Titanium Alloys	17
1.2.3 Powder Metallurgy of Titanium and Titanium Alloys	18
1.2.3.1 Microstructure and Mechanical Properties of Titanium and Titanium Alloys Produced by Powder Metallurgy	21
1.2.3.2 Powder Compact Forging of Titanium and Titanium Alloys ...	27
1.2.4 Summary	33
1.3 References	35
Chapter 2: Materials and Experimental Procedure	47
2.1 Starting Powders	47
2.1.1 Blended and Mechanical Alloyed Powders Synthesis	51
2.2 Powder Compact Forging Procedure	52
2.3 Heat Treatment of As-forged Parts	56
2.4 Characterization of Powders and Consolidated Samples	57
2.4.1 Particle Size Analysis	57
2.4.2 Oxygen Analysis	58
2.3.3 Thermal Analysis	58

2.3.4 Density Measurement	58
2.4.5 Optical Microscopy	59
2.4.6 Porosity Distribution Measurement	59
2.4.7 X-ray Diffraction.....	60
2.4.8 Scanning Electron Microscopy	60
2.4.9 Transmission Electron Microscopy	60
2.4.10 Tensile Testing.....	61
2.5 Reference	62
Chapter 3: Compacting and Induction Sintering of Ti and Ti-6Al-4V	
Powders	63
3.1 Introduction.....	63
3.2 Compacting of Ti and Ti-6Al-4V Powders	63
3.2.1 The Effect of Temperature on Compacting	64
3.2.2 Mechanism of Compacting HDH Ti, HDH Ti-6Al-4V and GA Ti-6Al-4V Powders Compact	67
3.3 Induction Sintering of Ti and Ti-6Al-4V Powder Compacts	71
3.3.1 Microstructure of As-sintered Parts.....	72
3.3.2 Mechanical Properties of As-sintered Powder Compacts	74
3.3.3 Fracture Morphology of As-sintered Powder Compacts.....	76
3.3.4 Mechanisms of Densification and Sintering during Induction Heating	78
3.4 Discussion	82
3.4.1 Effect of Compacting Temperature on Relative Density of Ti and Ti-6Al-4V Powder Compacts	82
3.4.2 Effect of Particle Shape and Oxygen Content on Ti-6Al-4V Powder Compacting.....	85
3.4.3 Effect of Particle Shape of Ti-6Al-4V Powder on Induction Sintering.....	86
3.4.4 Effect of Relative Density of Ti and Ti-6Al-4V Powder Compacts on Induction Sintering	87
3.5 Summary	87
3.6 References.....	88
Chapter 4: Powder Compact Forging of Ti and Ti-6Al-4V Powders	89
4.1 Introduction.....	89
4.2 Microstructure of As-forged Parts	89
4.3 Porosity Distribution of As-forged Parts	99
4.4 Mechanical Properties of As-forged Parts.....	105

4.5 Cold-shut of As-forged Parts	109
4.6 Improvement on Mechanical Properties of As-forged Ti Part	111
4.7 Fracture Behavior of As-forged Ti and Ti-6Al-4V Parts	116
4.7.1 Fracture Behavior of As-forged HDH Ti Part	116
4.7.2 Fracture Behavior of As-forged HDH Ti-6Al-4V Part	121
4.7.3 Fracture Behavior of As-forged GA Ti Part	125
4.7.4 Fracture Behavior of As-forged GA Ti-6Al-4V Part	129
4.8 Discussion	133
4.8.1 Improvement of Mechanical Properties of Ti and Ti-6Al-4V Parts by Powder Compact Forging	133
4.8.2 Mechanisms of Powder Consolidation by Powder Compact Forging	137
4.8.2.1 Enhanced Densification Mechanism of Powder Compact Forging.....	137
4.8.2.2 The Effect of Powder Shape on Densification of Powder Compact Forging	140
4.9 Summary	140
4.10 References.....	141
Chapter 5: Heat Treatment of Forged Ti and Ti-6Al-4V Parts.....	144
5.1 Introduction.....	144
5.2 Annealing of Forged HDH Ti Parts	144
5.3 Effect of Heat Treatment on the Microstructures of Forged HDH Ti-6Al-4V Parts	147
5.4 Effect of Heat Treatment on the Mechanical Properties and Fracture Behaviour of Forged HDH Ti-6Al-4V Parts.....	151
5.5 Effect of Heat Treatment on the Microstructures of Forged GA Ti-6Al-4V Parts	157
5.6 Effect of Heat Treatment on the Mechanical Properties and Fracture Behaviour of Forged GA Ti-6Al-4V Parts	160
5.7 Discussion	164
5.7.1 Effect of Heat Treatments on Mechanical Properties of Forged HDH Ti Part	164
5.7.2 The Microstructural Reasons of the Effects of Different Heat Treatments on Mechanical Properties of Forged HDH and GA Ti-6Al-4V Parts.....	165
5.7.3 The Role of Oxygen Content on the Effects of Heat Treatments..	167
5.7.4 Effect of Heat Treatment on Mechanical Properties of Forged HDH	

and GA Ti-6Al-4V Parts	169
5.7.5 Effect of Recrystallization on Powder Consolidation	171
5.8 Summary	172
5.9 Reference	172
Chapter 6: Powder Compact Forging of Blended and Mechanically Alloyed Ti-6Al-4V Powders.....	174
6.1 Introduction.....	174
6.2 Powder Compact Forging of Blend Elemental (BE) Ti-6Al-4V Powder	174
6.2.1 Blending of Powders	174
6.2.2 Phase Constituent and Element Distribution of As-forged BE Ti-6Al-4V Parts	176
6.2.3 Microstructure of As-forged BE Ti-6Al-4V Parts	181
6.2.4 Mechanical Properties of As-forged BE Ti-6Al-4V Part	184
6.3 Powder Compact Forging of Mechanical Alloyed (MA) Ti-6Al-4V Powder	190
6.3.1 Milling of Powder Mixtures	190
6.3.2 Phase Constituent and Element Distribution of As-forged MA Ti-6Al-4V Part	195
6.3.3 Microstructures of As-forged MA Ti-6Al-4V Parts	200
6.3.4 Mechanical Properties and Fracture Behaviour of As-forged MA Ti-6Al-4V Part	205
6.4 Discussion	209
6.4.1 Effect of Undissolved Al-40wt%V Master Alloy Particles on Microstructure, Mechanical Properties and Fracture Behaviours of BE Ti-6Al-4V Parts	209
6.4.2 Effects of Milling and Oxygen Content on Mechanical Properties and Fracture Behaviours of the Samples Produced by PCF of Composite Powders	212
6.5 Summary	213
6.6 Reference	213
Chapter 7: Conclusions and Recommendations for Future Work.....	214
7.1 Conclusions.....	214
7.2 Recommendations for Future Work	218

List of Figures

Figure 1.1: Conventional PM process.....	4
Figure 1.2: Effects of temperature on the green compact density of various metal powders [54].	6
Figure 1.3: Two spherical particle model for initial stage of sintering (a) without shrinkage and (b) with shrinkage [73].	7
Figure 1.4: Pores structure in immediate stage of sintering [73].	8
Figure 1.5: Pores structure in final stage of sintering [73].....	8
Figure 1.6: Schematic diagram of powder repressing and upsetting process [83]..	9
Figure 1.7: Powder forging process with different dies [83].	9
Figure 1.8: The effect of applied pressure on densification of alumina at 1500oC during sinter-forging process [72].....	10
Figure 1.9: A fracture limit determined by preform and forged height to diameter ratio: H/D [72].	10
Figure 1.10: Pore collapse in the final stage of sintering by hot forging and HIP [72].....	11
Figure 1.11: Relative density of powder compact as a function of forging pressure, including experimental data and AAE model in Ref. [26].	13
Figure 1.12: Typical microstructures of α , $\alpha+\beta$, β alloys [114].	14
Figure 1.13: Effect of oxygen content on the strength of Ti-6Al-4V [118].	16
Figure 1.14: Variety of methods used to produce PA and BE starting powder.	19
Figure 1.15: High-cycle fatigue results of Ti-6Al-4V at room temperature with different alloy status in Ref. [117].	21
Figure 1.16: Typical microstructures of BE Ti-6Al-4V alloy produced by cold pressing and sintering: (a) die compaction [17], (b) cold isostatic pressing [17], and (c) after the “broken up structure” (BUS) heat treatment [17].....	22
Figure 1.17: Two BE PM processes for making Ti-6Al-2.75Sn-4Zr-0.4Mo-0.4Si (Ti-1100) alloy [152].....	24
Figure 1.18: Microstructures of Ti-6Al-4V samples produced from PA powder using different powder consolidation conditions [17]: (a) HIP at 900 oC for 2 h with a pressure of 105 MPa in a steel mould; (b) HIP at 925 oC for 4 h with a pressure of 105 MPa in a ceramic mould; (c) Strain energizing process’ powder HIP-ed at 870 °C for 2 h with a pressure of 105 MPa in a steel mould.	25
Figure 1.19: Comparison of mechanical properties of Ti-6Al-4V parts produced from PA powder using different PM processes and ingot metallurgy [166].....	27
Figure 1.20: Compressive stress-strain curves of dense Ti-6Al-4V alloy specimens at high temperatures tested with a strain rate of 10^{-4} s^{-1} (a) and 10^{-3} s^{-1} (b) [169].	28

Figure 1.21: Sintering curves of titanium powder compact under variety of pressures and temperatures [170].	29
Figure 1.22: Sintering curves of titanium powder compact with different heating rates under the same pressure of 50 MPa [170].	29
Figure 1.23: Ti-5Al-2Sn-2Zr-4Mo-4Cr connecting rod produced by powder forging [100].	31
Figure 1.24: Effect of effective strain on the relative density [100].	32
Figure 1.25: Processing map of Ti-5Al-2Sn-2Zr-4Mo-4Cr powder alloy with true strain: (a) 0.3; (b) 0.5; (c) 0.7 [175].	32
Figure 2.1: Particle size distributions of starting powders, (1) curve shows the volume percent at the corresponding particle size, and (2) curve shows the volume percent under the corresponding particle size: (a) GA Ti; (b) HDH Ti; (c) GA Ti-6Al-4V; (d) HDH Ti-6Al-4V; (e) Al-40wt% V.	49
Figure 2.2: SEM images of starting powders used in this study. (a) GA Ti; (b) HDH Ti; (c) GA Ti-6Al-4V; (d) HDH Ti-6Al-4V; (e) Al-40wt% V master alloy.	50
Figure 2.3: Retsh PM 100 planetary ball mill.	51
Figure 2.4: The designed shape of the rocker arm to be produced by powder compact forging in this study.	52
Figure 2.5: Schematic diagram showing the procedure of powder compact forging.	53
Figure 2.6: Image of glove chamber.	53
Figure 2.7: Powder compaction die.	54
Figure 2.8: Forging die set. (a) upper die; (b) lower die.	55
Figure 2.9: Schematic diagram showing condition of annealing treatment for as-forged HDH Ti part.	57
Figure 2.10: Schematic diagrams showing conditions of heat treatments for as-forged Ti-6Al-4V parts.	57
Figure 2.11: Nextengine 3-D scanner.	59
Figure 2.12: Shape (a) and dimensions (b) of the tensile test specimen.	61
Figure 2.13: Schematic diagram of cutting tensile test specimens from as-forged rocker arm.	62
Figure 3.1: Image of a HDH Ti powder compact with mass of 120g for making Ti rocker arm by powder compact forging.	64
Figure 3.2: The relative density of HDH Ti and HDH and GA Ti-6Al-4V powder compacts as functions of temperature under the constant pressure: 544 MPa applied on HDH Ti powder, 726 MPa applied on HDH and GA Ti-6Al-4V powders.	65
Figure 3.3: Fracture surfaces of HDH Ti powder compacts made by compacting at different temperature respectively.	69
Figure 3.4: GA Ti-6Al-4V powder particle morphologies after compacting at different temperatures with a pressure of 726 MPa, respectively.	71

Figure 3.5: Microstructure of as-sintered powder compacts.....	74
Figure 3.6: Stress-strain curves of specimens cut from as-sintered compacts: (a) HDH Ti, relative density of 91%; (b) GA Ti-6Al-4V, relative density of 85.8%; (c) HDH Ti-6Al-4V, relative density of 80.8%. (AS=as-sintered)	75
Figure 3.7: SEM images with different magnifications of fracture morphology of as-sintered HDH Ti and GA and HDH Ti-6Al-4V powder compacts after tensile testing.	78
Figure 3.8: Powder morphologies of as-sintered powder compacts at the temperature of 1350°C.	80
Figure 3.9: Two-sphere model for necking formation showing the powder particle surface contact area caused by plastic deformation.	81
Figure 3.10: Comparison of relative density of Ti powder compacts as functions of temperature under the different pressure: 450 MPa [1] and 544 MPa (this work).	83
Figure 3.11: Comparison of relative density of Ti-6Al-4V powder compacts as functions of temperature under the different pressure: 970 MPa [5], 1366 MPa [5] and 726 MPa (this work).	84
Figure 3.12: Yield strength vs temperature curves of Grade 4 CP Ti and milled annealed Ti-6Al-4V bulk material [7].....	85
Figure 4.1: Images of as-forged rocker arms showing their top and bottom surfaces.	91
Figure 4.2: Low magnification images of as-forged parts: (a) HDH Ti; (b) GA Ti-6Al-4V; (c) HDH Ti-6Al-4V.....	92
Figure 4.3: Optical microscopy micrographs showing the microstructure of different regions of as-forged parts.....	93
Figure 4.4: SEM micrographs showing the microstructure of centre region of as-forged parts.....	95
Figure 4.5: TEM bright field images and SADPs of the microstructure of as-forged HDH Ti part.	96
Figure 4.6: TEM bright field images and SADP showing the microstructure of as-forged GA Ti-6Al-4V part.....	97
Figure 4.7: TEM bright field images and SADPs showing the microstructure of as-forged HDH Ti-6Al-4V part.....	99
Figure 4.8: Porosity distribution of as-forged parts perpendicular and along forging direction on cross section from the surface. (P and FD are the abbreviation of perpendicular and forging direction in the figures) 102	
Figure 4.9: Tensile stress-strain curves of specimens cut from the as-forged HDH Ti, GA Ti-6Al-4V and HDH Ti-6Al-4V parts in the order of sample numbers with increasing distance from the part surface. (AF = as-forged)	106
Figure 4.10: The distribution of mechanical properties along the distance from the surface of as-forged parts: (a) HDH Ti; (b) GA Ti-6Al-4V; (c) HDH Ti-6Al-4V.....	107
Figure 4.11: Surface quality improvement of as-forged HDH Ti rocker arms by the increase of die temperature.	110

Figure 4.12: Surface quality improvement of as-forged HDH Ti-6Al-4V rocker arms by the increase of die temperature.	111
Figure 4.13: Images of both top and bottom surfaces of as-forged rocker arm produced by powder compact forging of GA Ti powder.	112
Figure 4.14: Stress-strain curves of tensile specimens cut from the as-forged GA Ti part.	113
Figure 4.15: Mechanical properties of tensile test specimens cut from the as-forged GA Ti part as a function of the specimen number.	113
Figure 4.16: Stress-strain curves of tensile test specimens cut from the as-forged HDH Ti part made with a holding time of 5 minutes at forging temperature.	115
Figure 4.17: Microstructure as-forged HDH Ti part made with a holding time of 5 minutes at the forging temperature.	115
Figure 4.18: Mechanical properties of specimens cut from the as-forged HDH Ti part made with holding time of 5 minutes at forging temperature as a function of specimen number.	116
Figure 4.19: Fracture surface and corresponding longitudinal cross section of AF HDH Ti-1 specimen.	118
Figure 4.20: Fracture surface and corresponding longitudinal cross section of AF HDH Ti-4 specimen.	121
Figure 4.21: Fracture surface and corresponding longitudinal cross section of AF HDH Ti-6Al-4V-1 specimen.	123
Figure 4.22: Fracture surface and corresponding longitudinal cross section of AF HDH Ti-6Al-4V-3 specimen.	125
Figure 4.23: Fracture surface and corresponding longitudinal cross section of AF GA Ti-1 specimen.	127
Figure 4.24: Fracture surface and corresponding longitudinal cross section of AF GA Ti-6 specimen.	129
Figure 4.25: Fracture surface and corresponding longitudinal cross section of AF GA Ti-6Al-4V-3 specimen.	131
Figure 4.26: Fracture surface and corresponding longitudinal cross section of AF GA Ti-6Al-4V-5 specimen.	133
Figure 4.27: Schematic diagram of shear band deformation of a cylinder under compression.	135
Figure 4.28: Pore evolvment during powder compact forging process.	139
Figure 5.1: Stress-strain curves of tensile test specimens cut from forged HDH Ti part with oxygen content of 0.41% after annealing.	145
Figure 5.2: Microstructure of forged HDH Ti part with oxygen content of 0.41% after annealing.	146
Figure 5.3: Fracture surface of forged HDH Ti specimen with oxygen content of 0.41% after annealing.	147
Figure 5.4: Microstructure of different regions of forged HDH Ti-6Al-4V part with oxygen content of 0.52% after duplex annealing.	148
Figure 5.5: Microstructure of different regions of forged HDH Ti-6Al-4V part	

with oxygen content of 0.52% after solution and aging treatment. .	149
Figure 5.6: Microstructure of different regions of forged HDH Ti-6Al-4V part with oxygen content of 0.52% after recrystallization annealing.....	150
Figure 5.7: Microstructure of different regions of forged HDH Ti-6Al-4V part with oxygen content of 0.52% after beta annealing.....	151
Figure 5.8: Stress-strain curves of as-forged HDH Ti-6Al-4V specimen with oxygen content of 0.52% and those after different heat treatments.	152
Figure 5.9: Fracture surfaces of forged HDH Ti-6Al-4V specimens with oxygen content of 0.52% after different heat treatments.....	157
Figure 5.10: Microstructure of different regions of forged GA Ti-6Al-4V part with oxygen content of 0.14% after duplex annealing.	158
Figure 5.11: Microstructure of different regions of forged GA Ti-6Al-4V part with oxygen content of 0.14% after solution and aging treatment.	159
Figure 5.12: Microstructure of different regions of forged GA Ti-6Al-4V part with oxygen content of 0.14% after recrystallization annealing.....	160
Figure 5.13: Stress-strain curves of as-forged GA Ti-6Al-4V specimen with oxygen content of 0.14% and those after different heat treatments.	161
Figure 5.14: Fracture surfaces of forged GA Ti-6Al-4V specimens with oxygen content of 0.14% after different heat treatments.....	164
Figure 5.15: Comparison of mechanical properties of as-forged HDH Ti parts, forged HDH part after annealing and Grade 4 ingot metallurgy Ti.	165
Figure 5.16: Comparison of mechanical properties of as-forged HDH and GA Ti-6Al-4V parts made with different conditions compared with ingot metallurgy and the other pre-alloyed approaches.	170
Figure 5.17: Schematic diagrams showing recrystallization at a particle boundary.	172
Figure 6.1: Optical microscopy image of cross sections of blended HDH Ti and Al-V master alloy powder particles.	175
Figure 6.2: XRD patterns of three random batches of the powder mixture.	175
Figure 6.3: DTA heating curve of BE Ti-6Al-4V powder.....	176
Figure 6.4: Rocker arm produced by PCF of BE Ti-6Al-4V powder without holding at forging temperature.....	176
Figure 6.5: XRD patterns of Ti-6Al-4V BE powder mixture and as-forged parts produced using PCF of the powder.....	177
Figure 6.6: SEM images and EDS elemental mappings of cross sections of as-forged BE Ti-6Al-4V parts with different holding times at 1350 °C: (a) without holding; (b) holding time: 5 minutes; (c) holding time: 10 minutes.....	179
Figure 6.7: SEM images and results of EDS line scanning on the cross sections of the as-forged BE Ti-6Al-4V parts.....	180
Figure 6.8: Points selected for EDS analysis on the cross sections of as-forged BE Ti-6Al-4V parts made by PCF with different holding times: (a) without holding; (b) holding time of 5 minutes; (c) holding time of 10 minutes.....	181

Figure 6.9: Microstructure of as-forged parts made by PCF of BE Ti-6Al-4V powder with different holding times at 1350 °C.....	183
Figure 6.10: SEM images of microstructure of as-forged parts made by PCF of BE Ti-6Al-4V powder with different holding times.....	184
Figure 6.11: Engineering stress-strain curves of tensile test specimens cut from the samples produced by forging the compacts of powder mixture with different holding times at 1350 °C.....	186
Figure 6.12: Fracture surfaces of the tensile test specimens cut from samples produced by forging the compact of powder mixture with different holding times at 1350 °C.....	189
Figure 6.13: Optical microscopy images of cross sections of powder particles produced by milling HDH or GA Ti powder with Al60V40 master alloy powder at different milling speeds and after different milling times, respectively.....	191
Figure 6.14: XRD patterns of composite powders made by milling powder mixtures at different milling speeds and for different times.....	192
Figure 6.15: EDS mapping of composite powder particles made by milling HDH Ti and master alloy powders at different milling conditions.....	193
Figure 6.16: EDS mapping of a composite powder particle made by milling GA Ti and master alloy powders for 6 hours at a speed of 200 rpm.....	194
Figure 6.17: DTA curves of composite powder particles made at different milling condition using different raw powders.....	195
Figure 6.18: Rocker arms produced by forging MA powders.....	196
Figure 6.19: XRD patterns of as-forged parts made by PCF of HDH Ti/Al-40wt% V and GA Ti/Al-40wt% V composite powders.....	196
Figure 6.20: EDS mappings of as-forged parts produced by PCF of composite powders milled under different conditions.....	198
Figure 6.21: EDS line scanning results of as-forged parts produced by PCF of composite powders milled under different conditions.....	199
Figure 6.22: Points selected for EDS analysis on the cross sections of as-forged parts made by PCF of composite powders milled under different conditions. (a) HDH Ti/Al-40wt% V, 200 rpm/3hrs; (b) HDH Ti/Al-40wt% V, 200 rpm/6hrs; (c) GA Ti/Al-40wt% V, 200 rpm/6hrs.....	200
Figure 6.23: Optical microscopy images of microstructures of as-forged parts made using different composite powders.....	203
Figure 6.24: SEM images showing the microstructure of on the cross section of as-forged parts using different composite powders.....	205
Figure 6.25: Engineering stress-strain curves of tensile test specimens cut from as-forged parts made using different composite powders.....	206
Figure 6.26: Fracture surfaces of tensile test specimens cut from as-forged parts made using different composite powders.....	208
Figure 6.27: Comparison of mechanical properties of as-forged Ti-6Al-4V parts by powder mixture in this study with wrought material.....	211

List of Tables

Table 1.1: Compositions of four grades of CP Ti [118].	15
Table 1.2: Mechanical properties of four grades of CP Ti sheet, strip and plate [118].	15
Table 1.3: Mechanical properties of Ti-6Al-4V alloy [117].	16
Table 1.4: Ti-6Al-4V properties after heat treatments [114].	18
Table 1.5: Room temperature tensile properties of Ti alloys made by BE PM processes in Ref. [152].	24
Table 1.6: Mechanical properties of PM Ti-6Al-4V samples produced using BE and PA approaches and different PM processes [11].	26
Table 2.1: Powder particle size and composition (wt%). (“-“ Element not indicated by supplier).	47
Table 2.2: Results of particle size analysis of the starting powder.	48
Table 2.3: Conditions of powder mixing and milling.	52
Table 2.4: Conditions of powder compaction.	54
Table 2.5: Conditions of powder compact forging.	55
Table 2.6: Conditions of heat treatments of as-forged parts.	56
Table 3.1: Selected powder compacting temperatures for making powder compacts for further sintering and forging experiments and their density.	67
Table 3.2: Relative apparent and tap densities of raw powders.	68
Table 3.3: Relative density of as-sintered powder compacts.	72
Table 3.4: Summary of mechanical properties of as-sintered HDH Ti powder compact with relative density of 91% and oxygen content of 0.41%.	76
Table 4.1: Summary of mechanical properties of specimens cut from as-forged HDH Ti part.	108
Table 4.2: Summary of mechanical properties of specimens cut from as-forged GA Ti-6Al-4V part.	108
Table 4.3: Summary of mechanical properties of specimens cut from as-forged HDH Ti-6Al-4V part.	108
Table 4.4: Nitrogen and oxygen contents of the as-forged parts.	109
Table 4.5: Summary of mechanical properties of tensile test specimens cut from as-forged GA Ti part.	113
Table 4.6: Summary of mechanical properties of tensile test specimens cut from the as-forged HDH Ti part made with a holding time of 5 minutes.	116
Table 4.7: Mechanical properties of as-forged Ti and Ti-6Al-4V parts made by powder compact forging in this study and the typical corresponding mechanical properties of ingot metallurgy Ti and Ti-6Al-4V.	136
Table 5.1: Mechanical properties of different as-forged Ti parts and forged HDH	

Ti part after annealing.	145
Table 5.2: Summary of average mechanical properties of as-forged HDH Ti-6Al-4V parts with oxygen content of 0.52% and those after different heat treatments.	153
Table 5.3: Summary of average mechanical properties of as-forged GA Ti-6Al-4V parts with oxygen content of 0.14% and those after different heat treatments.	161
Table 6.1: Results of EDS points analysis at the points shown in Figure 6.8.	181
Table 6.2: Mechanical properties of the tensile test specimens cut from the sample produced by forging the compact of powder mixture with holding time of 10 minutes at 1350 °C.	186
Table 6.3: EDS points analysis data in Figure 6.22.	200
Table 6.4: Oxygen content of forged samples made using powder mixture and composite powders.	201
Table 6.5: Mechanical properties of the tensile test specimens cut from the sample produced by forging the compact of GA Ti/Al-40wt%V composite powder milled at the speed of 200 rpm for 6 hours.	207

Abbreviations

AAE	Arzt, Ashby, and Easterling
AF	As forged
AS	As sintered
BE	Blended elemental
BUS	Broken up structure
C	Compression
CCW	Counterclockwise
CHIP	Cold and hot isostatic pressing
CIP	Cold isostatic pressing
CW	Clockwise
DTA	Differential thermal analysis
ECAE	Equal channel angular extrusion
ECAP	Equal channel angular pressing
EDM	Electric discharge machining
EDS	X-ray spectrometer
EI	Elongation
ELI	Extra-low interstitial
FD	Forging direction
GA	Gas atomized
HCF	High cycle fatigue
hcp	Hexagonal close-packed
HDH	Hydride-dehydride
HEMM	High energy mechanical milling
HERS	Hot extrusion reaction synthesis
HIP	Hot isostatic pressing
HT	Heat treatment
HTC	Hot triaxial compaction
IHF	Isothermal hot forging

MA	Mechanically alloying
OM	Optical microscope
P&S	Single pressing and sintering
PA	Pre-alloyed
PCA	Process control agent
PCF	Powder compact forging
P-FD	Perpendicular forging direction
PIM	Powder injection moulding
PM	Powder metallurgy
RA	Reduction area
REP	Rotating electrode process
SADP	Selected area diffraction pattern
SEM	Scanning electron microscope
SEP	Strain Energizing Process
STA	Solution treatment and aging
T	Tensile
TEM	Transmission electron microscope
Ti64	Ti-6Al-4V
UTS	Ultimate tensile stress
VHP	Vacuum hot pressing
VS	Vacuum sintering
XRD	X-ray diffraction
YS	Yield stress

Chapter 1: Introduction and Literature Review

1.1 Introduction

Titanium and its alloys have been applied in various fields, including automobile [1, 2], aerospace [3], chemical engineering and medical devices such as orthopaedic implants [4], due to their high strength to density ratio, low modulus, high corrosion resistance and good biocompatibility. Plenty of titanium and titanium alloy products such as turbine blades [5], landing gears [6], fasteners [7], and artificial hip joints [8], have been manufactured by casting, cold and hot working.

Recently, more attention has been paid to titanium powder metallurgy (PM) [9-12] to produce near-net shaped parts with good dimensional tolerance, due to its outstanding advantages over ingot metallurgy, such as microstructural homogeneity, less compositional segregation and no constraint in alloy composition. So far powder injection molding (MIM) [13], hot isostatic pressing (HIP) [14], laser sintering [15] and powder forging [16] have been applied to manufacture near-net shaped parts. However, one main obstacle for wider industrial applications of titanium and its alloy manufactured by powder metallurgy is the high cost of good quality raw powders (i.e. powder produced by gas-atomization with a low oxygen level) [17], so a large amount of research [18, 19] has focussed on minimizing the cost of raw powders. Among these, a blended elemental approach (BE) is one of the common ways to manufacture titanium alloy products with low cost. However, the quality of the final products, in terms of their mechanical properties and porosity level, is poorer than those made by a pre-alloyed approach (PA) using powders with a low level of impurities. In order to manufacture titanium and titanium alloy products with high quality, a PA approach is preferred for structural parts in aerospace and the automobile industry

[1, 20, 21] regardless of the high cost of the raw powders. As one of several rapid consolidation methods, powder compact forging has been used in some industrial fields, such as automotive [22, 23]. Generally, there are three steps included in the powder forging process [24, 25]: (1) powder compaction; (2) sintering; (3) forging. To constrain grain growth, a powder forging process without a sintering step is used to produce nano-material and amorphous bulk material [26].

The purpose of this research is:

- To test the feasibility of making low cost titanium/titanium alloy rocker arms by powder compact forging.
- To determine the effects of processing parameters and raw powders on the relative density of HDH Ti, and HDH and GA Ti-6Al-4V powder compacts.
- To determine the factors that control the induction sintering of HDH Ti, HDH and GA Ti-6Al-4V powder compacts.
- To understand the effects of raw powders, powder compact forging parameters and heat treatment conditions on the microstructure and mechanical properties of as-forged HDH Ti parts and Ti-6Al-4V parts made using HDH and GA pre-alloyed Ti-6Al-4V powders.
- To determine the effects of raw powders, milling conditions and powder compact forging parameters on microstructure and mechanical properties of as-forged Ti-6Al-4V parts made using Ti and Al-V master alloy powders.

There are seven chapters in this thesis. A literature review on the powder metallurgy of titanium and its alloy is presented in Chapter 1. Chapter 2 introduces the experimental procedure including raw materials, experimental procedures and information on the testing equipment used. In Chapter 3, compaction and induction sintering of Ti and Ti-6Al-4V powders are investigated. The results of a study on powder compact forging of Ti and Ti-6Al-4V powders

using GA and HDH Ti, and GA and HDH pre-alloyed Ti-6Al-4V powders are presented and discussed in Chapter 4. This also includes an investigation of the fracture behaviour of as-forged Ti and Ti-6Al-4V parts. In Chapter 5, the effects of various heat treatments on the microstructure as-forged parts is investigated to improve the mechanical properties of as-forged Ti and Ti-6Al-4V parts with appropriate microstructural modification. In Chapter 6, the microstructure and mechanical properties of Ti-6Al-4V rocker arms made in two different ways are presented and discussed. Rocker arms were made by forging mixtures of Ti and Al60V40 (in wt%) master alloy powders, and also by using mechanically alloyed powders produced by high energy mechanical milling (HEMM) of mixtures of Ti and Al60V40 master alloy powders. The conclusions from these studies and recommendations for further work are presented in Chapter 7.

1.2 Literature Review

1.2.1 Powder Metallurgy in General

Powder metallurgy (PM) is widely used as one of the advanced technologies for manufacturing near-net shaped parts or structural members. The production boom in PM parts started from the 1970s and so far a lot of PM parts have been manufactured as structural and functional parts for automobile applications [27, 28] (such as connecting rods [29], gears [30]) and metal cutting wheels [31]), aerospace [32], biomedicine [33] and other fields [34, 35]. This is mainly due to the outstanding advantages of the PM process, including low-cost facilities for manufacturing products, low material waste, fewer steps to produce near-net shaped and fully consolidated parts with more complex geometries and high materials strength. There are also a few disadvantages of PM processing which restrict its applications. They include high raw material cost and low ductility and

strength due to high levels of porosity and contamination during some powder metallurgical processes, such as a powder injection molding approach.

In general, the processing steps in powder metallurgy consist of powder making, mixing, powder compaction and sintering as shown in Figure 1.1. In the first place, feedstock powder can be produced by various methods, such as atomization [36-40], mechanical methods [40], chemical and electrolytic methods [40]. In the second place, a homogeneous powder mixture is obtained by mixing elemental powder with alloying powders, and also lubricants are added to powders by mixing to reduce the internal friction between the particles during compaction. Thirdly, a powder compact of designed desired shape is made into a die. Finally, the powder compact is sintered, and the powder particles are bonded atomically.

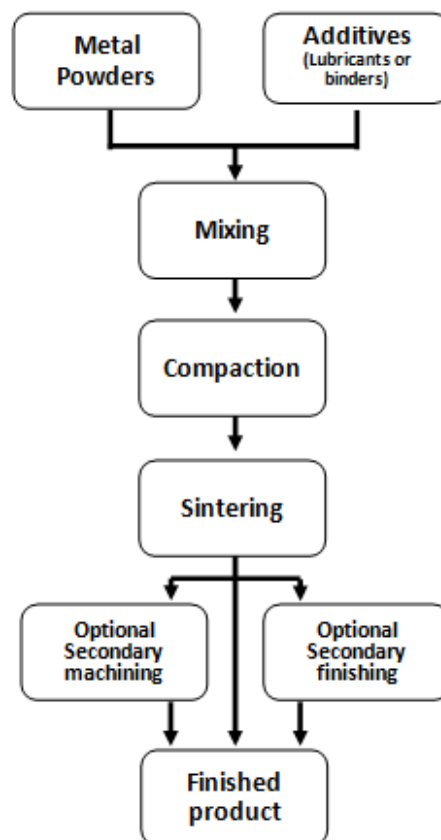


Figure 1.1: Conventional PM process.

1.2.1.1 Compaction

Generally, powder compacts for sintering are made by die compaction and cold isostatic pressing (CIP) [41-44]. Even though powder compaction is not the final step, it directly affects the sintering step which follows and the microstructure and mechanical properties of the material in the final parts. Die compaction is used to make powder compacts in a die under an axial compressive load. The effect of die compaction on metal powders can be described as having several stages. In the early stage of compaction, under low pressure, particle rearrangement occurs to fill the large gaps between particles leading to an increase in particle packing density. With a further increase in pressure, plastic deformation of powder particles occurs during the intermediate stage of compaction, then in the final stage, both cold welding and mechanical interlocking occur as the main mechanism for creating strength in the powder compact [45]. During die compaction, parameters such as the size [46, 47] and shape [48-50] of particles, friction between particles [51-54], work hardening [46], compacting pressure [48, 55-57], temperature and ejection force [54] all have an effect the density and density distribution of a powder compact [46].

Plastic deformation of powder particles occurs earlier [54] in warm compaction than in cold compaction. The parameters which influence the density of powder compacts made by warm compaction are the same as those which influence the density of powder compacts made by cold compaction, except that the compacting temperature plays a more important role in warm compaction. As shown in Figure 1.2, with increasing compaction temperature, the densities of different metal powder compacts, including Ti powder compacts, increase markedly. So warm compaction is an important and effective way to improve the density of titanium and titanium alloy powder compacts.

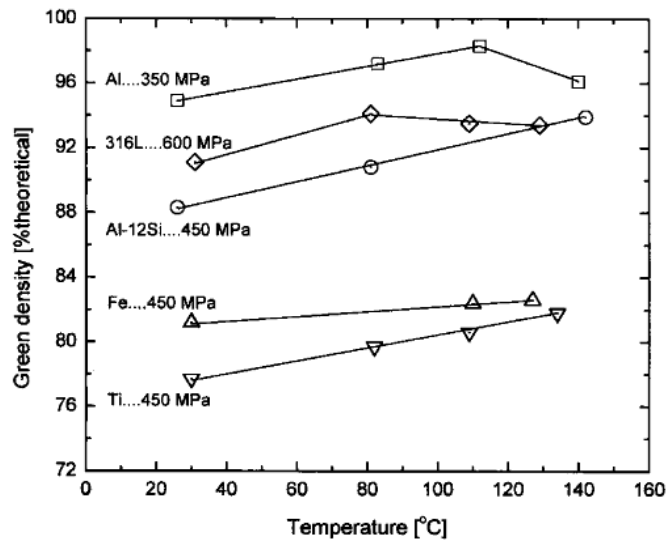


Figure 1.2: Effect of temperature on the green compact density of various metal powders [54].

1.2.1.2 Sintering

During sintering, gaps between the particles are reduced or eliminated, and bonds between particles are established by diffusion. Generally, during the sintering process, a powder compact is heated up to a temperature which is about 80% of the metal or alloy's melting temperature (in Kelvin scale), and then held at this temperature for a period of time to achieve near to full density. The biggest challenge for this process is that shrinkage occurs during sintering. If the shrinkage is not uniform in different directions, cracking or distortion of the powder compact may occur. Several novel methods have been developed to rapidly sinter a powder compact, such as induction sintering [58], spark plasma sintering [59-61], microwave sintering [62-68] and electrical resistance sintering [69, 70]. Furthermore overpressure sintering [71] is also used to accelerate the densification process.

The reduction in total interface energy as lower energy solid-solid interfaces form between powder particles is the main driving force for the sintering process. There are three stages in the solid state sintering process: an initial stage, an intermediate stage and a final stage. In the initial stage, necking forms between particles, and

the neck size is small. The end of the initial stage is determined by achieving a neck size to particle diameter ratio of 0.3 [72]. Several mass transport mechanisms, including surface diffusion, viscous flow, plastic flow, evaporation-condensation, volume diffusion and grain boundary diffusion operate in the process of neck growth [72]. The two spherical particle model is widely used to illustrate the neck growth in the initial stage, as shown in Figure 1.3, and the mass transport is driven by the curvature gradient at the neck area [72].

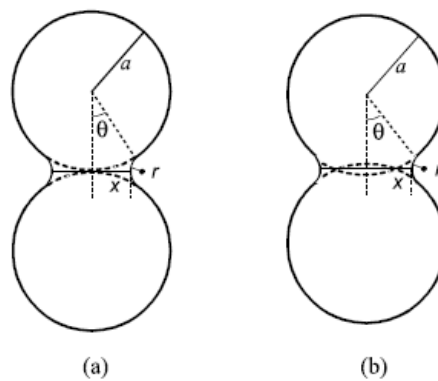


Figure 1.3: Two spherical particle model for initial stage of sintering (a) without shrinkage and (b) with shrinkage [73].

At the beginning of the intermediate stage, interconnected pores form in the powder compact, and the pore geometry is cylindrically-shaped and surrounding the necks on grain edges as shown in Figure 1.4. The grain is assumed to be a tetrakaidecahedron. There are two ways of mass transport in the intermediate stage [72]: volume diffusion and grain boundary diffusion. In the final stage of sintering, pores become closed and spherical, as shown in Figure 1.5. The process of isolation and spheroidization of pores in this stage is explained in Ref. [72]. Also both volume diffusion and grain boundary diffusion are densification mechanisms in the final stage, and the powder size and sintering temperature would determine which mechanism is dominant [72].

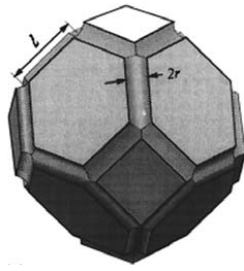


Figure 1.4: Pore structure in the intermediate stage of sintering [73].

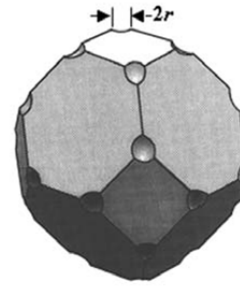


Figure 1.5: Pore structure in the final stage of sintering [73].

1.2.1.3 Powder Forging

Powder forging combines powder metallurgy (PM) and bulk material forging technology, and has the advantages of both processes. A variety of products with complex shapes can be produced by powder forging without considering the alloy constituent [74-81]. Generally, there are three steps [25] in the powder forging process: (1) to make the powder into a green compact with 10–30% porosity using an accurate powder mass, (2) to sinter the powder compact in a protective environment to eliminate the metal oxides and (3) forging the powder compact in a die to the designed shape. Powder forging is one kind of rapid densification process [82]. Powder repressing and powder upsetting in Figure 1.6 are two variations of powder forging [83], and they are distinguished by the degree of material flow. In a powder repressing process, the material flow is along the pressing direction, which is much less than in powder upsetting, while in a powder upsetting process, a large amount of material flows along the lateral direction. The parts made by powder upsetting have good mechanical properties due to high material flow, while those produced by powder repressing have a more complex shape. Also the powder forging process can be divided into two types, according to the type of forging die used, namely a trap die and an impression die with flash [83], as shown in Figure 1.7.

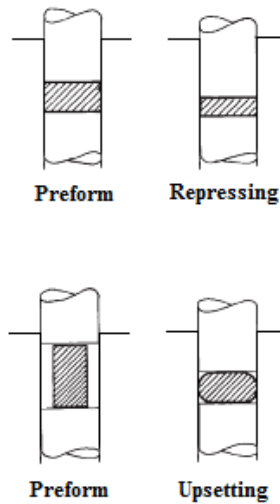


Figure 1.6: Schematic diagram of the powder repressing and upsetting processes [83].

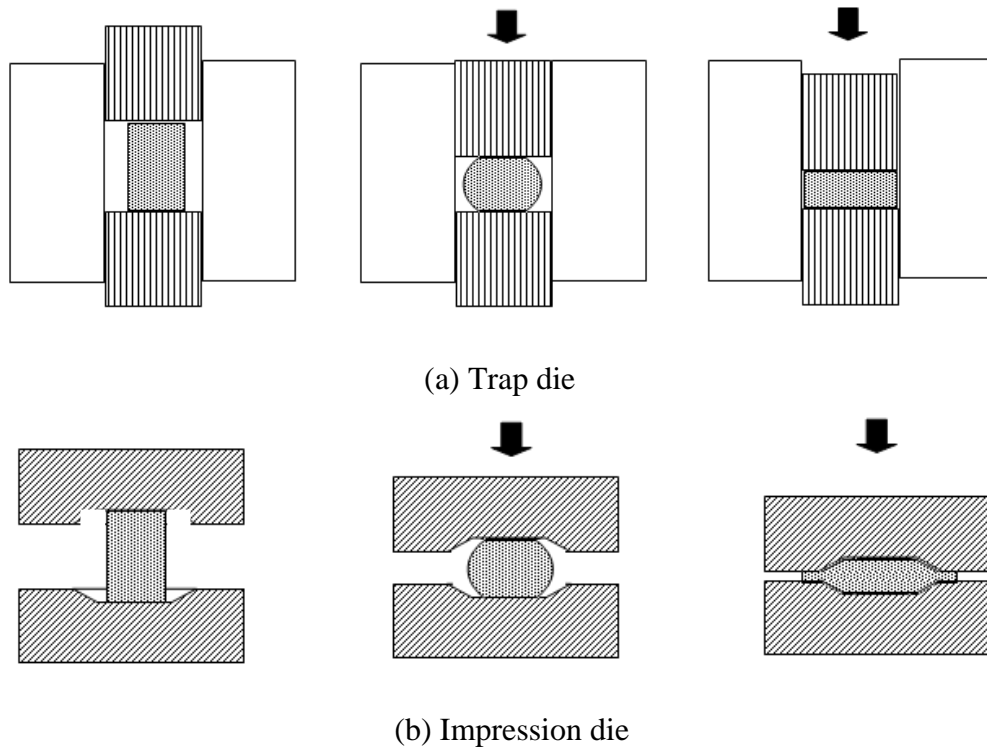


Figure 1.7: Powder forging process with different dies [83].

Also, a powder forging process has two variants [72]: high-strain-rate forging, which is a rapid densification under a stress which exceeds the material tensile strength, and low-strain-rate sinter-forging with a low stress and a time for forging which is similar to that required for sintering without stress. The effect of pressure on densification of alumina during a sinter-forging process has been investigated

and the results are shown in Figure 1.8 [72]. With increasing pressure, the densification rate increased. Also the stress required to achieve densification depends on temperature. With an increase in temperature, the yield strength of the material decreases and as a result, the material flows more easily, but large deformation could easily lead to cracking due to large circumferential tensile stresses. The forging window [72] in Figure 1.9 has been developed according to the fracture limit and the strain of 50% required by good particle bonding.

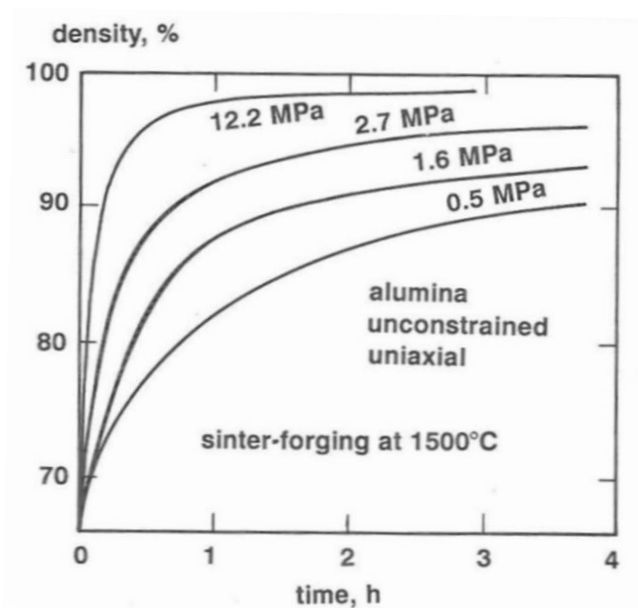


Figure 1.8: The effect of applied pressure on densification of alumina at 1500°C during sinter-forging process [72].

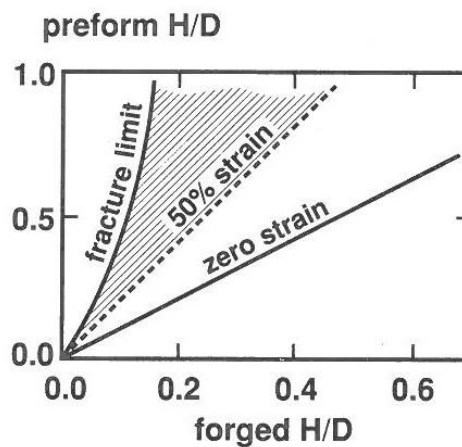


Figure 1.9: A fracture limit determined by preform and forged height to diameter ratio: H/D [72].

Isothermal forging [84-87] is also used to forge titanium alloys and nickel-base superalloy powder compacts. Due to its low strain rate, stable temperature and high die temperature compared with conventional powder forging, parts with good quality and properties can be obtained. Other powder forging techniques include “Orbital Forging” and the TR-Method, introduced in Ref. [83].

An axial compressive stress acts on a powder compact during powder forging, and the material flow laterally, which leads to numerous shear stress as a result of fresh surfaces being formed by the fracturing of oxide films on the powder particle leading to enhanced particle bonding. The way in which pores collapse by conventional hot forging is schematically contrasted with hot isostatic pressing in the final stage of sintering in Figure 1.10, based on a spherical closed pore in the powder compact [72]. The shear deformation of the powder compact caused by forging plays an important role in removing the pores in the compact completely, whereas the pores only shrink under the hydrostatic compressive stress during HIP. Although the pores in the powder compact can be removed completely by further diffusion assistance with pressure during HIP, this process requires a long time to complete. In contrast, the pores in a powder compact can be rapidly removed by plastic deformation during forging. Compared with other pressure-assisted sintering processes such as HIP and hot pressing, forging is the fastest densification process due to a collapsing of pores by plastic deformation.

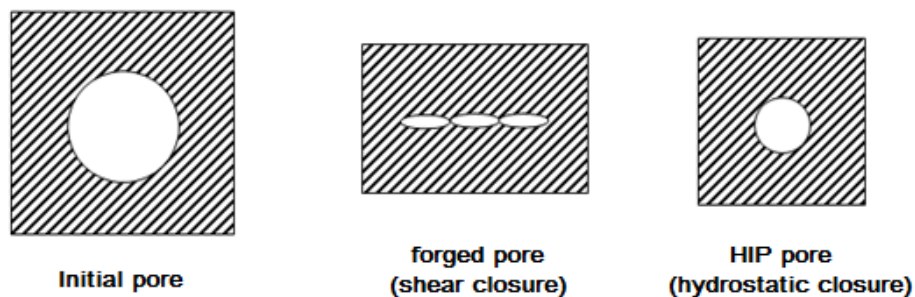


Figure 1.10: Pore collapse in the final stage of sintering by hot forging and HIP [72].

During the forging of a powder compact, an upsetting bulging deformation and densification occur simultaneously. This is different from the conventional solid material forging approach without a densification process. Several models [88-90] have been established to analyze and simulate the forging process. Among these models, the Arzt, Ashby and Easterling (AAE) model [26] was successfully used to simulate the rapid forging process of nanometer sized metal powders. In the AAE model, yielding, creep, and diffusion are three possible mechanisms for plastic flow of material, which controls the densification. The results show that creep plays an important role in the forging process. The relative density-pressure curves produced by only simulating creep without considering yield and diffusion effects are nearly the same as the relative density-pressure curves obtained through experiments, as shown in Figure 1.11. In the meantime, the AAE model can be modified to simulate the forging of micrometer-sized powders by replacing $D_b f$ for D_v in Eqs. [19] and [21] of Ref. [91], $K_K = 5.3 \left[\frac{A b D_b f}{K T \mu^{n-1}} \right] (P)^n$ and $K_K = \frac{3}{2} \left[\frac{A b D_b f}{K T \mu^{n-1}} \right] \left(\frac{3P}{2n} \right)^n$, K_k is a constant related to pressure, temperature, the parameters of diffusion and heat conductivity, etc, A is the Dorn constant, b is the Burgers vector, D_b is the grain boundary diffusion coefficient, f is the fraction of the material volume which is occupied by grain boundaries, K is a constant, μ is the shear modulus, T is the temperature, P is the pressure and n is a creep stress exponent. The densification rate due to creep is at least twice that due to diffusion and plastic yield, so it can be concluded that the dominant densification mechanism in this forging process at low temperature is creep, which is accelerated by having a nanostructure.

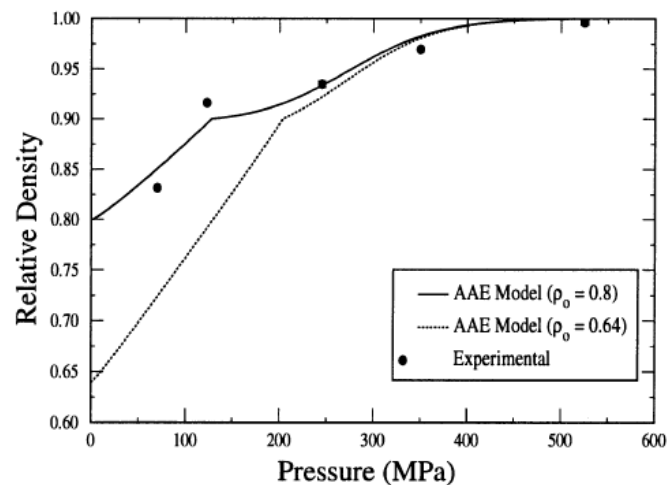


Figure 1.11: Relative density of powder compact as a function of forging pressure, including experimental data and AAE model in Ref. [26].

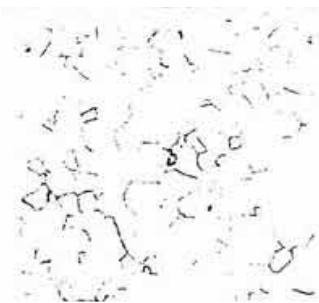
Powder forging has been used to manufacture components, such as gears [92-94], hubs [95], bearings [96], connecting rods [97-101] and so forth, and its material selection ranges from metal to ceramic, such as aluminum alloys [102-104], steel [105], titanium [99, 100], refractory metals including tungsten [106] and molybdenum [107], alumina [108, 109], silicon carbide [110, 111] and zirconia [112, 113].

1.2.2 Titanium and Its Alloys

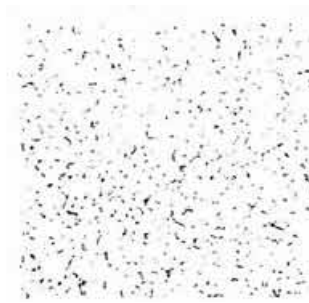
1.2.2.1 Classification of Titanium Alloys

Alloying elements added to titanium are classified into three types: neutral, α stabilizers, and β stabilizers. α stabilizers increase the α transus temperature, and they include Al, O, N and C. β stabilizers reduce the β transus temperature. There are two types of β stabilizers: isomorphous β stabilizers, which have a high solubility in titanium (e.g. Mo, V, Nb, Ta) and eutectoid β stabilizers which can form intermetallic compounds with titanium (e.g. Fe, Mn, Cr, Cu, Co, Ni, Si, H). Neutral elements don't change the α and β transus temperatures, and they include

Zr and Sn. There are five types of titanium alloys, namely α , near α , α/β , metastable β and β alloys. α alloys include unalloyed pure titanium and titanium alloys with additions of α stabilizers only. Near α alloys have a similar microstructures to α alloys, except a limited amount of β phase exists in the microstructure after heat treatment [114] due to adding a minor amount of β stabilizers into titanium. α/β alloys such as Ti-6Al-4V are widely used in various fields [115, 116], and they consist of an α phase and a retained or transformed β phase with a volume fraction in the range of 5-40% [117]. Both metastable β and β alloys retain the β phase at room temperature after cooling from high temperature. They do not experience martensite formation during fast quenching, but metastable β alloys will allow precipitation of the α phase during aging after quenching. The typical microstructures of Ti alloys are shown in Figure 1.12.



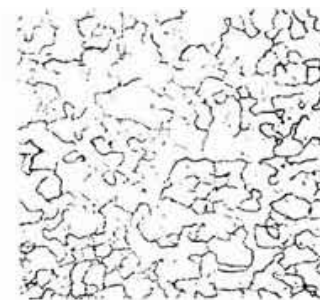
(a) Equiaxed α grains in CP Ti
after 1 h annealing at 699 °C



(b) Equiaxed $\alpha+\beta$ grains



(c) Acicular $\alpha+\beta$
in Ti-6Al-4V



(d) Equiaxed β grains
in Ti-13V-11Cr-3Al

Figure 1.12: Typical microstructures of α , $\alpha+\beta$, β alloys [114].

1.2.2.2 Commercially Pure (CP) Ti

There are four grades of CP Ti, each with increasing oxygen content as an interstitial element. The addition of oxygen increases the strength of CP Ti, but reduces its ductility. The compositions of the four grades of CP Ti are listed in Table 1.1. The equiaxed microstructure of CP Ti is shown in Figure 1.12. The mechanical properties of the four grades of CP Ti are summarized in Table 1.2. From the table, Grade 1 CP Ti has the lowest ultimate tensile strength (UTS) and yield strength of 240 MPa and 170 MPa and the highest elongation of 24%, among these four grades of CP Ti. Grade 4 Ti has the highest UTS and yield strength of 550 MPa and 480 MPa, respectively, and the lowest elongation of 15%, due to its highest oxygen content of 0.4% [117].

Table 1.1: Compositions of four grades of CP Ti [118].

CP Ti	O	N	C	Fe
Grade 1	≤0.18	≤0.03	≤0.10	≤0.20
Grade 2	≤0.25	≤0.03	≤0.10	≤0.30
Grade 3	≤0.35	≤0.05	≤0.10	≤0.30
Grade 4	≤0.40	≤0.07	≤0.10	≤0.50

Table 1.2: Mechanical properties of four grades of CP Ti sheet, strip and plate [118].

CP Ti	UTS (MPa)	Yield Strength (MPa)	Elongation (%)
Grade 1	240	170	24
Grade 2	345	275	20
Grade 3	445	380	18
Grade 4	550	480	15

1.2.2.3 Ti-6Al-4V Alloy

Ti-6Al-4V (wt%) alloy is the most popular and intensively studied titanium alloy so far since 1950's, due to its good balance of properties as shown in Table 1.3. Its Young's modulus ranges from 110 to 140 GPa, and its yield strength varies from 800 to 1100 MPa. Ti-6Al-4V is a typical $\alpha+\beta$ alloy, and its microstructure is

an acicular $\alpha+\beta$ as shown in Figure 1.12. The oxygen content has a significant effect on the mechanical properties of Ti-6Al-4V alloy. It ranges from 0.08 to 0.2wt% in Ti-6Al-4V alloy for commercial applications. As shown in Figure 1.13, the strength of Ti-6Al-4V alloy increases, but its elongation decreases with increasing oxygen content [119]. Ti-6Al-4V ELI (extra-low interstitial) [118] was developed with very low oxygen content ($<0.13\%$) and iron contents to get higher damage-tolerance properties.

Table 1.3: Mechanical properties of Ti-6Al-4V alloy [117].

	Hardness [HV]	E [GPa]	UTS [MPa]	YS [MPa]	El %	K_{Ic} [MPa m ^{1/2}]
Ti-6Al-4V	300-400	110-140	900-1200	800-1100	13-16	33-110

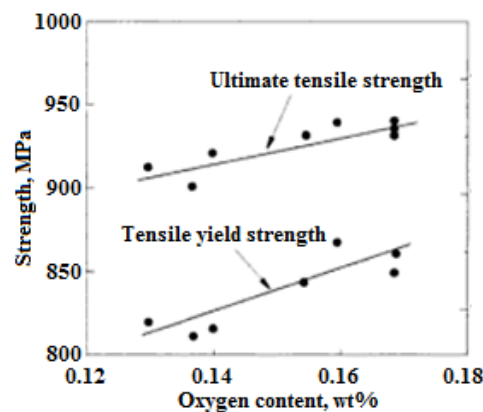


Figure 1.13: Effect of oxygen content on the strength of Ti-6Al-4V [118].

Both classical equiaxed and acicular $\alpha+\beta$ microstructures of Ti-6Al-4V alloy are shown in Figure 1.12. The microstructures of Ti-6Al-4V are changed with different thermomechanical treatments, including deformation, heat treatment, etc. The sizes of lamellae and equiaxed grains in the microstructures are significantly dependent on cooling rates and heat treatment temperature. In cooling from the β phase field, the lamellae become coarsened with a low furnace cooling rate, while martensitic transformation occurs with a fast cooling rate from water quenching. To obtain an equiaxed microstructure, deformation is necessary to break up the α

lamellae. Duplex microstructures consisting of lamellae and equiaxed grains are obtained by solution heat treatment just below the β transus temperature. A Ti-6Al-4V alloy with an equiaxed microstructure has high ductility and fatigue strength, while a lamellar microstructure can improve fracture toughness. Duplex microstructures give the best balance of properties.

1.2.2.4 Thermomechanical Processing and Heat Treatment of Titanium Alloys

Conventional titanium alloy processing involves four steps: (1) vacuum arc melting and ingot casting; (2) primary hot working to break down grains by hot forging; (3) recrystallization annealing and (4) secondary hot working. The grain sizes of titanium alloy ingots produced by vacuum arc melting and ingot casting range from 75 μm to 1.5 mm diameter [120], so it is necessary to break down the coarse grains by thermomechanical processing in the second step. In the second step, there are two types of hot forging, cogging [121, 122] and upsetting [123-125]. In the upsetting process, a round ingot is compressed along its axis, while the round ingot is elongated along its axis by several side pressing operations. An upsetting process is often followed by cogging down to get a uniform microstructure [123]. Recrystallization annealing causes the globularization of Widmanstätten α and grain boundary α [120]. Most of the secondary hot working of titanium alloys is done in the $\alpha+\beta$ phase field [126, 127], and the microstructure obtained is an equiaxed primary α in a transformed β matrix. Beta forging [123, 128] is another common type of hot working of titanium alloys. The high forging temperature allows the use of a low working pressure and effective die fill during forging. A Widmanstätten or acicular α microstructure are evolved after beta forging [120].

Heat treatments are often used to improve the mechanical properties of the hot worked parts. They include duplex annealing, solution treatment and aging, beta

annealing, beta quenching, recrystallization annealing and milling annealing. Duplex annealing includes annealing in the $\alpha+\beta$ phase field, followed by mill annealing, which can improve the creep resistance of Ti-6Al-2Sn-4Zr-2Mo alloy [129] significantly. During recrystallization annealing of Ti-6Al-4V alloy, a high volume fraction of equiaxed α grains with β particles at triple grain junctions form with a slow cooling rate of 50 °C/h, and such a microstructure provides high damage tolerance [130]. Beta annealing [131] is used for fracture critical components with high damage tolerance, but if the rate of cooling from the β phase field is high, the part can have a finer transformed microstructure which results in high tensile strength and lower damage tolerance. Solution treatment and aging [132] is used to increase the tensile strength. For $\alpha+\beta$ titanium alloys such as Ti-6Al-4V, the strength can be increased by ~200 MPa. The mechanical properties of Ti-6Al-4V alloy after different heat treatments are listed in Table 1.4.

Table 1.4: Ti-6Al-4V properties after heat treatments [114].

Condition	UTS (MPa)	Yield Strength (MPa)	Elongation (%)
Mill annealed	1060	945	10
Duplex annealed	965	917	18
Solution treated and aged	1151	1103	13

1.2.3 Powder Metallurgy of Titanium and Titanium Alloys

Owing to high specific strength and good biocompatibility, titanium and titanium alloys are used in many fields including automobile [1], aircraft and surgical implants [4]. However, compared with other light metals and alloys (aluminum and magnesium alloys), expensive raw materials and a difficulty in machining constrain the applications of titanium and titanium alloys. Near-net shape manufacturing can significantly reduce the manufacturing costs of titanium products with less material waste and shorter machining time. Due to lower cost,

uniform grain size and composition distribution, powder metallurgy is an effective near-net shape manufacturing process to replace casting and isothermal forging for producing titanium alloy products. Recently, Dynamet Technology, Inc has received qualification approval from Boeing to supply PM Ti-6Al-4V products for commercial aircraft applications, which is a milestone in the field of PM Ti [133].

Pre-alloyed (PA), and blended elemental (BE) approaches (shown in Figure 1.14) are two major methods which are widely used for making titanium and titanium alloy parts by powder metallurgy. For making structural titanium alloy parts used in the aircraft industry, a PA approach is the first choice to obtain the required mechanical properties of the final aircraft parts, while it is difficult to obtain such properties by a BE approach due to a higher porosity level caused by the salt impurities originating from the raw material (titanium sponge) used in titanium powder manufacturing process. Compared with a PA approach, the BE approach results in a lower manufacturing cost of the products, so it is favourable for less property demanding and more cost sensitive applications.

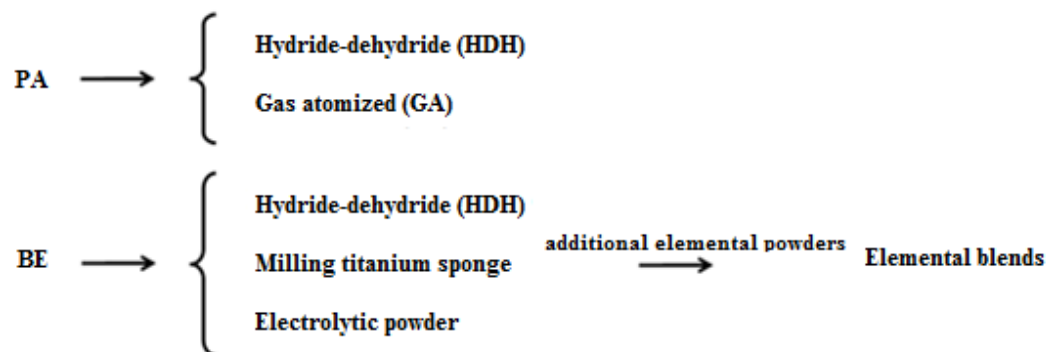


Figure 1.14: Variety of methods used to produce PA and BE starting powder.

As shown in Figure 1.14, the HDH process is widely used to produce titanium and titanium alloy powders, owing to its low cost and complexity. In the HDH process titanium sponge or titanium alloy machining chips are first combined with hydrogen to form titanium hydride. The brittle hydride sponge or chips are milled

to produce a finer titanium hydride powder and then finally hydrogen is desorbed in a vacuum at elevated temperature to produce titanium and titanium alloy powders. A controlled passivation is required to form a stable and dense TiO_2 film on the powder surface, so as a result, the oxygen and nitrogen level of HDH powders are increased [134]. Also in order to reduce the cost of HDH powders, a process has been developed where TiH_2 starting powder, generated from a modified Kroll process, is cooled down in hydrogen rather than in an inert gas, and the hydrogen is removed from the titanium hydride during vacuum sintering [135, 136]. Gas atomized (GA) titanium and titanium alloy powders have a lower content of impurities than found in HDH titanium and titanium alloy powders, but fine ceramic particles, such as yttrium, could be a source of contamination during this process. Also entrapped argon gas is another limitation of GA powder [134]. Similar to the GA process, spherical titanium and titanium powders can be produced by plasma atomization [134]. Titanium sponge fines can be produced by the Hunter process or Kroll process directly, but their coarse particle size (180-185 μm) and contamination by metallic-salt residues from these processes limit their application [134]. Milling titanium sponge is also a low cost process for producing titanium and titanium alloy powders with irregular particle morphology and relatively low impurity contents (such as chlorine and oxygen). The Rotating Electrode Process (REP) can produce high quality titanium and titanium alloy powders with a spherical particle morphology, but the production cost is relatively high. Low cost titanium and titanium alloy powders made by the HDH process always have a high oxygen content and residual chlorine when made using the Kroll and Hunter processes. In order to achieve low-cost, high-performance PM Ti parts, additions of rare earth (RE) elements in the form of oxides, hydrides and silicides (such as Y_2O_3 [137], YH_2 [138, 139] and CeSi_2 [140]) have been successfully introduced into titanium and titanium alloy powders to scavenge oxygen and chlorine from titanium. Also, a “meltless” titanium powder is

currently receiving much attention as a low cost way to produce titanium and titanium alloy powders. Such methods are the Armstrong process and the Fray, Farthing and Chen (FFC) Cambridge process [134].

Until now, many PM processes have been used to consolidate titanium and titanium alloy powders to make shaped components or samples for research. They include press and sintering [141], metal injection moulding, debinding and sintering [142], hot pressing [143], hot isostatic pressing [14], laser sintering [15], electron beam melting [144], plasma spark sintering [145], microwave sintering [146], electrical resistance sintering [147], powder compact forging [148], powder rolling [149] and powder extrusion [150, 151].

1.2.3.1 Microstructure and Mechanical Properties of Titanium and Titanium Alloys Produced by Powder Metallurgy

The microstructure and mechanical properties of titanium and titanium alloy powder metallurgy products are not only dependent on the powder stock (BE or PA), but also on the powder metallurgy conditions. The fatigue properties of titanium and titanium alloy PM products is better than that of the corresponding cast products, and close to that of the wrought products as shown in Figure 1.15.

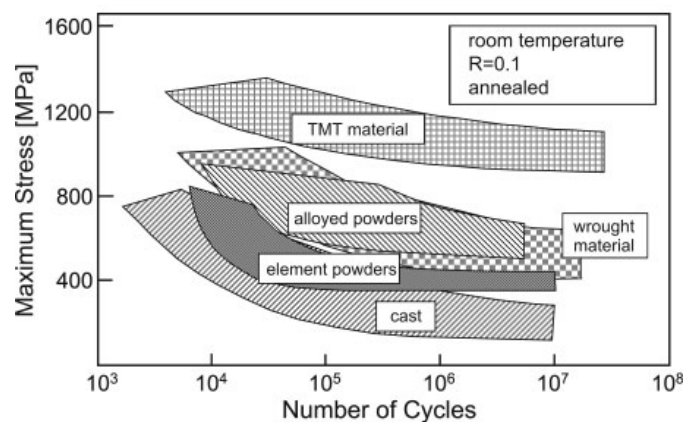


Figure 1.15: High-cycle fatigue results of Ti-6Al-4V at room temperature with different alloy status in Ref. [117].

The blended elemental (BE) PM approach manufactures titanium alloy products by mixing titanium powder and other elemental powders. One major drawback of this approach [152] and which is hindering its applications is the formation of a coarse colony microstructure [153] which is composed of aligned α platelets and a grain boundary α phase. Among the various microstructures in titanium alloys, a colony microstructure (shown in Figure 1.16(b)) leads to the lowest high cycle fatigue (HCF) strength [152].

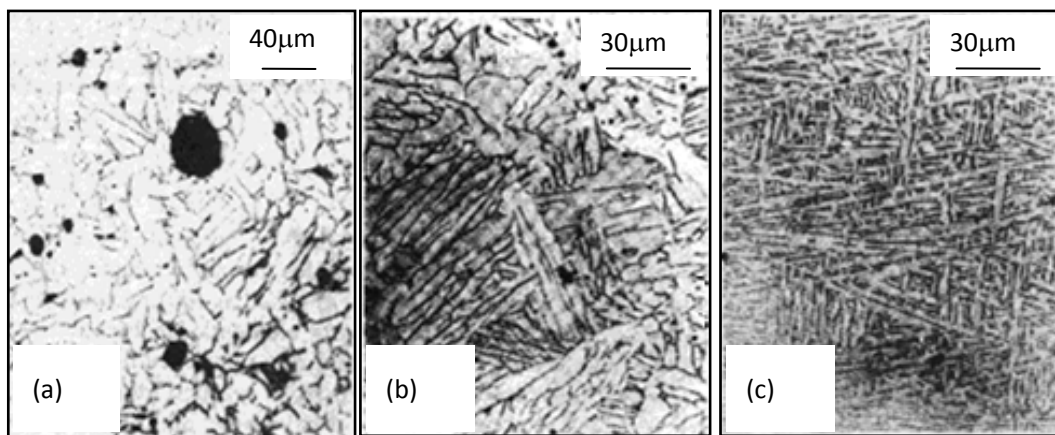


Figure 1.16: Typical microstructures of BE Ti-6Al-4V alloy produced by cold pressing and sintering: (a) die compaction [17], (b) cold isostatic pressing [17], and (c) after the “broken up structure” (BUS) heat treatment [17].

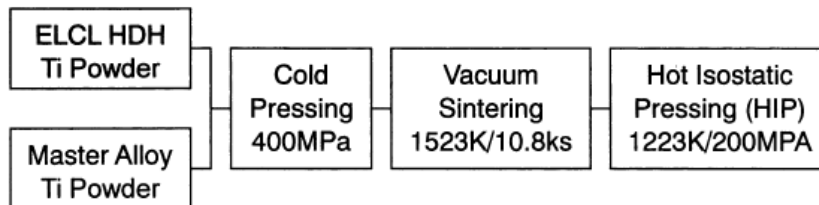
A typical microstructure of α platelets in as-sintered BE Ti-6Al-4V alloy produced by a conventional powder metallurgy process, including cold compaction followed by sintering, are shown in Figure 1.16(a) and (b). α platelets, with a low aspect ratio in as-sintered BE Ti-6Al-4V alloy and produced by cold die compaction and sintering, were achieved. These originated from small β grains. In contrast, typical α platelets with a high aspect ratio were obtained by cold isostatic pressing and sintering of a BE Ti-6Al-4V alloy. During microstructural evolution, large β grains formed at first and then the α platelets formed by a slow cooling rate from above the β transus temperature. The typical α platelets structure could be modified into a “broken-up” structure (BUS) shown in Figure 1.16(c) by heat treatment, and an improvement in fatigue behaviour can be realised by this

microstructural modification.

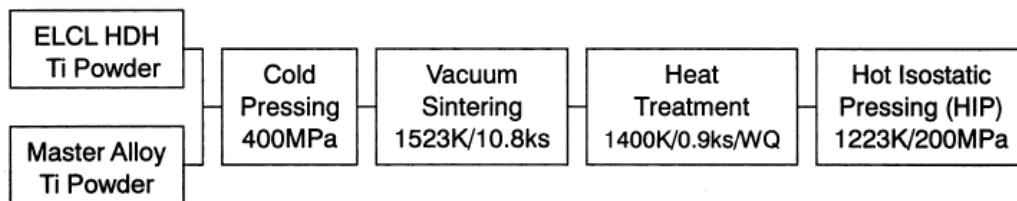
There are several ways to modify the microstructure of titanium alloys produced by powder metallurgy. For near- α and α/β titanium alloys, a colony microstructure can be changed into a finer equiaxed α microstructure (such as a “broken-up” structure) by deformation and beta heat treatment. The equiaxed microstructure, with small grains, can be obtained by deformation and subsequent annealing in the $\alpha+\beta$ two phase region, which leads to improved ductility and high-cycle fatigue (HCF) strength. However, for a BE titanium compact, the combination of deformation and beta heat treatment does not lead to an ideal microstructure. After a hot isostatically pressed (HIPped) titanium alloy is beta solution treated, water-quenched and then annealed in the $\alpha+\beta$ two phase region, an acicular microstructure consisting of α -platelets with a high aspect ratio forms. This microstructure results in an excellent HCF strength, but poor ductility, because of the coarsened prior β grains formed during beta solution heat treatment. To produce fatigue-tolerant titanium alloy products with good ductility by a BE approach, a new BE PM process [152], as shown in Figure 1.17, was developed. In this process, a heat treatment is done after the sintering step and before the final hot isostatic pressing step. It was shown that, compared with the conventional BE PM process, the new BE PM process produced an acicular microstructure consisting of α -platelets with low aspect ratio, leading to a clear improvement in tensile strength [152], as shown in Table 1.5.

The effect of an isothermal hot forging (IHF) on the microstructure and mechanical properties of a Ti-6Al-4V alloy produced by BE PM process were investigated in Ref. [152]. It was found that a low fatigue limit of 172 MPa was achieved from the as-forged samples produced by forging with a 30% reduction. This was because the lenticular α microstructure and residual porosity in the

products greatly influenced the nucleation and growth of fatigue cracks. On the other hand, when the forging reduction reached 78%, a fatigue strength of 485 MPa was achieved, since the resulting microstructure consisted of equiaxed grains with lenticular α platelets and no residual porosity.



Conventional BE PM process



New BE PM process

Figure 1.17: Two BE PM processes for making Ti-6Al-2.75Sn-4Zr-0.4Mo-0.4Si (Ti-1100) alloy [152].

Table 1.5: Room temperature tensile properties of Ti alloys made by BE PM processes in Ref. [152].

Alloy	Method	YS (MPa)	UTS (MPa)	EI. (%)	RA (%)	σ_f (MPa)
Ti-6Al-2.75Sn-4Zr -0.4Mo-0.4Si	Conventional	887	971	11	13	420
	New	1003	1088	10	23	530
Ti-6Al-2Sn -4Zr-Mo	Conventional	892	980	15	31	412
	New	990	1088	15	26	647
Ti-6Al-2Sn -4Zr-Mo-0.1Si	Conventional	970	1058	18	27	
	New	1020	1117	13	18	
Ti-6Al-4V	Conventional	833	921	14	36	411
	New	862	951	15	42	588

The microstructure and mechanical properties of Ti-6Al-4V samples made from PA powders using a variety of powder consolidation methods have been

investigated. A microstructure consisting of α plates in a β matrix is obtained by HIP at temperatures below the beta transus temperature, as shown in Figure 1.18(a). It has been proved that a microstructure consisting of small equiaxed α grains as shown in Figure 1.18(b) is better than a microstructure with coarser or lenticular α grain morphology [17] for improving the fatigue properties of the products made by a PM processes. An equiaxed α grain morphology can be obtained from the HIP process. It is well recognised that a lower α platelet aspect ratio in the microstructure is beneficial to mechanical properties and increasing plastic strain in the α particles caused by plastic deformation is an effective way to reduce the aspect ratio of the α particles (this is called the Strain Energizing Process [154]). This PM process uses a low temperature and high pressure to consolidate the powder, and results in a microstructure consisting of equiaxed α grains and acicular α , as shown in Figure 1.18(c). The original α particle shape can still be observed in some regions where recrystallization did not occur. The fatigue strength of the material can be ameliorated with this PM process.

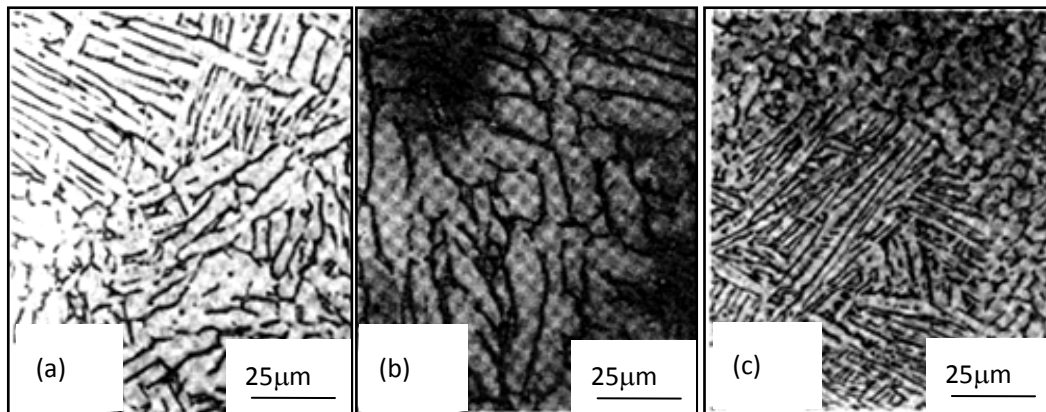


Figure 1.18: Microstructures of Ti-6Al-4V samples produced from PA powder using different powder consolidation conditions [17]: (a) HIP at 900 °C for 2 h with a pressure of 105 MPa in a steel mould; (b) HIP at 925 °C for 4 h with a pressure of 105 MPa in a ceramic mould; (c) Strain energizing process' powder HIP-ed at 870 °C for 2 h with a pressure of 105 MPa in a steel mould.

An uniform recrystallized microstructure consisting of equiaxed α grains can be

obtained by hot pressing of PA Ti-6Al-4V powder, and the favourable Widmanstatten microstructure can be produced by using a high hot pressing temperature and a low heating rate [155]. However, to obtain a fine microstructure, a rapid-heating and short-hold vacuum hot pressing (VHP) process was developed [156]. Compared with Ti-6Al-4V samples produced by HIP, Ti-6Al-4V samples produced by powder forging possess better mechanical properties due to a fine microstructure [157, 158]. The mechanical properties of Ti-6Al-4V parts produced using different BE and PA approaches and different PM processes are listed in Table 1.6, and schematically illustrated in Figure 1.19.

Table 1.6: Mechanical properties of PM Ti-6Al-4V samples produced using BE and PA approaches and different PM processes [11].

	Relative density (%)	UTS (MPa)	YS (MPa)	EI. (%)	Ref.
Conventional BE	95	773	683	6	[159]
CIP+VS BE	95	830	740	6	[160]
MR-9 TM BE	99.2	932	849	14	[159]
CHIP BE	~100	960	882	17	[161]
P&S+HT+HIP	~100	921	1000	17	[161]
TIARA BE	99.6	926	809	19	[162]
PA	~100	992	930	15	[163, 164]
Ceramic mold PA	~100	958	889	14	[165]
Wrought	~100	978	923	16	[163]

*BE: blended elemental approach. CIP: cold isostatic pressing. VS: vacuum sintering. CHIP: cold and hot isostatic pressing. P&S: single pressing and sintering. HT: heat treatment. HIP: hot isostatic pressing. PA: pre-alloyed approach. MR-9TM: a patented blended elemental approach. TIARA: a patented blended elemental approach.

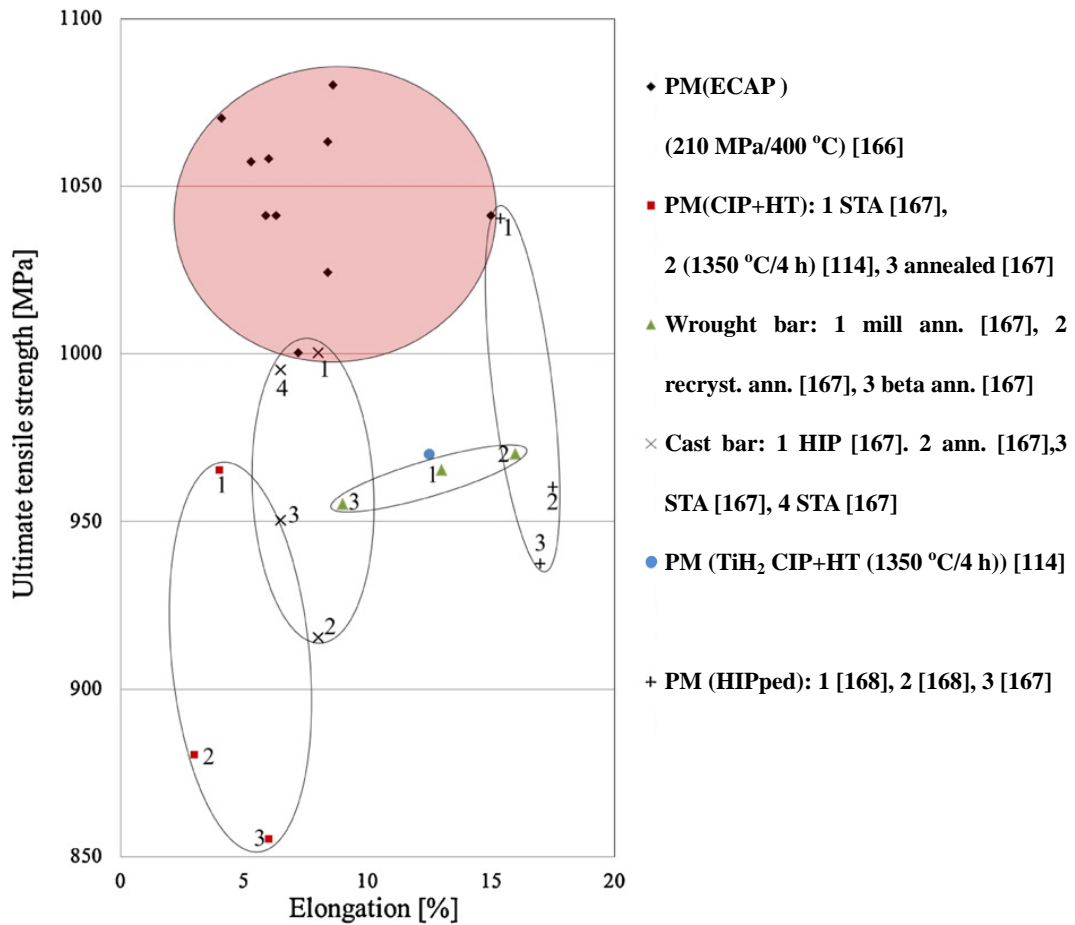


Figure 1.19: A comparison of mechanical properties of Ti-6Al-4V parts produced from PA powder using different PM processes and ingot metallurgy [166].

1.2.3.2 Powder Compact Forging of Titanium and Titanium Alloys

Hot forging of powder compacts is an effective way to consolidate titanium and titanium alloy powders. There are several parameters associated with hot forging which affect the powder consolidation process. Temperature controls two parameters of the powder compact forging process. Firstly, as shown in Figures 1.19 and 1.20, with increasing temperature, the flow stress of the powder particles is reduced, so the required applied pressure becomes lower, and the densification process becomes easier. On the other hand, atomic diffusion directly influences the powder sintering process, and the diffusivity of atoms is controlled by the temperature in accordance with the Arrhenius equation: $D = D_0 e^{-\frac{Q}{RT}}$. So the

densification and sintering are accelerated by increasing temperature. The temperature range selected for forging Ti-6Al-4V alloy powder compacts was 850 to 950 °C [169].

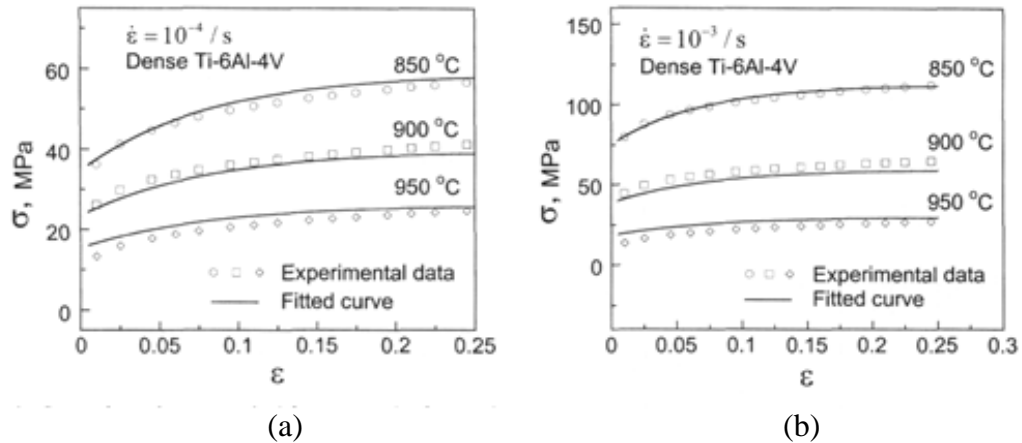


Figure 1.20: Compressive stress-strain curves of dense Ti-6Al-4V alloy specimens at high temperatures tested with a strain rate of 10^{-4} s^{-1} (a) and 10^{-3} s^{-1} (b) [169].

Pressure is another important parameter of the powder compact forging process. At constant temperature during the forging process, the higher the pressure on the powder compact, the higher the density that can be achieved as shown in Figure 1.21. The deformation of titanium and titanium alloys is easier in the β phase region where the titanium phase has a bcc crystal structure, and the deformation temperature is higher, compared with that in the α phase region where the titanium phase has a hcp crystal structure and the deformation temperature is lower. As shown in Figure 1.20, the strain rate significantly influences the flow stress of a Ti-6Al-4V alloy, especially at temperatures lower than 850 °C. Overall, the maximum flow stress at a strain rate of $10^{-3}/\text{s}$ is approximately twice that at a strain rate of $10^{-4}/\text{s}$.

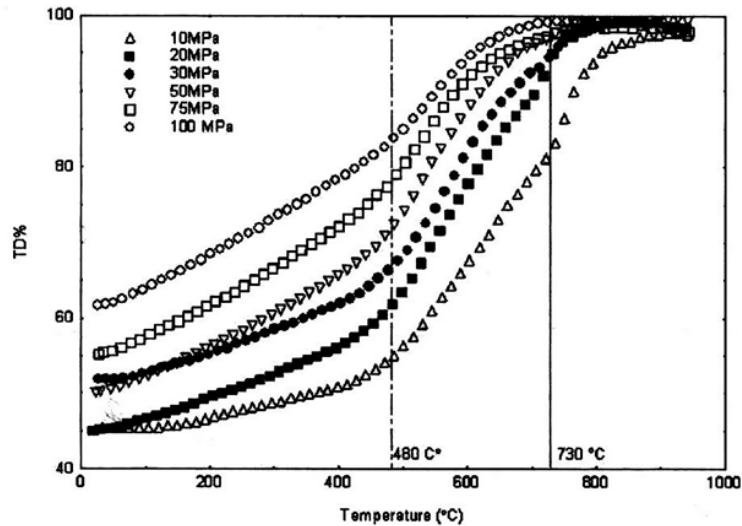


Figure 1.21: Sintering curves for a titanium powder compact at a variety of pressures and temperatures [170].

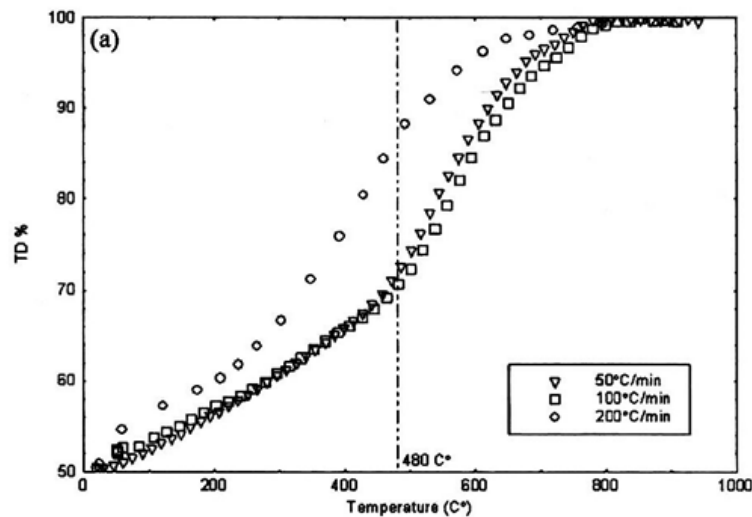


Figure 1.22: Sintering curves for a titanium powder compact at different heating rates under the same pressure of 50 MPa [170].

Because of the inconspicuous effect of heating rate on powder compact densification, it had not been recognized in conventional powder compact forging that fast powder compact densification and sintering can occur in some pressure assisted sintering processes such as spark plasma sintering [59, 60]. As shown in Figure 1.22, a high heating rate (200 K/min) significantly accelerates the densification process of titanium powder compacts at temperatures lower than 850

°C, and by the time the powder compact reaches 950 °C, it has achieved full density. This temperature is the same as that for the samples to achieve full density when the heating rate is 50 and 100 K/min. This means that there is no obvious difference in densification behaviour in the temperature range of 850-950 °C due to an increase in heating rate from 50 to 200 K/min, so the heating rate only affects the densification of Ti powder at temperatures lower than 850 °C.

A lot of titanium and titanium alloy samples have been made by isothermal powder compact forging. One example is Ti-10V-2Fe-3Al (Ti-1023) alloy [171]. The microstructure of the as-forged Ti-1023 alloy samples consisted of fine, recrystallized equiaxed α grains [172], and their room temperature mechanical properties were excellent. Isothermal forging of Ti-6Al-4V blended elemental powder compacts at temperatures below the β transus temperature were studied by Weiss et al. [173]. They obtained as-forged samples which had a microstructure consisting of fine equiaxed α grains giving superior fatigue properties. Also quasi-isostatic forging has been used to consolidate cryomilled CP Ti powders [174]. The blended powders used, which consisted of 15 pct liquid-argon-cryomilled CP Ti powder and 85 pct unmilled CP Ti powder, were forged and mechanically tested. This approach gave balanced mechanical properties, with a yield strength of 601 MPa, a UTS of 711 MPa and an elongation to fracture of 30%. Recently, a Ti connecting rod shown in Figure 1.23 has been made successfully by a powder forging process using elemental Ti-1.5Fe-2.25Mo alloy powders [99, 100]. Two different types of microstructures were achieved in an as-forged part: a lamellar $\alpha+\beta$ structure in the crank pin end, fork part and piston pin end, and a through-transus bi-modal phase structure, consisting of a fine martensitic microstructure and equiaxed grains with branched internal dendrites, in the shank. This variation of structure is caused by the cooling rate after forging, but their density is improved by the effective strain

during powder forgings shown in Figure 1.24. On the other hand, isothermal forging has also been used to improve the microstructure and properties of hot isostatically pressed Ti-5Al-2Sn-2Zr-4Mo-4Cr powder compacts using deformation parameters determined by processing maps with different true strain, such as those shown in Figure 1.25 [175]. The shaded regions in the processing maps are for unstable flow and the temperature of isothermal forging was determined to be either as above the beta transus or below the beta transus with suitable deformation parameters. An ultra-fine grained microstructure in the hot isostatically pressed Ti-5Al-2Sn-2Zr-4Mo-4Cr part had much improved mechanical properties than found in a wrought part made by isothermal forging.

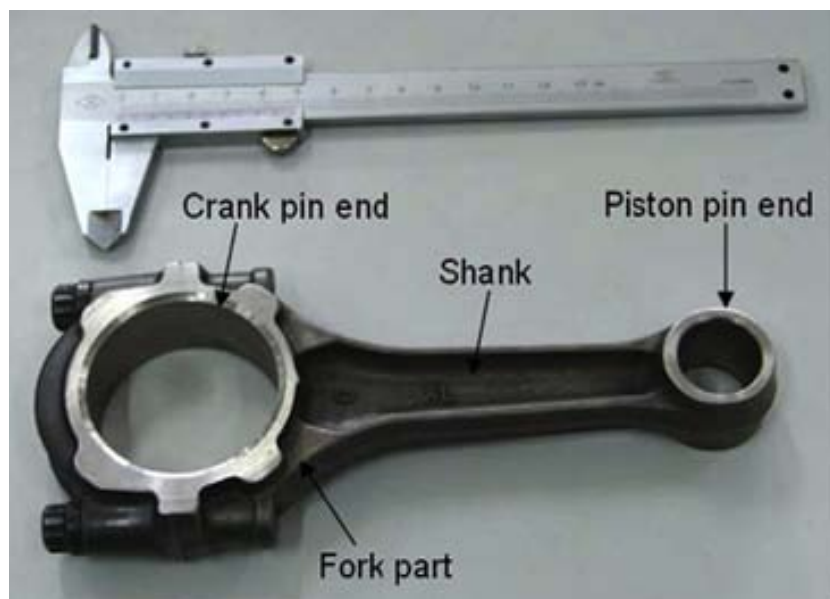


Figure 1.23: Ti-5Al-2Sn-2Zr-4Mo-4Cr connecting rod produced by powder forging [100].

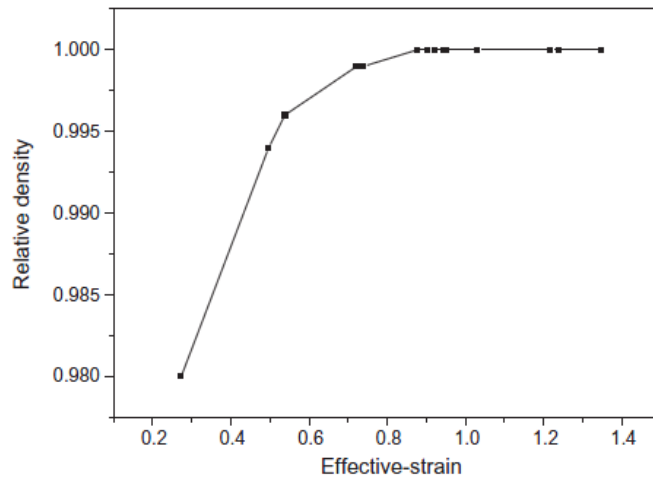


Figure 1.24: Effect of effective strain on the relative density [100].

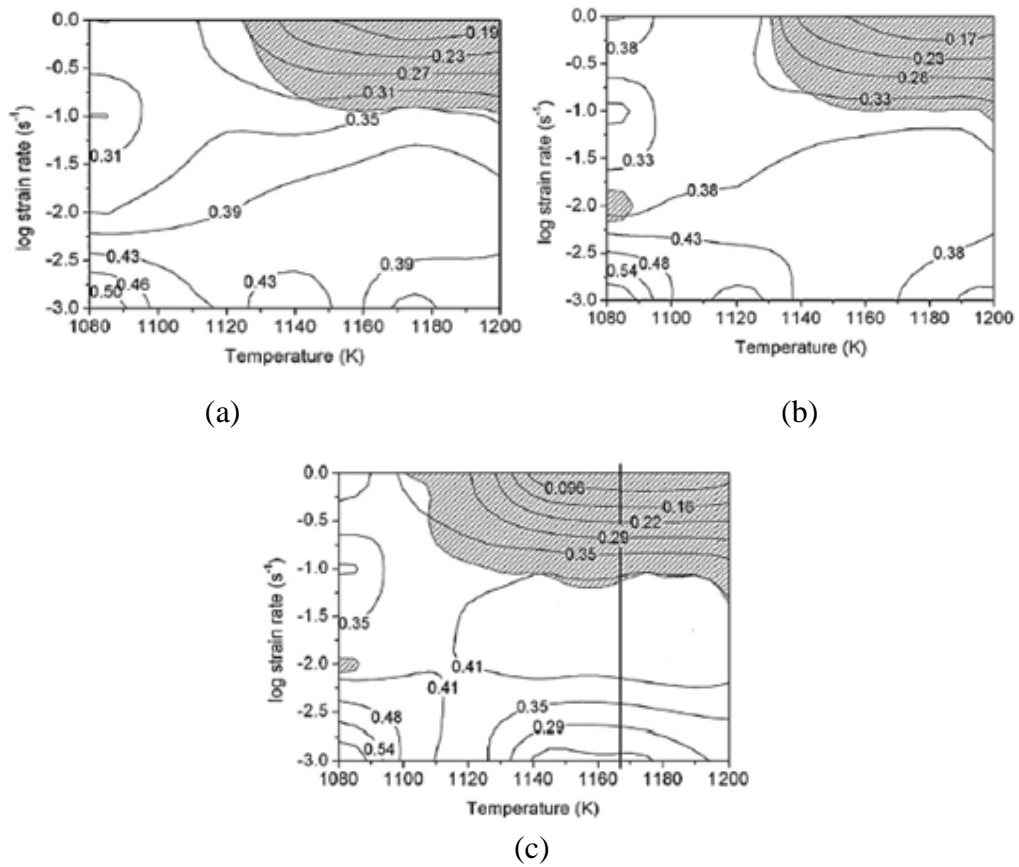


Figure 1.25: Processing map of Ti-5Al-2Sn-2Zr-4Mo-4Cr powder alloy with true strain: (a) 0.3; (b) 0.5; (c) 0.7 [175].

1.2.4 Summary

Conventional powder metallurgy processes have been reviewed in this chapter in the order of powder compaction, sintering and powder forging. Ingot metallurgy and the powder metallurgy of titanium and its alloys have also been reviewed. The conclusions from the three parts of this literature review are summarized as below:

PM has been widely used to produce near-net shaped parts with higher material strength than parts made by ingot metallurgy, but the main issue restricting its further application is the raw material cost. Nowadays more attention has been paid to reducing the cost of raw powders. Rapid consolidation processes, such as pressure assisted sintering and powder forging have been used to produce amorphous and nanomaterial from powders by constraining grain growth.

The effects of oxygen content and heat treatment conditions on microstructure and mechanical properties of CP Ti and Ti-6Al-4V alloy has been studied widely, and the microstructural modification of Ti-6Al-4V alloy by different heat treatments can improve its mechanical properties.

Pre-alloyed (PA) and blended elemental (BE) approaches are regarded as two major methods to produce titanium and titanium alloy parts by powder metallurgy. A PA approach produces parts with good mechanical properties, but the raw powder is relatively expensive; a BE approach can manufacture parts using lower cost powder, but at a cost of a higher porosity level.

For titanium and titanium alloy powder metallurgy, the effects of various parameters affecting the relative density and microstructure of powder compact forgings have been studied. Powder Compact Forging is a promising powder

metallurgy process to consolidate titanium and its alloy powders to make parts with good mechanical properties and an optimized microstructure.

1.3 References

1. Anokhin, V.M., O.M. Ivasishin, and A.N. Petrunko, *Structure and properties of sintered titanium alloyed with aluminum, molybdenum and oxygen*. Materials Science and Engineering: A, 1998. **A243**(1-2): p. 269-272.
2. Hu, R.-H. and J.-K. Lim, *Hardness and wear resistance improvement of surface composite layer on Ti-6Al-4V substrate fabricated by powder sintering*. Materials & Design, 2010. **31**(5): p. 2670-2675.
3. Filice, L., et al., *FE simulation and experimental considerations on Ti alloy superplastic forming for aerospace applications*. International Journal of Material Forming, 2010. **3**(1): p. 41-46.
4. Taddei, E., et al., *Production of new titanium alloy for orthopedic implants*. Materials Science and Engineering: C, 2004. **24**(5): p. 683-687.
5. Wu, L., et al., *Analysis of diamond-like carbon and Ti/MoS₂ coatings on Ti-6Al-4V substrates for applicability to turbine engine applications*. Surface and Coatings Technology, 2000. **130**(2): p. 207-217.
6. Wagner, V., et al., *Experimental characterization of behavior laws for titanium alloys: application to Ti5553*. Key Engineering Materials, 2010. **446**: p. 147-155.
7. Kim, J.H., et al., *Effect of surface treatment on the hot forming of the high strength Ti-6Al-4V fastener*. Materials Transactions, 2009. **50**(08): p. 2050-2056.
8. Österle, W., et al., *Potential of wear resistant coatings on Ti-6Al-4V for artificial hip joint bearing surfaces*. Wear, 2008. **264**(7): p. 505-517.
9. Borisovskaya, E., et al., *Mechanical properties of powder titanium at different production stages. I. Densification curves for titanium powder billets*. Powder Metallurgy and Metal Ceramics, 2008. **47**(7): p. 406-413.
10. Li, C., Z. Zhu, and T. Liu, *Microhardness of pore walls in porous titanium prepared with novel powder metallurgy*. Powder Metallurgy, 2005. **48**(3): p. 237-240.
11. Liu, Y., et al., *Design of powder metallurgy titanium alloys and composites*. Material Science and Engineering: A, 2006. **418**(1): p. 25-35.
12. Ryan, G.E., A.S. Pandit, and D.P. Apatsidis, *Porous titanium scaffolds fabricated using a rapid prototyping and powder metallurgy technique*. Biomaterials, 2008. **29**(27): p. 3625-3635.
13. Froes, F.H., *Advances in titanium metal injection molding*. Powder Metallurgy and Metal Ceramics, 2007. **46**(5): p. 303-310.
14. Das, S., et al., *Processing of titanium net shapes by SLS/HIP*. Material & Design, 1999. **20**(2): p. 115-121.
15. Fischer, P., et al., *Sintering of commercially pure titanium powder with a Nd:YAG laser source*. Acta Materialia, 2003. **51**(6): p. 1651-1662.
16. Hanson, A., et al., *Titanium near net shapes from elemental powder blends*.

- International Journal of Powder Metallurgy, 1990. **26**(2): p. 157-164.
17. Froes, F. and D. Eylon, *Powder metallurgy of titanium alloys- A review*. Powder Metallurgy International, 1985. **17**: p. 163-167.
 18. Froes, F., et al., *The technologies of titanium powder metallurgy*. JOM, 2004. **56**(11): p. 46-48.
 19. Martinez, A.M., et al., *New method for low-cost titanium production*. Key Engineering Materials, 2010. **436**: p. 41-53.
 20. Arcella, F.G. and F. Froes, *Producing titanium aerospace components from powder using laser forming*. JOM, 2000. **52**(5): p. 28-30.
 21. Henriques, V.A.R., et al., *Production of titanium alloys for advanced aerospace systems by powder metallurgy*. Materials Research, 2005. **8**(4): p. 443-446.
 22. Jang, G., M. Hur, and S. Kang, *A study on the development of a substitution process by powder metallurgy in automobile parts*. Journal of Materials Processing Technology, 2000. **100**(1): p. 110-115.
 23. Whittaker, D., *PM structural parts move to higher density and performance*. Powder Metallurgy, 2007. **50**(2): p. 99-105.
 24. Duggirala, R. and R. Shivpuri, *Effects of processing parameters in P/M steel forging on part properties: A review part I powder preparation, compaction, and sintering*. Journal of Materials Engineering and Performance, 1992. **1**(4): p. 495-503.
 25. Yang, T.S. and Y.C. Hsu, *Study on the bulging deformation of the porous metal in upsetting*. Journal of Materials Processing Technology, 2006. **177**(1): p. 154-158.
 26. Shaik, G.R. and W. Milligan, *Consolidation of nanostructured metal powders by rapid forging: Processing, modeling, and subsequent mechanical behavior*. Metallurgical and Materials Transactions A, 1997. **28**(13): p. 895-904.
 27. Fujiki, A., *Present status and future themes of PM technologies from parts application point of view*. Funtai Oyobi Fummatsu Yakin/Journal of the Japan Society of Powder and Powder Metallurgy, 1996. **43**(11): p. 1318-1322.
 28. Mocarski, S. and D.W. Hall, *PM parts for automotive applications*. Metal Powder Report, 1987. **42**(11): p. 754-762.
 29. Dale, J.R., *Wrought versus powder forged connecting rods*. Powder Metallurgy, 2005. **48**(1): p. 5.
 30. Engstrom, U., et al. *Opportunities to replace wrought gears with high performance PM gears in automotive applications*. in *Fall Technical Meeting of the American Gear Manufacturers Association 2006, October 22, 2006 - October 24, 2006*. 2006. Orlando, FL, United states: Curran Associates Inc.
 31. Barrow, D.A., *Developments in powder metallurgy (PM) materials*. Materials & Design, 1988. **9**(6): p. 345-354.
 32. Eylon, D., et al., *Titanium PM parts for aerospace applications*. Materials Engineering, 1985. **101**(2): p. 35-37.

33. Teoh, S., R. Thampuran, and W. Seah, *Coefficient of friction under dry and lubricated conditions of a fracture and wear resistant P/M titanium-graphite composite for biomedical applications*. *Wear*, 1998. **214**(2): p. 237-244.
34. Nemkov, V., R.C. Goldstein, and R.T. Ruffini. *Soft magnetic powdered metal materials for high frequency industrial applications*. in *Advances in Powder Metallurgy and Particulate Materials - 2001, May 13, 2001 - May 17, 2001*. 2001. New Orleans, LA, United states: Metal Powder Industries Federation.
35. Liu, B.B., J.X. Xie, and X.H. Qu, *Fabrication of W-Cu functionally graded materials with high density by particle size adjustment and solid state hot press*. *Composites Science and Technology*, 2008. **68**(6): p. 1539-1547.
36. Lagutkin, S., et al., *Atomization process for metal powder*. *Materials Science and Engineering: A*, 2004. **383**(1): p. 1-6.
37. Moll, J.H. *Production and characterization of rapidly solidified steel, superalloy and titanium alloy powders made by gas atomization*. in *1986 Annual Powder Metallurgy Conference Proceedings*. 1986. Boston, MA, USA: Metal Powder Industries Federation.
38. Riley, M.F., *Method for producing powder by gas atomization*. 1991, Google Patents.
39. Grant, N.J., *Rapid Solidification of Metallic Particulates*. 1982.
40. German, R.M., *Powder Metallurgy Science*. 1984. p. 77-81.
41. Kim, K. and H. Lee, *Effect of friction between powder and a mandrel on densification of iron powder during cold isostatic pressing*. *International Journal of Mechanical Sciences*, 1998. **40**(6): p. 507-519.
42. Yang, H., J. Kim, and K. Kim, *Rubber isostatic pressing and cold isostatic pressing of metal powder*. *Materials Science and Engineering: A*, 2004. **382**(1): p. 41-49.
43. Lin, C.S. and S.T. Lin, *Effects of granule size and distribution on the cold isostatic pressed alumina*. *Journal of Materials Processing Technology*, 2008. **201**(1-3): p. 657-661.
44. Turner, C. and M. Ashby, *The cold isostatic pressing of composite powders—I. Experimental investigations using model powders*. *Acta materialia*, 1996. **44**(11): p. 4521-4530.
45. Poquillon, D., et al., *Cold compaction of iron powders—relations between powder morphology and mechanical properties: Part II. Bending tests: results and analysis*. *Powder Technology*, 2002. **126**(1): p. 75-84.
46. Al-Qureshi, H., et al., *Analyses of the fundamental parameters of cold die compaction of powder metallurgy*. *Journal of Materials Processing Technology*, 2008. **199**(1-3): p. 417-424.
47. Song, M., H. Kim, and K. Kim, *Creep densification of copper powder compact*. *International journal of mechanical sciences*, 1996. **38**(11): p. 1197-1208.
48. Poquillon, D., et al., *Cold compaction of iron powders-relations between*

- powder morphology and mechanical properties. I. Powder preparation and compaction.* Powder Technology, 2002. **126**(1): p. 65-74.
49. Baco-Carles, V., et al., *Correlation between the morphology of cobalt oxalate precursors and the microstructure of metal cobalt powders and compacts.* Powder Technology, 2008. **185**(3): p. 231-238.
 50. Gai, G., et al., *Particle shape modification and related property improvements.* Powder Technology, 2008. **183**(1): p. 115-121.
 51. Canta, T. and D. Frunza, *Friction-assisted pressing of PM components.* Journal of Materials Processing Technology, 2003. **143**: p. 645-650.
 52. Hovanski, Y., K.S. Weil, and C.A. Lavender, *Developments in Die Pressing Strategies for Low-Cost Titanium Powders.* 2009, Pacific Northwest National Laboratory (PNNL), Richland, WA (US).
 53. Kim, K. and J. Cho, *A densification model for mixed metal powder under cold compaction.* International Journal of Mechanical Sciences, 2001. **43**(12): p. 2929-2946.
 54. Simchi, A. and G. Veltl, *Behaviour of metal powders during cold and warm compaction.* Powder Metallurgy, 2006. **49**(3): p. 281-287.
 55. Moon, I.H. and K.H. Kim, *Relationship between compacting pressure, green density, and green strength of copper powder compacts.* Powder Metallurgy, 1984. **27**(2): p. 80-84.
 56. Tu, G.C. and I.T. Chen, *The pressure-density-strength relationships of aluminum alloy powder compacts.* Journal of the Chinese Institute of Engineers, 1990. **13**(3): p. 259-271.
 57. Halldin, G., K. Yung, and T. Tsai, *A new analysis of compressibility and green strength of metal powders.* Progress in Powder Metallurgy, 1982. **37**: p. 383-393.
 58. Hermel, W., G. Leitner, and R. Krumphold, *Review of induction sintering: fundamentals and applications.* Powder Metallurgy, 1980. **23**(3): p. 130-135.
 59. Omori, M., *Sintering, consolidation, reaction and crystal growth by the spark plasma system (SPS).* Materials Science and Engineering: A, 2000. **287**(2): p. 183-188.
 60. Mamedov, V., *Spark plasma sintering as advanced PM sintering method.* Powder Metallurgy, 2002. **45**(4): p. 322-328.
 61. Munir, Z., U. Anselmi-Tamburini, and M. Ohyanagi, *The effect of electric field and pressure on the synthesis and consolidation of materials: A review of the spark plasma sintering method.* Journal of Materials Science, 2006. **41**(3): p. 763-777.
 62. Oghbaei, M. and O. Mirzaee, *Microwave versus conventional sintering: A review of fundamentals, advantages and applications.* Journal of Alloys and Compounds, 2010. **494**(1-2): p. 175-189.
 63. Lynn Johnson, D., *Microwave and plasma sintering of ceramics.* Ceramics International, 1991. **17**(5): p. 295-300.

64. Clark, D.E., D.C. Folz, and J.K. West, *Processing materials with microwave energy*. Materials Science and Engineering: A, 2000. **287**(2): p. 153-158.
65. Roy, R., et al., *Definitive experimental evidence for microwave effects: radically new effects of separated E and H fields, such as decrystallization of oxides in seconds*. Materials Research Innovations, 2002. **6**(3): p. 128-140.
66. Ramesh, P.D., D. Brandon, and L. Schächter, *Use of partially oxidized SiC particle bed for microwave sintering of low loss ceramics*. Materials Science and Engineering: A, 1999. **266**(1): p. 211-220.
67. Gupta, D. and A.K. Sharma, *Copper coating on austenitic stainless steel using microwave hybrid heating*. Proceedings of the Institution of Mechanical Engineers, Part E: Journal of Process Mechanical Engineering, 2012. **226**(2): p. 132-141.
68. Wu, K., H.-S. Park, and M. Willert-Porada, *Pyrolysis of polyurethane by microwave hybrid heating for the processing of NiCr foams*. Journal of Materials Processing Technology, 2012. **212**(7): p. 1481-1487.
69. Maki, S., Y. Harada, and K. Mori, *Application of resistance sintering technique to fabrication of metal matrix composite*. Journal of Materials Processing Technology, 2001. **119**(1): p. 210-215.
70. Montes, J., et al., *Consolidation by electrical resistance sintering of Ti powder*. Journal of Materials Science, 2011: p. 1-11.
71. Eksi, A. and A. Yuzbasioglu, *Effect of sintering and pressing parameters on the densification of cold isostatically pressed Al and Fe powders*. Materials & Design, 2007. **28**(4): p. 1364-1368.
72. German, R.M., *Sintering Theory and Practice*. Vol. 1. 1996.
73. Kang, S.J.L., *Sintering*. 2005: Wiley Online Library.
74. Das, J., et al., *Hardness and tensile properties of Fe-P based alloys made through powder forging technique*. Materials Science and Engineering: A, 2008. **479**(1-2): p. 164-170.
75. Dashwood, R.J. and G.B. Schaffer, *Powder forging of a sintered Al-3.8Cu-1Mg-0.8Si-0.1Sn alloy*. Materials Science and Engineering: A, 2002. **323**(1-2): p. 206-212.
76. Lee, J.-H., Y.-H. Kim, and W.-B. Bae, *A study on flash- and flashless-precision forging by the upper-bound elemental technique*. Journal of Materials Processing Technology, 1997. **72**(3): p. 371-379.
77. Leonowicz, M., et al., *Processing of high-performance anisotropic permanent magnets by die-upset forging*. Journal of Materials Processing Technology, 2004. **153-154**(0): p. 860-867.
78. Narayanasamy, R. and K.S. Pandey, *A study on the barrelling of sintered iron preforms during hot upset forging*. Journal of Materials Processing Technology, 2000. **100**(1-3): p. 87-94.
79. Park, J.-O., et al., *An experimental study on the optimization of powder forging process parameters for an aluminum-alloy piston*. Journal of

- Materials Processing Technology, 2001. **113**(1–3): p. 486-492.
80. Ragab, A.R., *Fracture limit curve in upset forging of cylinders*. Materials Science and Engineering: A, 2002. **334**(1–2): p. 114-119.
 81. Singh, S., A.K. Jha, and S. Kumar, *Upper bound analysis and experimental investigations of dynamic effects during sinter-forging of irregular polygonal preforms*. Journal of Materials Processing Technology, 2007. **194**(1–3): p. 134-144.
 82. Kim, Y.J. and N.R. Chitkara, *Determination of preform shape to improve dimensional accuracy of the forged crown gear form in a closed-die forging process*. International Journal of Mechanical Sciences, 2001. **43**(3): p. 853-870.
 83. Bose, A. and W.B. Eisen, *Hot consolidation of powders & particulates*. 2003: Metal Powder Industries Federation.
 84. Koul, A.K. and J.P.A. Immarigeon, *Modelling of plastic flow in coarse grained nickel-base superalloy compacts under isothermal forging conditions*. Acta Metallurgica, 1987. **35**(7): p. 1791-805.
 85. Zhao, Z., et al., *Deformation behavior of isothermally forged Ti-5Al-2Sn-2Zr-4Mo-4Cr powder compact*. Journal of Materials Processing Technology, 2009. **209**(15-16): p. 5509-5513.
 86. Zhao, Z.L., et al., *High strain rate superplasticity of ultrafined Ti-10V-2Fe-3Al compact prepared by sintering and isothermal forging*. Materials Science and Technology, 2009. **25**(4): p. 511-14.
 87. Zhao, Z.L., et al., *The microstructure and properties of ultra-fine grained Ti-17 powder compact improved through isothermal forging*. Journal of Materials Processing Technology, 2012. **212**(7): p. 1495-500.
 88. Camacho-Montes, H., et al. *Simulation of the stress-assisted densification behavior of a powder compact: Effect of constitutive laws*. 2008. 350 Main Street, Malden, MA 02148, United States: Blackwell Publishing Inc.
 89. Kim, H.Y., et al., *A study of the FEM forming analysis of the Al power forging piston*. Transactions of the Korean Society of Mechanical Engineers, A, 2010. **34**(10): p. 1543-1548.
 90. Ohdar, R.K. and S. Pasha, *Prediction of the process parameters of metal powder preform forging using artificial neural network (ANN)*. Journal of Materials Processing Technology, 2003. **132**: p. 227-34.
 91. Helle, A., K.E. Easterling, and M. Ashby, *Hot-isostatic pressing diagrams: New developments*. Acta Metallurgica, 1985. **33**(12): p. 2163-2174.
 92. Aren, B.G.A., *Optimizing the preform shape in powder forging of a linear gear profile*. Powder Metallurgy, 1975. **7**(1): p. 12-16.
 93. Koenig, W., G. Roeber, and M. Stroemgren, *Powder forging of helical gears for car manual gear boxes - concept and properties*. Metal Powder Report, 1990. **45**(4): p. 269, 272-273.
 94. Whittaker, D., *Powder metallurgy for gear production. Current status and*

- potential future trends*. *Materials and Design*, 1991. **12**(2): p. 97-100.
95. Jang, G.B., M.D. Hur, and S.S. Kang, *Study on the development of a substitution process by powder metallurgy in automobile parts*. *Journal of Materials Processing Technology*, 2000. **100**(1): p. 110-115.
 96. Adams, J.S. and D. Glover. *Hot forged powder metal rolling bearings*. in *1975 SAE Off-Highway Vehicle Meeting, September 8, 1975 - September 11, 1975*. 1975. Milwaukee, WI, United states: SAE International.
 97. Ilija, E., et al. *Benchmarking the industry: Powder forging makes a better connecting rod*. in *2005 SAE World Congress, April 11, 2005 - April 14, 2005*. 2005. Detroit, MI, United states: SAE International.
 98. Jinka, A.G.K., M. Bellet, and L. Fourment, *New three-dimensional finite element model for the simulation of powder forging processes: application to hot forming of P/M connecting rod*. *International Journal for Numerical Methods in Engineering*, 1997. **40**(21): p. 3955-3978.
 99. Qiu, J.W., et al., *Optimizing the hot-forging process parameters for connecting rods made of PM titanium alloy*. *Journal of Materials Science*, 2012. **47**(8): p. 3837-48.
 100. Qiu, J.W., et al., *Microstructures and mechanical properties of titanium alloy connecting rod made by powder forging process*. *Materials & Design*, 2012. **33**: p. 213-19.
 101. Wang, G. and G. Zhao, *Powder forging of a motorcycle connecting rod*. *Journal of Materials Science and Technology*, 2002. **18**(6): p. 544-548.
 102. Dashwood, R.J. and G.B. Schaffer, *Powder forging of a sintered Al-3.8Cu-1Mg-0.8Si-0.1Sn alloy*. *Materials Science and Engineering: A*, 2002. **323**(1-2): p. 206-212.
 103. Otsuki, M., S. Kakehashi, and T. Kohno. *Powder forging of rapidly solidified aluminum alloy powders and mechanical properties of their forged parts*. in *Proceedings of the 1990 Powder Metallurgy Conference and Exhibition, May 20, 1990 - May 23, 1990*. 1990. Pittsburgh, PA, USA: Publ by Metal Powder Industries Federation.
 104. Park, J.-O., et al. *An experimental study on the optimization of powder forging process parameters for an aluminum-alloy piston*. in *5th Asia Pacific Conference on Materials Processing, June 25, 2001 - June 25, 2001*. 2001. Seoul, Korea, Republic of: Elsevier Ltd.
 105. Huppmann, W.J. and G.T. Brown, *Steel powder-forging process- A general review*. *Powder Metallurgy*, 1978. **21**(2): p. 105-114.
 106. Katavic, B. and Z. Odanovic, *Investigation of deformation and heat treatment effects on properties of PM 92.5W-5Ni-2.5Fe heavy alloys*. *Powder Metallurgy*, 2004. **47**(2): p. 191-9.
 107. Parteder, E., H. Riedel, and R. Kopp, *Densification of sintered molybdenum during hot upsetting: experiments and modelling*. *Materials Science and Engineering: A*, 1999. **264**(1): p. 17-25.

108. Kwon, O.H., C.S. Nordahl, and G.L. Messing, *Submicrometer transparent alumina by sinter forging seeded γ -Al₂O₃ powders*. Journal of the American Ceramic Society, 1995. **78**(2): p. 491-589.
109. Nordahl, C.S. and G.L. Messing, *Transformation and densification of nanocrystalline θ -alumina during sinter forging*. Journal of the American Ceramic Society, 1996. **79**(12): p. 3149-3154.
110. Wetzell, K., et al., *Preparation of dense nanocrystalline silicon carbide ceramics by sinter forging in the presence of a liquid phase*. Advanced Engineering Materials, 2005. **7**(6): p. 520-524.
111. Lee, S.-H., et al., *Mechanical properties of hot-forged silicon carbide ceramics*. Scripta materialia, 2005. **52**(2): p. 153-156.
112. Hague, D.C. and M.J. Mayo, *Sinter-forging of nanocrystalline zirconia: I, Experimental*. Journal of the American Ceramic Society, 1997. **80**(1): p. 149-156.
113. Skandan, G., et al., *The effect of applied stress on densification of nanostructured zirconia during sinter-forging*. Materials Letters, 1994. **20**(5): p. 305-309.
114. Matthew J. Donachie, J., *Titanium: A Technical Guide*. 1988: ASM INTERNATIONAL.
115. Gurrappa, I., *Characterization of titanium alloy Ti-6Al-4V for chemical, marine and industrial applications*. Materials Characterization, 2003. **51**(2-3): p. 131-139.
116. Niinomi, M., *Mechanical properties of biomedical titanium alloys*. Materials Science and Engineering: A, 1998. **243**(1-2): p. 231-236.
117. Christoph Leyens, M.P., *Titanium and Titanium Alloys: Fundamentals and Applications*. 2003, Weinheim: WILEY-VCH Verlag GmbH & Co. KGaA.
118. Rodney Boyer, G.W., E. W. Collings, *Materials Properties Handbook: Titanium Alloys*. 1994: ASM International.
119. Ogden, H. and R. Jaffee, *Effects of Carbon, Oxygen, and Nitrogen on the Mechanical Properties of Titanium and Titanium Alloys*. 1955.
120. Weiss, I., R. Srinivasan, P.J. Bania, D. Eylon, S.L. Semiatin, *Advances in the Science and Technology of Titanium Alloy Processing*. 1996, California: The Minerals, Metals & Materials Society.
121. Li, A., et al., *Hot working of Ti-6Al-3Mo-2Zr-0.3 Si alloy with lamellar α + β starting structure using processing map*. Materials & Design, 2009. **30**(5): p. 1625-1631.
122. Prasad, Y. and T. Seshacharyulu, *Processing maps for hot working of titanium alloys*. Materials Science and Engineering: A, 1998. **243**(1): p. 82-88.
123. Semiatin, S., V. Seetharaman, and I. Weiss, *The thermomechanical processing of alpha/beta titanium alloys*. JOM Journal of the Minerals, Metals and Materials Society, 1997. **49**(6): p. 33-39.
124. Yeom, J.T., et al., *Ring-rolling design for a large-scale ring product of*

- Ti-6Al-4V alloy*. Journal of Materials Processing Technology, 2007. **187**: p. 747-751.
125. Tamirisakandala, S., R. Bhat, and B. Vedam, *Recent advances in the deformation processing of titanium alloys*. Journal of Materials Engineering and Performance, 2003. **12**(6): p. 661-673.
126. Fujii, H., *Strengthening of $\alpha+\beta$ titanium alloys by thermomechanical processing*. Materials Science and Engineering: A, 1998. **243**(1-2): p. 103-108.
127. Weiss, I., et al., *Modification of alpha morphology in Ti-6Al-4V by thermomechanical processing*. Metallurgical and Materials Transactions A, 1986. **17**(11): p. 1935-1947.
128. Williams, J., *Thermo-mechanical processing of high-performance Ti alloys: recent progress and future needs*. Journal of Materials Processing Technology, 2001. **117**(3): p. 370-373.
129. Boyer, R.R., *Titanium and Its Alloys: Metallurgy, Heat Treatment and Alloy Characteristics*. Encyclopedia of Aerospace Engineering.
130. Robles, E.J.R., *Effect of Boron on the Microstructure and Properties of Ti-6Al-4V*, in *Department of Applied Physics and Mechanical Engineering*. 2010, Luleå University of Technology: Luleå, Sweden.
131. Boyer, R., R. Bajoraitis, and W. Spurr, *The effects of thermal processing variations on the properties of Ti-6Al-4V*. The Metallurgical Society, Inc, 1987: p. 149-170.
132. Wood, J.R., et al., *Thermomechanical processing and heat treatment of Ti-6Al-2Sn-2Zr-2Cr-2Mo-Si for structural applications*. Materials Science and Engineering: A, 1998. **243**(1-2): p. 109-118.
133. *Dynamet supplies titanium alloys to Boeing 2012*; Available from: <http://www.metal-powder.net/view/25636/dynamet-supplies-titanium-alloys-to-boeing/>.
134. McCracken, C.G., C. Motchenbacher, and D.P. Barbis, *Review of titanium-powder-production methods*. International Journal of Powder Metallurgy, 2010. **46**(5): p. 19-26.
135. Zak Fang, Z. and P. Sun, *Pathways to optimize performance/cost ratio of powder metallurgy titanium—A perspective*. Key Engineering Materials, 2012. **520**: p. 15-23.
136. Ivasishin, O.M., et al., *Role of surface contamination in titanium PM*. Key Engineering Materials, 2012. **520**: p. 121-132.
137. Low, R., M. Qian, and G. Schaffer, *Sintering of titanium with yttrium oxide additions for the scavenging of chlorine impurities*. Metallurgical and Materials Transactions A, 2012. **43**(13): p. 5271-5278.
138. Yan, M., et al., *In-situ synchrotron radiation to understand the pathways for the scavenging of oxygen in commercially-pure Ti and Ti-6Al-4V by yttrium hydride*. Scripta Materialia, 2012.

139. Yan, M., et al., *Simultaneous gettering of oxygen and chlorine and homogenization of the β phase by rare earth hydride additions to a powder metallurgy Ti-2.25 Mo-1.5 Fe alloy*. Scripta Materialia, 2012. **67**(5): p. 491-494.
140. Yang, Y., et al., *Impurity scavenging, microstructural refinement and mechanical properties of powder metallurgy Titanium and Titanium Alloys by a small addition of cerium Silicide*. Materials Science and Engineering: A, 2013.
141. Chen, W., et al., *The investigation of die-pressing and sintering behavior of ITP CP-Ti and Ti-6Al-4V powders*. J. Alloys Compd., 2012. **541**: p. 440-447.
142. Ismail, M.H., et al., *Formation of microporous NiTi by transient liquid phase sintering of elemental powders*. Mater. Sci. Eng. C, 2012. **32**(6): p. 1480-1485.
143. Kim, K. and H. Yang, *Densification behavior of titanium alloy powder during hot pressing*. Mater. Sci. Eng. A, 2001. **313**(1): p. 46-52.
144. Heintl, P., et al., *Cellular Ti-6Al-4V structures with interconnected macro porosity for bone implants fabricated by selective electron beam melting*. Acta Biomater., 2008. **4**(5): p. 1536-1544.
145. Zadra, M., et al., *Microstructure and mechanical properties of cp-titanium produced by spark plasma sintering*. Powder Metall., 2008. **51**(1): p. 59-65.
146. Luo, S., et al., *Sintering of titanium in vacuum by microwave radiation*. Metall. Mater. Trans. A, 2011. **42**(8): p. 2466-2474.
147. Montes, J., et al., *Consolidation by electrical resistance sintering of Ti powder*. J. Mater. Sci., 2011. **46**(15): p. 5197-5207.
148. Ertorer, O., et al., *Mechanical behavior of cryomilled CP-Ti consolidated via quasi-isostatic forging*. Metall. Mater. Trans. A, 2009. **40**(1): p. 91-103.
149. Cantin, G., et al., *Innovative consolidation of titanium and titanium alloy powders by direct rolling*. Powder Metall., 2011. **54**(3): p. 188-192.
150. Lee, T. and C. Lee, *Microstructure and mechanical properties of TiB₂/TiAl composites produced by reactive sintering using a powder extrusion technique*. J. Mater. Sci. Lett., 1999. **18**(10): p. 801-803.
151. Threrujirapong, T., et al., *Mechanical properties of a titanium matrix composite reinforced with low cost carbon black via powder metallurgy processing*. Materials Transactions, 2009. **50**(12): p. 2757.
152. Hagiwara, M. and S. Emura, *Blended elemental P/M synthesis and property evaluation of Ti-1100 alloy*. Materials Science and Engineering: A, 2003. **352**(1): p. 85-92.
153. Eylon, D., *Faceted fracture in beta annealed titanium alloys*. Metallurgical and Materials Transactions A, 1979. **10**(3): p. 311-317.
154. Mahajan, Y., D. Eylon, and C. Kelto, *Modification of titanium powder metallurgy alloy microstructures by strain energizing and rapid omni-directional compaction*. Powder Metallurgy International, 1985. **17**(2):

- p. 75-78.
155. Henriques, V.A.R., C.E. Bellinati, and C.R.M. da Silva, *Production of Ti-6% Al-7% Nb alloy by powder metallurgy (P/M)*. Journal of Materials Processing Technology, 2001. **118**(1): p. 212-215.
 156. Eylon, D., W.A. Ernst, and D.P. Kramer. *Development of Ultra-Fine Microstructure in Titanium via Powder Metallurgy for Improved Ductility and Strength*. 2009: Trans Tech Publ.
 157. Smarsly, W. and W. Bunk, *Influence of combined die forging(CDF) of prealloyed Ti-6Al-4V powder on microstructure and mechanical properties*. PM Aerospace Materials, 1984. **1**: p. 1984.
 158. Smarsly, W. and W. Bunk, *Microstructure and texture of combined die forged(CDF) prealloyed Ti-6Al-4V powder compacts*. Powder Metallurgy International, 1985. **17**(2): p. 63-67.
 159. Park, J., et al., *Blended elemental powder metallurgy of titanium alloys*. Titanium Net Shape Technologies, 1984: p. 95-105.
 160. Abkowitz, S. and D. Rowell, *Significant cost savings for the manufacture of near-net shape titanium alloy components by advanced powder metal technology*. Titanium 1986, 1987: p. 816-830.
 161. Hagiwara, M., Y. Kaieda, and Y. Kawabe, *Improvement of mechanical properties of blended elemental alpha-beta Ti alloys by microstructural modification*. Titanium 1986, 1987: p. 850-858.
 162. Fujita, T., et al., *Microstructure and properties of titanium alloy produced in the newly developed blended elemental powder metallurgy process*. Materials Science and Engineering: A, 1996. **213**(1): p. 148-153.
 163. Froes, F.H. and D. Eylon, *Titanium net shape technologies*. Los Angeles, 1984: p. 1984.
 164. Parsons, L., et al., *Titanium P/M comes of age*. Metal progress, 1984. **126**(4): p. 83-94.
 165. Moll, J.H., *Powder Metallurgy for Full Density Products*. Vol. 8. 1985, Princeton: Metal Powder Industries.
 166. Haase, C., et al., *Production of Ti-6Al-4V billet through compaction of blended elemental powders by equal-channel angular pressing*. Materials Science and Engineering: A, 2012.
 167. Ivasishin, O. *Cost-effective manufacturing of titanium parts with powder metallurgy approach*. 2005.
 168. Wang, L., Z.B. Lang, and H.P. Shi, *Properties and forming process of prealloyed powder metallurgy Ti-6Al-4V alloy*. Transactions of Nonferrous Metals Society of China. **17**: p. 639-643.
 169. Kim, K., H. Yang, and S. Hong, *Densification behaviour of titanium alloy powder compacts at high temperature*. Powder Metallurgy, 2001. **44**(1): p. 34-40.
 170. Eriksson, M., Z. Shen, and M. Nygren, *Fast densification and deformation of*

- titanium powder*. Powder Metallurgy, 2005. **48**(3): p. 231-236.
171. Guo, H., et al., *The powder sintering and isothermal forging of Ti-10V-2Fe-3Al*. JOM Journal of the Minerals, Metals and Materials Society, 2008. **60**(11): p. 47-49.
172. Zhao, Z., et al., *High strain rate superplasticity of ultrafined Ti-10V-2Fe-3Al compact prepared by sintering and isothermal forging*. Materials Science and Technology, 2009. **25**(4): p. 511-514.
173. Weiss, I., et al., *Effect of isothermal forging on microstructure and fatigue behavior of blended elemental Ti-6Al-4V powder compacts*. Metallurgical and Materials Transactions A, 1986. **17**(3): p. 549-559.
174. Ertorer, O., et al., *Mechanical Behavior of Cryomilled CP-Ti Consolidated via Quasi-Isostatic Forging*. Metallurgical and Materials Transactions A, 2009. **40**(1): p. 91-103.
175. Zhao, Z.L., et al., *The microstructure and properties of ultra-fine grained Ti-17 powder compact improved through isothermal forging*. Journal of Materials Processing Technology, 2012. **212**(7): p. 1495-1500.

Chapter 2: Materials and Experimental Procedure

2.1 Starting Powders

In this study, titanium and pre-alloyed Ti-6Al-4V (wt%) powders produced by gas atomization (GA) and hydride-dehydride (HDH) methods, were used directly to carry out powder compact forging experiments, HDH powders were supplied by Xi'an Lilin International Trade Co., Ltd. (Xi'an, China), while GA powder was supplied by Phelly materials (USA) Inc. (New Jersey, USA). Al-40wt%V master alloy powder supplied by Xi'an Lilin International Trade Co., Ltd. (Xi'an, China) was also blended and mechanically alloyed with Ti powder to make Ti-6Al-4V (Ti64) powders used in the powder compact forging experiments. The particle size and compositions of the starting powders are listed in Table 2.1, compared with GA Ti and Ti-6Al-4V powders, HDH Ti and Ti-6Al-4V powders are low cost and have high oxygen content.

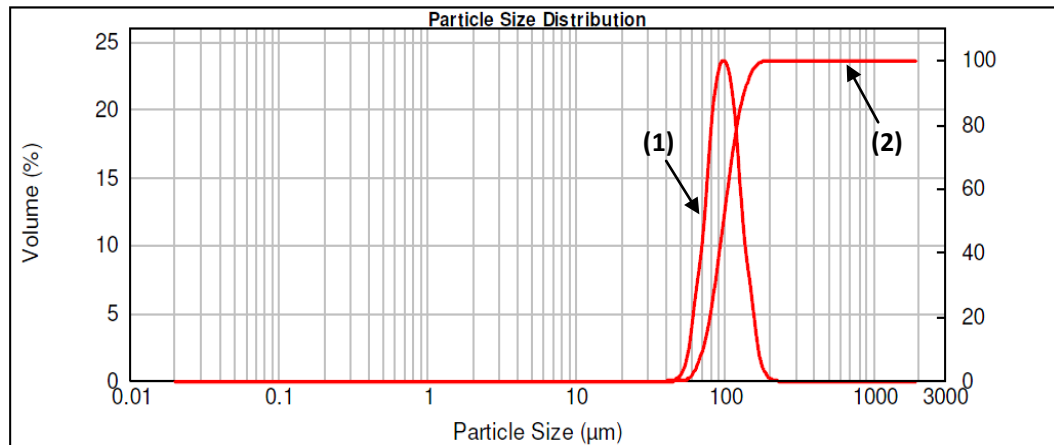
Table 2.1: Powder particle size and composition (wt%). (“-“ Element not indicated by supplier).

Powder	Particle size	H	O	N	C	Fe	V	Al	Ti
HDH Ti	-200 mesh	0.023	0.35	-	0.07	-	-	-	Bal
GA Ti	-100 mesh	0.027	0.11	0.02	0.01	0.11	-	-	Bal
HDH Ti64	-200 mesh	0.039	0.50	0.18	0.02	0.05	3.9	6.00	Bal
GA Ti64	-100 mesh	0.0045	0.13	0.02	0.02	0.05	4.1	6.07	Bal
Al-40%V	-250 mesh	-	0.24	-	0.003	0.16	42.24	Bal	-

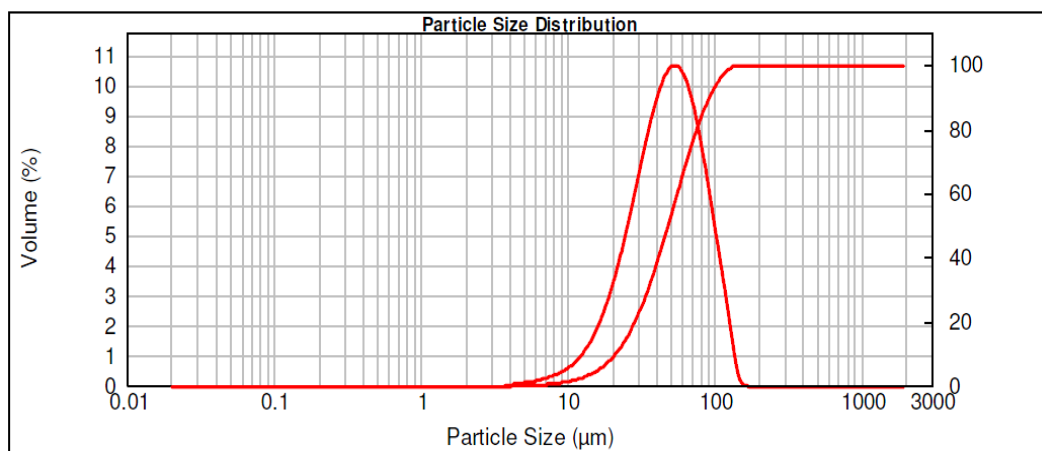
The particle size distributions of the starting powders, shown in Figure 2.1, were determined by a Malvern Mastersizer 2000 laser-scattering instrument. The $d(0.1)$, $d(0.5)$ and $d(0.9)$ values for the powders are summarized in Table 2.2. Here $d(0.1)$, $d(0.5)$ and $d(0.9)$ mean that 10%, 50% and 90% of the volume fraction of the powder particles have sizes below a particular value (in micrometer), respectively.

Table 2.2: Results of particle size analysis of the starting powder.

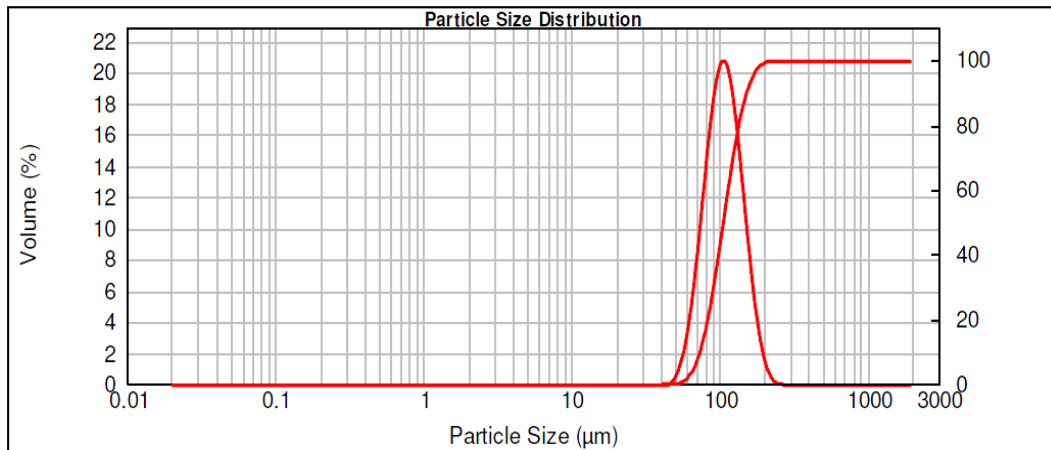
Powder	Particle size	d(0.1)	d(0.5)	d(0.9)
GA Ti	-100 mesh	70.530	97.008	133.547
HDH Ti	-200 mesh	20.843	47.559	90.759
GA Ti64	-100 mesh	72.290	104.085	149.479
HDH Ti64	-200 mesh	10.234	45.645	97.630
Al-40wt% V	-325 mesh	6.658	39.320	89.396



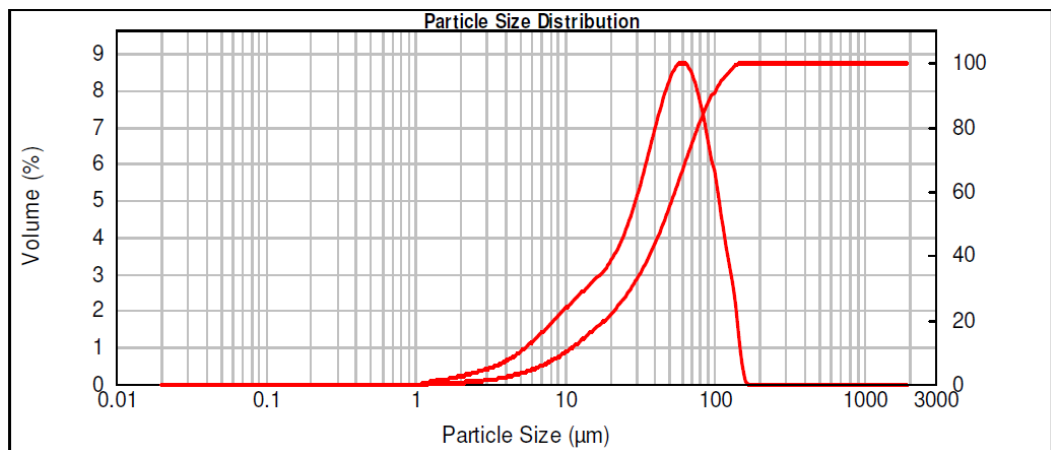
(a)



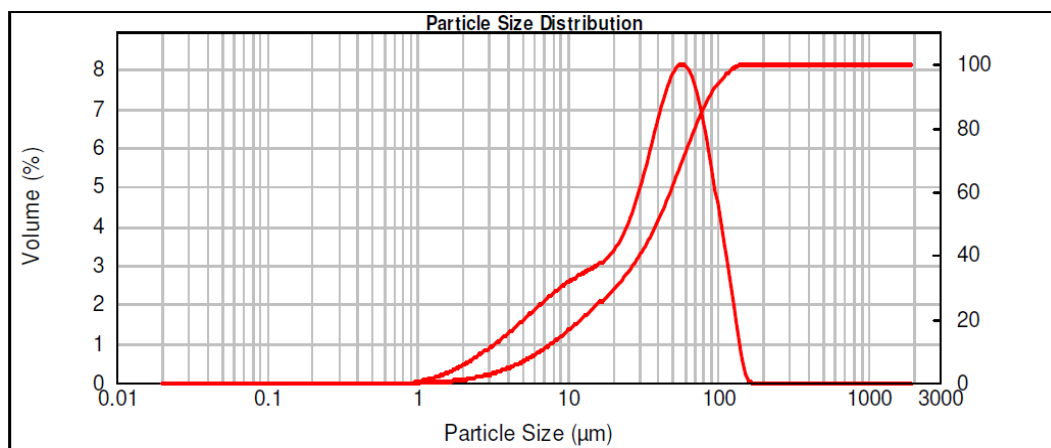
(b)



(c)



(d)



(e)

Figure 2.1: Particle size distributions for starting powders, curve (1) shows the volume percent at the corresponding particle size, and curve (2) shows the volume percent under the corresponding particle size: (a) GA Ti; (b) HDH Ti; (c) GA Ti-6Al-4V; (d) HDH Ti-6Al-4V; (e) Al-40wt% V.

The particle morphologies of the starting powders were examined by scanning electron microscopy (SEM), as shown in Figure 2.2. Due to the nature of the powder production processes, both GA Ti and Ti-6Al-4V powders have a spherical particle shape, while both HDH Ti and Ti-6Al-4V powders have an irregular particle shape.

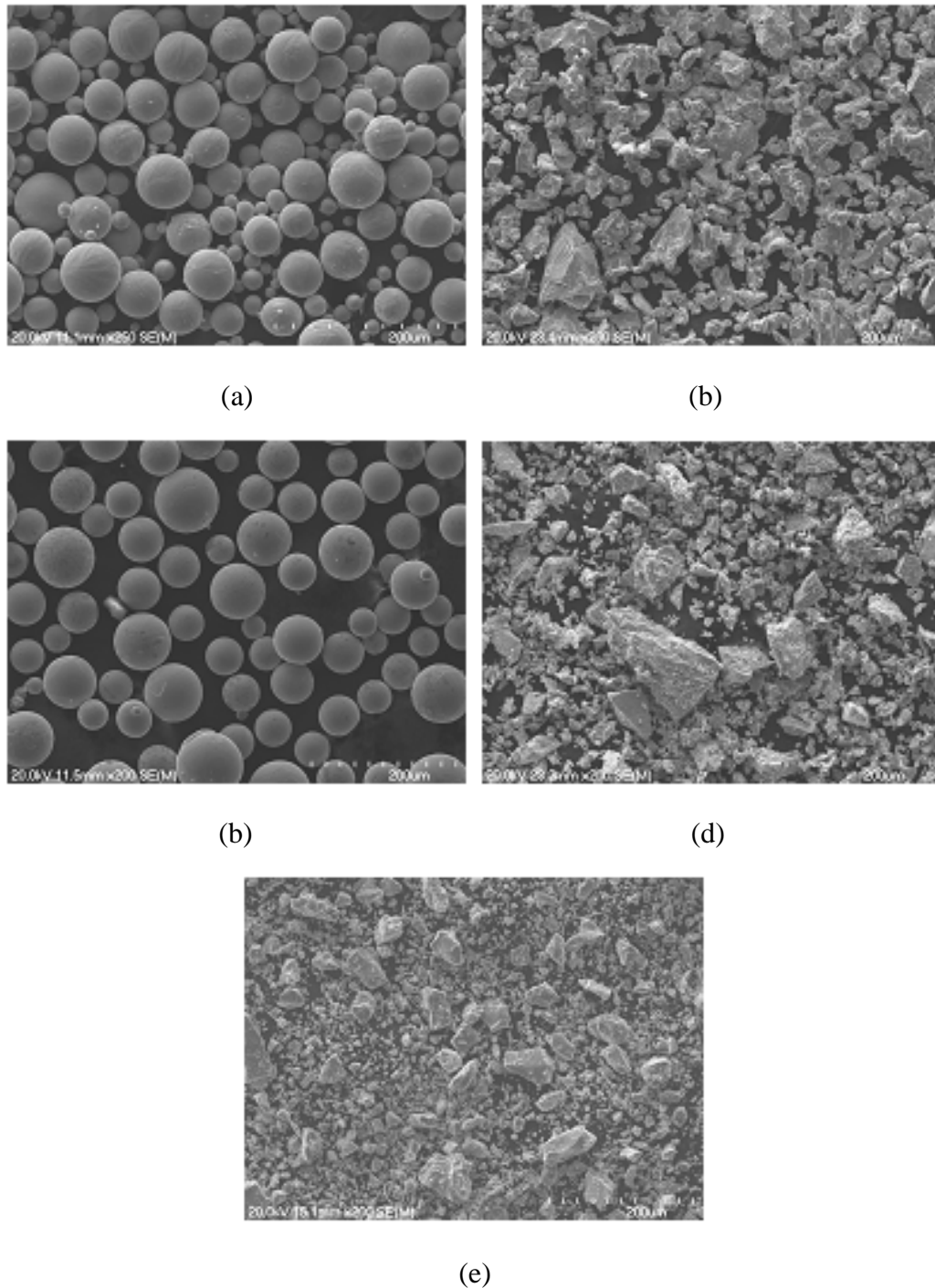


Figure 2.2: SEM images of starting powders used in this study. (a) GA Ti; (b) HDH Ti; (c) GA Ti-6Al-4V; (d) HDH Ti-6Al-4V; (e) Al-40wt% V master alloy.

2.1.1 Blended and Mechanical Alloyed Powder Synthesis

Ti-6Al-4V powder mixture was produced by blending HDH Ti and Al-40wt%V master alloy powders with a mass ratio of 9:1 in a planetary ball mill (shown in Figure 2.3), 150g of raw powders and 300g of stainless steel balls with a diameter of 6 mm (ball:powder weight ratio was 2:1) were placed a steel vial which was then sealed under high purity argon. The powder milling was done for 6 hours using a rotational speed of 100 rpm, as summarized in Table 2.3.



Figure 2.3: Retsh PM 100 planetary ball mill.

For mechanical alloyed Ti-6Al-4V powder production by high energy mechanical milling (HEMM), HDH and GA Ti powders were mixed with Al-40wt%V master alloy powder, respectively, with the powder mass ratio of 9:1. Before powder milling, 110g of Ti and master alloy powders were mixed in a planetary ball mill, at a rotation speed of 100 rpm for 6 hours, under argon using a similar operating procedure as that used for blending Ti and master alloy powder to make a Ti-6Al-4V powder mixture mentioned above. The difference was that both the mass and diameter of the stainless steel balls were changed to 550g (ball:powder ratio is 5:1) and 12.5 mm, respectively. After powder mixing, the powders were milled directly without opening the vial using the planetary ball mill at a speed of 200 rpm or 400 rpm without using a process control agent (PCA) to avoid

contamination. With a milling speed of 400 rpm, the milling was stopped for 30 minutes after every 30 minute interval, and the net total milling time was 6 hours. For a milling speed of 200 rpm the process was continuous. The conditions used for powder milling are listed in Table 2.3.

Table 2.3: Conditions of powder mixing and milling.

	Matrix Powder	Master alloy powder	Speed of milling (rpm)	Milling time (hours)
Blended powder	HDH Ti	Al-40wt% V	100	6
Powder milling	HDH Ti	Al-40wt% V	200	3
			200	6
			400	6
			200	6
	GA Ti	Al-40wt% V	200	6

2.2 Powder Compact Forging Procedure

In this study, powder compact forging was used to consolidate raw powders into fully dense rocker arm parts with the designed shape shown in Figure 2.4.

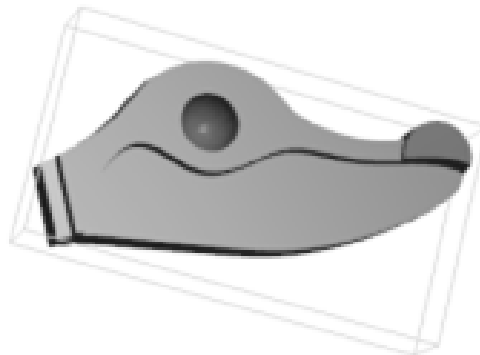


Figure 2.4: The designed shape of the rocker arm to be produced by powder compact forging in this study.

The procedure used for powder compact forging is shown in Figure 2.5. The powder was poured into a powder compaction die, then compacted by uniaxial pressing, and finally the green powder compact was ejected from the die. The green powder compact was placed in the center of an induction coil, which was manufactured using copper tube, and heated up to 1350 °C in a glove chamber (in

Figure 2.6) under argon (Oxygen content of the argon is below 200 ppm). The temperature of the powder compact was measured using a K-type thermocouple connected to a temperature controller. After heating to the desired temperature, the powder compact was forged into rocker arm shape using an impression die set driven by a 100 ton hydraulic press in a glove chamber. To improve the microstructure and properties of as-forged parts, heat treatments were conducted in a muffle furnace under air.

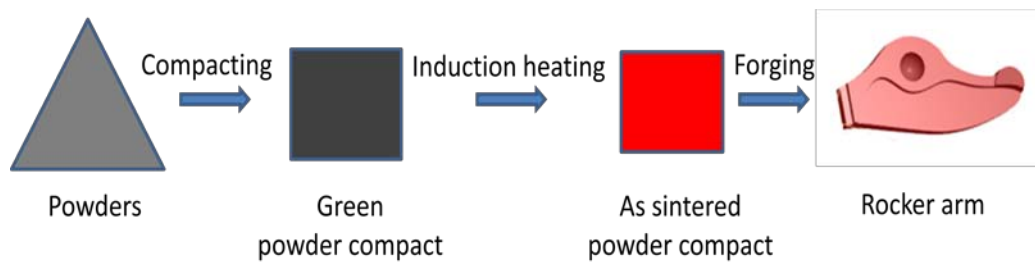


Figure 2.5: Schematic diagram showing the procedure of powder compact forging.



Figure 2.6: Image of glove chamber.

Warm compaction was used to manufacture the powder compacts in this study. After the powders were poured into the powder compact die, shown in Figure 2.7, the die was heated up to a desired powder compacting temperature by band heater. If the desired powder compacting temperature was 300 °C or lower, the powder compacting was done in air, otherwise, it was done under argon. To reduce the

friction between powders and the wall of the powder compact die, colloidal graphite was used as a die wall lubricant and was coated on the inner wall surface of the powder compacting die. The conditions used for powder compaction for each kind of powder are listed in Table 2.4.

Table 2.4: Conditions of powder compaction.

Raw powder	Sample	Temperature (°C)	Pressure (MPa)	Atmosphere
HDH Ti	1	25	544	Air
	2	150		
	3	250		
	4	400		
	5	450		
	6	500		
GA Ti-6Al-4V	7	450	726	Argon
	8	500		
	9	550		
GA Ti	10	450	726	Argon
HDH Ti-6Al-4V	11	25	726	Air
	12	250		
	13	300		
	14	450		
	15	500		
	16	550		
	17	250		
MA Ti-6Al-4V	18	250	726	Air



Figure 2.7: Powder compaction die.

During a powder compact forging process, the powder compact was heated to 1350 °C by induction heating, and the powder compact forging temperature was kept constant in this study. Before forging the powder compact using the impression die set shown in Figure 2.8, the upper and lower dies were both coated with colloidal graphite at room temperature, and heated to different temperatures up to 500 °C by cartridge elements inserted into the dies. Before forging, the holding time at the forging temperature (1350 °C) was varied, but was in the range of 0-10 minutes. The conditions for powder compact forging are summarized in Table 2.5.

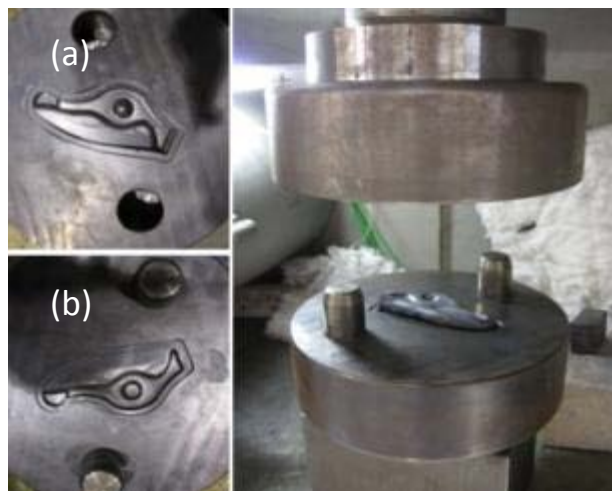


Figure 2.8: Forging die set. (a) upper die; (b) lower die.

Table 2.5: Conditions of powder compact forging.

Powder compact	Temperature (°C)	Holding time (Minutes)
HDH Ti	1350	0
		5
GA Ti	1350	0
HDH Ti-6Al-4V	1350	0
GA Ti-6Al-4V	1350	0
Blended Ti-6Al-4V	1350	0
		5
		10
MA Ti-6Al-4V	1350	0

2.3 Heat Treatment of As-forged Parts

After powder compact forging, as-forged rocker arms were heat treated in a Muffle furnace under air. An annealing treatment was chosen to relieve the internal stress of as-forged HDH Ti parts. Four types of heat treatment were used for as-forged HDH and GA Ti-6Al-4V parts: duplex annealing, a solution and aging treatment, recrystallization annealing and beta annealing. The heat treatment processes are described in Table 2.6 and schematically shown in Figures 2.9 and 2.10. The temperature was selected to be in the same range for the corresponding heat treatment of wrought material in Ref.[1].

Table 2.6: Conditions of heat treatments of as-forged parts.

As-forged part		Heat treatment	Condition
	HDH Ti ✓	Annealing	Anneal at 550 °C for 6 hours, air cool.
HDH Ti-6Al-4V ✓	GA Ti-6Al-4V ✓	Duplex annealing	Solution treat at 920 °C for 2 hours, air cool and age at 550 °C for 6 hours, air cool.
✓	✓	Solution and Aging	Solution treat at 955 °C for 2 hours, water quench and age at 550 °C for 6 hours, air cool.
✓	✓	Recrystallization annealing	Heat treat at 925 °C for 4 hours, furnace cool at 50 °C/h to 750 °C, air cool.
✓		Beta annealing	Solution treat at 1010 °C for 1 hour, air cool and age at 700 °C for 2 hours, air cool.

*✓ indicates that the condition was chosen in this study.

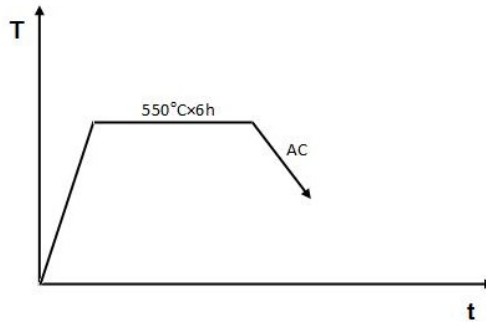


Figure 2.9: Schematic diagram of the annealing treatment for an as-forged HDH Ti part.

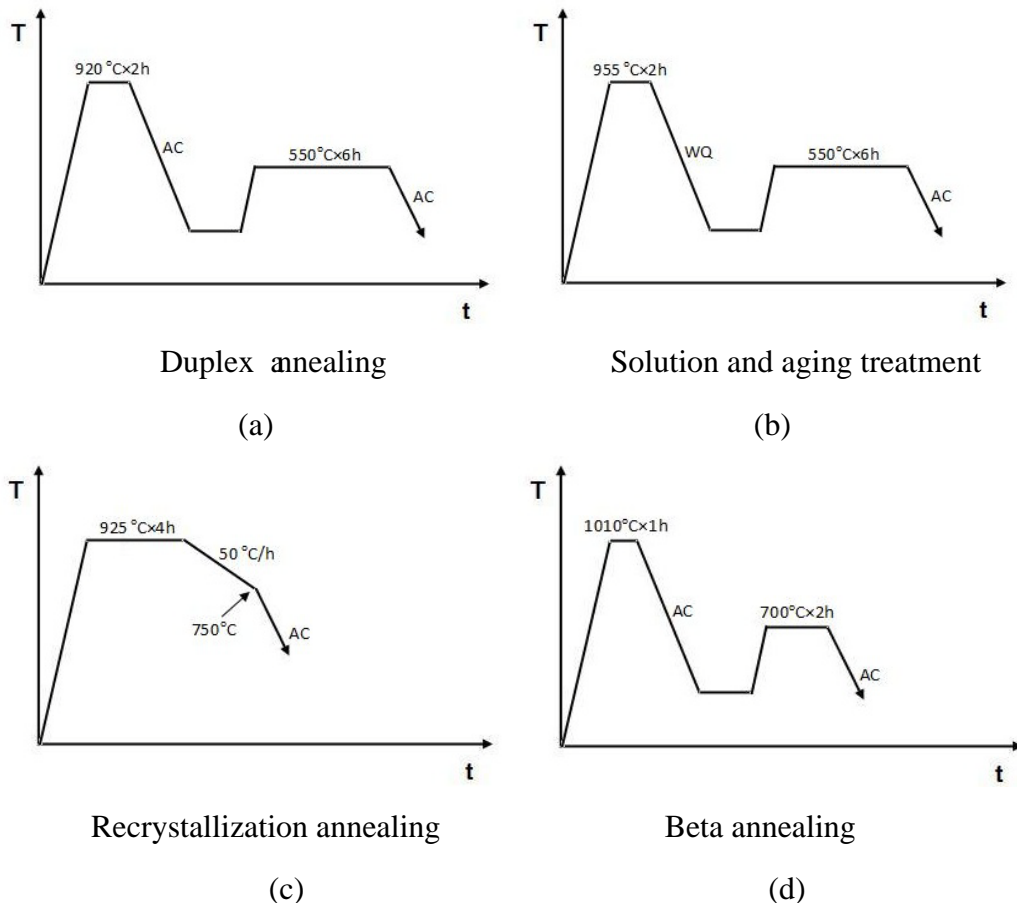


Figure 2.10: Schematic diagrams showing the schedule fused for heat treating as-forged Ti-6Al-4V parts.

2.4 Characterization of Powders and Consolidated Samples

2.4.1 Particle Size Analysis

The particle size distribution for all powders used and produced in this study was

analyzed by a Malvern Mastersizer 2000 laser-scattering instrument. For the analysis, a few grams of a powder sample were dispersed in water to reach the detection level for determining the particle size distribution. The maximum diameter of powder particles which can be detected is 2 mm.

2.4.2 Oxygen Analysis

As-forged samples was cut into 1mm×1mm×1mm cubes, and then quantitative chemical analysis (oxygen, nitrogen and hydrogen) was done at Durkee Testing Laboratories, Inc. USA, using a LECO combustion method.

2.3.3 Thermal Analysis

Differential thermal analysis (DTA) was carried out on blended and milled powders using a TA Instrument SDT 2960. The powders were heated up to 1300 °C in an alumina crucible at a heating rate of 10 °C/min, with flowing argon as the protective atmosphere.

2.3.4 Density Measurement

The density of green and as-sintered powder compacts were calculated in Equation 2.1 by dividing their mass with their corresponding volumes, measured by a Nextengine 3D scanner shown in Figure 2.11.

$$\text{Density} = \frac{\text{Mass}}{\text{Volume}} \quad (2.1)$$

To evaluate the porosity eliminated by sintering, a densification parameter is calculated from the sintered density and green density of a powder compact as follows:

$$\text{Densification parameter} = \frac{\text{sintered density} - \text{green density}}{\text{theoretical density} - \text{green density}} \quad (2.2)$$



Figure 2.11: Nextengine 3-D scanner.

2.4.5 Optical Microscopy

An examination of the powder and the as-forged and heat treated parts by optical microscopy was carried out using an Olympus BX60 optical microscope equipped with a digital camera. For metallographic examination of the powders, samples were prepared by mounting the powders in an epoxy resin at room temperature. For examining consolidated parts, samples for metallography were cut from the as-forged and heat treated parts by electric discharge machining (EDM) wire cutting. Both mounted and bulk samples were ground step by step using 120, 320, 600, 1200, 2000 and 4000 grit SiC papers to produce flat surfaces. After grinding, the flat surfaces were polished to a “mirror” finish using an alumina dispersion with a particle size of 0.3 μm . The polished samples were used for X-ray diffraction (XRD) analysis, optical microscopy (OM), porosity distribution measurement and scanning electron microscopy (SEM).

To observe the microstructure of the samples, their polished surfaces were etched using Kroll’s solution, consisting of 2 ml HF, 6 ml HNO_3 and 92 ml distilled water. Images of the microstructures were captured using digital cameras attached to the optical microscope and scanning electron microscope.

2.4.6 Porosity Distribution Measurement

Images of polished cross-sections of as-forged parts were captured by a digital

camera attached to an optical microscope. Two-dimensional porosity distributions, perpendicular to and along the forging direction, were determined by analyzing these digital OM images using IQ image analysis software. The OM images were taken at equal intervals of distance from the edge to the center of the parts along the two directions mentioned above.

2.4.7 X-ray Diffraction

X-ray diffraction (XRD) analysis was carried out using a Philips X'pert system diffractometer with Cu K α radiation source and an incidence beam at a scan rate of 2°/min. The working conditions of the X-ray tube were a voltage of 20 kV and current of 40mA. The scan range of 2 θ was from 20 °C to 90 °C, and the results were matched with standard X-ray diffraction powder pattern from PDF cards of Ti, AlV and Ti-6Al-4V.

2.4.8 Scanning Electron Microscopy

A Hitachi S4700 scanning electron microscope (SEM) was used to observe the microstructures and morphology of specimens, and the elemental content and distribution of specimens were measured by an energy dispersive X-ray spectrometer (EDS) attached to the scanning electron microscope. Resin mounted specimens were coated by a thin layer of carbon before examination, but it was not necessary to coat the bulk samples since they are electrically conductive.

2.4.9 Transmission Electron Microscopy

The microstructure of as-forged parts was examined using a CM30 Philips transmission electron microscope (TEM). A double tilt holder was used to hold the specimens. To prepare specimens for TEM, slices with a thickness of around 0.5 mm were cut from as-forged parts using an EDM wire cutter, and then the slices were ground to reduce their thickness to about 50 μ m by 120, 320, 600, 1200 and 2000 grit SiC abrasive papers. Then several disks with a diameter of 3

mm were punched from each slice, and finally each disk was further thinned by electrical jet polishing to produce a hole. The conditions used for jet polishing were a voltage of 10 mV a current of 10 mA and a temperature ranging from -40 °C to -30 °C. The jet polishing solution was composed of 60vol.% methanoll, 35vol.% Butanol and 5vol.% perchloric acid.

2.4.10 Tensile Testing

The shape and dimensions of specimens used for tensile testing are shown in Figure 2.12. Tensile testing was done using an Instron 33R4204 universal testing machine with a load cell of 5 kN at room temperature. An extensometer with a gauge length of 10 mm was used to record the strain during tensile testing. A strain rate of $8.3 \times 10^{-5} \text{ s}^{-1}$ was used for all of the tensile tests. For the as-forged parts, tensile test specimens were cut one by one in a direction perpendicular to the forging direction using an EDM wire cutter, as shown in Figure 2.13. Specimens from as-sintered parts, were cut along the powder pressing direction. The rough surfaces of the cut specimens were ground by 120, 320, 600, 1200 and 2000 grit SiC papers to remove the effect of surface roughness on tensile properties.

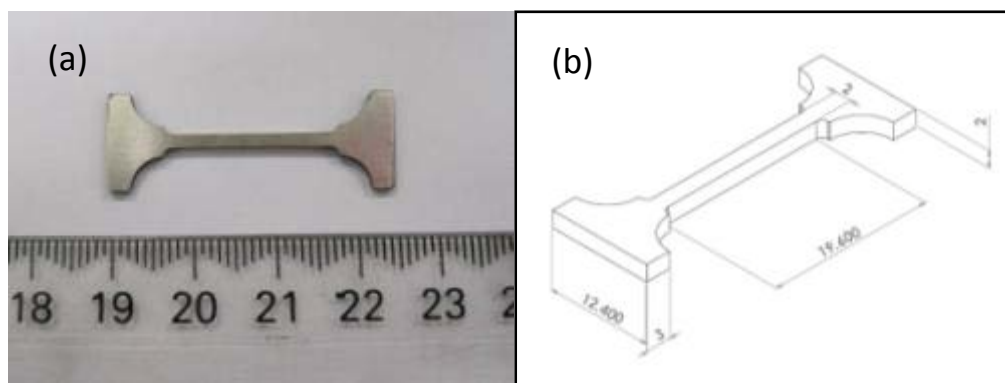


Figure 2.12: Shape (a) and dimensions (b) of the tensile test specimens.



Figure 2.13: A schematic diagram showing the orientation used for cutting tensile test specimens from an as-forged rocker arm.

2.5 Reference

1. Matthew J. Donachie, J., *Titanium: A Technical Guide*. 1988: ASM INTERNATIONAL.

Chapter 3: Compacting and Induction Sintering of Ti and Ti-6Al-4V Powders

3.1 Introduction

To achieve high relative density in Ti and Ti-6Al-4V powder compacts, the effect of compacting temperature on the relative density of HDH Ti, HDH and GA Ti-6Al-4V powder compacts was investigated in this study. Based on the time taken for making the powder compacts and their quality, the HDH Ti and HDH Ti-6Al-4V powder compacts made using the highest compacting temperature in air were selected to do the powder compact forging experiments. Using GA Ti-6Al-4V powder, compacts could not be made in air using the highest attainable pressure for the equipment of 726 MPa, even at temperatures up to 300°C. For this reason, the GA Ti-6Al-4V powder compacts were made at a compacting temperature of 550 °C, which was close to the working temperature limit of the powder compacting die. The effectiveness of the different particle shapes found in HDH and GA powders, on the degree of particle interlocking and cold welding during the powder compacting process, were studied. The powder compacts were partially sintered while being heated up in an induction furnace to the forging temperature. The microstructure and mechanical properties of as-sintered HDH Ti and HDH and GA Ti-6Al-4V powder compacts were investigated, and the mechanism of induction sintering of these Ti and Ti-6Al-4V powders was analyzed in this chapter.

3.2 Compacting of Ti and Ti-6Al-4V Powders

Figure 3.1 shows the shape of an HDH Ti powder compact which was produced by pressing HDH Ti powder in a powder compacting die shown in Figure 2.7. The upper and lower surfaces of the powder compact had some features of the rocker arm to be made by powder compact forging using the upper and lower forging die halves shown in Figure 2.8. These features were designed so that for powder

compact forging experiments, the powder compact could be easily and accurately located and fitted to the powder forging die.



Figure 3.1: Image of an HDH Ti powder compact with mass of 120g for making a Ti rocker arm by powder compact forging.

3.2.1 The Effect of Temperature on Compacting

For the powder compacting process, close attention was paid to achieving a high density and uniform density distribution in the powder compacts to obtain final products with good quality after powder consolidation. In this study, warm compaction was used to make powder compacts with a high density, by reducing the flow stress of powder particles through increasing temperature. In the warm compaction process, temperature and pressure are the main parameters that influence the density of powder compacts [1]. HDH Ti and Ti-6Al-4V alloy powders were compacted at temperatures in the range of room temperature to 550 °C under pressures of 544 and 726 MPa, respectively. The difference in the pressure used for compacting HDH Ti and Ti-6Al-4V powders is due to the higher flow stress of Ti-6Al-4V powder particles compared with Ti powder particles at the same temperature. Powder compacting at temperatures of 300 °C or lower was done in air, and when the compacting temperature was increased to above 300 °C, an argon protective atmosphere (Oxygen content is below 200 ppm) was used as a protective atmosphere. The upper limit for the powder compacting temperature was 550 °C, which was set by the maximum working temperature of the powder

compacting die made of heat treated H13 steel. Compared with HDH Ti and HDH Ti-6Al-4V powders with irregular particle shapes, as shown in Figure 2.2, GA Ti-6Al-4V powder, with a spherical particle shape, was difficult to compact at relatively low temperatures between room temperature and 450 °C. Therefore, in this study, it was only compacted at temperatures between 450 to 550 °C using a pressure of 726 MPa under argon atmosphere. The conditions used for powder compacting are summarized in Table 2.4.

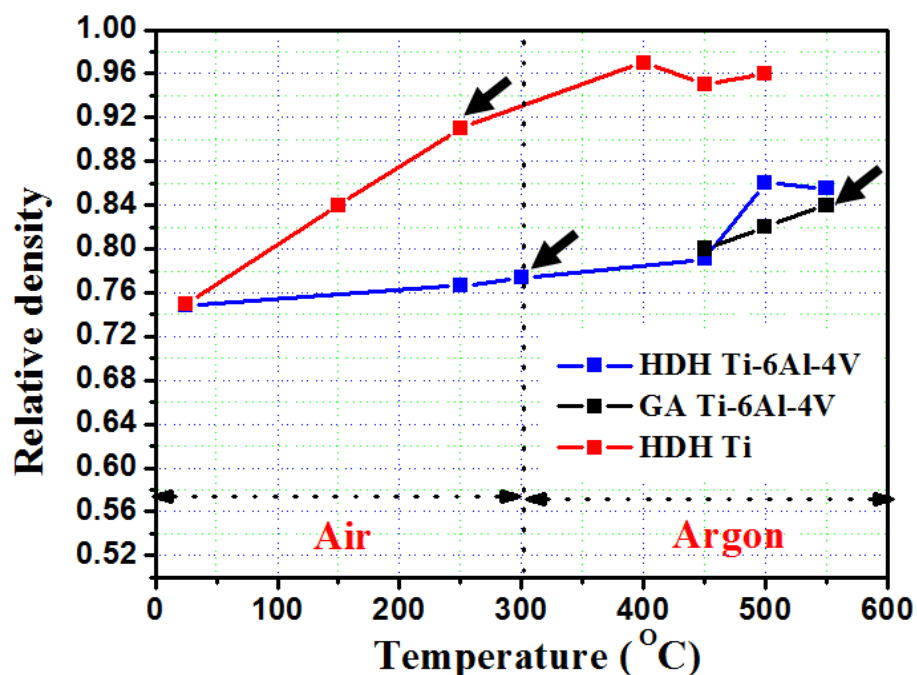


Figure 3.2: The relative density of HDH Ti and HDH and GA Ti-6Al-4V powder compacts as functions of temperature under constant pressure: 544 MPa applied to HDH Ti powder, 726 MPa applied to HDH and GA Ti-6Al-4V powders.

The density of the powder compacts is given by Equation 2.1, and the relative density of HDH Ti, HDH and GA Ti-6Al-4V powder compacts as functions of temperature are shown in Figure 3.2. From the relative density vs temperature curves shown in Figure 3.2, the density of powder compacts increases with increasing compacting temperature, as the flow stress of the powder particles decreases with increasing temperature. The influence of compacting temperature on the relative density of HDH Ti powder compacts is more significant than that

on the relative density of Ti-6Al-4V powder compacts. The relative density of HDH Ti powder compacts increases from 75% to a maximum value of 97% with increasing powder compacting temperature from room temperature to 400 °C. The relative density of HDH Ti-6Al-4V powder compacts increases slightly from 75% to 79% with increasing compaction temperature from room temperature to 450 °C, and then increases significantly from 79% to a maximum value of 84% with increasing compaction temperature from 450 to 500 °C. The relative density of GA Ti-6Al-4V powder compacts gradually increases from 80% to a maximum value of 84% with increasing powder compaction temperature from 450 to 550 °C. For HDH Ti powder compacts, a further increase of compacting temperature beyond 400 °C does not cause any further increase in the relative density of powder compacts. The amount of increase in relative density in HDH Ti-6Al-4V powder, as a result of increasing the compaction temperature from 450 to 500 °C is clearly greater than that for GA Ti-6Al-4V powder, with the same compacting temperature increase. This means that the shape of the powder particles affects powder compaction behavior. Due to the difficulty of compacting GA Ti-6Al-4V powder at temperatures lower than 450 °C, the effect of powder particle shape on powder compacting behaviour at lower temperatures (below 450 °C) was not determined in this study.

Considering the difficulty and cost of producing powder compacts with high density, the selected temperatures for compacting HDH Ti and HDH Ti-6Al-4V powders for making powder compacts for forging experiments were 250 and 300 °C, respectively. Due to the relatively low temperatures, powder compaction was done in air. For making powder compacts for forging experiments, GA Ti-6Al-4V powder was compacted at 550 °C under an argon protective atmosphere. These powder compaction conditions are shown by the arrows in Figure 3.2. The powder compaction temperatures for making powder compacts for subsequent sintering and forging of HDH Ti, HDH and GA Ti-6Al-4V powder compacts and their

relative density are listed in Table 3.1.

Table 3.1: Selected powder compacting temperatures for making powder compacts for further sintering and forging experiments and their density.

Powders	HDH Ti	GA Ti-6Al-4V	HDH Ti-6Al-4V
Temperature (°C)	250	550	300
Relative density	90.3%	84%	77.4%

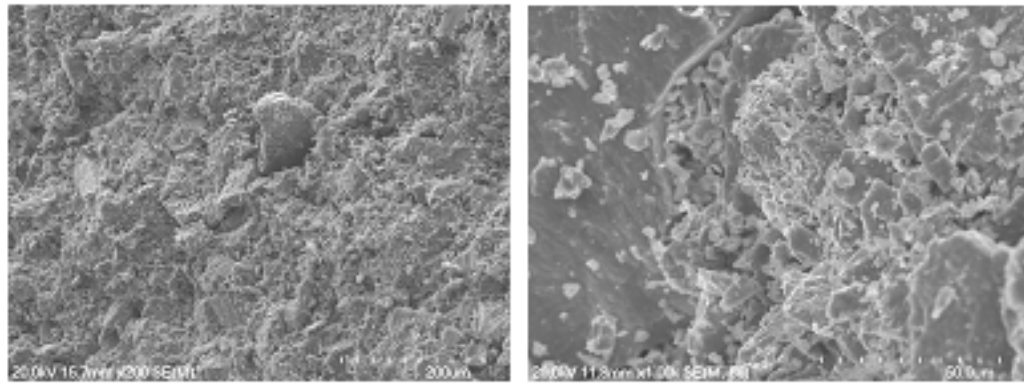
3.2.2 Mechanism of Compacting HDH Ti, HDH Ti-6Al-4V and GA Ti-6Al-4V Powders Compact

According to the results from the powder compaction experiments, it can be concluded that HDH Ti and Ti-6Al-4V powders are much easier to compact to a complete shape than GA Ti-6Al-4V powder. This is especially true at low temperatures, ranging from room temperature to 300 °C, because of their rough particle surfaces and irregular particles shape as shown in Figure 2.2. There are two stages in the powder compaction process with increasing external pressure, as described in Chapter 1, namely particle rearrangement and sliding and plastic deformation. Based on the tap density of HDH Ti, HDH and GA Ti-6Al-4V powders shown in Table 3.2, Ti-6Al-4V GA powder has a higher tap density than HDH Ti and HDH Ti-6Al-4V powders, which can be attributed to the difference in shape of the powder particles and the friction between powder particles. GA Ti-6Al-4V powder particles with a spherical shape can be rearranged because they slide more easily than HDH Ti and HDH Ti-6Al-4V powder particles with more irregular shapes. GA powder particles have a lower surface roughness than HDH powder particles and this reduces the internal friction between adjacent powder particles.

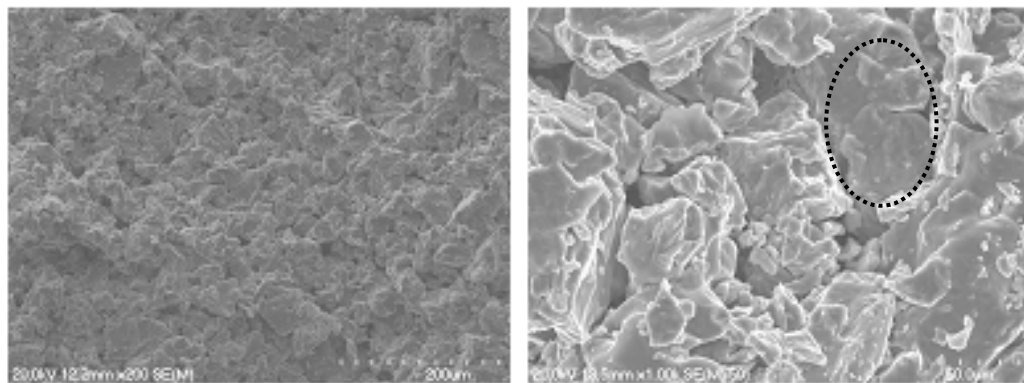
Table 3.2: Relative apparent and tap densities of raw powders.

Powder	HDH Ti	GA Ti-6Al-4V	HDH Ti-6Al-4V
Powder size	-200 mesh	-100 mesh	-200 mesh
Shape	Irregular	Spherical	irregular
Relative apparent density	35.4%	61.2%	33.4%
Relative tap density	37.7%	65.2%	41.7%

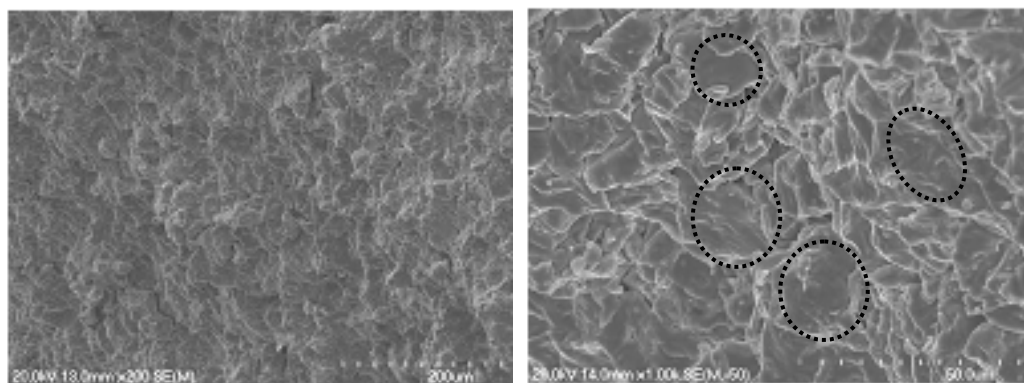
Cold welding and interlocking are two mechanisms for powder compaction. After breaking HDH Ti powder compacts, it can be seen that the contact surfaces between the powder particles (Figure 3.3) are much smoother than in the raw powder particles, showing that the powder particles were cold welded as a result of the friction between particles. The friction between powder particles is regarded as harmful to densification of a powder compact by some researchers, but here it is shown that the friction between powder particles is beneficial for bonding between particles. Also the interlocking of HDH Ti and HDH Ti-6Al-4V powder particles occurs easily due to their rough surfaces. As shown in Figure 3.3, as the density of powder compacts increases because of an increase in compacting temperature, the surfaces of HDH powder particles become smoother. These are highlighted in the figure and suggest that the powders were deformed more severely. Also according to the particle size distributions of raw powders shown in Figure 2.1, even though the average particle size of the -100 mesh GA powder was larger than that of the -200 mesh HDH powder, the range of particle sizes of the HDH powder was much wider than that of the GA powder. The small powder particles are located among the large powder particles as bridges, so during powder compacting, small powder particles can be deformed more easily than large powder particles under the same external pressure. This is another reason why HDH powder can be compacted more easily than GA powder.



(a) Room temperature



(b) 150 °C

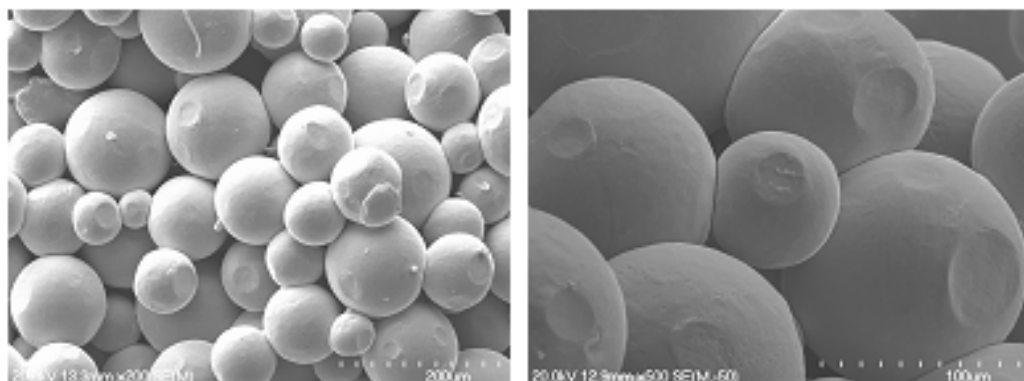


(c) 250 °C

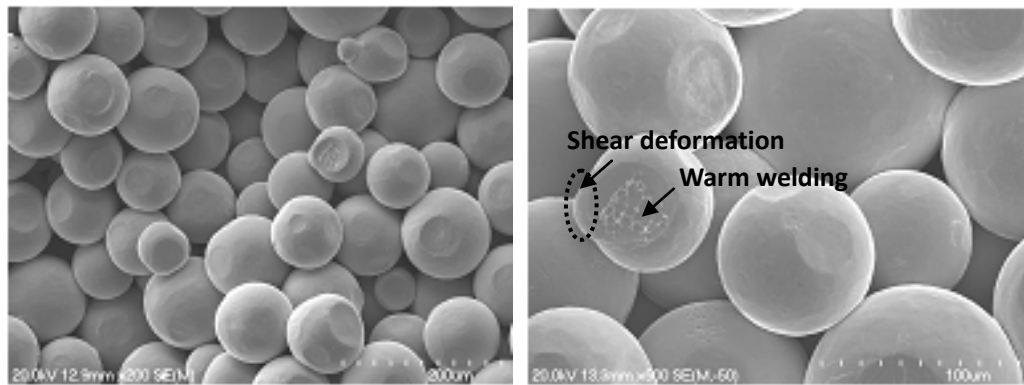
Figure 3.3: Fracture surfaces of HDH Ti powder compacts made by compacting at different temperature respectively.

The morphologies of GA Ti-6Al-4V powder particle surfaces after compacting at different temperature are shown in Figure 3.4. Due to good flowability and the spherical shape of GA powder particles, particle rearrangement and sliding can

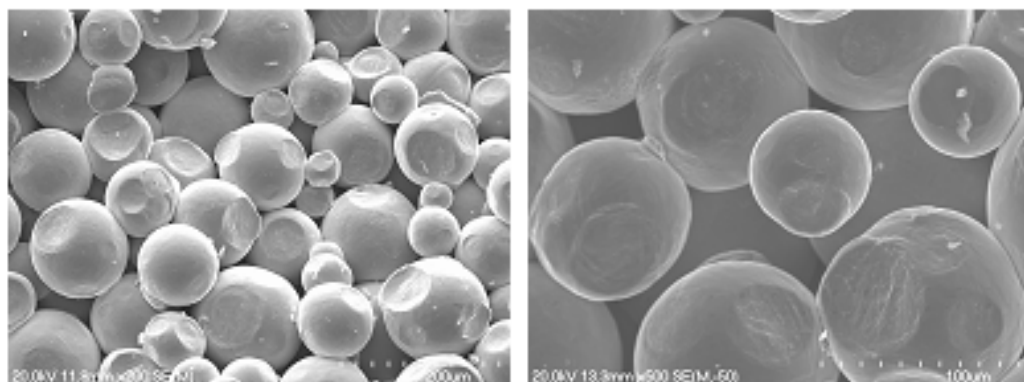
more easily occur during compacting the GA powder than compacting the HDH powder. This makes it difficult to produce GA powder compacts, especially at low temperatures. Cold welding between two adjacent powder particles is also hard to achieve because of the lower surface roughness of GA powder particles compared with HDH powder particles. In Figure 3.4, the warm welding areas in a GA powder compact are difficult to observe, but the deformed areas in those powder particles with flattened surfaces caused by compaction can be seen more clearly than observed in the HDH powder compacts in Figure 3.3. With increasing compaction temperature, the areas of the flattened surfaces in GA powder particles became larger due to a larger amount of deformation. As shown in Figure 3.4, the area of welding between two adjacent powder particles, caused by plastic deformation during compacting at 500 °C, is larger than that during compacting at 450 °C. It can also be seen that in the welding area there is a large amount of shear deformation in the powder particles. This means that welding between GA powder particles occurred by shear deformation of two adjacent powder particles rather than normal deformation. This can be explained by the breaking of the oxide surface layers on powder particles to form new surfaces which are easily welded together. So the main mechanism for powder compaction of GA Ti-6Al-4V powder is by warm welding.



(a) 450 °C



(b) 500 °C



(c) 550 °C

Figure 3.4: GA Ti-6Al-4V powder particle morphologies after compaction at different temperatures with a pressure of 726 MPa, respectively.

3.3 Induction Sintering of Ti and Ti-6Al-4V Powder Compacts

Before powder compact forging, powder compacts were heated up to the forging temperature at a high heating rate using an induction furnace. During induction heating, some pre-sintering of the powder compacts occurred. The as-sintered powder compacts were characterized in this study. HDH Ti, HDH and GA Ti-6Al-4V powder compacts with relative density of 90.3%, 77.4% and 84%, respectively, as shown in Table 3.1, were selected to be sintered by induction heating. The powder compacts were heated up from room temperature to 1350 °C in 3 minutes, and then cooled down under an argon protective atmosphere. Shrinkage of powder compacts occurred during sintering, so the as-sintered

powder compacts became denser than the green powder compacts as shown in Table 3.3. Because of the sintering during induction heating the relative density of HDH Ti and HDH and GA Ti-6Al-4V powder compacts increased by 0.7%, 3.4% and 1.8% and corresponding porosity of 7.2%, 15% and 11.3% had been eliminated, as indicated by their densification parameters.

Table 3.3: Relative density of as-sintered powder compacts.

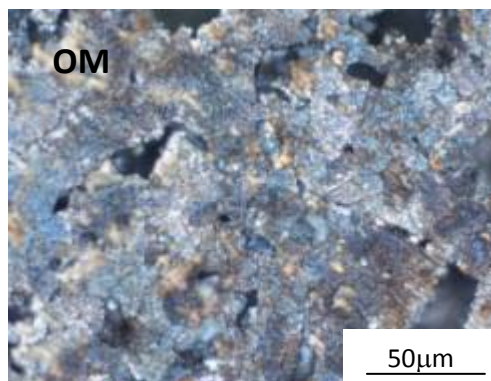
Powder	HDH Ti	HDH Ti-6Al-4V	GA Ti-6Al-4V
Relative density	91%	80.8%	85.8%
Densification parameter	7.2%	15%	11.3%

3.3.1 Microstructure of As-sintered Parts

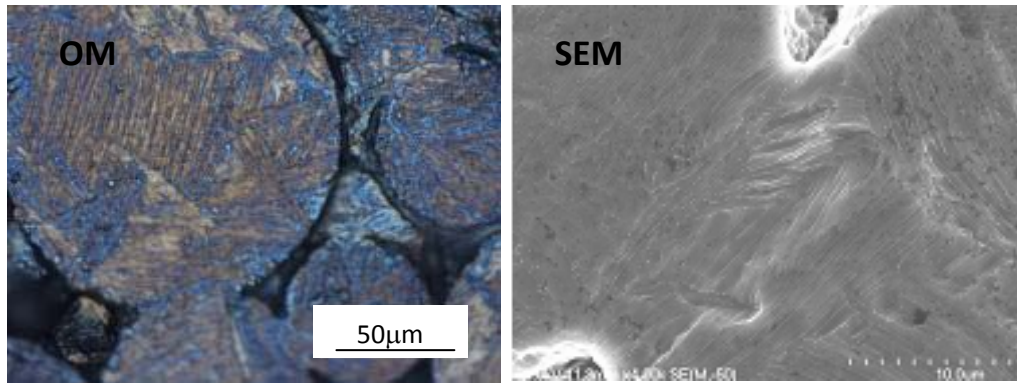
An as-sintered HDH Ti powder compact, with a relative density of 91%, contained a large fraction of isolated pores formed during sintering, and the powder compact became stronger due to neck formation between powder particles by atomic diffusion at the high temperatures up to the forging temperature of 1350 °C. The as-sintered Ti powder compact showed a microstructure consisting of equiaxed α grains, as shown in Figure 3.5(a). The as-sintered HDH and GA Ti-6Al-4V powder compacts contained both open and closed pores formed during sintering. The different microstructures of as-sintered GA and HDH Ti-6Al-4V powder compacts are shown in Figures 3.5(b) and (c). The as-sintered GA Ti-6Al-4V powder compact had a microstructure consisting of α acicular in an α/β lamellar matrix (Figure 3.5(b)), and the width of the α acicular was around 500nm. In contrast to this, the as-sintered HDH Ti-6Al-4V powder compact had a microstructure consisting of primary α particles in a coarse α/β lamellar matrix (Figure 3.5(c)). The coarse primary α lamellae, which formed at the β grain boundaries during cooling from the β phase region, were transformed into $\alpha+\beta$ two phase regions, with most of the β grain boundaries evolving from powder particle contacts during sintering. With further cooling into the α phase region, a coarse α lamellae formed β grains, leading to the formation of a coarse α/β matrix

with a primary α lamellar structure. From SEM images of the microstructure of an as-sintered HDH Ti-6Al-4V powder compact, it can be seen that both primary coarse α lamellar and the α lamellar in β grains are coarser than the α acicular.

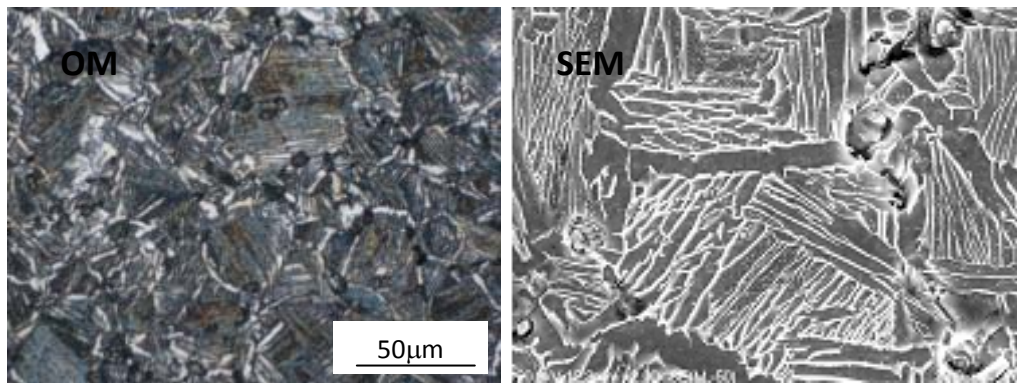
The reasons for the microstructural difference between as-sintered HDH and GA Ti-6Al-4V powder compacts are the composition of the raw powders and the powder production process. HDH powder is produced from ingots by a hydride and dehydride process, and the powder particles still keep the microstructure of the equilibrium microstructure of the ingots. However, the GA powder is produced by rapid solidification of liquid droplets during fast cooling, and the powder particles have a non-equilibrium microstructure. When the powder compacts were heated up to the forging temperature, an acicular structure formed in the GA Ti-6Al-4V powder compacts, while a coarse lamellar structure formed in HDH Ti-6Al-4V powder compacts. Also oxygen is an alpha stabilizer. The oxygen content of the GA Ti-6Al-4V powder is lower than that of the HDH Ti-6Al-4V powder used in this work, as shown in Table 2.1, so this is the other reason why a coarse α lamellar structure formed in the as-sintered HDH Ti-6Al-4V powder compact, while an α acicular structure formed in the as-sintered GA Ti-6Al-4V powder compacts.



(a) Optical microscopy (OM) image of an as-sintered HDH Ti powder compact



(b) OM and SEM images of an as-sintered GA Ti-6Al-4V powder compact



(c) OM and SEM images of an as-sintered HDH Ti-6Al-4V powder compact

Figure 3.5: Microstructure of as-sintered powder compacts.

3.3.2 Mechanical Properties of As-sintered Powder Compacts

The tensile properties of as-sintered powder compacts for different relative densities are shown in Figure 3.6. The tensile stress-strain curves of the specimens cut from an as-sintered HDH Ti powder compact with a relative density of 91% showed that the material had clear yield points and an elongation to fracture of 6.6%-8.9%. On the other hand, the tensile stress-strain curves of specimens cut from as-sintered HDH and GA Ti-6Al-4V powder compacts with a lower relative density, showed that the material did not clearly yield before fracturing and their elongation to fracture was very small, being in the range of 0.4%-1.4%.

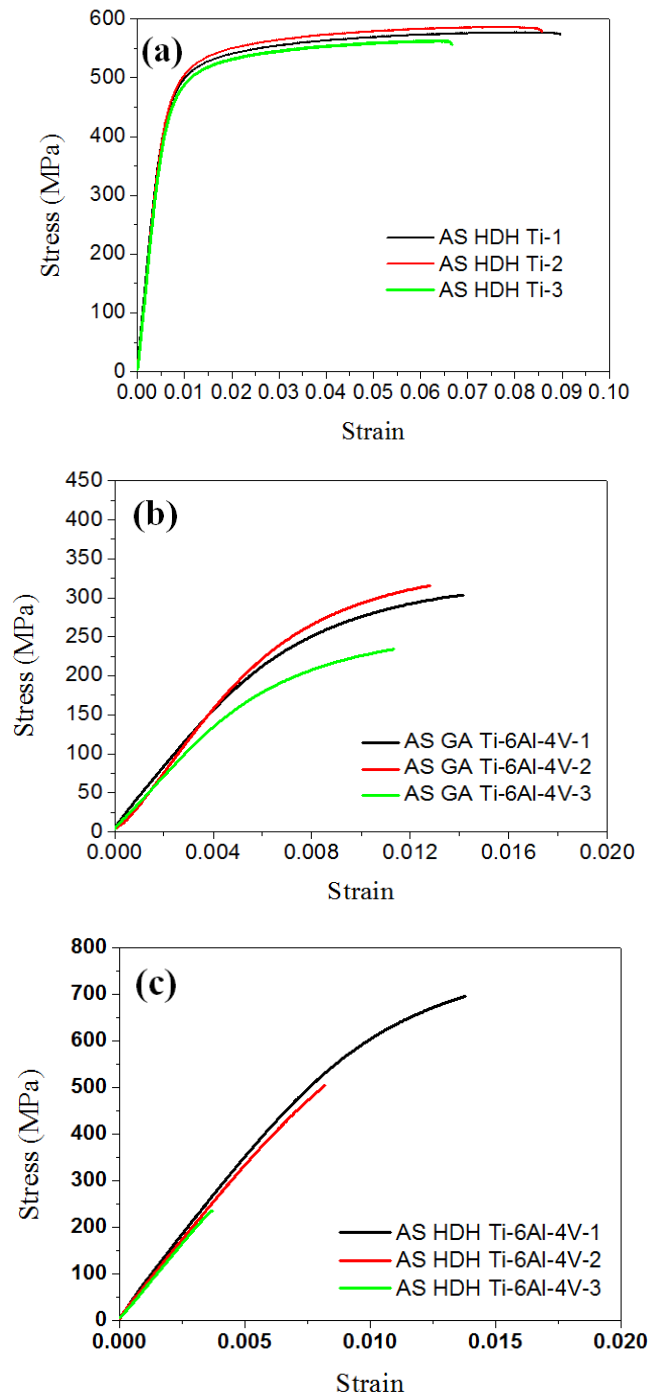


Figure 3.6: Stress-strain curves of specimens cut from as-sintered compacts: (a) HDH Ti, relative density of 91%; (b) GA Ti-6Al-4V, relative density of 85.8%; (c) HDH Ti-6Al-4V, relative density of 80.8%. (AS=as-sintered)

From the stress-strain curves in Figure 3.6(a), the average ultimate tensile strength (UTS) of as-sintered Ti specimens could reach 575.4 MPa, and the average yield strength was 470 MPa, with the average elongation to fracture being 7.5% (Table 3.4). These properties are far different from those of bulk titanium with full

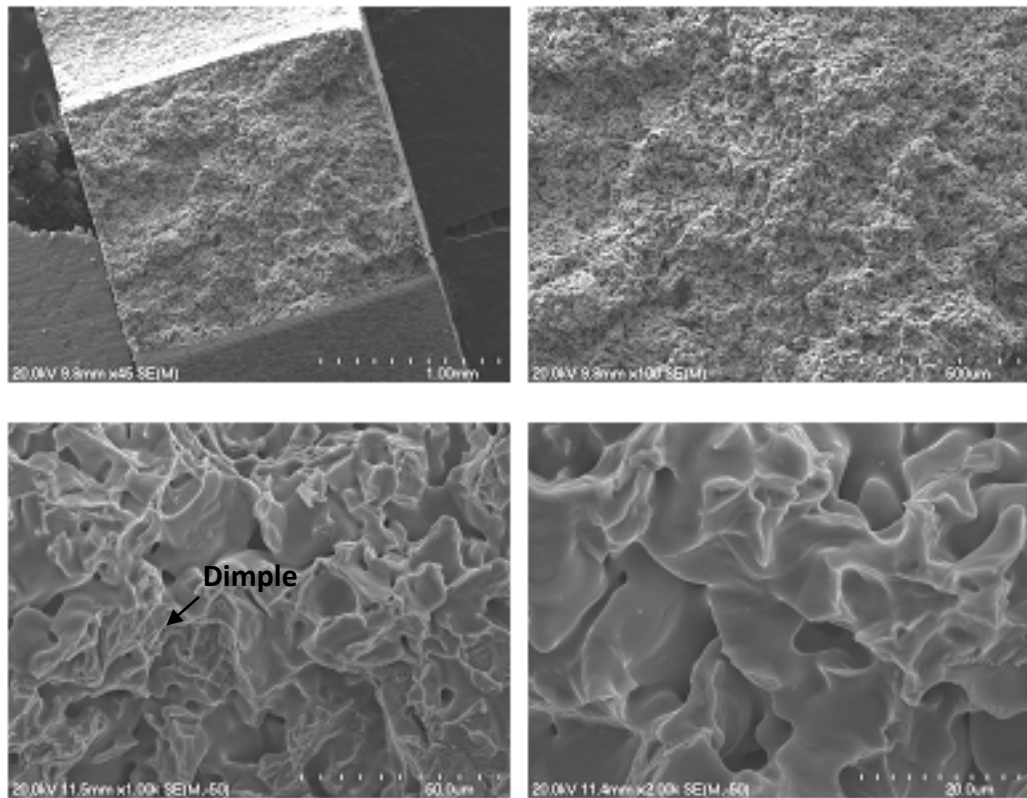
density. Even though there are a lot of pores in the as-sintered HDH Ti powder compact with a relative density of 91%, it is not a brittle material. Nevertheless, the large isolated pores play an important role as fracture initiators and cause a reduction in elongation to fracture. As shown in Figures 3.6(b) and (c), the tensile stress-strain curves of as-sintered HDH and GA Ti-6Al-4V powder compacts showed a very small elongation to fracture, and their UTS was lower than 700 MPa. The brittleness of the as-sintered HDH and GA Ti-6Al-4V powder compacts can be attributed to their low relative density of about 80%, as shown in Table 3.3.

Table 3.4: Summary of mechanical properties of as-sintered HDH Ti powder compact with relative density of 91% and oxygen content of 0.41%.

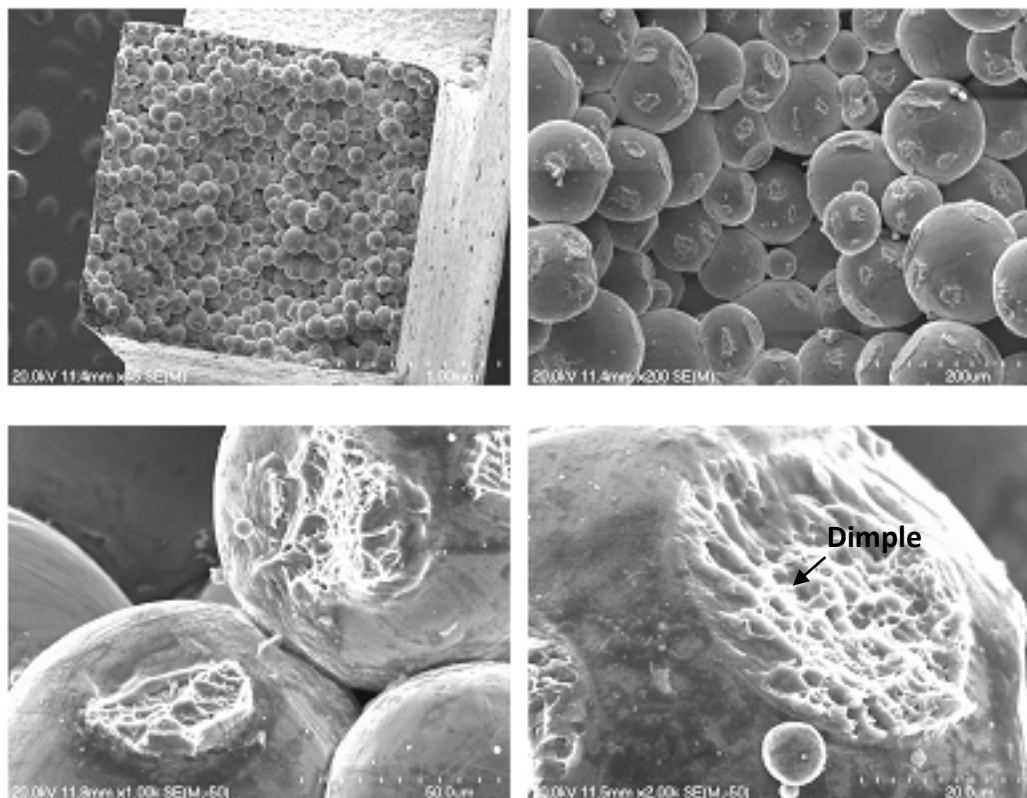
Sample	YS(MPa)	UTS(MPa)	Elongation
AS HDH Ti-1	470.6	577.1	8.4%
AS HDH Ti-2	476.5	586.1	8.0%
AS HDH Ti-3	462.7	563.0	6.1%
Average	470.0	575.4	7.5%

3.3.3 Fracture Morphology of As-sintered Powder Compacts

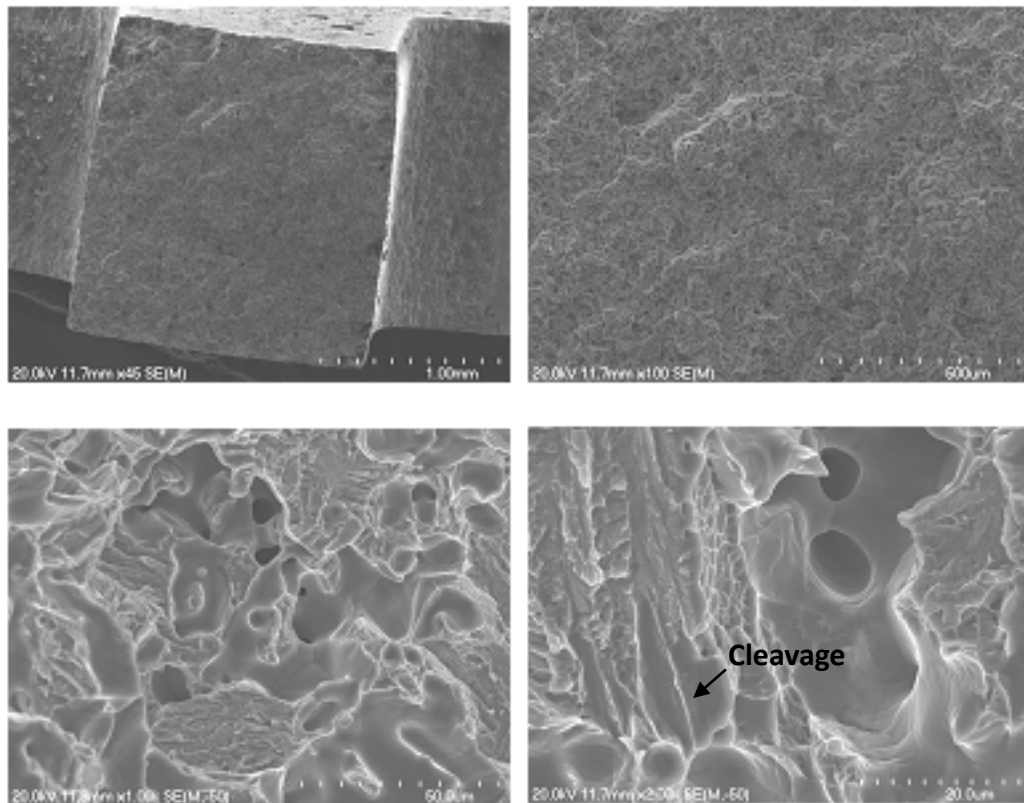
After tensile testing, the fracture surfaces of the specimens were examined by SEM, as shown in Figure 3.7. The main fracture mechanism in the as-sintered powder compacts is the fracture of the necks formed between powder particles. This is shown in Figure 3.7(b), where the SEM images of the fracture surface of an as-sintered GA Ti-6Al-4V powder compact show the concave and convex shapes of the fracture surfaces. This is especially so where a sinter-neck was torn off due to insufficient sintering. At high magnifications, the SEM images show that the fracture morphology of the necks between powder particles in as-sintered HDH Ti and GA Ti-6Al-4V powder compacts have dimples, indicating that the fracture was ductile. However, a cleavage morphology was seen on the fracture surfaces of the necks between the powder particles in the as-sintered HDH Ti-6Al-4V powder compact (Figure 3.7(c)).



(a) HDH Ti, relative density of 91%



(b) GA Ti-6Al-4V, relative density of 85.8%



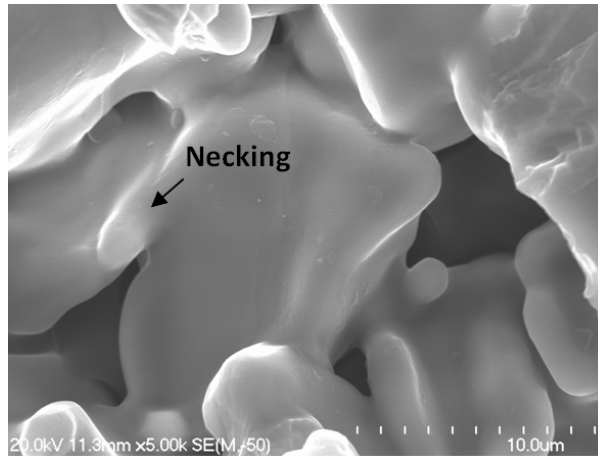
(c) HDH Ti-6Al-4V, relative density of 80.8%

Figure 3.7: SEM images at different magnifications of the fracture morphology of as-sintered HDH Ti and GA and HDH Ti-6Al-4V powder compacts after tensile testing.

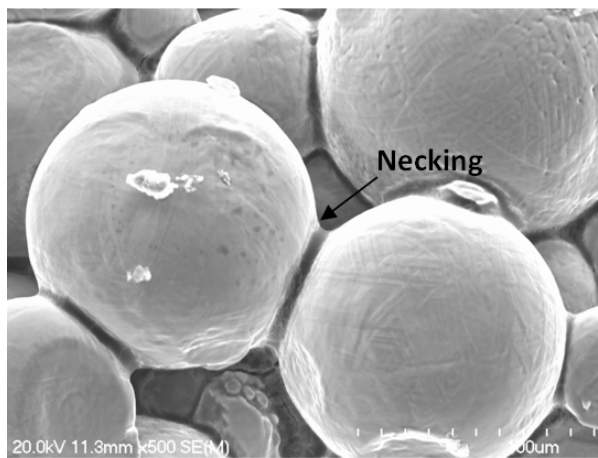
3.3.4 Mechanisms of Densification and Sintering during Induction Heating

A reduction of surface energy is the thermodynamic driving force for forming necks between two powder particles in contact, which is the initial stage of the sintering process. When the powder compacts were heated to 1350 °C, the necking between two neighboring particles in the powder compacts occurred as shown in Figure 3.8. The necking between neighboring GA spherical powder particles was seen more clearly (Figure 3.8(b)) than that between neighboring HDH powder particles with irregular shapes (Figures 3.8(a) and (c)). The extent of necking between powder particles in the HDH Ti and HDH Ti-6Al-4V powder compacts (Figures 3.8(a) and (c)) during induction heating was much more

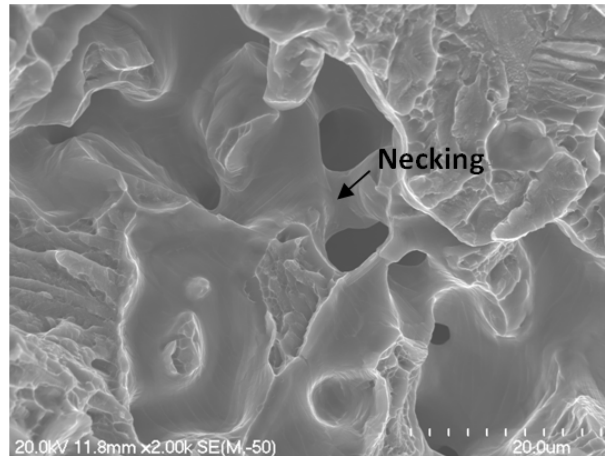
significant than that found in a GA Ti-6Al-4V powder compact. This is reflected by the extent of the change in powder particle surface morphology caused by the induction heating. This can be attributed to the fact that the HDH powder particles, with irregular shapes have more surface energy than the spherical GA powder particles.



(a) As-sintered HDH Ti powder compact



(b) As-sintered GA Ti-6Al-4V powder compact



(c) As-sintered HDH Ti-6Al-4V powder compact

Figure 3.8: Powder morphologies of as-sintered powder compacts sintered at a temperature of 1350°C.

As described in Chapter 1, the driving force for necking is the curvature gradient at the neck. For a green powder compact heated up by a furnace with heating elements, the heat energy is transferred into the powder compact by the outside atmosphere acting as a heating agent. When induction heating is used, induction sintering depends on eddy current heating. An alternating electromagnetic field induces eddy currents in a conductive material, by electromagnetic induction and an alternating current in a loop is induced in the alternating magnetic field. The formula is described as Faraday - Lenz's law below:

$$E = \frac{d\Phi}{dt} \quad (3.1)$$

where E is voltage, Φ is magnetical flux and t is time.

For the Joule-effect, the thermal power generated when an electrical current flows through a conductive material can be calculated using the following equation:

$$P = I^2 \times R \quad (3.2)$$

where P is power, I is electric current and R is resistance.

From the above two equations, the absorption of heat energy in the powder compact by induction heating can be calculated, assuming the electric current is

constant [2]. With a two-sphere model shown in Figure 3.9, the resistance R can be calculated by the following equation:

$$R = \rho \frac{dL}{A} \quad (3.3)$$

where ρ is the resistivity of the conductor material, dL is unit length and A is the cross-sectional area.

During powder compaction, two adjacent spherical particles are deformed as shown in Figure 3.9. Assuming that the diameter of the contact area of two adjacent particles, shown Figure 3.9 is X_1 , the electrical resistance at the particle contact area can be described as: $R = 4\rho \frac{dL}{\pi X_1^2}$. The resistance at the particle contacts is the highest, so the temperature at the contact area of two particles is higher than any other region in the two particles, and this can accelerate the formation of necking. This means that the necking area grows faster during induction heating than heating using other methods such as radiation heating which does not involve passing electrical currents through powder particles and the contacts between them. Also due to the existence of an oxide layer on the surfaces of Ti and Ti-6Al-4V powder particles, the electrical resistance at the contact area between powder particles is much larger than that in the body of the powder particles. Therefore heat energy is very concentrated at the particle contact areas, which makes the temperature of these areas much higher than that in the particle body.

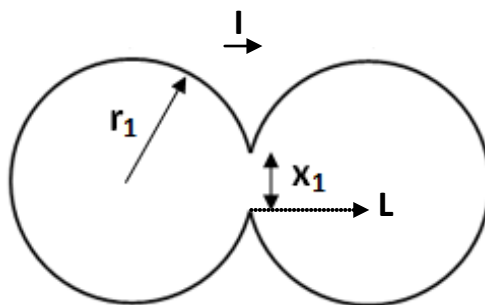


Figure 3.9: Two-sphere model for necking formation showing the powder particle surface contact area caused by plastic deformation.

3.4 Discussion

3.4.1 The effect of Compacting Temperature on the Relative Density of Ti and Ti-6Al-4V Powder Compacts

The relationship between compaction temperature and the relative density of Ti powder compacts was studied from room temperature to 140 °C under air in Ref. [1, 3]. With an increase in powder compaction temperature, the relative density of Ti powder compacts increases slightly from 77.7% to a maximum value of 81.6% as shown in Figure 3.10. When the powder compaction temperature was extended to 500 °C, which is close to the maximum working temperature of the powder compaction die made of heat treated H13 steel in this study, the relative density of HDH Ti powder compacts increases significantly from 75% to a maximum value of 97% at 400 °C. Also from the relative density versus temperature curve for an HDH Ti powder compact, a relative density of 92% was produced at a powder compaction temperature of 250 °C (this is below 276 °C which is the starting temperature for the onset of severe oxidation for pure titanium [4]) in air without an argon protective atmosphere, under a pressure of 544 MPa). Powder compacts with a relative density of over 90% were pressed at room temperature with a pressure greater than 1000 MPa [5], so in order to produce a Ti powder compact with a high relative density and with an increase in powder compacting temperature, the compacting pressure was decreased a lot. This is beneficial for increasing the working life of the powder compacting die.

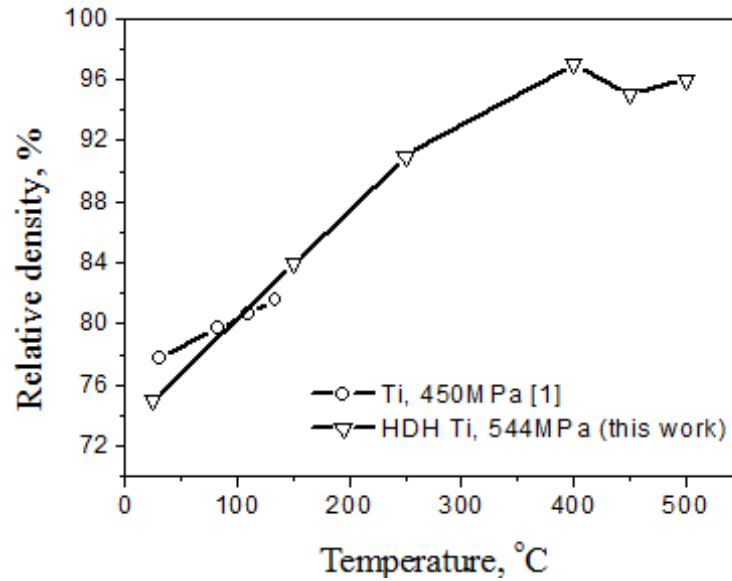


Figure 3.10: Comparison of relative density of Ti powder compacts as functions of temperature under different pressures: 450 MPa [1] and 544 MPa (this work).

For the warm compaction of Ti-6Al-4V powder, there is little information reported in the literature. Most Ti-6Al-4V powder compacts [5, 6] were produced by cold compaction. In Ref. [5], Ti-6Al-4V powder compacts with a relative density of 80% were pressed uniaxially at room temperature under a compacting pressure of 970 MPa. In this study, to produce both HDH and GA Ti-6Al-4V powder compacts with the same relative density of 80%, the compacting pressure was slightly decreased to 726 MPa by increasing the compacting temperature to 450 °C. As shown in Figure 3.11 the relative density of a Ti-6Al-4V powder compact was increased to 84.5% by increasing the compaction pressure to 1366 MPa at room temperature [5]. To get the same relative density in a powder compact, the compaction temperature was only increased from 450 to 550 °C for both HDH and GA Ti-6Al-4V powder compacts. So for GA and HDH Ti-6Al-4V powder, a compaction temperature within the range of 450-550 °C can significantly influence the compaction pressure needed to achieve the desired density.

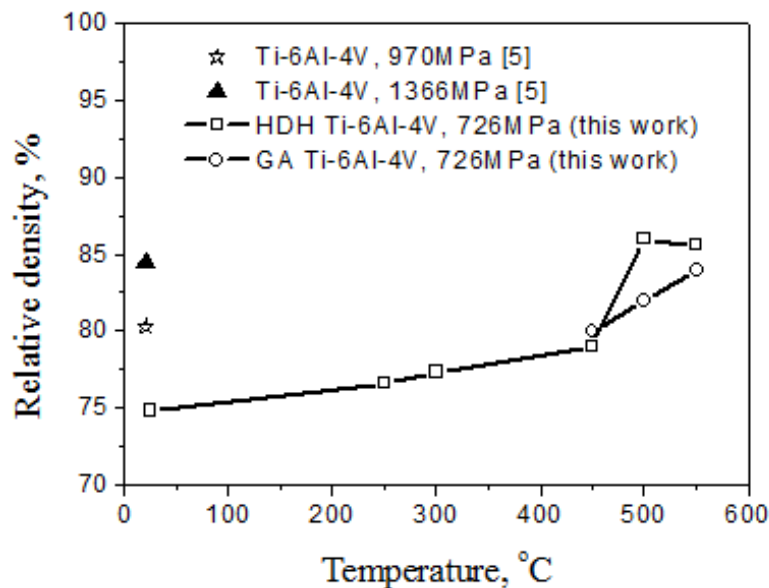


Figure 3.11: A comparison of the relative density of Ti-6Al-4V powder compacts as a function of temperature at different pressures: 970 MPa [5], 1366 MPa [5] and 726 MPa (this work).

The effect of compaction temperature on the relative density of Ti and Ti-6Al-4V powder compacts in this study can be explained by the relationship between yield stress and temperature of the bulk material shown in Figure 3.12. In this figure, the yield stress of Grade 4 CP Ti bulk material dropped significantly with increasing temperature from room temperature to 300 °C, and then changed slightly up to 500 °C, which is consistent with the change in relative density of an HDH Ti powder compact with compaction temperature. Also, a curve of yield stress vs temperature for Ti-6Al-4V bulk material after mill annealing, shows that the yield stress falls gradually with increasing temperature to 450 °C, then drops more sharply when the temperature is further increased to 550 °C. This is the reason why the change in the relative density of HDH Ti-6Al-4V powder compacts during compaction in the temperature range of 450-550 °C was more significant than for those made using a compaction temperature less than 450 °C.

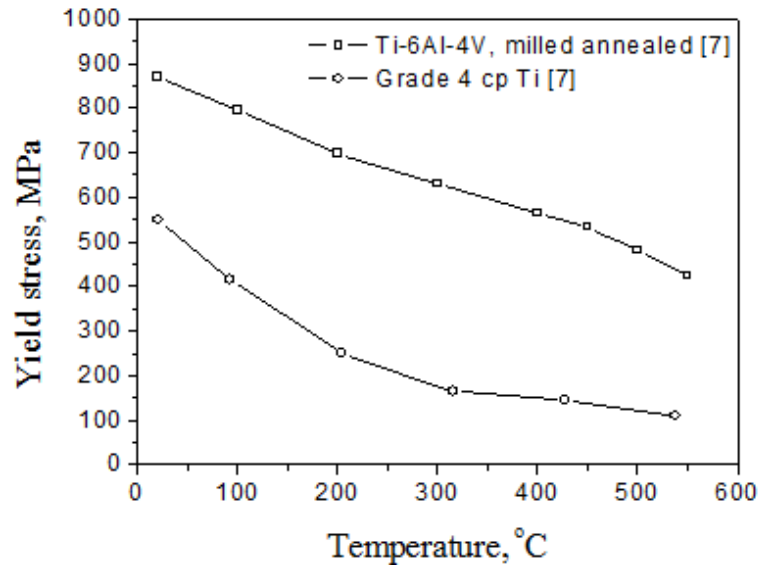


Figure 3.12: Yield strength vs temperature curves of Grade 4 CP Ti and milled annealed Ti-6Al-4V bulk material [7].

3.4.2 The effect of Particle Shape and Oxygen Content on Ti-6Al-4V Powder Compaction

As shown by the results in Figure 3.11 for GA and HDH Ti-6Al-4V powder compaction in this study, at a compaction temperature of 450 °C, the relative densities of HDH and GA Ti-6Al-4V powder compacts are the same. However, with increasing compaction temperature to 500 or 550 °C, the relative density of HDH Ti-6Al-4V powder compacts is much higher than that for GA Ti-6Al-4V powder compacts. As shown in Table 2.1, the oxygen content of HDH Ti-6Al-4V powder is 0.5wt%, which is much higher than that of the GA Ti-6Al-4V powder, which is 0.13wt%. Therefore the HDH Ti-6Al-4V powder particles are more difficult to deform than GA Ti-6Al-4V powder particles based on the correlation between the oxygen content and yield stress of Ti-6Al-4V shown in Ref. [7]. This means that a powder compact made from HDH Ti-6Al-4V powder should have a lower relative density than one made using GA Ti-6Al-4V powder without taking the effect of particle shape into account. The effect of particle shape on the density of a green powder compact was reported in Ref. [8]. According to these results, a higher green powder compact density should be produced by using powders with

irregularly shaped particles. Therefore, the fact that a higher relative density is obtained when compacting HDH Ti-6Al-4V alloy powder, means that particle shape plays a more important role in controlling the density of a green powder compact than the oxygen content, at a high compacting temperature of 500 or 550 °C.

3.4.3 The effect of Particle Shape on Induction Sintering in Ti-6Al-4V Powder

The densification rate dV_S/dt of a powder compact can be described as [9]:

$$\frac{dV_S}{dt} = (1 - V_S)Bg \frac{\gamma_{SV}}{x} \quad (3.4)$$

where V_S represents the fraction of solid, B is a collection of parameters which includes diffusivity, temperature, particle size, g is a geometric term, γ_{SV} is solid-vapor surface energy, x is the scale of the microstructure. In Equation 3.4, the densification rate of a powder compact is proportional to the solid-vapour surface energy. Compared with spherical GA Ti-6Al-4V powder, the densification rate of an HDH Ti-6Al-4V powder compact was higher because of its irregularly shaped powder particles and larger surface energy due to a rougher surface. As a result, the relative density of an HDH Ti-6Al-4V powder compact increased more rapidly than that for a GA Ti-6Al-4V powder compact during induction heating. The large surface energy of raw powder enhances the powder sintering. From a comparison of the results from tensile testing, both as-sintered HDH and GA Ti-6Al-4V powder compacts had a small elongation to fracture, but the stress to fracture for an as-sintered HDH Ti-6Al-4V powder compact was higher than that for an as-sintered GA Ti-6Al-4V powder compact. This was found even though the relative density of an as-sintered GA Ti-6Al-4V powder compact was much higher than that for an as-sintered HDH Ti-6Al-4V powder compact.

3.4.4 The effect on Induction Sintering of the Relative Density of Ti and Ti-6Al-4V Powder Compacts.

As described in Equation 3.4, the densification rate of a powder compact is proportional to the fraction of porosity ($1-V_s$), so a green powder compact with a lower porosity had a lower densification rate after sintering, which is consistent with the experimental results in this study. The relative density of an HDH Ti powder compact increased less than that for HDH and GA Ti-6Al-4V powder compacts during induction sintering. Also green powder compacts with a higher relative density, consolidate much better after induction sintering, and a large area of neck forms between two adjacent contact particles. This makes the particles bond more strongly after induction sintering and this is the reason why as-sintered an HDH Ti powder compact had a higher UTS and elongation to fracture than as-sintered HDH and GA Ti-6Al-4V powder compacts.

3.5 Summary

In this chapter, three types of raw powders, HDH Ti, HDH Ti-6Al-4V and GA Ti-6Al-4V powders, were used to make powder compacts by warm compaction.

- The relative density of HDH Ti powder compacts increased more significantly with increasing compaction temperature than Ti-6Al-4V powder compacts within a compacting temperature range from room temperature to 550 °C.
- Interlocking and cold welding mechanisms are both significant for HDH Ti and HDH Ti-6Al-4V powder compaction, while warm welding is the main mechanism for the compaction of GA Ti-6Al-4V powder.
- After induction sintering, the as-sintered HDH and GA Ti-6Al-4V powder compacts were brittle with very little elongation to fracture, while HDH Ti

powder compacts had an average elongation to fracture of 7.5%, UTS of 575.4 MPa and yield strength of 470 MPa.

- The mechanisms for the induction sintering of powder compacts investigated in this study were explained by the electrical resistance distribution in two adjacent particles in contact and with a spherical shape. Necking forms and grows faster during induction heating than found in other methods of heating which do not involve the passing of an electric current through powder particles and the contacts between them.

3.6 References

1. Simchi, A. and G. Veltl, *Behaviour of metal powders during cold and warm compaction*. Powder Metallurgy, 2006. **49**(3): p. 281-287.
2. Hermel, W., G. Leitner, and R. Krumphold, *Review of induction sintering: fundamentals and applications*. Powder Metallurgy, 1980. **23**(3): p. 130-135.
3. He, S.W., *Warm compacting behavior of pure titanium powders*. Advanced Materials Research, 2011. **189**: p. 2775-2779.
4. Gemelli, E. and N. Camargo, *Oxidation kinetics of commercially pure titanium*. Revista matéria, 2007. **12**(3): p. 525-531.
5. Robertson, I. and G. Schaffer, *Review of densification of titanium based powder systems in press and sinter processing*. Powder Metallurgy, 2010. **53**(2): p. 146-162.
6. Chen, W., et al., *Cold compaction study of Armstrong Process® Ti-6Al-4V powders*. Powder Technology, 2011. **214**(2): p. 194-199.
7. Rodney Boyer, G.W., E. W. Collings, *Materials Properties Handbook: Titanium Alloys*. 1994: ASM International.
8. Poquillon, D., et al., *Cold compaction of iron powders-relations between powder morphology and mechanical properties. I. Powder preparation and compaction*. Powder Technology, 2002. **126**(1): p. 65-74.
9. German, R.M., *Sintering Theory and Practice*. Vol. 1. 1996.

Chapter 4: Powder Compact Forging of Ti and Ti-6Al-4V Powders

4.1 Introduction

In the previous chapter, powder compaction and induction sintering of Ti and Ti-6Al-4V powder compacts were studied. In this chapter, the microstructure and mechanical properties of as-forged rocker arms produced by powder compact forging of HDH and GA Ti and Ti-6Al-4V powders were studied. During induction sintering of a powder compact as a pre-sintering step before forging, necking between adjacent powder particles occurred. However, if sintered parts with nearly full density are desired, a longer sintering time will be needed. Forging of a pre-sintered compact can be used to accelerate any remaining powder consolidation. This is achieved by severe plastic deformation, which rapidly makes a consolidated part with full density, compared with conventional sintering methods.

In this chapter, the factors which influence the microstructure, porosity distribution and mechanical properties of as-forged parts produced by a powder compact forging process are investigated. After powder compact forging, quantitative chemical analyses of the as-forged parts were conducted to determine the oxygen, nitrogen and hydrogen pick-up during forging. The fracture behaviour of as-forged parts during tensile testing were analyzed by examining both the fracture surfaces and the longitudinal surfaces of the fractured specimens cut from the as-forged parts. The powder consolidation mechanism in powder compact forging is discussed.

4.2 Microstructure of As-forged Parts

As-forged HDH Ti, HDH and GA Ti-6Al-4V rocker arms are shown in Figure 4.1. From the figure, the surface quality of an as-forged HDH Ti rocker arm is better

than that of as-forged HDH and GA Ti-6Al-4V rocker arms, as reflected by fewer cold-shuts and cracks on the surface of the HDH Ti rocker arm. Due to a lower relative density in HDH and GA Ti-6Al-4V green powder compacts compared with an HDH Ti powder compact, there are more pores and weaker particle bonding after induction sintering. This makes the HDH and GA Ti-6Al-4V powder compacts more easily fractured during forging. The lower flow stress of Ti powder particles compared with Ti-6Al-4V powder particles at the forging temperature is another reason why an HDH Ti powder compact has better flowability than HDH and GA Ti-6Al-4V powder compacts during forging.



(a) HDH Ti



(b) HDH Ti-6Al-4V



(c) GA Ti-6Al-4V

Figure 4.1: Images of as-forged rocker arms showing their top and bottom surfaces.

As forging is one kind of non-homogeneous plastic deformation process, streamlines were observed in as-forged HDH Ti, HDH and GA Ti-6Al-4V parts when cross-sections along the forging direction were examined by optical microscopy at low magnification, in Figure 4.2. Large localized deformed regions were concentrated in the center of the as-forged parts, while the powder particles were either not deformed or deformed little near the surface of the part resulting in the formation of streamlines. The streamlines in the cross sections of as-forged HDH Ti and HDH Ti-6Al-4V parts were clearer than those in the cross section of a GA Ti-6Al-4V part, as shown in Figure 4.2. This is caused by better flowability during forging of spherical powder particles in a GA powder compact compared with HDH powder particles with irregular shapes. This leads to a lower stress concentration during forging. On the other hand, large localized deformation assists in the consolidation of the powder and a reduction in the grain size. This will be further discussed in more detail in the latter part of this chapter.

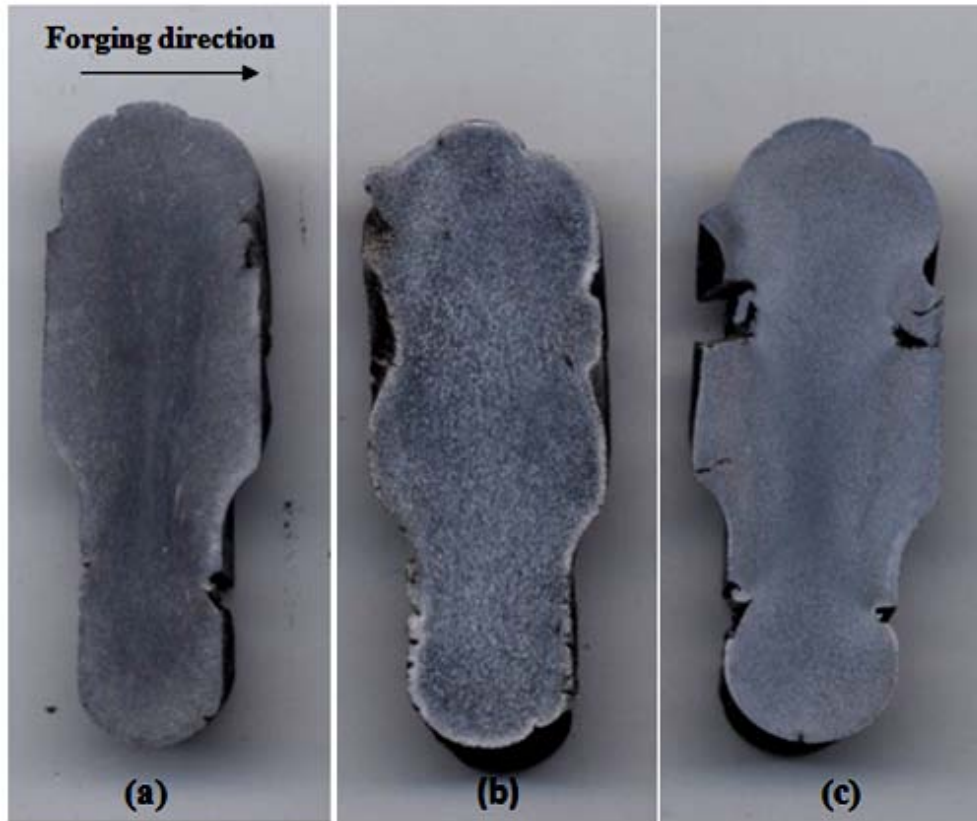
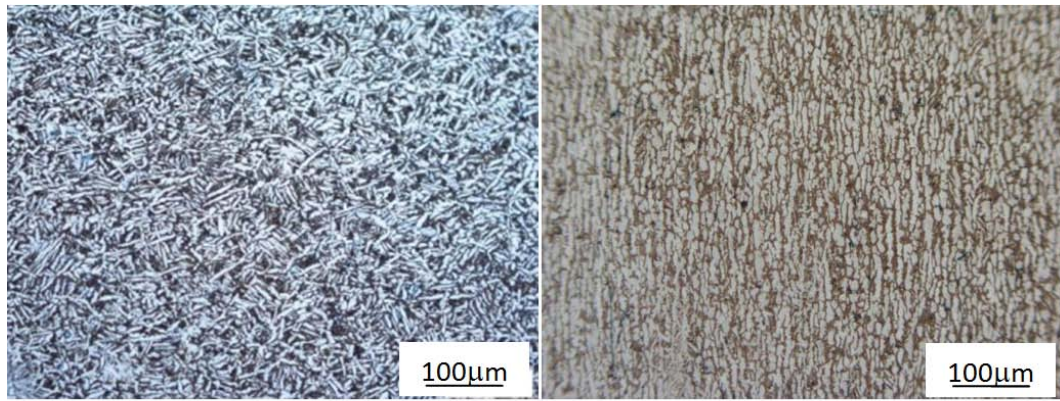


Figure 4.2: Low magnification images of as-forged parts: (a) HDH Ti; (b) GA Ti-6Al-4V; (c) HDH Ti-6Al-4V.

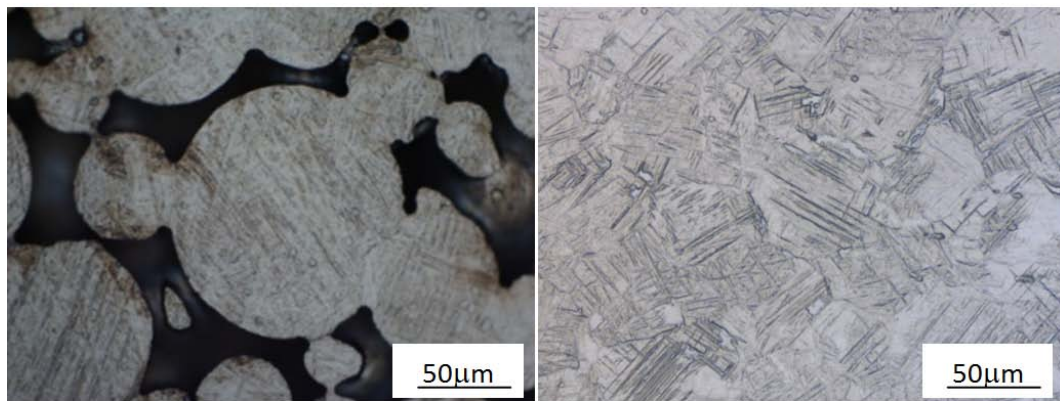
The microstructure of as-forged HDH Ti, HDH Ti-6Al-4V and GA Ti-6Al-4V parts was examined by optical microscopy, as shown in Figure 4.3. Unlike the equiaxed structure of the α phase in an as-sintered Ti powder compact, the as-forged HDH Ti part had a lamellar structure with α lamellae randomly orientated near the surface of the part, and being mainly along the streamline in the center of the part, where the amount of deformation was large. The SEM micrograph in Figure 4.4(a) shows equiaxed grains, with clear grain boundaries and a size of around 2 μm , between α lamellae. There were no obvious large pores existing both near the surface and in the centre of the as-forged HDH Ti part.



Near the surface

In the center

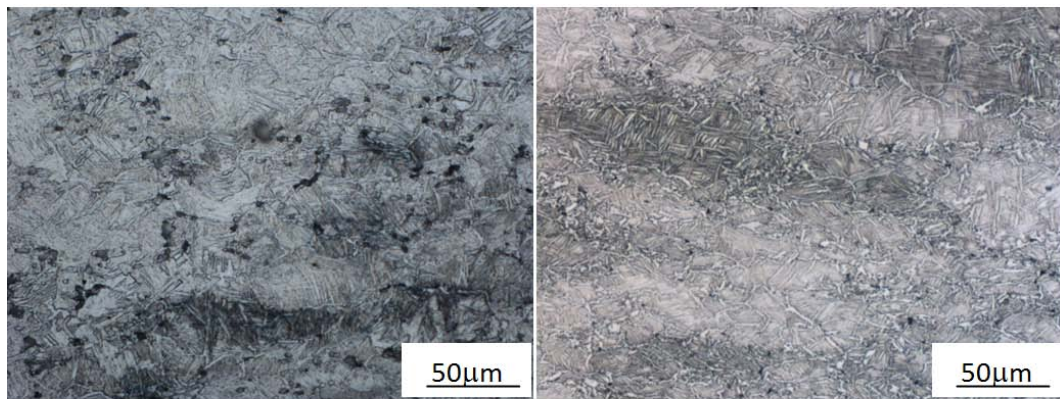
(a) HDH Ti



Near the surface

In the center

(b) GA Ti-6Al-4V



Near the surface

In the center

(c) HDH Ti-6Al-4V

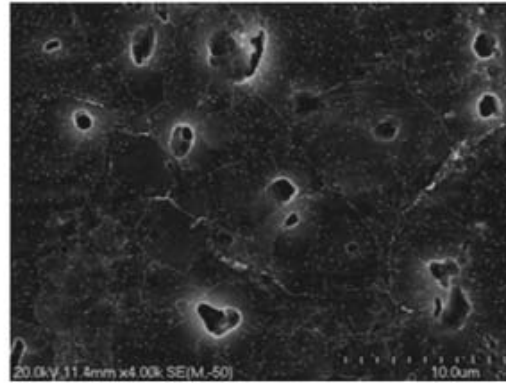
Figure 4.3: Optical micrographs showing the microstructure of different regions of the as-forged parts.

As shown in Figure 4.3(b), the spherical shape of the undeformed GA powder

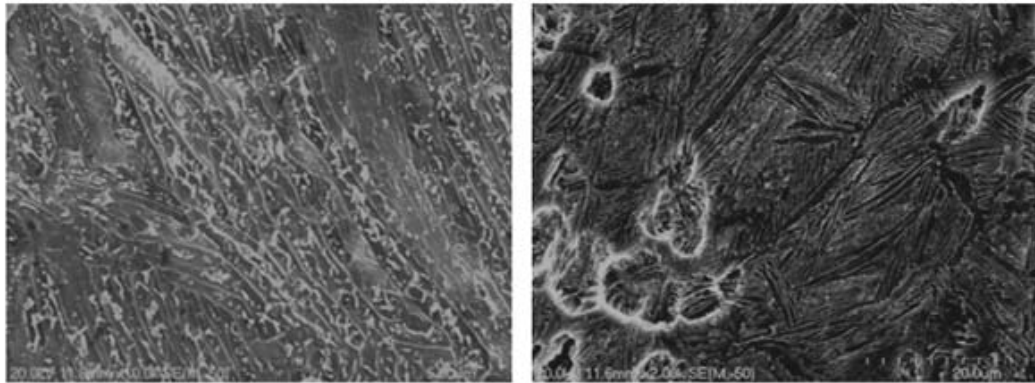
particles can be seen clearly near the surface of the as-forged GA Ti-6Al-4V part, showing that there was little plastic deformation in this region. The microstructure in this region was the same as that for an as-sintered GA Ti-6Al-4V powder compact shown in Figure 3.5(b), which consists of α acicular in an α/β matrix. In the centre of the as-forged part, α acicular has been broken into shorter plates (Figure 4.3(b)) and the spherical powder particles were deformed into a polygonal shape. The interparticle boundaries can be seen in general, but not very clearly. There was no obvious porosity in the center, so the powder was fully consolidated. With increasing distance from the surface to the centre of the part, the powder particles were deformed by a larger amount and the grain sizes became smaller, with a smaller aspect ratio in the α acicular in the centre compared with that of the α acicular near the surface of the part. As observed by SEM (Figure 4.4(b)), α acicular and fine transformed β lamellae between the α needles were visible, and the width of the α acicular was the same as that of the α acicular in the as-sintered part (Figure 3.5(b)) which was around 500 nm.

The microstructure near the surface and in the center of an as-forged HDH Ti-6Al-4V part consisted of primary α lamellae in a coarse α/β matrix as shown in Figure 4.3(c). In this structure, the primary α lamellae are nucleated firstly on the β grain boundaries, and then secondly in the grain. Finally a coarse α/β matrix structure is formed in the prior β grains [1], so the microstructure evolution is the same as that for an as-sintered HDH Ti-6Al-4V powder compact. The microstructure near the surface of an as-forged part was porous. Due to non-homogeneous deformation, primary α lamellae in the microstructure in the centre of the part were thinner than those near the surface. The prior β grain size became smaller in the centre, due to fine grains produced by dynamic recrystallization caused by plastic deformation. In the meantime, there were no large pores in the center, showing that the powder particles in this region were fully consolidated. The difference in the microstructure of as-forged parts

produced using the two kinds of Ti-6Al-4V powders is caused by the difference in their particle shapes and composition, as discussed in Chapter 3.



(a) HDH Ti

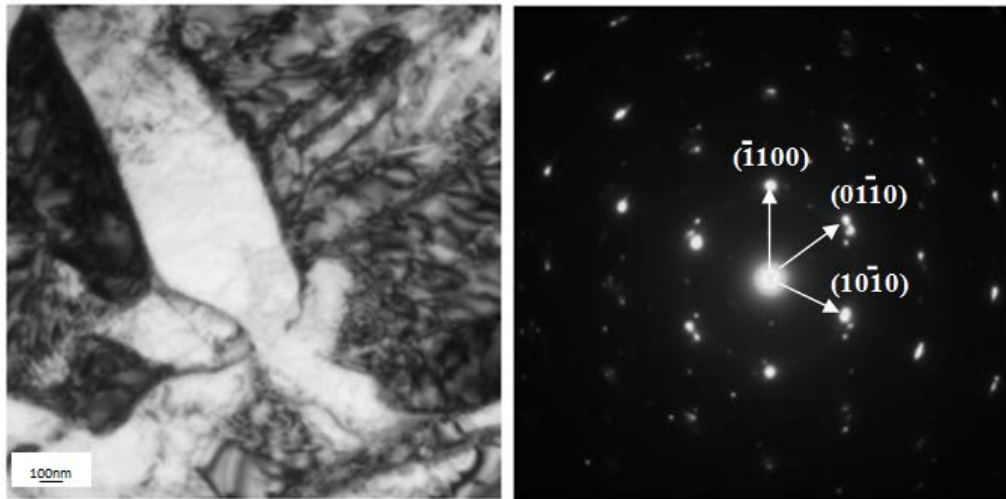


(b) GA Ti-6Al-4V

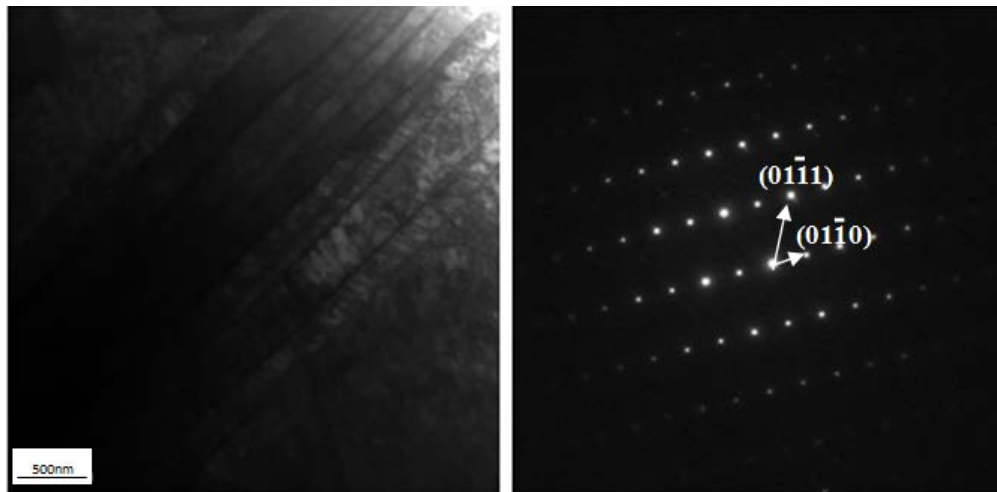
(c) HDH Ti-6Al-4V

Figure 4.4: SEM micrographs showing the microstructure of the centre region of as-forged parts.

The microstructure in the centre of an as-forged HDH Ti part was examined in detail by TEM. Equiaxed α grains with sizes of around 2 μm and fine α lamellae with a thickness in the range of 100-300 nm were observed by TEM. The reason for formation of fine α lamellae can be explained by the deformation behavior of the hcp crystal structure during forging. As twinning is the main deformation mechanism of α grains, twin boundaries are formed in the α grains during plastic deformation in the forging process. Finally the twins evolve into fine α lamellae.



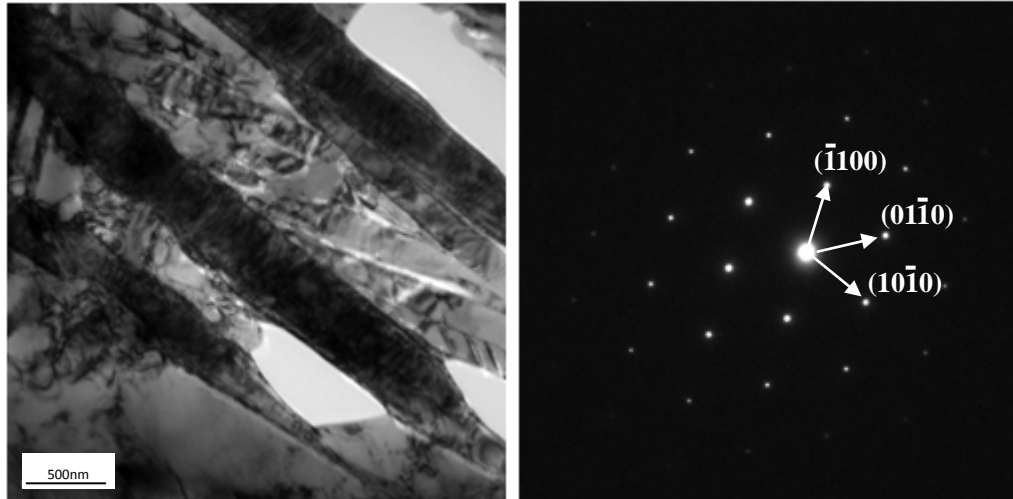
(a) Equiaxed α grain



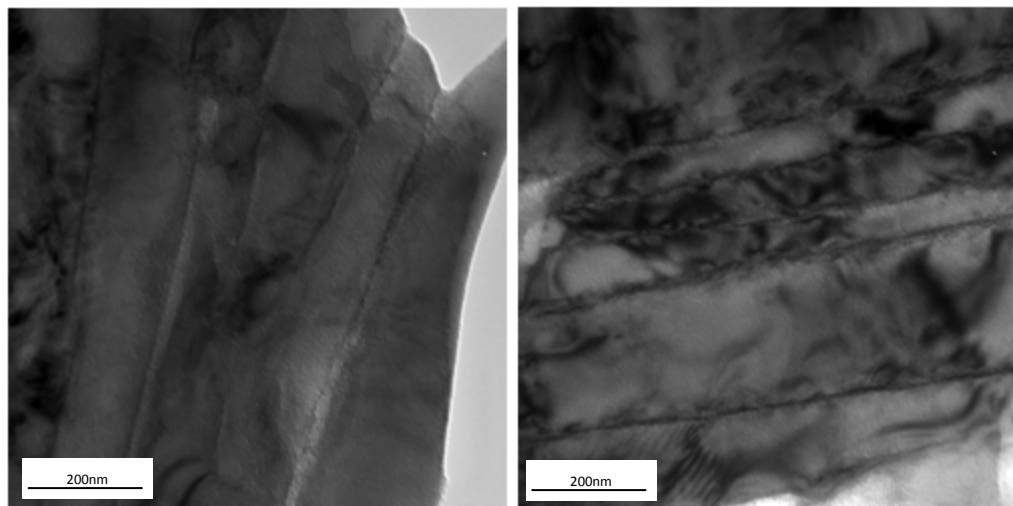
(b) α lamellae

Figure 4.5: TEM bright field images and SADPs of the microstructure of an as-forged HDH Ti part.

As shown in Figure 4.6, α acicular containing a high density of dislocations and fine β laths between the α acicular were in the microstructure of an as-forged GA Ti-6Al-4V part. The width of the α acicular was in the range of 100-300 nm, and the width of the β laths was about 15 nm.



(a) α acicular

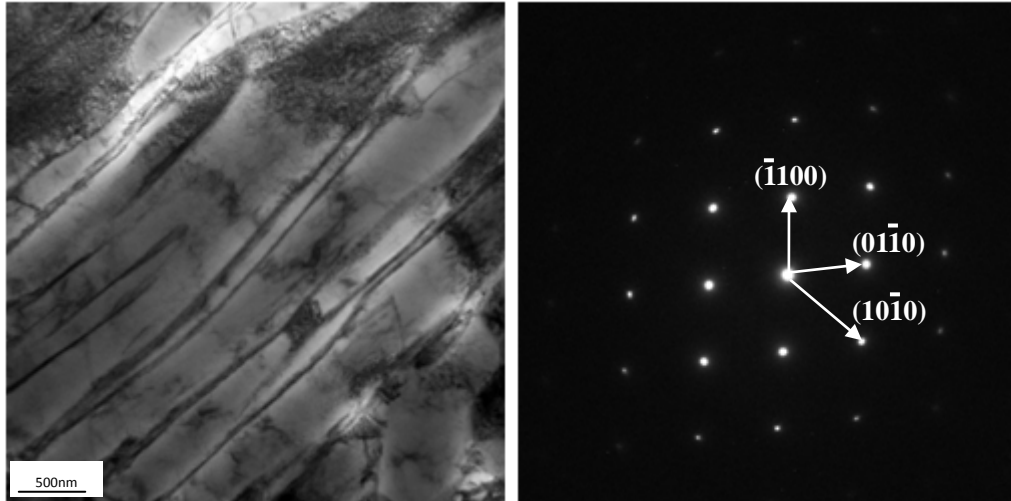


(b) α acicular with fine β lath

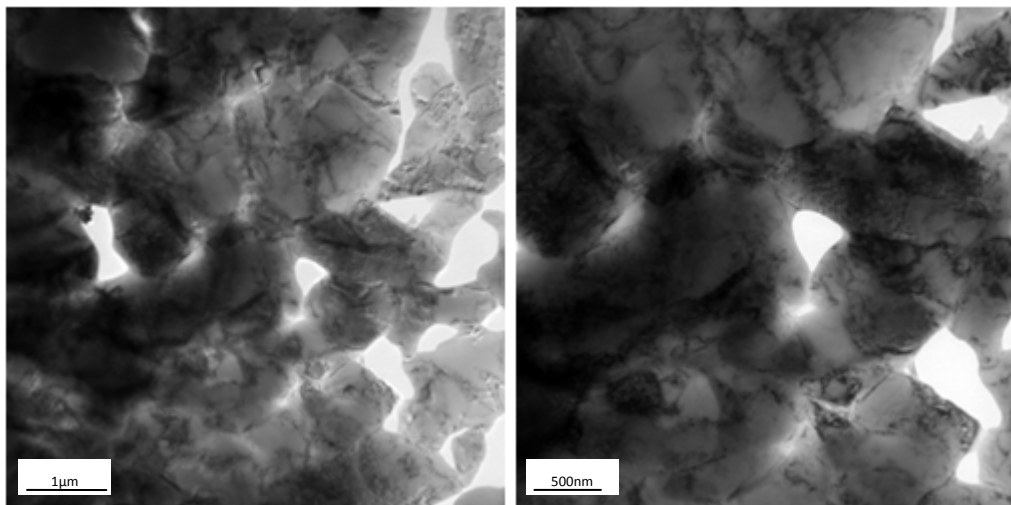
Figure 4.6: TEM bright field images and SADP showing the microstructure of an as-forged GA Ti-6Al-4V part.

The microstructure of an as-forged HDH Ti-6Al-4V part, as observed by TEM is shown in Figure 4.7. Compared with the microstructure of an as-forged GA Ti-6Al-4V part shown in Figure 4.6, the α lamellar boundaries were not quite as straight, and the width of the α lamellae was larger, being in the range of 100-600 nm. Based on the shape and sizes of the α lamellae shown in Figure 4.7(a), it was determined that they were α lamellae in a coarse α/β matrix with a lamellar structure. As shown in Figure 4.7(b), coarse α grains with sizes greater than 1 μm and separated from the primary α lamellae were observed. It is likely that they

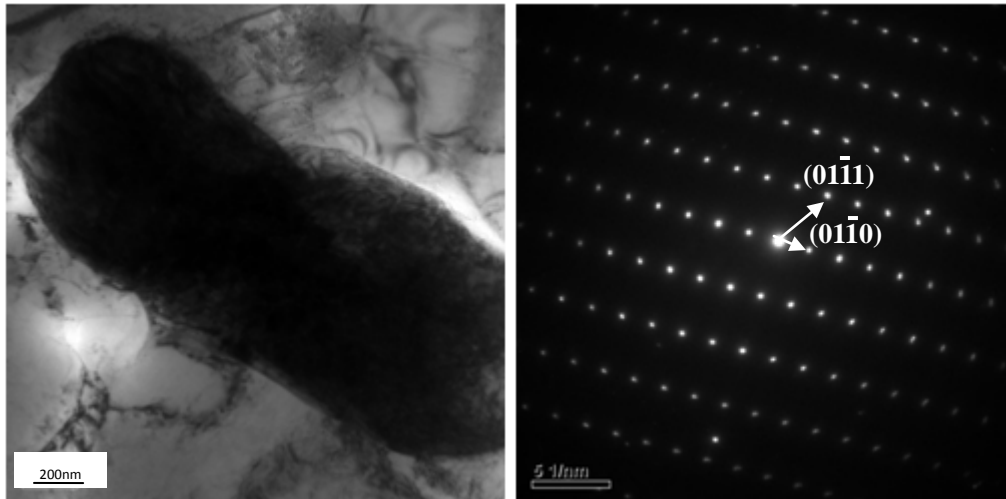
were induced by the large amount of localized deformation in the forging process. Coarse α grains were observed in the microstructure as shown in Figure 4.7(c).



(a) α/β matrix with a lamellar structure and the corresponding SADP



(b) Coarse equiaxed α grains formed between primary α lamellae

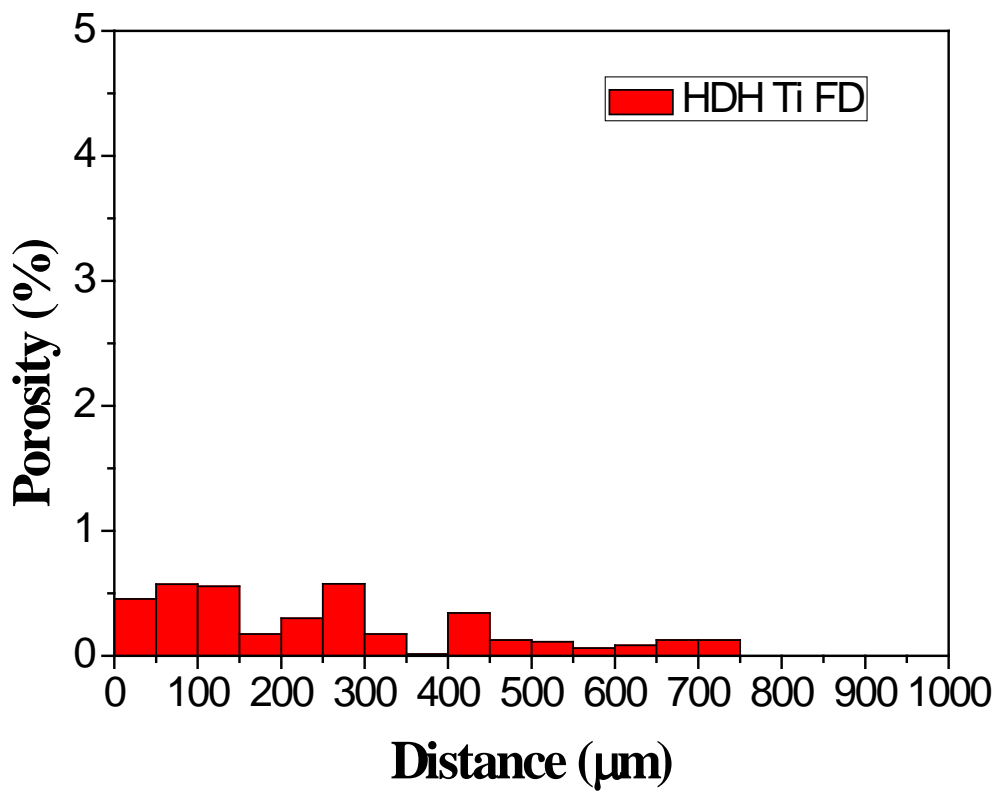
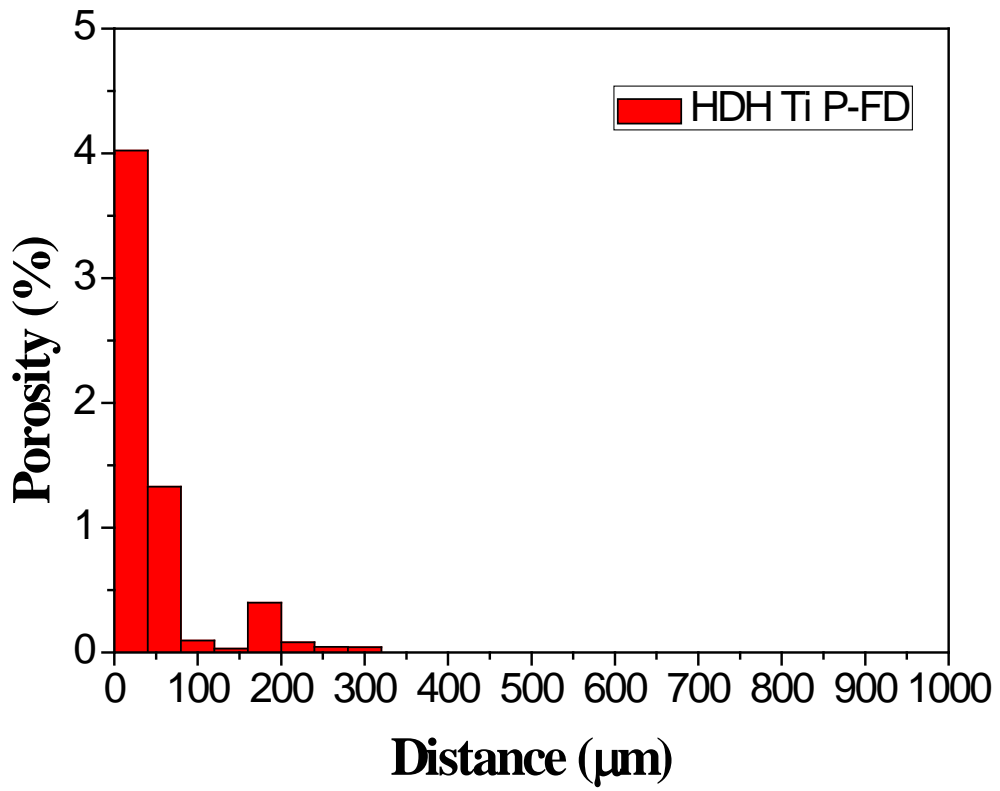


(c) An isolated coarse α grain and corresponding SADP

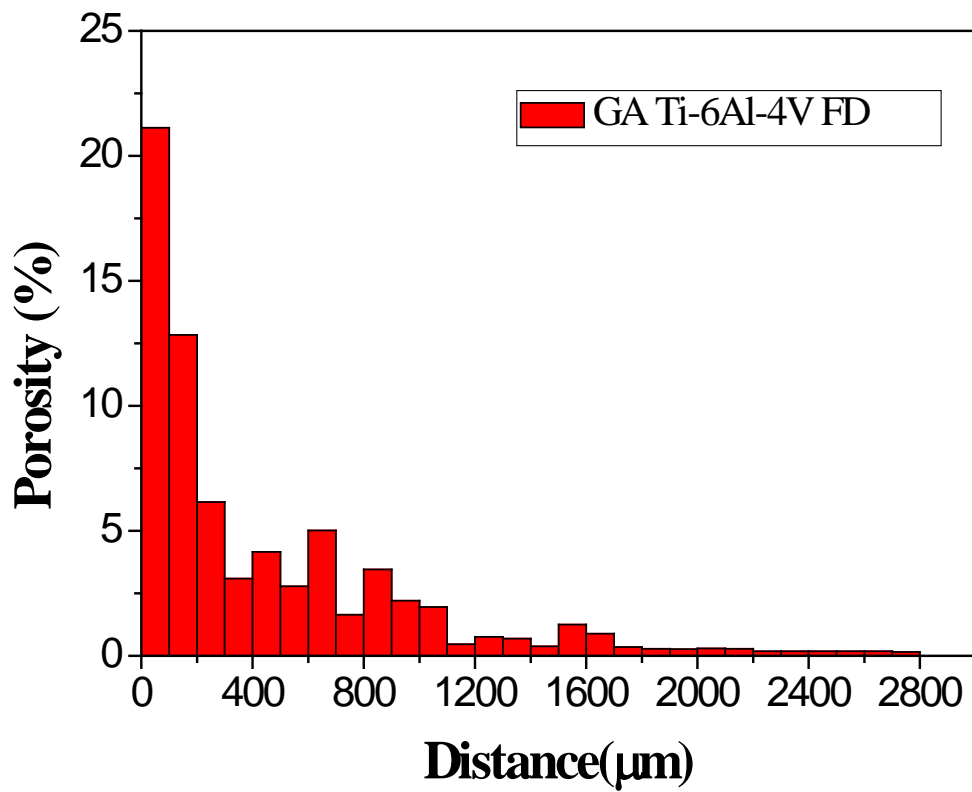
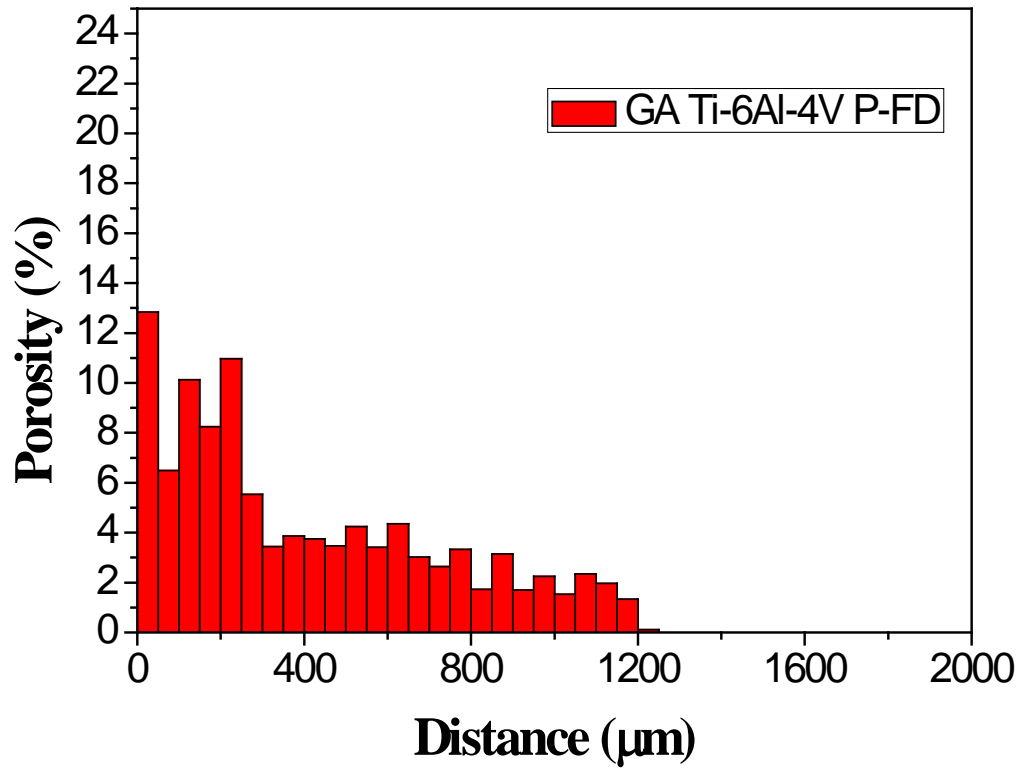
Figure 4.7: TEM bright field images and SADPs showing the microstructure of as-forged HDH Ti-6Al-4V part.

4.3 Porosity Distribution in As-forged Parts

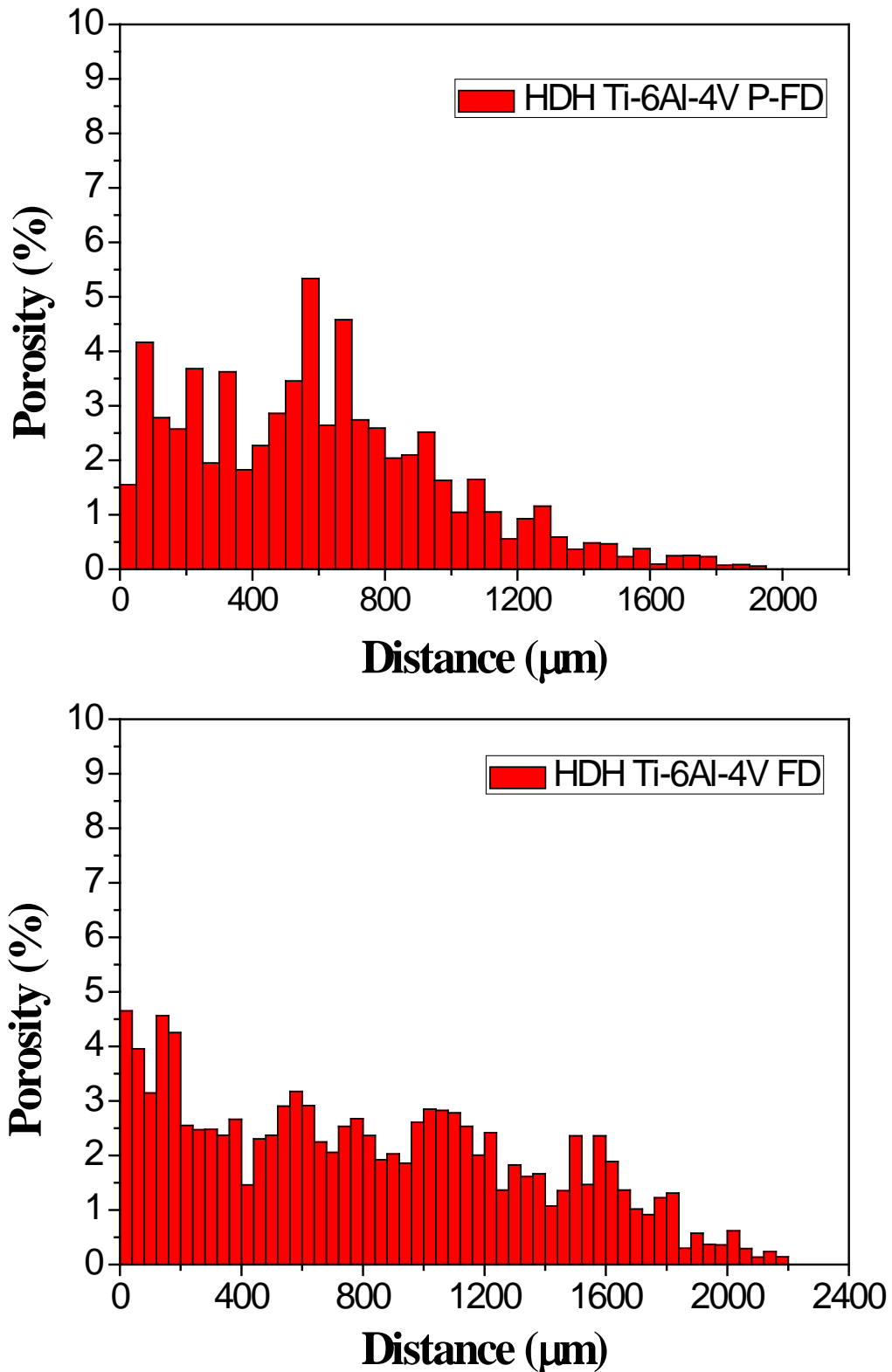
The formation of streamlines, as shown in Figure 4.2, suggests that the plastic deformation in the powder compact caused by forging was not uniform, with the material in the centre of the part experiencing a larger amount of deformation than that near the surface. As the degree of powder consolidation depends on the amount of plastic deformation, there are more pores near the surface of the part due to less plastic deformation, while in the centre of the part, the powder is completely consolidated due to the larger amount of localized plastic deformation. Therefore, with increasing distance from the surface to the centre of the part, the porosity is reduced. To get a part with good quality and necessitating low material removal after forging, the thickness of the surface layer with porosity greater than an accepted level needs to be as small as possible. Qualitative measurement of the porosity distribution on a cross section of each as-forged part, along directions perpendicular to and along the forging direction (P-FD and FD) respectively, was conducted for each as-forged part by analyzing optical microscopy images. The results are shown in Figure 4.8.



(a) As-forged HDH Ti part



(b) As-forged GA Ti-6Al-4V part



(c) As-forged HDH Ti-6Al-4V part

Figure 4.8: Porosity distribution of as-forged parts perpendicular to and along the forging direction on a cross section from the surface. (P and FD are the abbreviations for perpendicular and forging direction in the figures)

As shown in Figure 4.8, along a direction perpendicular to the forging direction the porosity distribution in as-forged GA and HDH Ti-6Al-4V parts are similar, both showing that the porosity decreased to zero with increasing distance from the surface to the centre of the part. For the as-forged HDH Ti part, with increasing distance from the surface of the part from 0 to 0.24 mm, its porosity decreased from 4% to 0.028%, so the material became fully consolidated beyond this distance. For an as-forged GA Ti-6Al-4V part, beyond a distance of 1.2 mm from the surface, there were no obvious pores, and the relative density reached 99.9%, as shown in Figure 4.8(b). In contrast, the relative density of the part was 87.2% in the surface region. As shown in Figure 4.8(c), the porosity distribution in an as-forged HDH Ti-6Al-4V part along a direction perpendicular to the forging direction was similar to that for an as-forged GA Ti-6Al-4V part, and the distance from the surface of the part beyond which the powder was completely consolidated, with relative density of 99.9%, was 1.85 mm. Generally speaking, the porosity distribution along a direction perpendicular to the forging direction in as-forged parts shows that the relative density of the as-forged parts increased rapidly with distance from the surface, and reached almost 100% at a certain distance. This distance is the shortest for the as-forged HDH Ti part among the three parts.

Due to the chilling effect of the forging die, caused by the large temperature difference between the forging die and hot powder compact, there was a porosity distribution along the forging direction on the cross-section of the as-forged part. As shown in Figure 4.8(a), the porosity gradually decreased from 0.45% to zero with increasing distance from the surface of the as-forged HDH Ti part to 0.75 mm. For the as-forged GA and HDH Ti-6Al-4V parts, the porosity distribution along the forging direction followed the same trend, as shown in Figures 4.8(b) and (c). However, the distance from the surface of the part beyond which the as-forged part became fully dense was much larger, being 2.8 mm and 2.2 mm for

as-forged GA and HDH Ti-6Al-4V parts, respectively. This shows that an as-forged HDH Ti part has the thinnest surface layer with pores, and the as-forged GA and HDH Ti-6Al-4V parts have porous surface layers with similar thickness. The pores were much larger in the as-forged GA Ti-6Al-4V part than the as-forged HDH Ti-6Al-4V part.

Comparing the porosity distribution along a direction perpendicular to the forging direction with that along the forging direction as shown in Figure 4.8, it can be concluded that in a direction perpendicular to the forging direction the distance from the surface of the porosity distribution is much larger than that along the forging direction. This can be explained by the mechanism for formation of pores during the forging process. Pores near a surface at the side of a part are caused by the non-homogeneous plastic deformation of the powder compact as a result of the upset forging. Because a surface at the side is a free surface, there is less plastic deformation than in the center of the part. Pores near the top and bottom surfaces of the part are caused by the chilling effect of the forging die halves. When the hot powder compact touches the cold surface of the forging die halves during forging, fast heat transfer from the powder compact to the forging die occurs, and makes the top and bottom surface layers of the part cool down more rapidly than the centre. When the temperature of the top and bottom surface layers decreases to a sufficiently low level, the flow stress of the material becomes large enough to prevent further material flow and continue the powder consolidation. This leads to the formation of residual pores in the top and bottom surface layers of the part. The distance of the porosity distribution in an as-forged HDH Ti part, along both the direction perpendicular to the forging direction and the forging direction, is shorter than that in as-forged GA and HDH Ti-6Al-4V parts, as shown in Figure 4.8. This can be attributed to the high relative density of the green powder compact made from HDH Ti powder and the relatively lower flow stress of CP Ti at elevated temperatures. The density of a green powder compact

and the high temperature mechanical properties of metals are two of the most important factors which control the quality of as-forged parts produced by powder compact forging.

4.4 Mechanical Properties of As-forged Parts

Specimens for tensile testing were cut from as-forged parts at an interval of 2 mm in thickness along a direction perpendicular to the forging direction, as shown in Figure 2.13. The first specimens from as-forged HDH Ti, HDH and GA Ti-6Al-4V parts were cut at a distance 2 mm, 3 mm and 3 mm away from the surface of the part, respectively. As shown by the tensile stress-strain curves in Figure 4.9, with increasing distance from the surface of the parts, the tensile strength and ductility of the specimens improved gradually. The yield strength (YS), ultimate tensile strength (UTS) and elongation to fracture are summarized in Tables 4.1-4.3 and plotted in Figure 4.10. For the as-forged HDH Ti part, with increasing distance from the surface, the elongation to fracture of the specimen increased from 9% to 14.3%, and its UTS and yield strength increased from 767.4 MPa to 800.4 MPa and from 631.3 MPa to 663.2 MPa, respectively. For the as-forged GA Ti-6Al-4V part, with increasing distance from the surface, the elongation to fracture of the specimen increased from 1.7% to 10.9%, and its UTS and yield strength improved from 845.1 MPa to 1054.4 MPa and from 737.8 MPa to 948.4 MPa, respectively. The mechanical properties of an as-forged HDH Ti-6Al-4V part showed a similar improvement with increasing distance from the surface: the elongation to fracture increased from 0.7% to 7.9%; the UTS increased from 1217.2 MPa to 1302.9 MPa; and the yield strength increased from 1160.9 MPa to 1180.5 MPa.

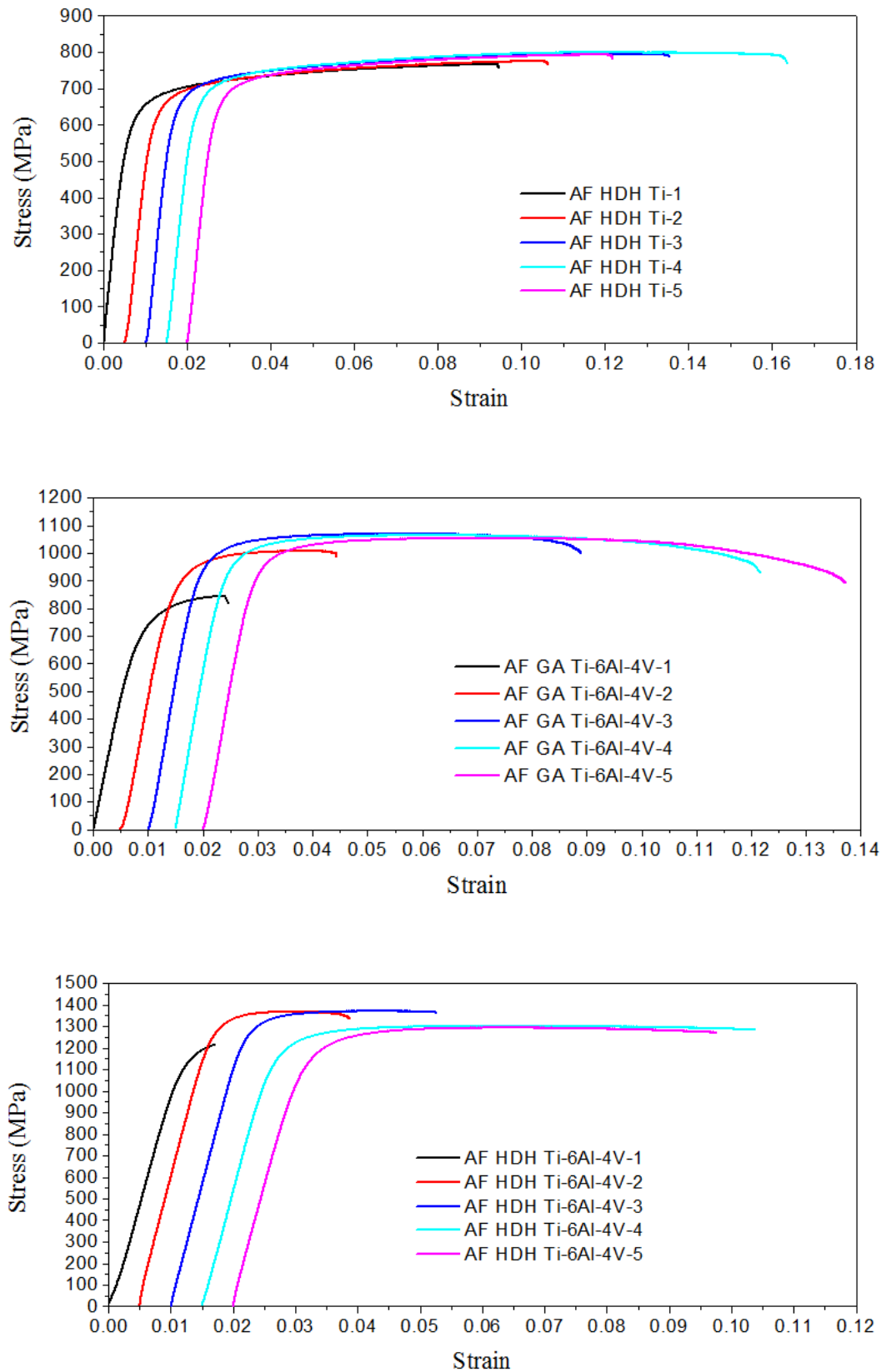


Figure 4.9: Tensile stress-strain curves for specimens cut from the as-forged HDH Ti, GA Ti-6Al-4V and HDH Ti-6Al-4V parts in the order of sample numbers with increasing distance from the part surface. (AF = as-forged)

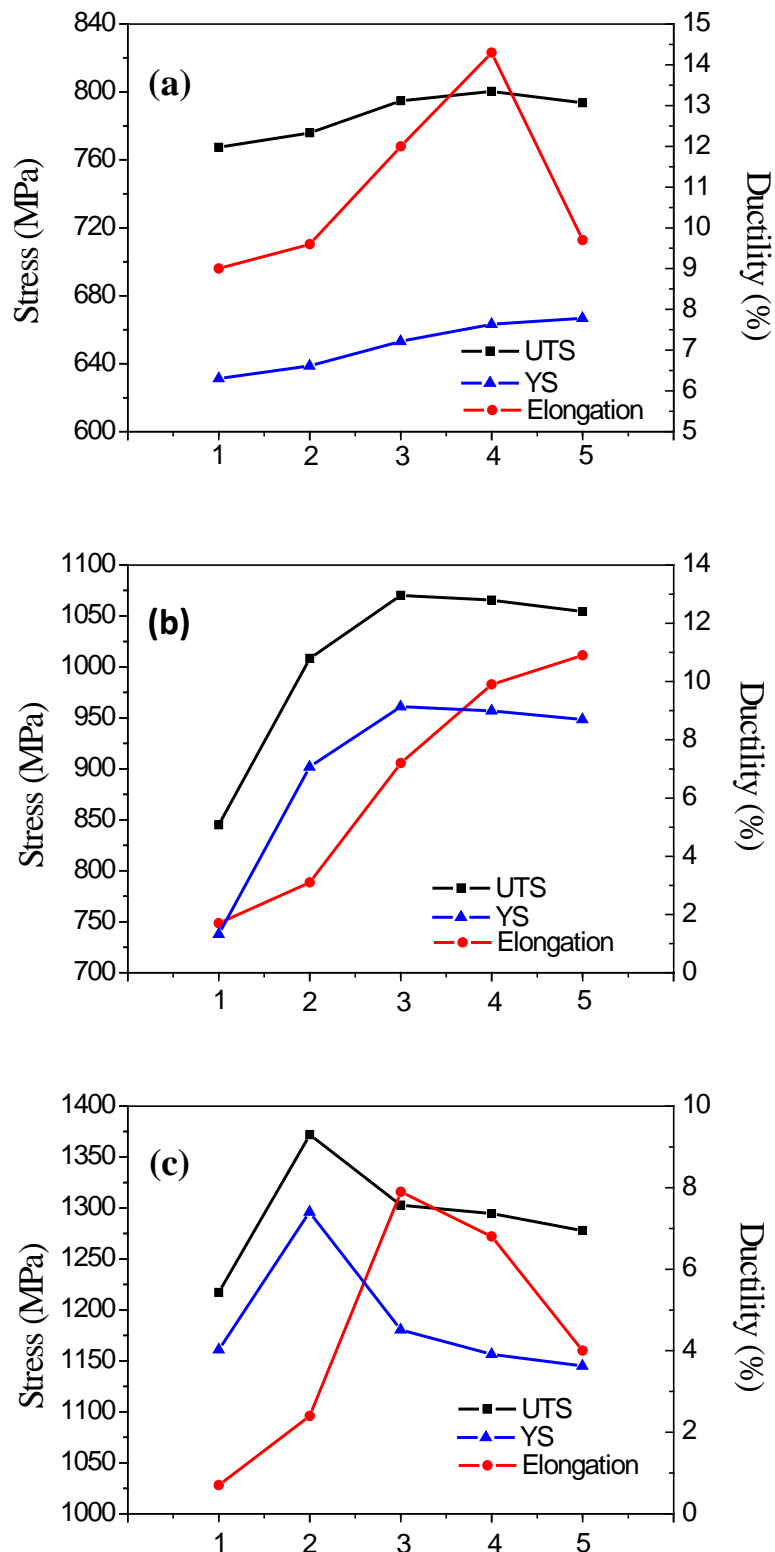


Figure 4.10: The distribution of mechanical properties with distance from the surface of as-forged parts: (a) HDH Ti; (b) GA Ti-6Al-4V; (c) HDH Ti-6Al-4V.

Table 4.1: Summary of mechanical properties of specimens cut from an as-forged HDH Ti part.

Sample	YS(MPa)	UTS(MPa)	Ductility
1	631.3	767.4	9%
2	638.7	775.9	9.6%
3	653.1	794.8	12%
4	663.2	800.4	14.3%
5	666.8	793.6	9.7%

Table 4.2: Summary of mechanical properties of specimens cut from an as-forged GA Ti-6Al-4V part.

Sample	YS(MPa)	UTS(MPa)	Ductility
1	737.8	845.1	1.7%
2	901.8	1008.6	3.1%
3	960.8	1070.4	7.2%
4	956.8	1065.5	9.9%
5	948.4	1054.4	10.9%

Table 4.3: Summary of mechanical properties of specimens cut from an as-forged HDH Ti-6Al-4V part.

Sample	YS(MPa)	UTS(MPa)	Ductility
1	1160.9	1217.2	0.7%
2	1296.0	1372.0	2.4%
3	1180.5	1302.9	7.9%
4	1156.5	1294.6	6.8%
5	1144.9	1277.8	4%

The changes in mechanical properties with distance from the surface to the centre of as-forged HDH Ti, GA Ti-6Al-4V and HDH Ti-6Al-4V parts are in line with their porosity distributions along the same direction. The mechanical properties of the material improve with decreasing porosity. From the mechanical properties and porosity distributions for the as-forged HDH and GA Ti-6Al-4V parts along the forging direction, pores have a significant effect on both elongation to fracture and tensile strength, and the effect of a reduction in porosity on elongation to fracture is more dramatic than that on the tensile strength. The difference between the maximum values of elongation to fracture, yield strength and UTS of the as-forged HDH and GA Ti-6Al-4V parts is mainly due to their difference in

oxygen content. The oxygen content of HDH Ti-6Al-4V powder is 0.5%, while that of GA Ti-6Al-4V powder is 0.13%. Also, as shown in Table 4.4, during the powder compact forging process, an as-forged HDH Ti part picked up 0.06% oxygen, while as-forged GA and HDH Ti-6Al-4V parts only picked up 0.01% and 0.02% of oxygen, due to the formation of a denser Al_2O_3 oxide film, respectively. This shows that the oxygen pick-up was controlled to a low level by a flowing argon protective atmosphere during the forging process. Also, the oxygen content of the raw powders plays a much more important role on the mechanical properties of as-forged parts.

Table 4.4: Nitrogen and oxygen contents of the as-forged parts.

As-forged part	Nitrogen (%)	Oxygen (%)
HDH Ti	0.026	0.41
HDH Ti-6Al-4V	0.035	0.52
GA Ti-6Al-4V	0.03	0.14

4.5 Cold-shuts in As-forged Parts

As shown in Figure 4.1, there were several deeper cracks on the surfaces of the as-forged HDH Ti, HDH and GA Ti-6Al-4V parts, which were caused by cold-shuts. In metal casting, a cold-shut is defined as a surface defect in a casting caused by two merging liquid streams failing to coalesce during casting. Here the same term can be used to describe the same surface defect caused by two streams of solid material failing to coalesce. The depth of the cracks is dependent on the temperature difference between the hot powder compact and the cold forging die. Furthermore the porosity distribution in as-forged parts, along the forging direction as shown in Figure 4.8, can be improved by reducing the cold-shut effect. To study the cold-shut effect, the effect of forging die temperature on the surface quality of as-forged HDH Ti and Ti-6Al-4V parts was investigated. As shown in Figure 4.11, with increasing die temperature from room temperature to 300, 400 and 500 °C, respectively, the cracks on the surface of the as-forged HDH Ti parts

caused by the cold-shut effect became narrower and finally disappeared at a die temperature of 500 °C. For as-forged HDH Ti-6Al-4V parts, the cracks caused by the cold-shut effect became narrower with increasing die temperature, as shown in Figure 4.12. However, additional cracks formed on the surfaces of the part due to a larger amount of deformation. When the hot powder compact was in contact with the cold forging die, the surface layers of the powder compact cooled down rapidly, and the cracks formed in these layers and were extended by further deformation driven by the forging pressure. Compared with the as-forged HDH Ti part, the as-forged HDH Ti-6Al-4V part is less ductile, so it is easy to form cracks under the same deformation condition. With an increase in die temperature, the number of both kinds of cracks was reduced. With a die temperature of 500 °C, which is close to the limit of the die working temperature, the surface quality of the as-forged HDH Ti-6Al-4V part was improved significantly.

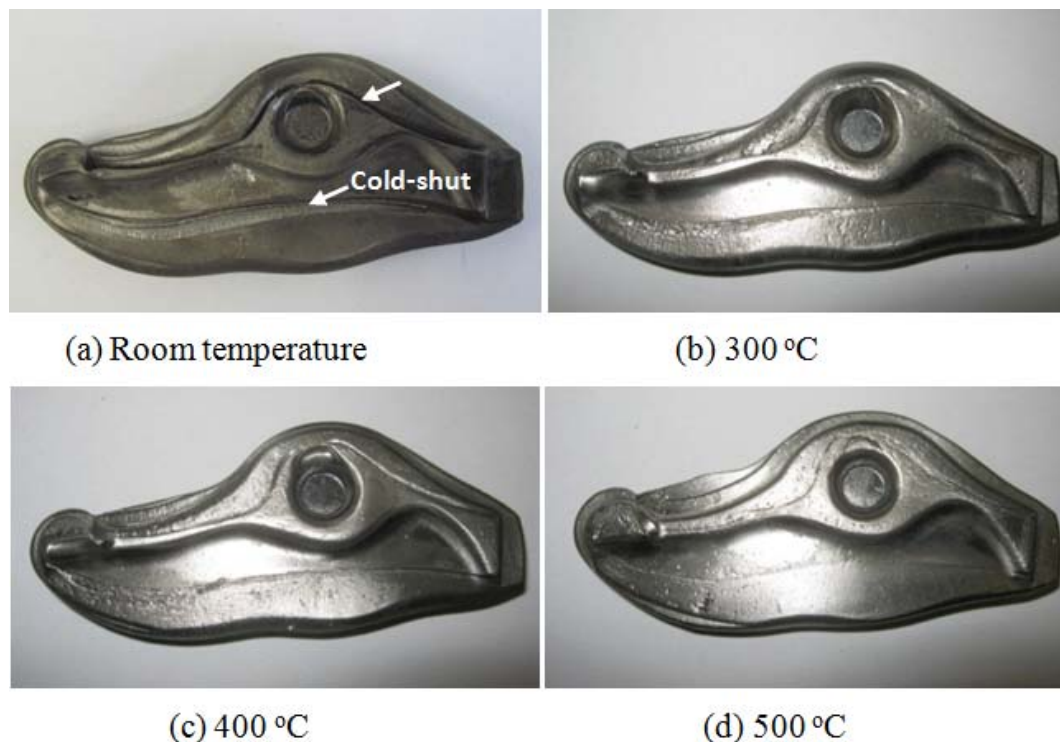


Figure 4.11: Surface quality improvement of as-forged HDH Ti rocker arms by an increase in die temperature.

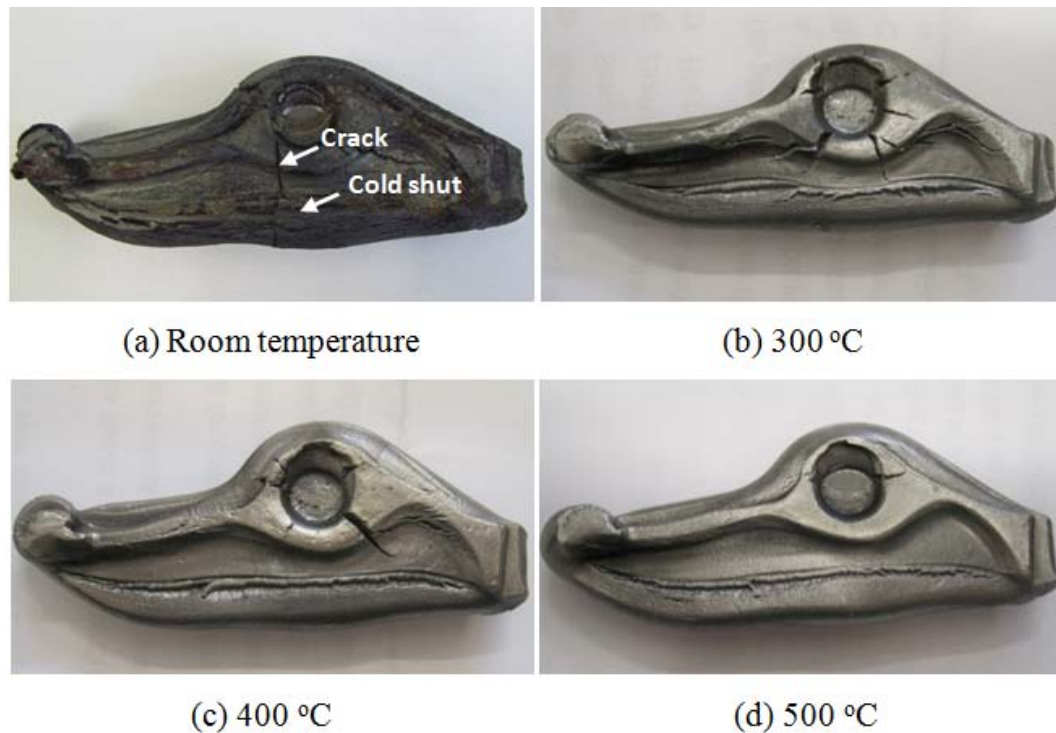


Figure 4.12: Surface quality improvement in as-forged HDH Ti-6Al-4V rocker arms by an increase in die temperature.

4.6 Improvement in the Mechanical Properties of an As-forged Ti

Part

As shown in Table 4.1, the best mechanical properties for specimens cut from an as-forged HDH Ti part are 14.3% for elongation to fracture, 800.4 MPa for UTS and 663.2 MPa for yield strength, so the ductility of the titanium in the as-forged HDH part is far lower than that obtained from ingot metallurgy Ti (30%-40%). Two factors are considered to be the reasons for the worse ductility of the powder metallurgy titanium: the high content of interstitial elements, especially oxygen, and the degree of powder consolidation. Here GA Ti powder with a much lower oxygen content (0.11wt% in GA Ti, compared with 0.35wt% in HDH Ti powder) was used to improve the mechanical properties of as-forged Ti parts. The powder was compacted at a temperature of 450 °C and pressure of 726 MPa, as shown in Table 2.4, and then forged using the same conditions as those used for forging

HDH Ti powder compacts. To improve the level of powder consolidation, the holding time at the forging temperature was also increased.

The GA Ti powder compact was forged at 1350 °C with a die temperature of 500 °C. Images of the as-forged GA Ti part are shown in Figure 4.13. The number of cold-shuts was reduced by increasing the die temperature to 500 °C.



Figure 4.13: Images of both the top and bottom surfaces of an as-forged rocker arm produced by powder compact forging of GA Ti powder.

The stress-strain curves for the tensile test specimens cut from the as-forged GA Ti part along a direction perpendicular to the forging direction are shown in Figure 4.14. From the curves, the tensile strength of the specimens cut from the as-forged GA Ti part is much lower than that of the specimens cut from the as-forged HDH Ti part, whereas their ductility is clearly higher in general. The mechanical properties of the specimens are plotted as a function of the specimen number, which corresponds to the distance of the specimens from the surface of the as-forged GA Ti part (Figure 4.15), and are summarized in Table 4.5. As shown by the graphs and table, the maximum UTS and yield strength are 589.7 MPa and 499.6 MPa, respectively. The specimens cut from the centre of the as-forged part have an elongation to fracture of over 14%, with the maximum elongation to fracture reaching 27.3%. Compared with the mechanical properties of an as-forged HDH Ti part, the as-forged GA Ti part sacrifices a certain amount of tensile strength, but gains from having much better ductility, which can be attributed to the much lower oxygen content of the raw powder.

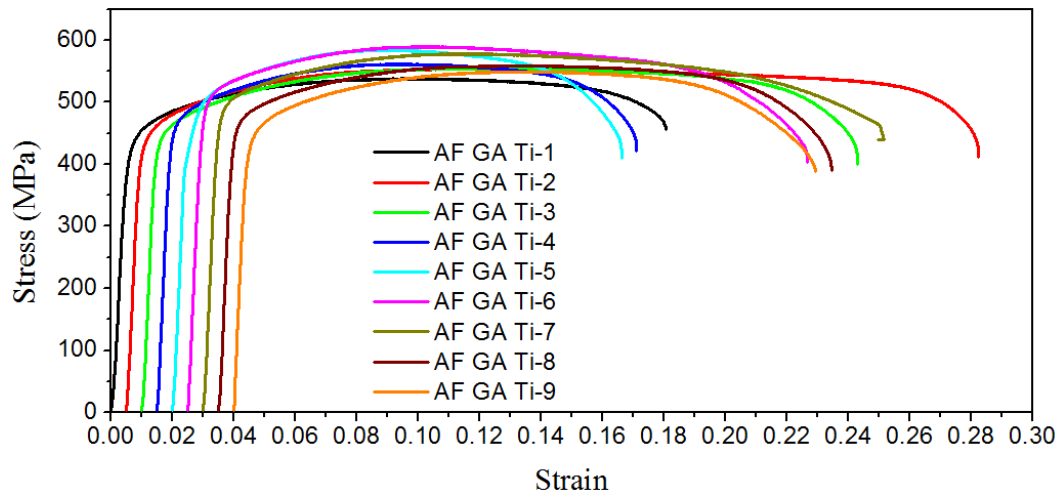


Figure 4.14: Stress-strain curves of tensile specimens cut from the as-forged GA Ti part.

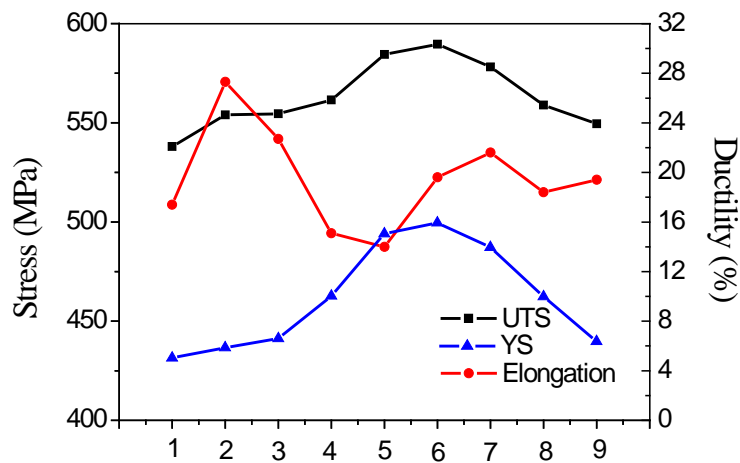


Figure 4.15: Mechanical properties of tensile test specimens cut from the as-forged GA Ti part as a function of the specimen number.

Table 4.5: A summary of the mechanical properties of tensile test specimens cut from an as-forged GA Ti part.

Sample	YS(MPa)	UTS(MPa)	Elongation to fracture(%)
1	431.5	538.0	17.4
2	436.6	554.0	27.3
3	441.2	554.6	22.7
4	462.7	561.5	15.1
5	494.0	584.5	14.0
6	499.6	589.7	19.6
7	487.2	578.2	21.6
8	462.4	559.0	18.4
9	439.8	549.5	19.4
Average	461.7	563.2	19.5

As mentioned in Chapter 3, necking between particles occurred rapidly during induction heating of the powder compact. To improve the level of powder consolidation by powder compact forging, the HDH Ti powder compact was held at the forging temperature of 1350 °C for 5 minutes to get a denser powder compact. The die temperature was set at room temperature. The stress-strain curves for tensile test specimens cut from the as-forged part are shown in Figure 4.16. The tensile strengths are the same as those for the specimens cut from the as-forged HDH Ti part made without a holding time at the forging temperature, but the ductility has been improved a lot, and there are no pores evident in the microstructure shown in Figure 4.17. The mechanical properties of the specimens are plotted as a function of the specimen number, which corresponds with the distance from the surface of the part, as shown in Figure 4.18 and summarized in Table 4.6. The elongation to fracture of all specimens is over 16.3%, with the best value reaching 27.1%. This shows that the ductility of the as-forged HDH Ti part, made with a holding time of 5 minutes at the forging temperature, is much higher than that of an as-forged HDH Ti part made without a holding time. The ductility of an as-forged HDH Ti part, made with a holding time of 5 minutes at the forging temperature, is also comparable with that of the as-forged GA Ti part made without a holding time. However, its tensile strength is much higher than that of the as-forged GA Ti part, so an improvement in mechanical properties of an as-forged HDH Ti part can be achieved by increasing the holding time at the forging temperature to 5 minutes.

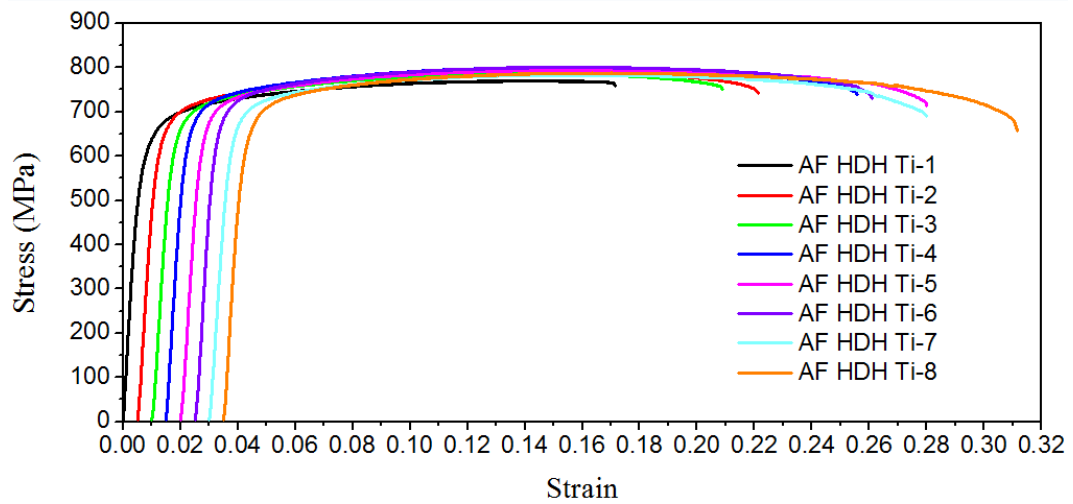


Figure 4.16: Stress-strain curves of tensile test specimens cut from the as-forged HDH Ti part made with a holding time of 5 minutes at the forging temperature.



Figure 4.17: Microstructure an as-forged HDH Ti part made with a holding time of 5 minutes at the forging temperature.

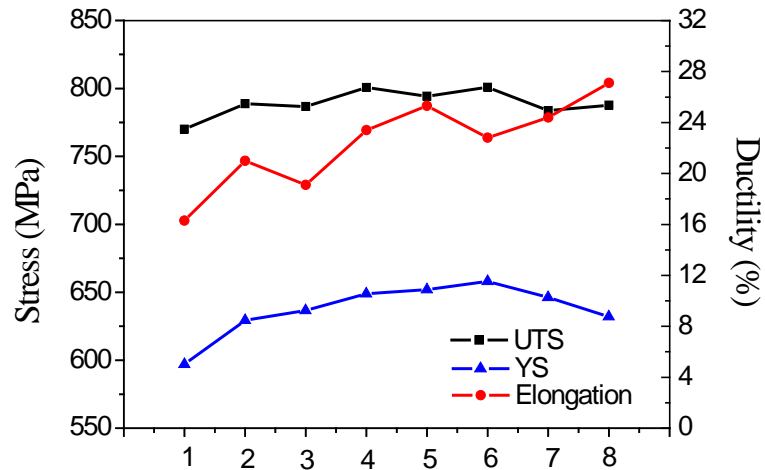


Figure 4.18: Mechanical properties of specimens cut from the as-forged HDH Ti part made using a holding time of 5 minutes at the forging temperature as a function of specimen number.

Table 4.6: Summary of the mechanical properties of tensile test specimens cut from the as-forged HDH Ti part made with a holding time of 5 minutes.

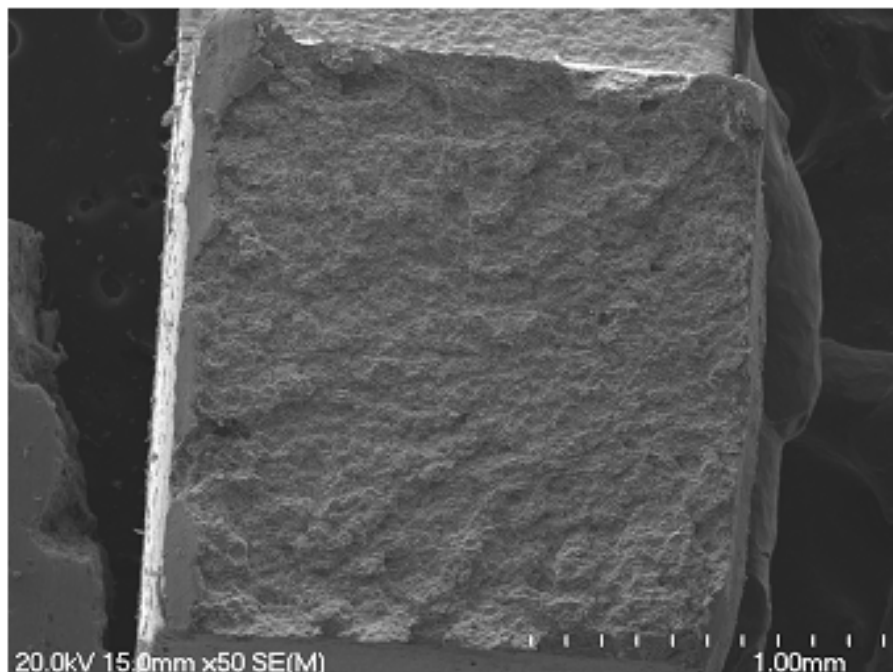
Sample	YS(MPa)	UTS(MPa)	Elongation to fracture(%)
1	597.1	770.1	16.3
2	629.4	788.8	21.0
3	636.6	786.7	19.1
4	648.9	800.8	23.4
5	651.9	794.4	25.3
6	658.0	800.9	22.8
7	646.3	783.7	24.4
8	632.1	787.7	27.1
Average	637.5	789.1	22.4

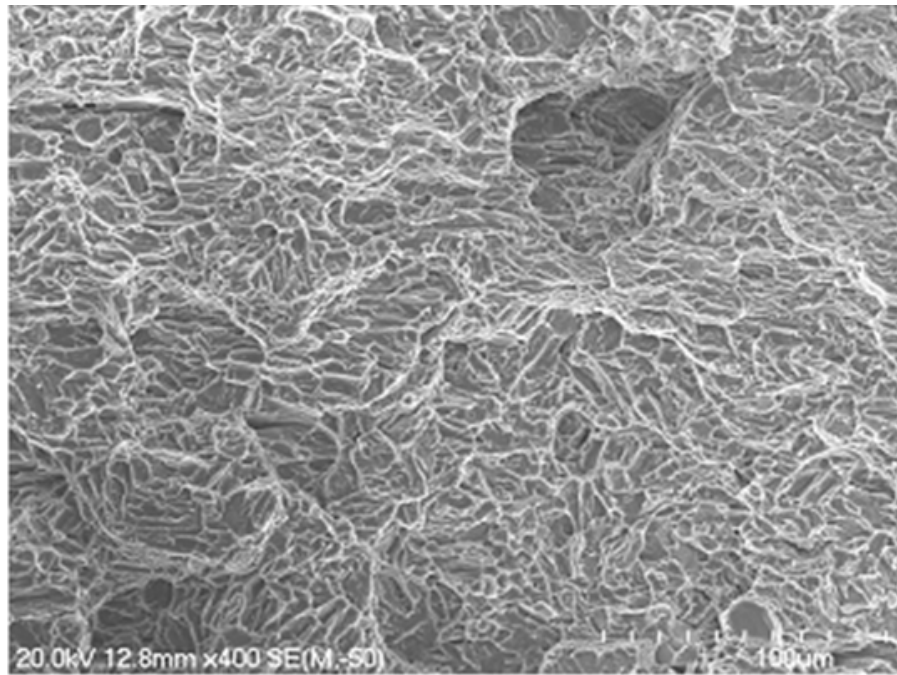
4.7 Fracture Behavior of As-forged Ti and Ti-6Al-4V Parts

4.7.1 Fracture Behavior of an As-forged HDH Ti Part

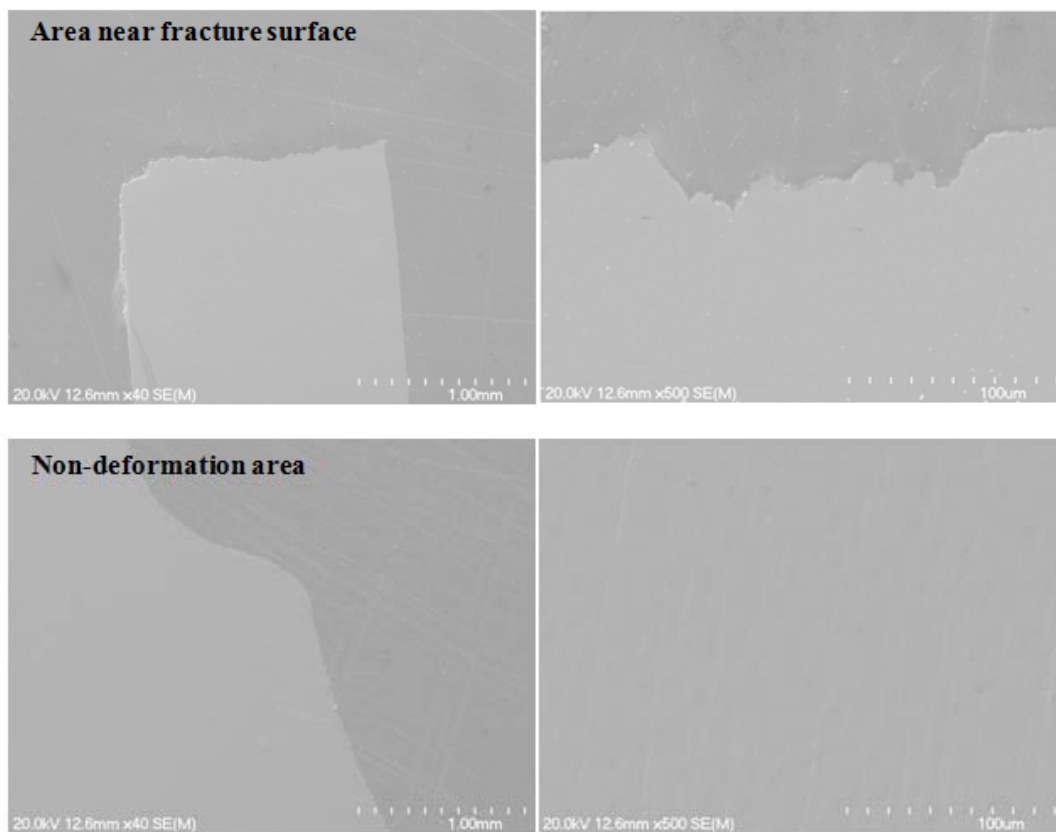
The fracture surfaces of selected tensile test specimens cut from the as-forged HDH Ti part were characterized by SEM, as shown in Figure 4.19(a). At low magnification, the fractograph of an AF HDH Ti-1 specimen with the ductility of 9%, which is near the surface of the part, showed features resembling the irregular

shape of HDH powder particles. While at high magnification, the powder particle boundaries cannot be seen, only a dimple pattern is shown in the figure. Also on the longitudinal cross section in Figure 4.19(b), there are no observable pores in both the area near the fracture surface and the non-deformed area. This means that powder bonding is strong enough to resist the stress up to the point of fracturing the solid material of the specimen, i.e. the specimen is consolidated very well, otherwise the material would have fractured prematurely, without any ductility, before plastic yielding. According to the morphology of the fracture surface and longitudinal cross section, the fracture behavior of an AF HDH Ti-1 specimen near the surface of the part is by inter-particle fracturing, and the fracturing of the specimen occurred at the grain boundaries formed from the interparticle boundaries of the powder compacts. This might be the reason for features of the fracture surfaces, at low magnification, resembling the shape of HDH powder particles as shown in Figure 4.19(a). The dimple features were formed by powder particle separation.





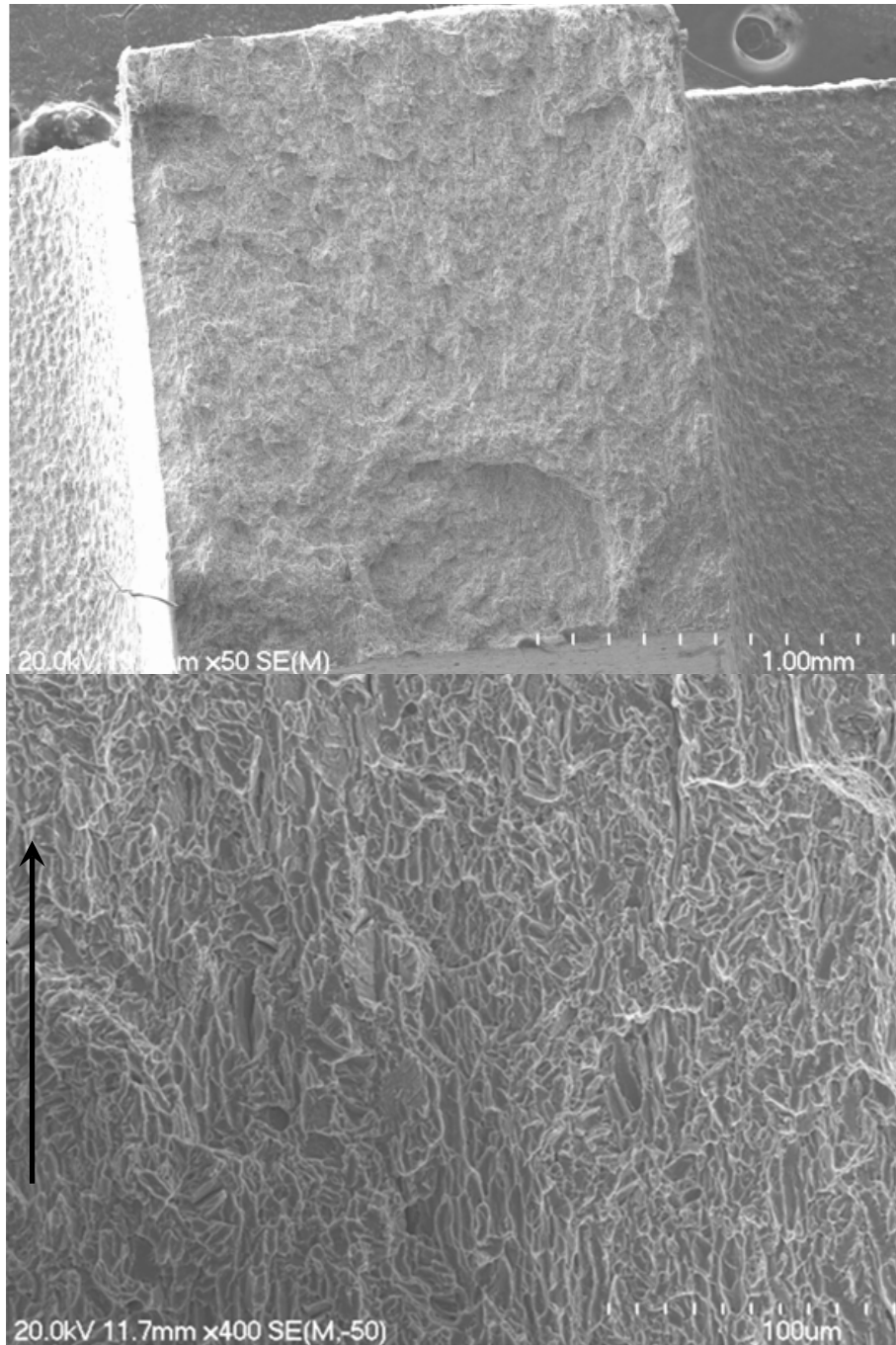
(a) Fracture surface



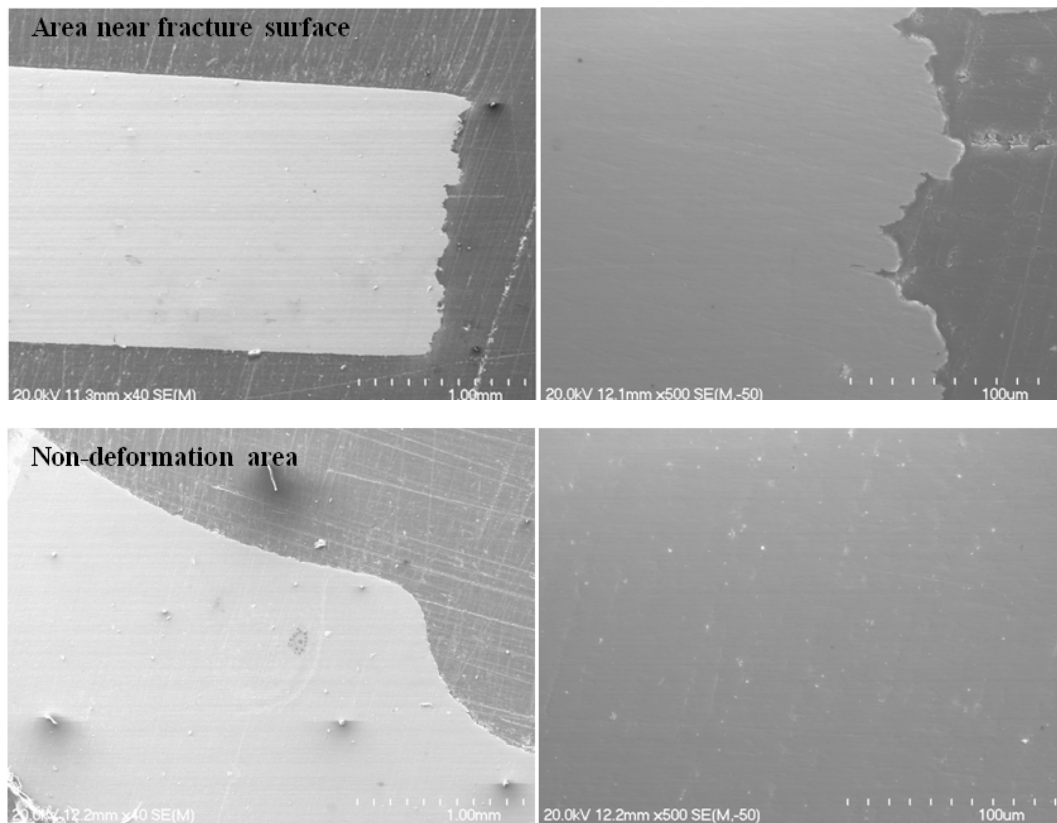
(b) Longitudinal cross section

Figure 4.19: Fracture surface and corresponding longitudinal cross section of AF HDH Ti-1 specimen.

In contrast, the fracture surface of an AF HDH Ti-4 specimen which was cut from the center of the part and had an elongation to fracture of 14.3%, the highest among all the tensile test specimens cut from this part, did not show distinguishable powder particle shapes at low magnification (Figure 4.20(a)) and showed a large number of dimples at a higher magnification. In contrast to the dimples on the fracture surface of the AF HDH Ti-1 specimen, shown in Figure 4.20(b), the dimples in Figure 4.20(a) were oriented in one direction, as shown by the arrow in the figure, which is the orientation of the α lamellae shown in Figure 4.3(a). The sizes of the dimples were about 5 μm in width which matched the thickness of α lamellae very well. This suggests that the specimen fractured by delamination and transgranular fracture of α lamellae. The longitudinal cross section of the specimen, as shown in Figure 4.20(b), did not show any cavities in either the area near the fracture surface or the non-deformation area. This shows that the grain boundaries, formed by transformation of the interparticle boundaries, were strong enough to resist the high stress which eventually caused fracture through the body of the powder particles. This suggests that the powder in this specimen was better consolidated than that in the AF HDH Ti-1 specimen. The better powder consolidation state is the reason for an AF HDH Ti-4 specimen having a better ductility than an AF HDH Ti-1 specimen.



(a) Fracture surface



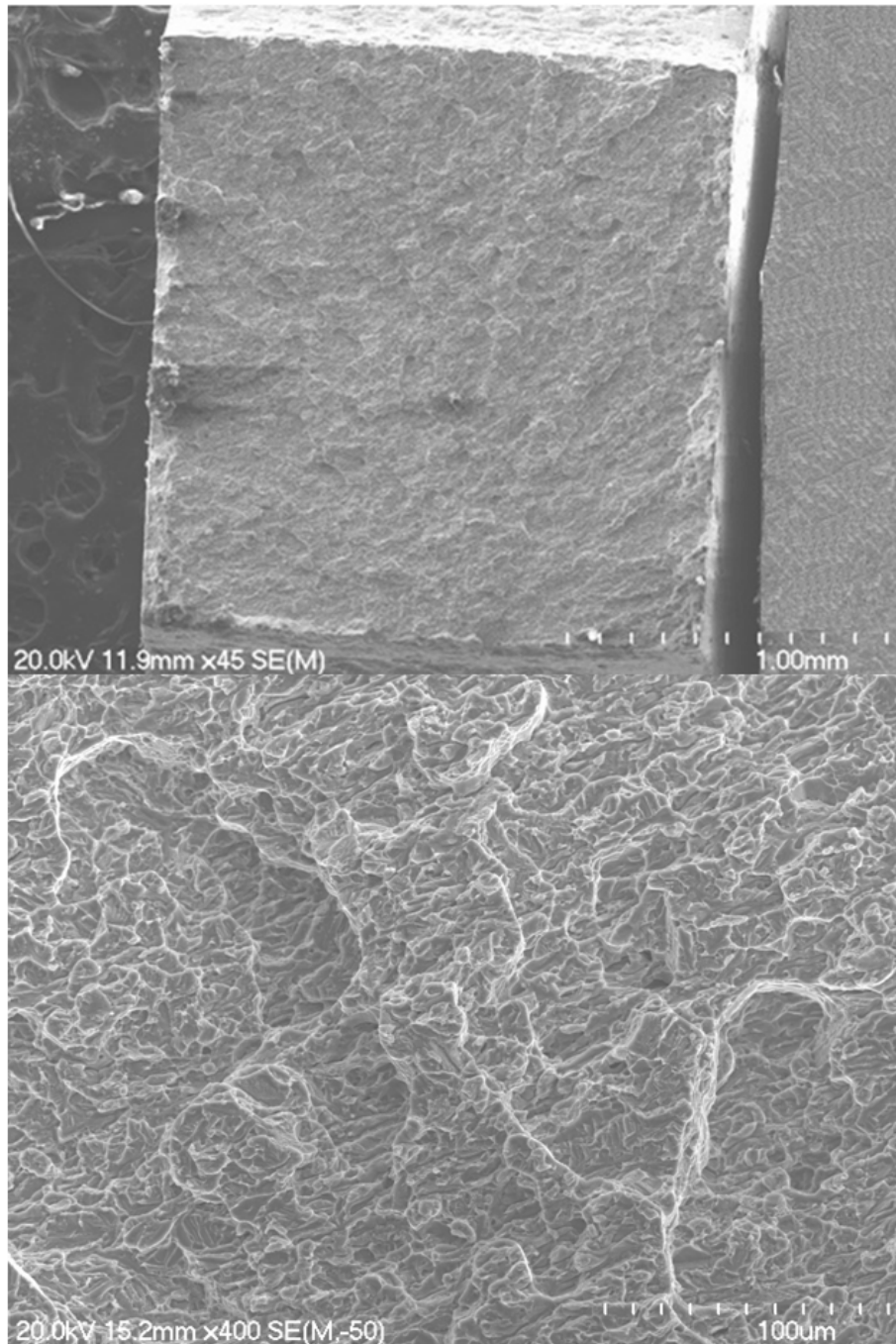
(b) Longitudinal cross section

Figure 4.20: Fracture surface and corresponding longitudinal cross section of an AF HDH Ti-4 specimen.

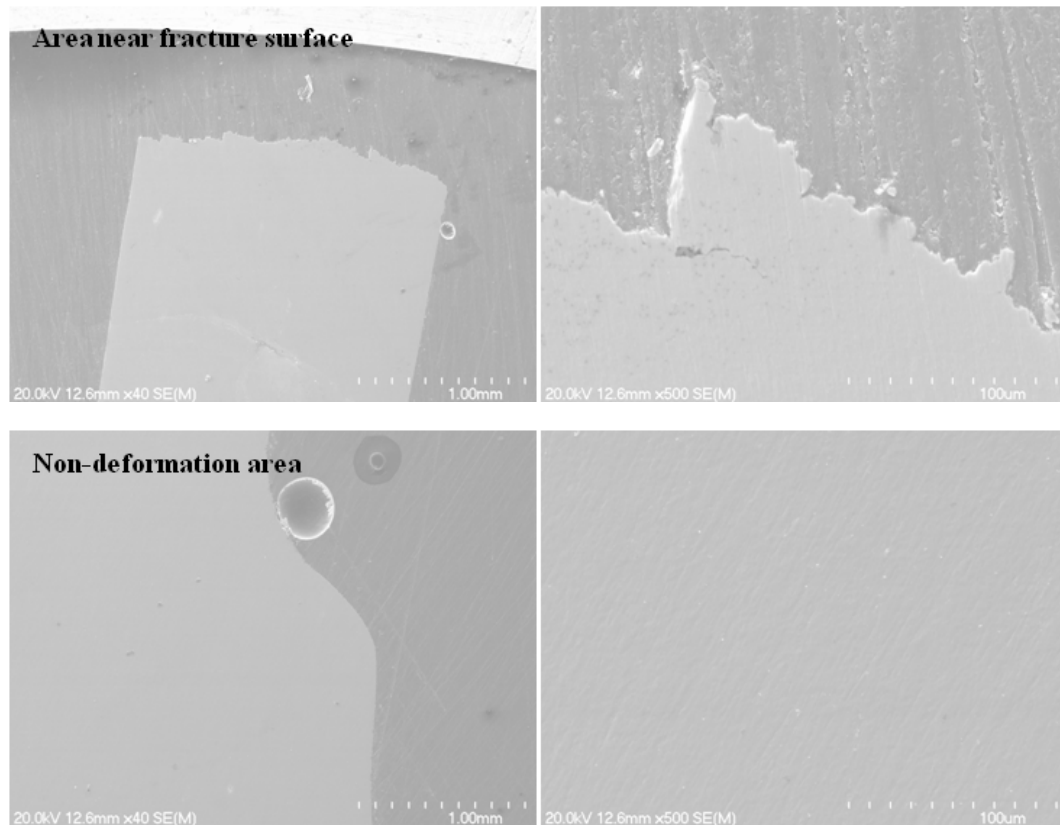
4.7.2 Fracture Behavior of an As-forged HDH Ti-6Al-4V Part

Similarly to the fracture surface of an AF HDH Ti-1 specimen, shown in Figure 4.19(a), the fracture surface of an AF HDH Ti-6Al-4V-1 specimen taken from a position near the surface of the part, had features that resembled the irregular shapes of HDH powder particles, and did not have clear dimples, as shown in Figure 4.21(a). On the longitudinal cross section of this specimen, as shown in Figure 4.21(b), there were no pores or cavities in either the area near the fracture surface or the non-deformation area, so the powder compact in the specimen was well consolidated to full density. The fracture of the specimen occurred through intergranular fracturing. The AF HDH Ti-6Al-4V-1 specimen had an elongation to fracture of 0.7% which is much lower than that AF of an HDH Ti-1 specimen,

even though the degree of powder consolidation of the two specimens was the same. This might be due to the fact that the Ti-6Al-4V part has a lower elongation than a Ti part with the same oxygen content [2].



(a) Fracture surface

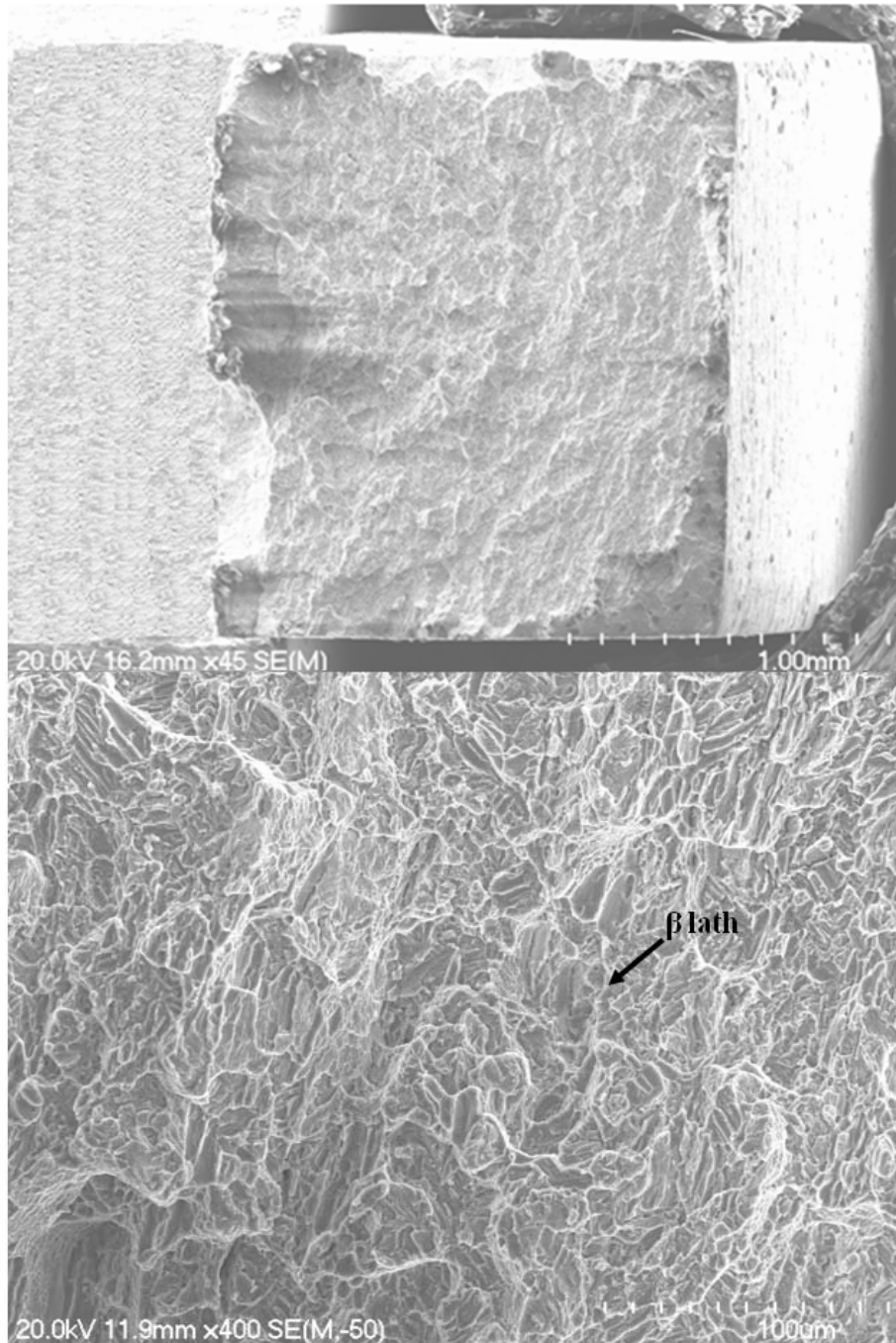


(b) Longitudinal cross section

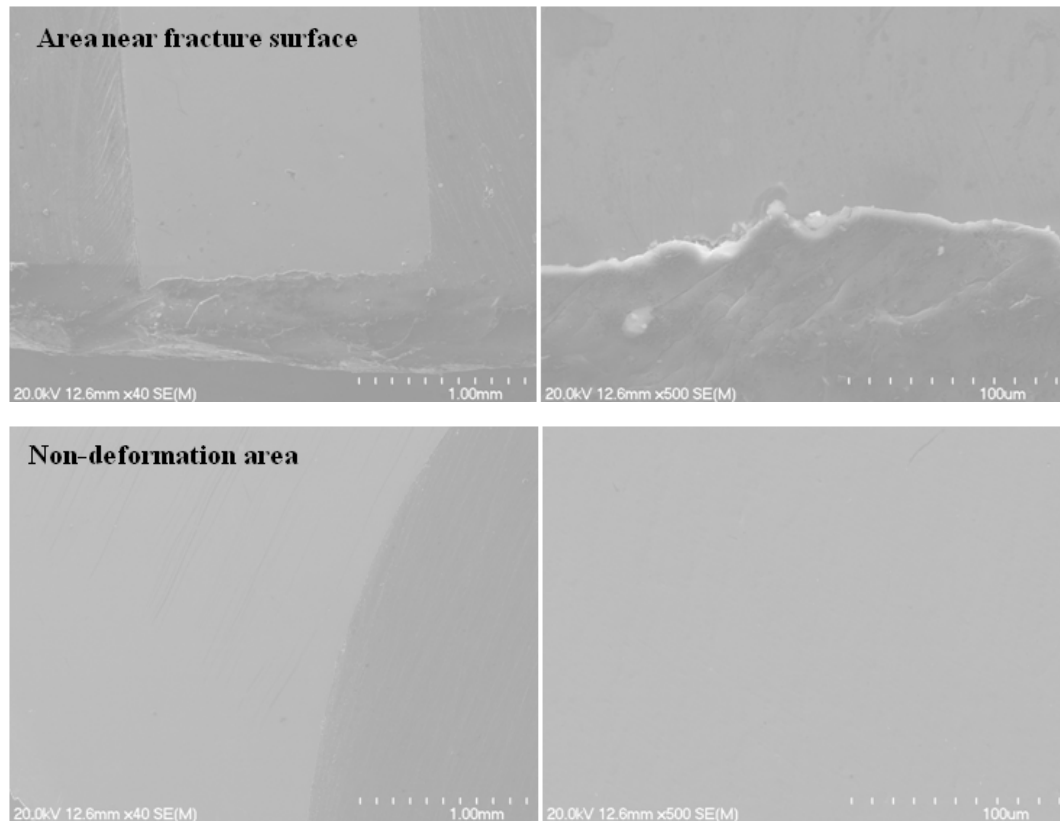
Figure 4.21: Fracture surface and corresponding longitudinal cross section of an AF HDH Ti-6Al-4V-1 specimen.

As shown in Figure 4.22, the fracture surface of the AF HDH Ti-6Al-4V-3 specimen, which had an elongation to fracture of 7.9% and was cut from the centre of the part, had a large number of fine dimples at the lath boundaries due to fracturing of the β phase. These are typical features of the fracture surface of a Ti-6Al-4V alloy with fine primary α grains in a coarse α/β matrix microstructure. On the longitudinal cross section of this specimen, there were no cavities in both the area near the fracture surface and in the non-deformed area, so the powder compact in the position of the specimen was very well consolidated with full density. The fracture mode of the specimen was transgranular, in line with its microstructure consisting of an α/β lath structure. Compared with an intergranular fracture without the formation of cavities in the AF HDH Ti-6Al-4V-1 specimen, the transgranular fracture with the formation of cavities at the lath boundaries in

the AF HDH Ti-6Al-4V-3 specimen renders better ductility.



(a) Fracture surface



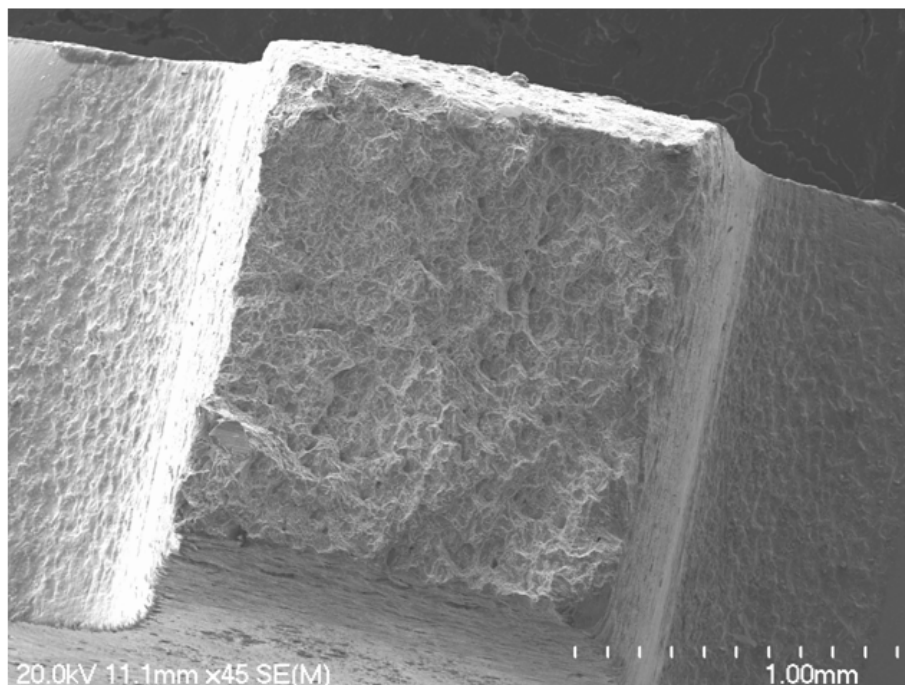
(b) Longitudinal cross section

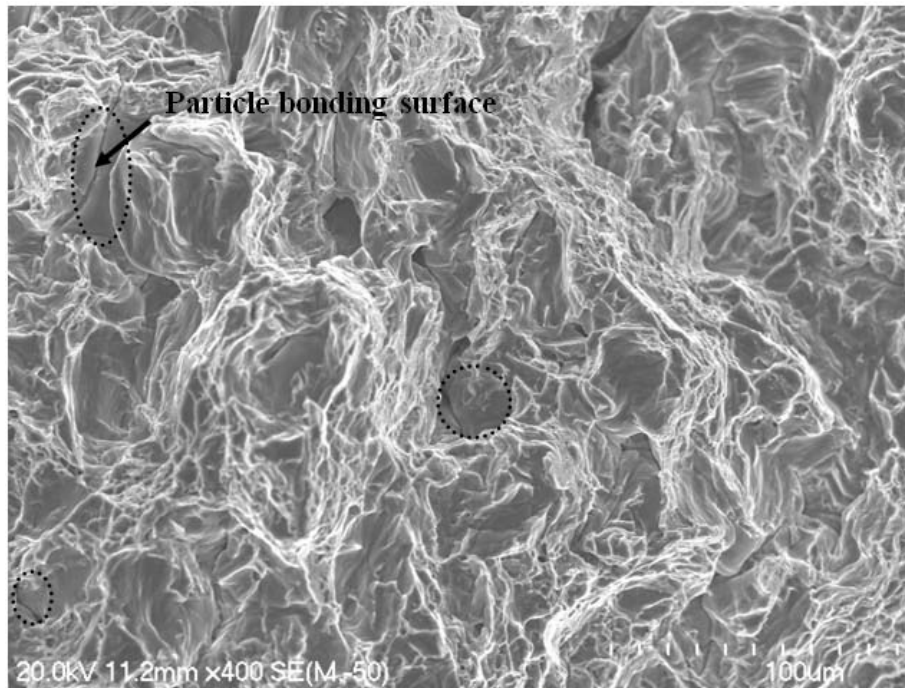
Figure 4.22: Fracture surface and corresponding longitudinal cross section of the AF HDH Ti-6Al-4V-3 specimen.

4.7.3 Fracture Behavior of an As-forged GA Ti Part

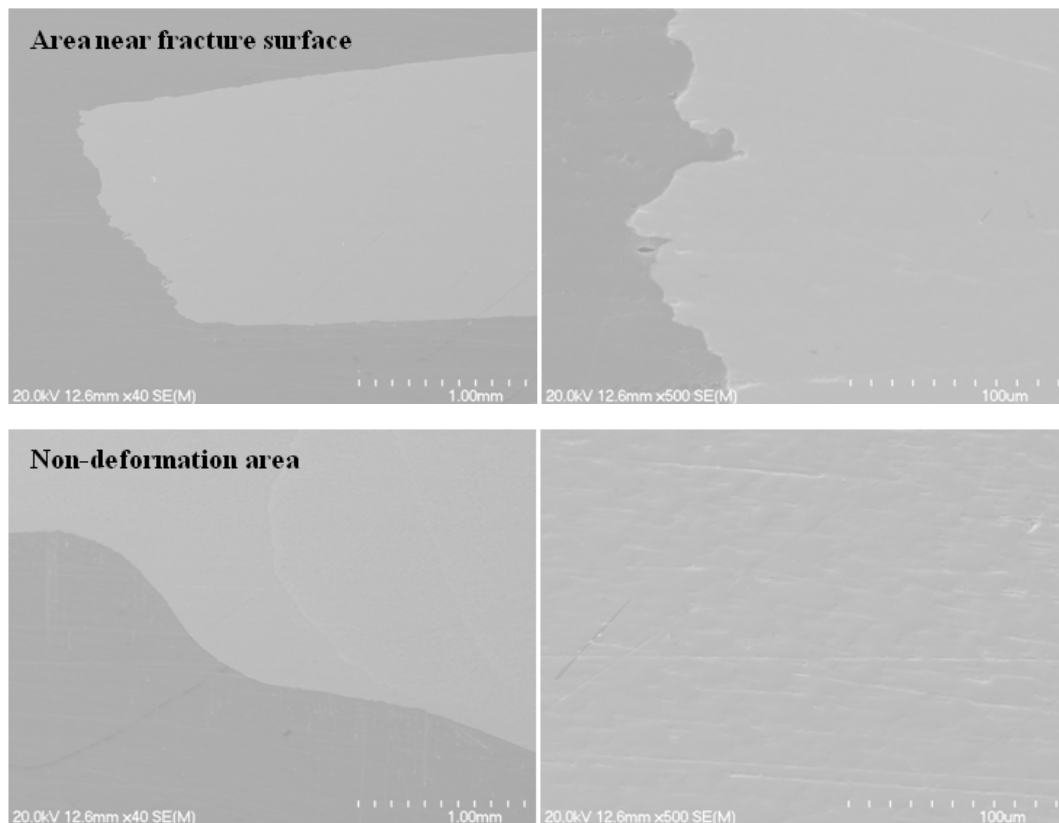
Specimens cut from an as-forged GA Ti part, with low oxygen content, had better ductility than the specimens cut from the as-forged HDH Ti part, with a high oxygen content, no matter whether they were cut from near the surface or in the center of the part. The minimum elongation to fracture of as-forged GA Ti specimens was 14%, suggesting that the GA Ti powder compacts were consolidated very well by powder compact forging. Particle bonding surfaces, as shown in Figure 4.23(a) were clearly observed on the fracture surface of the AF GA Ti-1 specimen, which was cut near to the surface of the part, but the longitudinal cross section of this specimen (Figure 4.23(b)) did not show any cavities. This means that the GA Ti powder compact in the AF GA Ti-1 specimen

was very well consolidated, with most of the interparticle boundaries having strong bonding and only in a few regions was the powder particle bonding weak, as circled in Figure 4.23(a). It appeared that the weak particle bonding in these regions did not affect the ductility of the specimen very much as evidenced by its elongation to fracture of 17.4%, and the fracture surface showed a large number of dimples, reflecting the ductile fracture behavior of the AF GA Ti-1 specimen. The fracture surface of the AF GA Ti-6 specimen, cut from the centre of the part, as shown in Figure 4.24, showed a large number of dimples of various sizes in the range of 2-20 μm , reflecting the ductile fracture behaviour of the specimen. Particle bonding surfaces could not be observed on the fracture surface of the specimen, and no cavities were visible on a longitudinal cross section of the specimen in both the area near to the fracture surface and the non-deformed area. This suggests that the powder compact in the location of the specimen was very well consolidated with full density, and there were no regions where the particle bonding was weak.



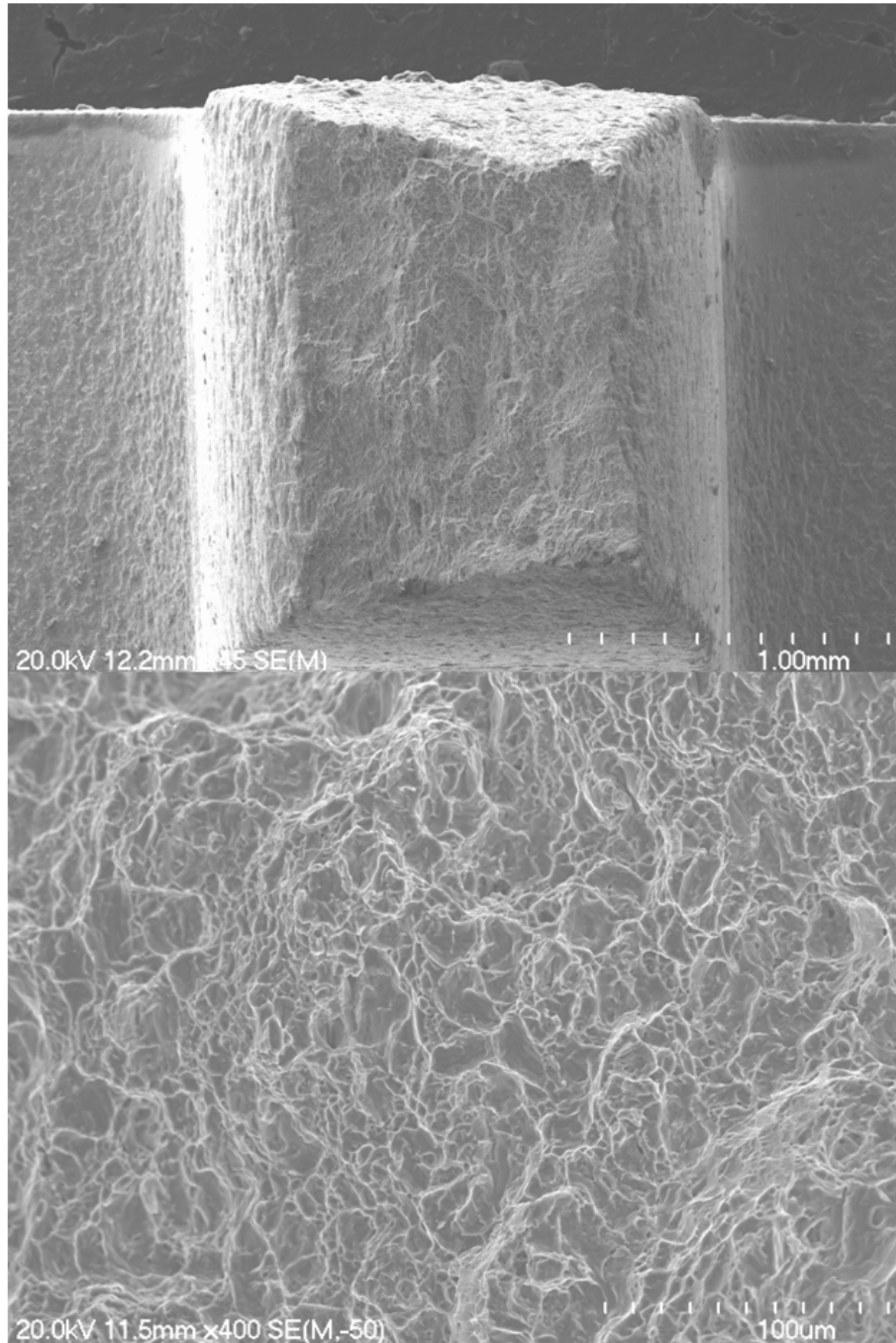


(a) Fracture surface

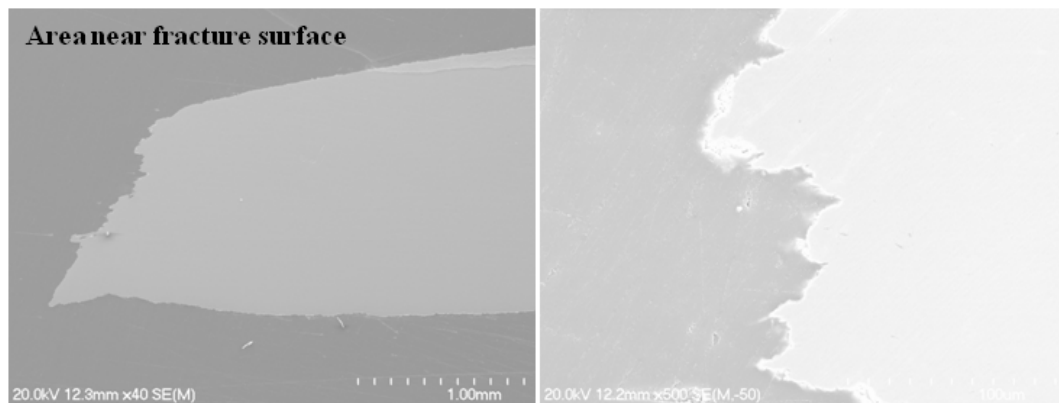


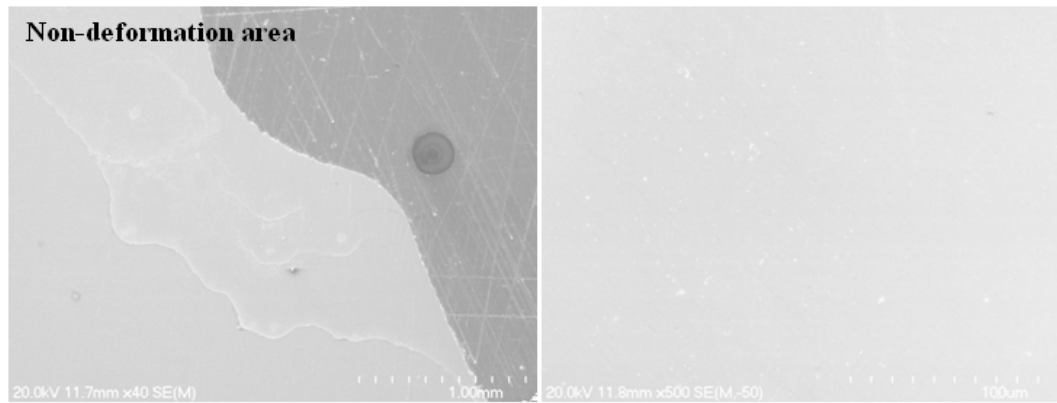
(b) Longitudinal cross section

Figure 4.23: Fracture surface and corresponding longitudinal cross section of AF GA Ti-1 specimen.



(a) Fracture surface





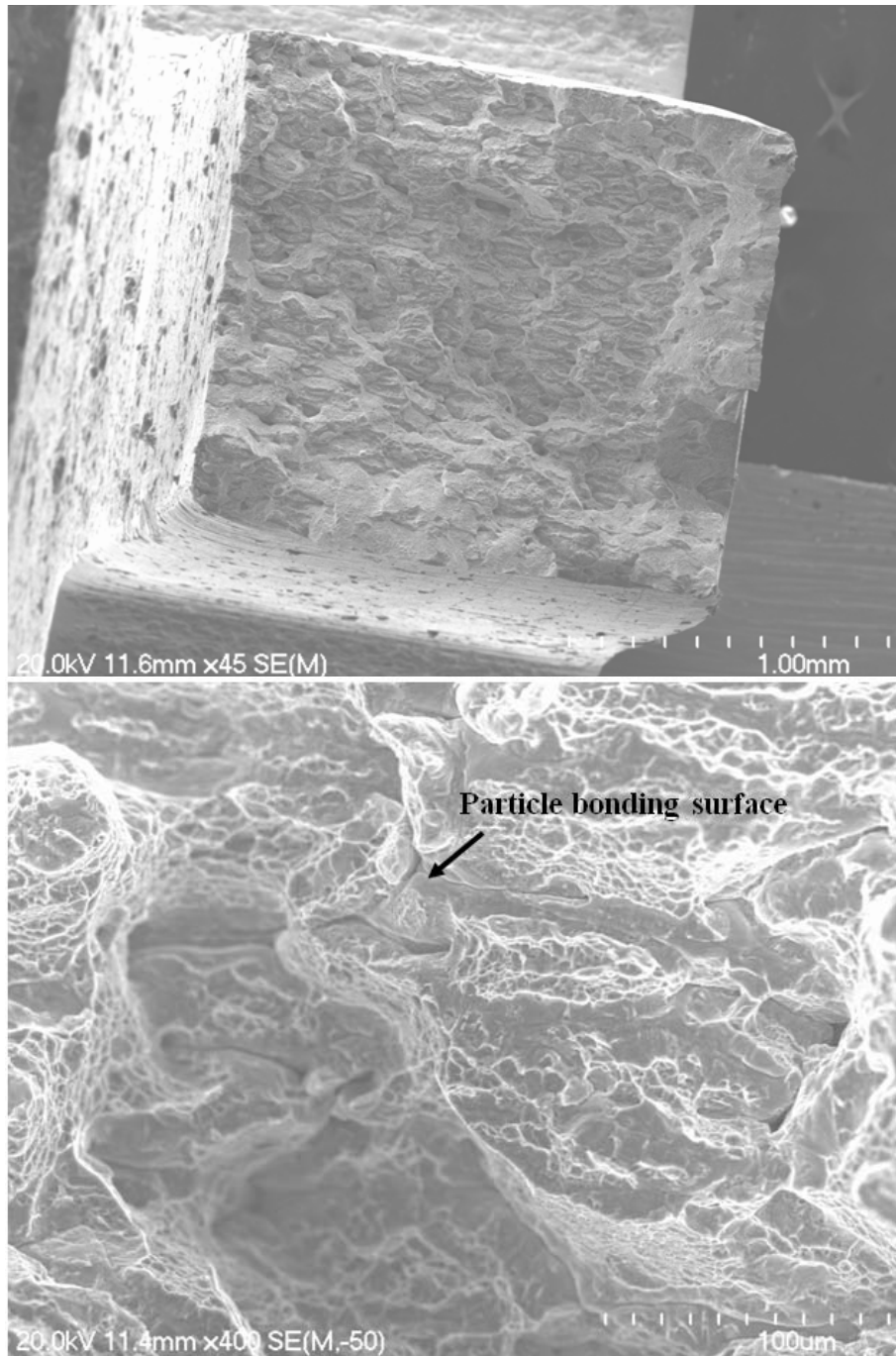
(b) Longitudinal cross section

Figure 4.24: Fracture surface and corresponding longitudinal cross section of the AF GA Ti-6 specimen.

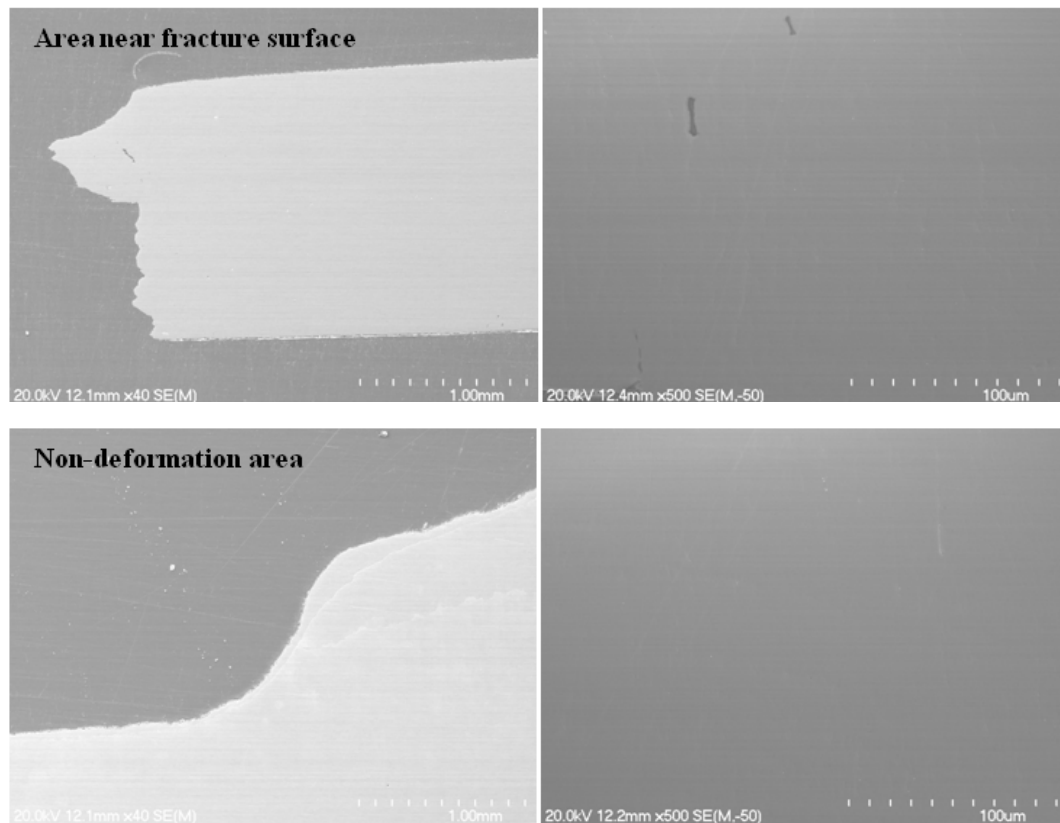
4.7.4 Fracture Behavior of an As-forged GA Ti-6Al-4V Part

The fracture surface of the AF GA Ti-6Al-4V-3 specimen, which had an elongation to fracture of 7.2% and was cut near to the surface of the part, showed the shapes of the deformed spherical powder particles which were elongated along a direction perpendicular to the forging direction, as shown in Figure 4.25(a). Particle bonding surfaces were also clearly seen on the fracture surface when these were examined in the SEM at a high magnification (Figure 4.25(a)). The fracture surface had a large number of dimples, reflecting the ductile fracture behaviour of the specimen. On a longitudinal cross section of the specimen, there were a few cavities in the area near the fracture surface, as shown in Figure 4.25(b). It appeared that these cavities were formed by powder particle debonding, because there were no such cavities in the non-deformed area. This suggests that the particle bonding strength in some regions cannot resist the tensile stress up to the yield strength of the specimen during tensile testing, and the bonded particles separate under the tensile stress, causing the formation of cavities, which finally led to the fracturing of the specimen and a low elongation to fracture. Overall, it appears that the powder compact in the AF GA Ti-6Al-4V-3 specimen was fairly well consolidated to nearly full density, despite a few regions where the particle

bonding was weak.



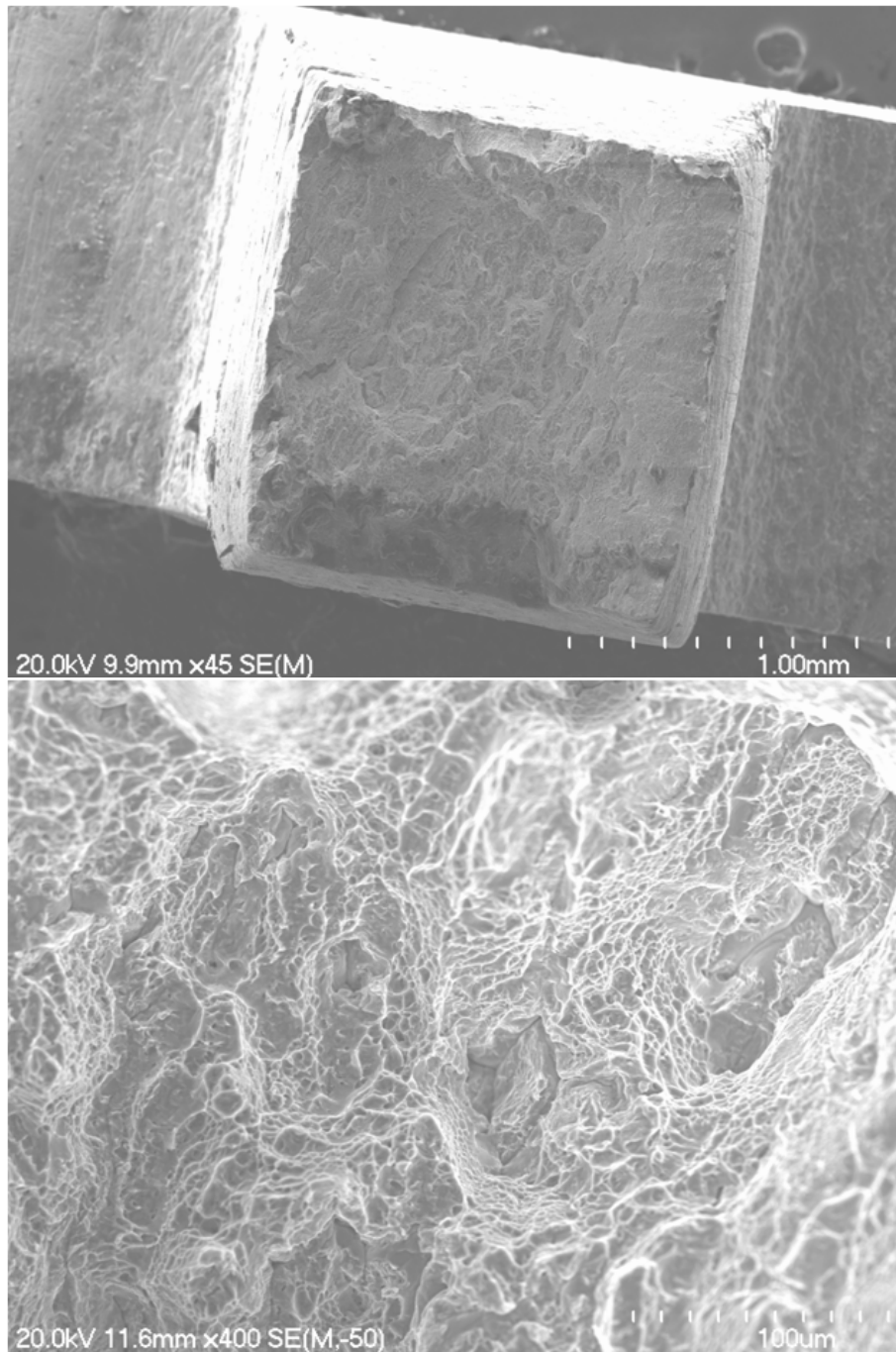
(a) Fracture surface



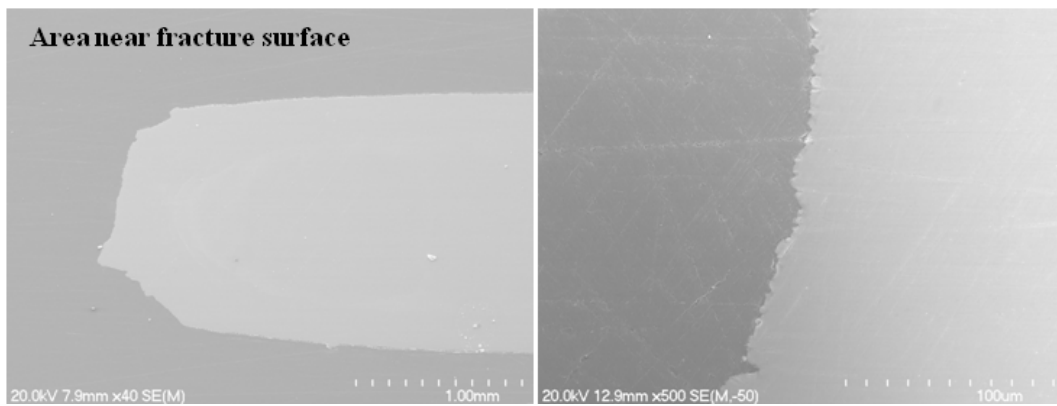
(b) Longitudinal cross section

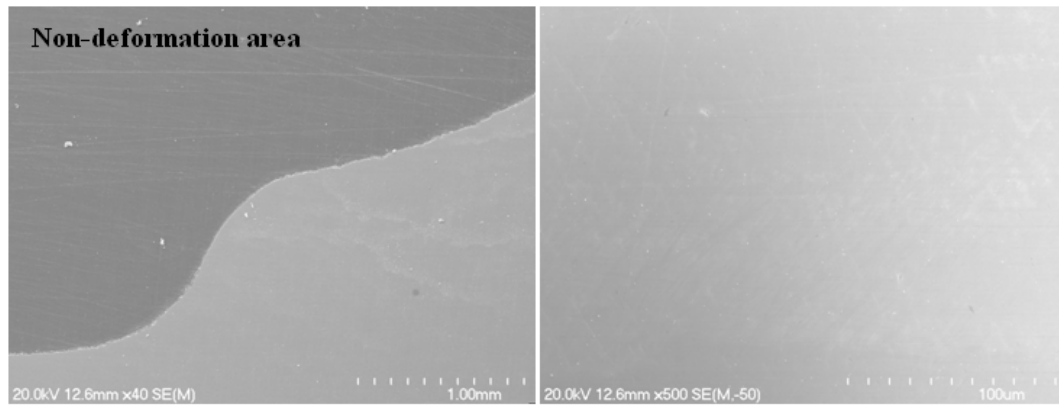
Figure 4.25: Fracture surface and corresponding longitudinal cross section of the AF GA Ti-6Al-4V-3 specimen.

The fracture surface of the GA Ti-6Al-4V-5 specimen, which had an elongation to fracture of 10.9% and was cut from a location near the centre of the part, showed a large number of fine dimples with sizes in the range of 1-10 μm , as shown in Figure 4.26(a), reflecting the ductile fracture behaviour of the specimen. There were no features in the fracture surface which resembled the powder particle shapes, so the powder compact in the location of the specimen was consolidated very well with full density. This was further proved by the fact that there were no cavities in both the area near to the fracture surface and the non-deformed area in a longitudinal cross section of the specimen.



(a) Fracture surface





(b) Longitudinal cross section

Figure 4.26: Fracture surface and corresponding longitudinal cross section of the AF GA Ti-6Al-4V-5 specimen.

4.8 Discussion

4.8.1 Improvement in the Mechanical Properties of Ti and Ti-6Al-4V Parts by Powder Compact Forging

Compared with conventional powder hot consolidation techniques, the powder compact forging process without a separate sintering step used in this study is a rapid consolidation technique. The process is completed in less than 10 minutes, being faster than HIP [3-8], hot pressing [9-14] and powder forging with a powder compact sintering step [15-17], all of which require several hours to consolidate the powders and achieve full density.

In the powder compact forging process, the main mechanism of densification is material flow by plastic deformation to remove the pores, so diffusion plays only a small role in densification during this process. As pointed out by German [20], powder particle shearing is essential to break up the particle surface films and obtain fresh surfaces which are needed to improve particle bonding. On the other hand, if the particle surface film is not broken, when the two adjacent particles are pressed together under pressure, the strength of particle bonding at the

interparticle boundaries is close to zero, meaning that real powder consolidation is not realized, despite achieving full density. Under tensile stress, disc-shaped pores are formed by this weak particle bonding, and the stresses are concentrated at the edges of the pore shape, which is preferable to premature fracturing of the material. So the extent of particle shearing controls the degree of powder consolidation and the strength of particle bonding. In this study, the streamlines in the as-forged HDH Ti, HDH and GA Ti-6Al-4V parts in Figure 4.2 were formed by shear bands during the powder forging process, and the shear band formation developed with increasing reduction, as shown in Figure 4.27 [18]. It was observed that the mechanical properties of as-forged HDH Ti, GA Ti-6Al-4V and HDH Ti-6Al-4V parts changed with distance from the surface to the centre of the part, where a large amount of shear band deformation is preferable for particle bonding, along a direction perpendicular to the forging direction. As a result, the ductility of the material improved with increasing distance from the surface to the centre of as-forged parts. This is the reason why, in as-forged HDH Ti parts, GA Ti-6Al-4V and HDH Ti-6Al-4V parts, the specimens cut from positions near the surface have a lower ductility than the specimens cut from the centre of the parts, even though there is no evidence of particle debonding or pores in these specimens. So shear deformation is important for powder consolidation by powder compact forging, and this work gives both experimental and theoretical explanations for the role of shear deformation in powder consolidation by powder compact forging.

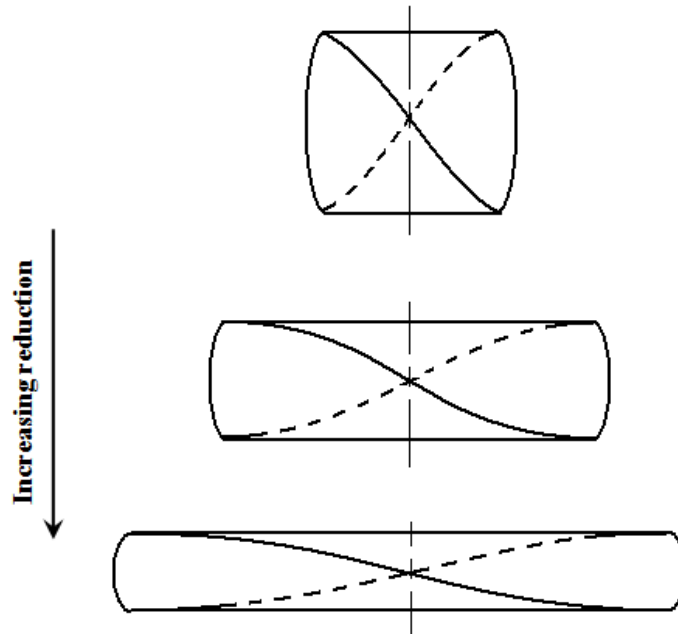


Figure 4.27: Schematic diagram of shear band deformation in a cylinder under compression.

Based on the porosity distributions in as-forged HDH Ti and GA and HDH Ti-6Al-4V parts, the powders were completely consolidated, except in the regions near their surfaces. The fracture surfaces of specimens, cut from the centre of as-forged HDH and GA Ti parts, GA and HDH Ti-6Al-4V parts, showed the same features as those found in the fracture surfaces of wrought Ti and Ti-6Al-4V alloy specimens with the same oxygen content and similar microstructure [19]. The mechanical properties of a fully consolidated HDH Ti part and GA and HDH Ti-6Al-4V parts made by powder compact forging were determined by averaging the mechanical properties of three specimens cut from the centre of the parts. They are listed in Table 4.7, together with the typical corresponding mechanical properties from ingot metallurgy Ti and Ti-6Al-4V.

Table 4.7: Mechanical properties of as-forged Ti and Ti-6Al-4V parts made by powder compact forging in this study and the typical corresponding mechanical properties of ingot metallurgy Ti and Ti-6Al-4V.

Sample	Oxygen content(%)	YS(MPa)	UTS(MPa)	Elongation to fracture(%)
As-forged HDH Ti	0.41	661.0	796.3	12
As-forged HDH Ti with holding time of 5 mins	0.42	637.5	789.1	22.4
As-forged GA Ti	0.12	461.7	563.2	19.5
Grade 1 Ti ingot [22]	≤0.18	240	170	24
Grade 4 Ti ingot [22]	≤0.40	550	480	15
As-forged HDH Ti-6Al-4V	0.52	1160.6	1291.8	6.2
As-forged GA Ti-6Al-4V	0.14	955.3	1063.4	9.3
Ti-6Al-4V ingot [22]	0.08-0.2	800-1100	900-1200	13-16

The mechanical properties of as-forged Ti-6Al-4V parts are sensitive to oxygen content in a similar to the effect of oxygen on the mechanical properties of parts made by ingot metallurgy. An as-forged HDH Ti-6Al-4V part with an oxygen content of 0.52% had a tensile strength ~200 MPa higher than that in an as-forged HDH Ti-6Al-4V part with an oxygen content of 0.14%.

From Table 4.7, it can be concluded that the as-forged GA Ti part, made in this study, had a higher tensile strength and similar ductility to a Grade 1 Ti ingot, while the as-forged HDH Ti part made in this study had a higher tensile strength and similar ductility to a Grade 4 Ti ingot. Furthermore a higher ductility in the as-forged HDH Ti part was achieved by holding the powder compact at the forging temperature for 5 minutes prior to forging. The mechanical properties of an as-forged HDH Ti-6Al-4V part cannot be directly compared with those made by ingot metallurgy Ti-6Al-4V, because the oxygen content of the part made by powder compact forging was 0.52%, which is much higher than of the 0.2% maximum in ingot metallurgy Ti-6Al-4V. However, this study shows that as-forged HDH Ti-6Al-4V parts have 6.2% elongation to fracture, a high tensile

strength of 1291.8 MPa, and are therefore ductile, strong and light materials desirable for many industrial applications. The mechanical properties of an as-forged GA Ti-6Al-4V part fall well into the range of mechanical properties of ingot metallurgy Ti-6Al-4V having a similar oxygen content [22]. The mechanical properties of as-forged Ti-6Al-4V parts are sensitive to oxygen content as shown by a mechanical property comparison between an as-forged GA Ti-6Al-4V part and an as-forged HDH Ti-6Al-4V part. This is similar to the effect of oxygen content on the mechanical properties of parts made by ingot metallurgy. So an as-forged HDH Ti-6Al-4V part with an oxygen content of 0.52% had a tensile strength of ~200 MPa higher than that for an as-forged HDH Ti-6Al-4V part with an oxygen content of 0.14%. In summary, powder compact forging was successfully used to produce a consolidated rocker arm for an internal combustion engine from HDH and GA Ti and HDH and GA Ti-6Al-4V powders. The parts have a higher tensile strength and slightly lower ductility than those made using the corresponding ingot metallurgy Ti and Ti-6Al-4V. The improvement in mechanical properties is attributed to the constraint in grain growth. In this study, even though the forging temperature is well above the β transus temperature, the time for the material to be at the temperatures above the β transus temperature is very short, being less than 10 minutes, and thus the grain growth in the consolidated parts was significantly restricted.

4.8.2 Mechanisms of Powder Consolidation by Powder Compact Forging

4.8.2.1 Enhanced Densification Mechanism in Powder Compact Forging

Since the powder compact forging process is one kind of pressure-assisted sintering technique [23-25], the densification mechanism for pressure-assisted sintering can be used to explain the fast densification in the Ti and Ti-6Al-4V powder compact forging process. According to pressure enhanced densification theory, shown in Ref. [20], the densification rate of a powder compact under pressure can be described using the equation below:

$$\frac{dV_S}{dt} = (1 - V_S)B(g\frac{\gamma_{SV}}{x} + P_E - P_P) \quad (4.1)$$

where dV_S/dt represents densification rate, V_S is the fraction of solid, B is a collection of parameters which includes diffusivity, temperature, particle size, g is a geometric term, γ_{SV} is solid-vapor surface energy, x is the scale of the microstructure, P_E is the effective pressure amplified from the applied stress, and P_P is the gas pressure in the pores.

In Equation 4.1, the effect of external pressure on the densification rate of a powder compact is expressed by the term $(P_E - P_P)$. P_E is a positive factor which enhances densification, while P_P is a negative factor which resists densification. The gas pressure in the pores is due to the gas trapped in the pores during densification. With pore shrinkage, the gas pressure in the pores increases, and this is the reason why more time is required to remove the closed pores and the densification rate significantly decreases in the final stage of sintering. Even though external pressure can enhance densification, the gas pressure in the pores still significantly hinders the densification. This is the reason why during HIP, the can containing the powder must be evacuated before being sealed to remove the trapped gas [20].

Compared with conventional powder forging, there was no sintering step before the powder compact forging procedure used in this study. This further enhances pore collapse in a powder compact as shown in Figure 4.28. A four spherical particle model, shown in the figure, is assumed to explain the evolution of pore shape and collapse during powder compact forging without an individual sintering step. Due to free material flow in the radial direction, the material will fill the gaps between the powder particles and pore collapse occurs directly to consolidate the powder compact to full density under a high external pressure. This is faster than spherical pore collapse in Ref. [20]. On the other hand, during powder compact forging, grain growth can be constrained [26]. The powder compact

forging used in this work is one kind of rapid densification process, where the pores collapse by plastic deformation without any entrapped gas forming during sintering. According to Equation 4.1, the densification rate is significantly enhanced by external pressure without the negative effect of gas pressure in the pores, so the powder compact is consolidated into full density instantly, which is different from powder consolidation by long time diffusion, such as in HIPing [3-8] and hot pressing [9-14]. So the experimental results for the microstructure and porosity distributions of an as-forged HDH Ti part and GA and HDH Ti-6Al-4V parts match the above assumption. There are no pores at the center of the parts, where large, localized plastic deformation occurred, as reflected by the streamlines shown in the low magnification optical microscopy images in Figure 4.2.

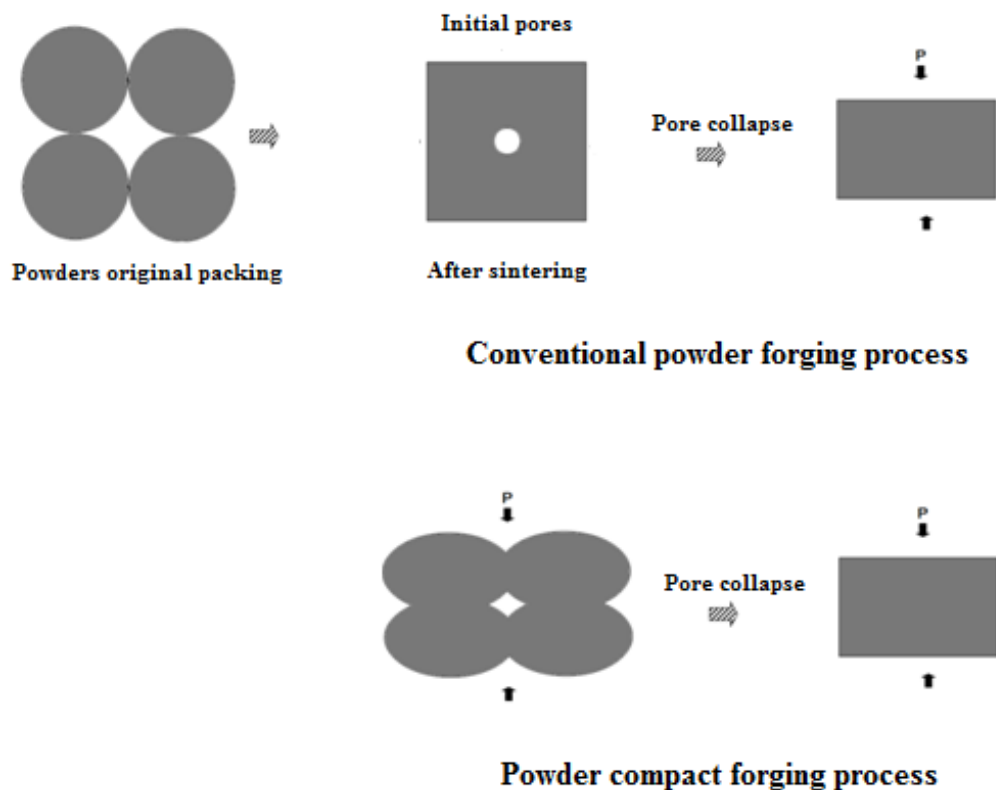


Figure 4.28: Pore evolution during powder the compact forging process.

4.8.2.2 The Effect of Powder Shape on Densification of Powder Compact Forging

According to the porosity distribution in as-forged parts, the HDH Ti-6Al-4V part produced by powder compact forging was much denser than the GA Ti-6Al-4V part, and there were many more large pores near to the surface of the as-forged GA Ti-6Al-4V part than near the surface of the as-forged HDH Ti-6Al-4V part. The density of an HDH Ti-6Al-4V powder compact was lower than that of a GA Ti-6Al-4V powder compact. Both of these observations show that the powder particle shape significantly influences powder consolidation. The spherically shaped GA Ti-6Al-4V powder has better flowability and lower friction than the irregularly shaped HDH Ti-6Al-4V powder. The streamlines shown in the cross sections of an as-forged HDH Ti-6Al-4V part were clearer than those on the cross sections of a GA Ti-6Al-4V part, so the region of localized plastic deformation in the as-forged GA Ti-6Al-4V part is smaller than that in an HDH Ti-6Al-4V part. Under pressure powder particle flow weakens the effect of material flow on the collapsing pores, and reduces the shear stress in the powder particles. This leads to a decrease in the level powder consolidation. In the meantime, due to a lower friction coefficient between GA Ti-6Al-4V powder particles than between HDH Ti-6Al-4V powder particles, the shear stress in the particles near the surface, which controls particle surface film rupture is also reduced [20], leading to lower strength particle bonding. This is the reason why particle debonding was clearly shown in the fracture surface of the AF GA Ti-6Al-4V-3 specimen, which was cut near the surface of an as-forged GA Ti-6Al-4V part. In contrast, there was no occurrence of particle debonding in the specimens cut from a position near to the surface of as-forged HDH Ti and Ti-6Al-4V parts.

4.9 Summary

The work presented in this chapter illustrates that HDH Ti and HDH and GA Ti-6Al-4V powder compacts can be well consolidated by powder compact forging. This is indicated by the porosity distribution, mechanical properties and fracture

behaviour of tensile test specimens cut from various locations in the forged compacts.

- The finer microstructure in specimens cut from the centre of an as-forged HDH Ti part and HDH and GA Ti-6Al-4V parts with full density had better mechanical properties than those made by ingot metallurgy, in Ref. [22]. Increasing the holding time at the forging temperature improves the mechanical properties of as-forged HDH Ti parts, and the surface quality of the powder compact forged parts was improved by increasing the die temperature to 500 °C.
- The powder compact forging studied in this work is a rapid consolidation process for Ti and Ti-6Al-4V powders. Material flow, driven by large amounts of localised plastic deformation, causes pores to collapse during powder compact forging. Therefore the densification rate is significantly enhanced, compared with other hot consolidation processes, such as conventional powder forging with a long sintering step before forging.
- The changes in the mechanical properties with distance from the surface to the centre of an as-forged HDH Ti part and HDH and GA Ti-6Al-4V parts, along a direction perpendicular to the forging direction are caused by an increasing degree of powder consolidation, which is controlled by shear deformation of the powder particles. GA powder, with spherical powder particles and good flowability, experiences a lower material flow effect on powder consolidation.

4.10 References

1. Matthew J. Donachie, J., *Titanium: A Technical Guide*. 1988: ASM INTERNATIONAL.

2. Christoph Leyens, M.P., *Titanium and Titanium Alloys: Fundamentals and Applications*. 2003, Weinheim: WILEY-VCH Verlag GmbH & Co. KGaA.
3. Zhang, K., et al., *Effect of hot-isostatic-pressing parameters on the microstructure and properties of powder Ti-6Al-4V hot-isostatically-pressed samples*. Metallurgical and Materials Transactions A, 2010. **41**(4): p. 1033-1045.
4. Schüller, E., et al., *Hot isostatic pressing (HIP) of elemental powder mixtures and prealloyed powder for NiTi shape memory parts*. Advanced Engineering Materials, 2003. **5**(12): p. 918-924.
5. Wright, R., B. Rabin, and J. Knibloe, *Consolidation of Ni₃Al powders by hot isostatic pressing*. Material and Manufacturing Process, 1989. **4**(1): p. 25-37.
6. Rao, G.A., M. Srinivas, and D. Sarma, *Influence of modified processing on structure and properties of hot isostatically pressed superalloy Inconel 718*. Materials Science and Engineering: A, 2006. **418**(1): p. 282-291.
7. Wadley, H., et al., *Sensing and modeling of the hot isostatic pressing of copper pressing*. Acta metallurgica et materialia, 1991. **39**(5): p. 979-986.
8. Habel, U. and B.J. McTiernan, *HIP temperature and properties of a gas-atomized γ -titanium aluminide alloy*. Intermetallics, 2004. **12**(1): p. 63-68.
9. Bolzoni, L., et al., *Microstructural evolution and mechanical properties of the Ti-6Al-4V alloy produced by vacuum hot-pressing*. Materials Science and Engineering: A, 2012. **546**(0): p. 189-197.
10. Jia, C., et al., *Hot pressing of nanometer WC-Co powder*. International Journal of Refractory Metals and Hard Materials, 2007. **25**(1): p. 53-56.
11. Meng, J., C. Jia, and Q. He, *Effect of mechanical alloying on the structure and property of Ni₃Al fabricated by hot pressing*. Journal of alloys and compounds, 2006. **421**(1-2): p. 200-203.
12. Montealegre Meléndez, I., E. Neubauer, and H. Danninger, *Consolidation of titanium matrix composites to maximum density by different hot pressing techniques*. Materials Science and Engineering: A, 2010. **527**(16-17): p. 4466-4473.
13. Nie, X.W., S.Q. Lu, and K.L. Wang, *Effect of mechanical alloying on the structure and properties of NbCr₂ Laves phase fabricated by hot pressing*. Powder Technology, 2008. **184**(3): p. 333-336.
14. Tang, F., et al., *Pure Al matrix composites produced by vacuum hot pressing: tensile properties and strengthening mechanisms*. Materials Science and Engineering: A, 2004. **383**(2): p. 362-373.
15. Kim, K., H. Yang, and S. Hong, *Densification behaviour of titanium alloy powder compacts at high temperature*. Powder Metallurgy, 2001. **44**(1): p. 34-40.
16. Duggirala, R. and R. Shivpuri, *Effects of processing parameters in P/M steel forging on part properties: A review part I powder preparation, compaction, and sintering*. Journal of Materials Engineering and Performance, 1992. **1**(4): p. 495-503.

17. Yang, T.S. and Y.C. Hsu, *Study on the bulging deformation of the porous metal in upsetting*. Journal of Materials Processing Technology, 2006. **177**(1): p. 154-158.
18. Dieter, G.E., *Mechanical metallurgy*. Vol. 3. 1976: McGraw-Hill New York.
19. Joshi, V.A., *Titanium alloys: an atlas of structures and fracture features*. 2006: CRC.
20. German, R.M., *Sintering Theory and Practice*. Vol. 1. 1996.
21. Dieter, G.E. and D. Bacon, *Mechanical metallurgy*. Vol. 3. 1986: McGraw-Hill New York.
22. Rodney Boyer, G.W., E. W. Collings, *Materials Properties Handbook: Titanium Alloys*. 1994: ASM International.
23. Skandan, G., et al., *The effect of applied stress on densification of nanostructured zirconia during sinter-forging*. Materials Letters, 1994. **20**(5): p. 305-309.
24. Skandan, G., *Processing of nanostructured zirconia ceramics*. Nanostructured materials, 1995. **5**(2): p. 111-126.
25. Liao, S.C., K. Pae, and W. Mayo, *The effect of high pressure on phase transformation of nanocrystalline TiO₂ during hot-pressing*. Nanostructured materials, 1995. **5**(3): p. 319-325.
26. Shaik, G.R. and W. Milligan, *Consolidation of nanostructured metal powders by rapid forging: Processing, modeling, and subsequent mechanical behavior*. Metallurgical and Materials Transactions A, 1997. **28**(13): p. 895-904.

Chapter 5: Heat Treatment of Forged Ti and Ti-6Al-4V Parts

5.1 Introduction

Since the powder compact forging process involves severe plastic deformation, as reflected by the formation of streamlines shown in Figure 4.2, there is residual stress in the as-forged parts, which can reduce their mechanical properties. In addition, the ductility of the as-forged Ti and Ti-6Al-4V parts produced by powder compact forging is clearly lower than the expected ductility of Ti and Ti-6Al-4V alloy produced by ingot metallurgy with a similar level of interstitial elements such as oxygen. Therefore, heat treatment of the forged parts was done to eliminate internal residual stress and to optimize the microstructure in order to improve their mechanical properties. Forged Ti parts were just annealed. For forged GA and HDH Ti-6Al-4V parts, four types of heat treatment were carried out: beta annealing - annealing at a temperature just above the β transus temperature; duplex annealing - annealing at a temperature in the $\alpha+\beta$ phase field; a recrystallization heat treatment and solution treatment and aging. Details of the heat treatment conditions are shown in Chapter 2. This chapter presents the effects of heat treatment conditions on the strength and ductility of forged Ti and Ti-6Al-4V parts and uses these results to determine the optimum heat treatment conditions for achieving balanced tensile strength and ductility in forged parts.

5.2 Annealing of Forged HDH Ti Parts

An as-forged HDH Ti part was annealed for 6 hours at 550 °C, which is in the α phase region, and cooled in air. As shown by the stress-strain curves of the annealed specimens in Figure 5.1, after annealing, the ductility of forged HDH Ti parts greatly improved, while their tensile strength decreased by about 100 MPa. The average mechanical properties of the different as-forged Ti parts and forged HDH Ti part after annealing are summarized in Table 5.1.

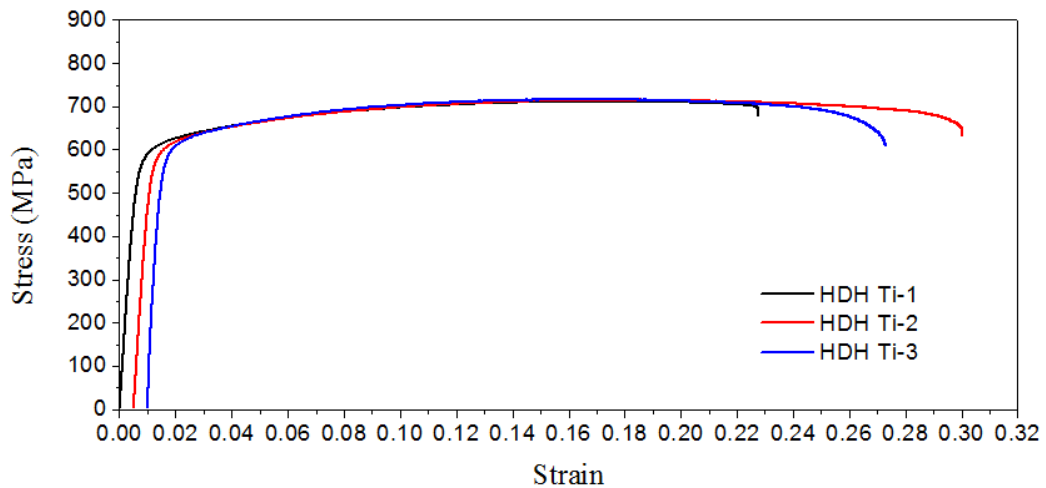


Figure 5.1: Stress-strain curves of tensile test specimens cut from a forged HDH Ti part with an oxygen content of 0.41% after annealing.

Table 5.1: Mechanical properties of different as-forged Ti parts and forged HDH Ti part after annealing.

Sample	YS(MPa)	UTS(MPa)	Elongation to fracture(%)
As-forged HDH Ti part	661.0	796.3	12
As-forged GA Ti part	461.7	563.2	19.5
As-forged HDH Ti part with holding time of 5 minutes	637.5	789.1	22.4
Forged HDH Ti part after annealing treatment	573.0	715.0	25.6

As shown in Table 5.1, annealing of a forged HDH Ti part produced by PCF without prior holding at the forging temperature increased the average elongation to fracture from 12 to 25.6%, and its UTS and yield strength decreased from 796.3 to 715.4 MPa and from 661.0 to 573.4 MPa, respectively. This high elongation to fracture is comparable to that of an as-forged GA Ti part and an as-forged HDH Ti part made with a holding time of 5 minutes at forging temperature prior to forging. This significant ductility improvement of the forged HDH Ti part after annealing may have been caused by grain growth during annealing as shown in Figure 5.2. With grain growth, the primary particle boundaries disappear or migrate as a grain boundary, so the weak particle bonding improves during this process. Furthermore

the degree of consolidation will be increased, as shown Figure 5.3 by the large sized dimples, formed by ductile fracture of equiaxed α grains, in the fracture surfaces of as-forged HDH Ti specimens after annealing where there are.

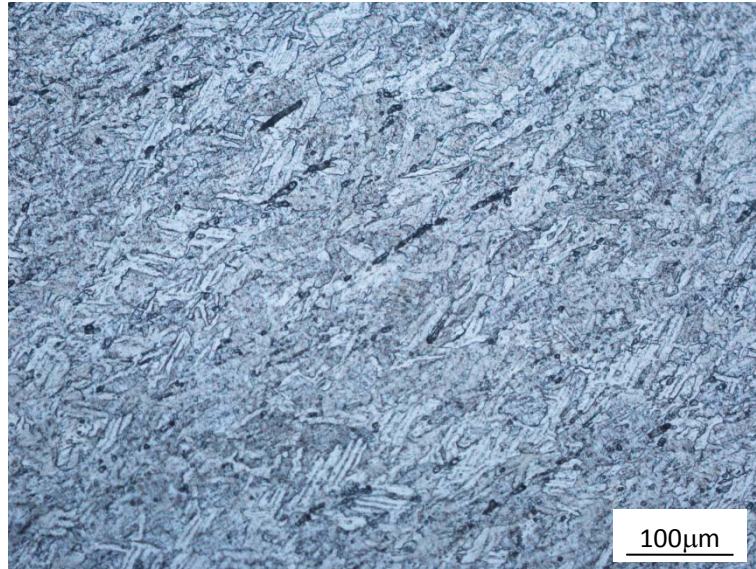
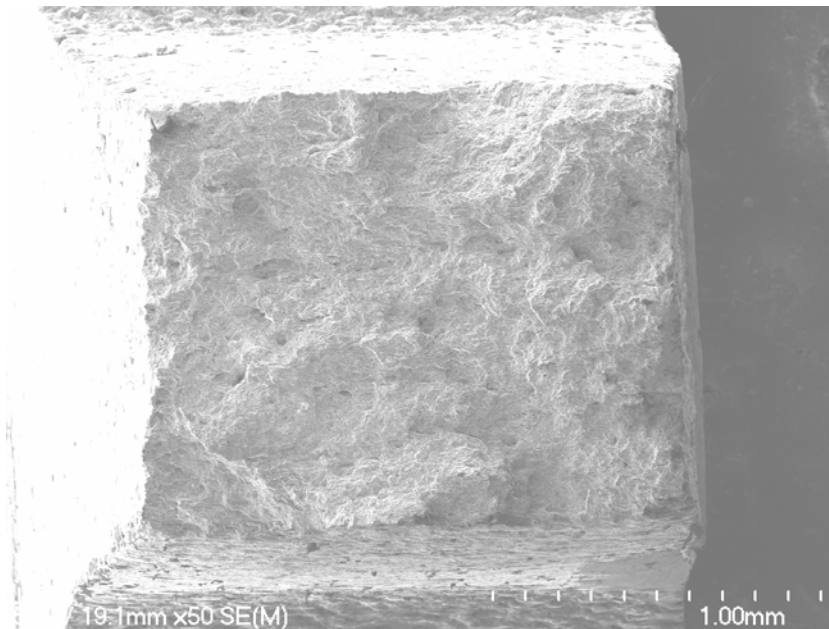


Figure 5.2: Microstructure of a forged HDH Ti part with an oxygen content of 0.41% after annealing.



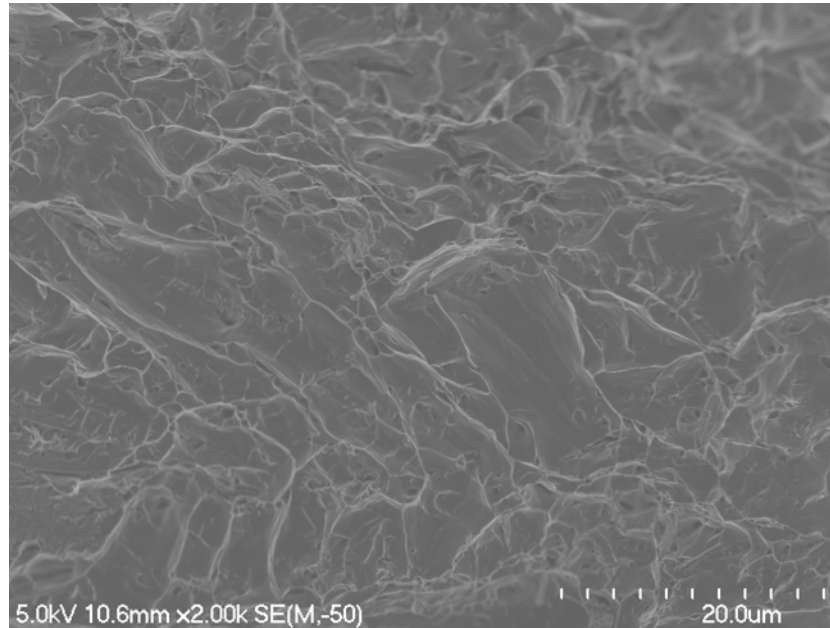
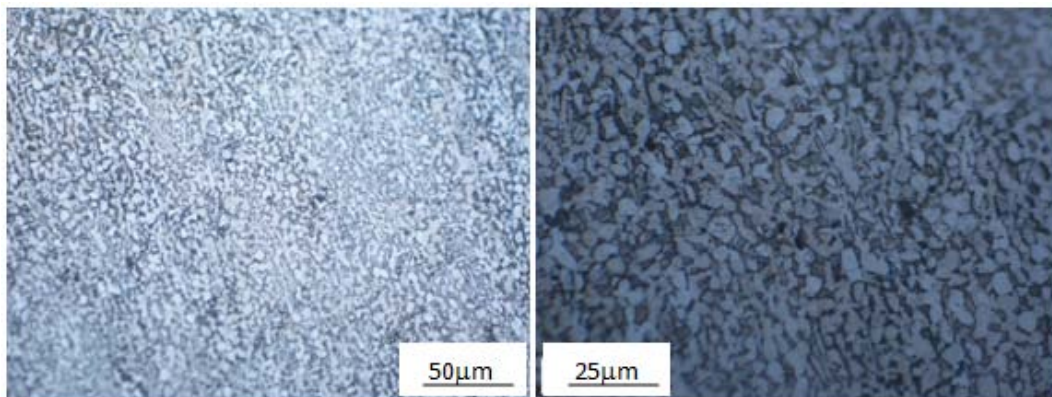


Figure 5.3: Fracture surface of a forged HDH Ti specimen with an oxygen content of 0.41% after annealing.

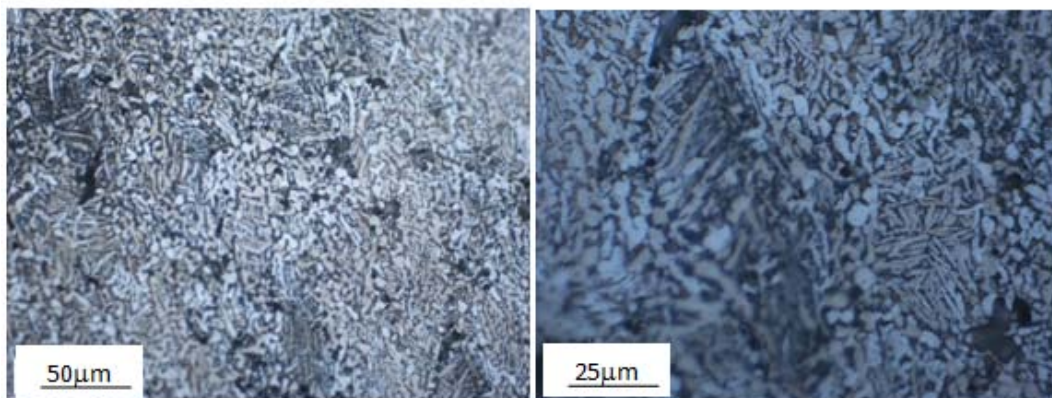
5.3 Effect of Heat Treatment on the Microstructures of Forged HDH Ti-6Al-4V Parts

As shown in Figure 4.3(c) in Chapter 4, the microstructure of as-forged HDH Ti-6Al-4V parts consisted of primary α lamellae in a coarse α/β matrix with a lamellar structure. There were thinner primary α lamellae and smaller prior β grains in the microstructure in the centre of the part than in the region near the surface, due to non-homogeneous deformation and dynamic recrystallization. After duplex annealing, there was still a difference in microstructure between the centre of the part and the region near to the surface of the part, as shown in Figure 5.4. In the centre of the HDH Ti-6Al-4V part, the microstructure consisted of equiaxed grains and a small volume fraction of α lamellae, as shown in Figure 5.4(a). In contrast, the region near to the surface had a bimodal type of microstructure consisting of equiaxed α grains and α lamellae as shown in Figure 5.4(b). This means that there are a much higher fraction of α lamellae in the region near the surface of the part than in the centre, possibly due to

recrystallization of deformed grains.



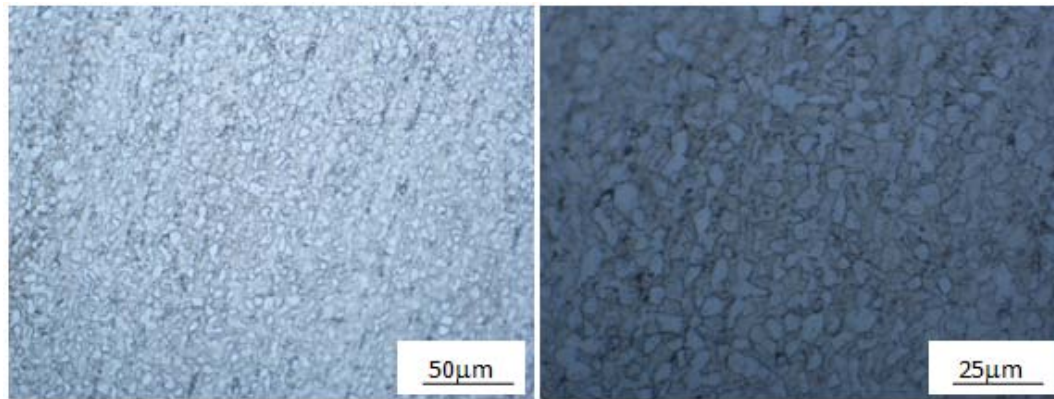
(a) In the center



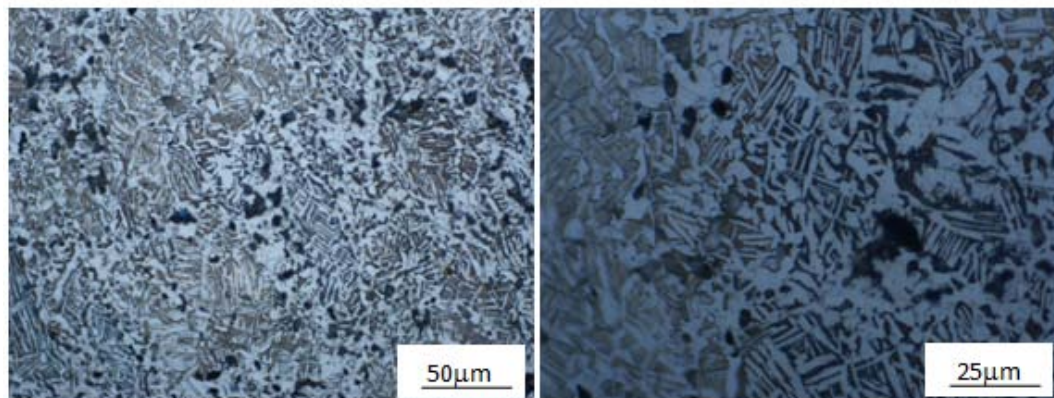
(b) Near the surface

Figure 5.4: Microstructure in different regions of a forged HDH Ti-6Al-4V part with an oxygen content of 0.52% after duplex annealing.

As shown in Figure 5.5, after a solution and aging treatment, the microstructure in the centre of the HDH Ti-6Al-4V part consisted of equiaxed α grains together with fine acicular α , while the microstructure in the surface region of the part consisted of equiaxed α grains and α lamellae. The difference in the fraction of equiaxed α grains between the centre and the surface region in the HDH Ti-6Al-4V part might be due to recrystallization of deformed grains during solution treatment.



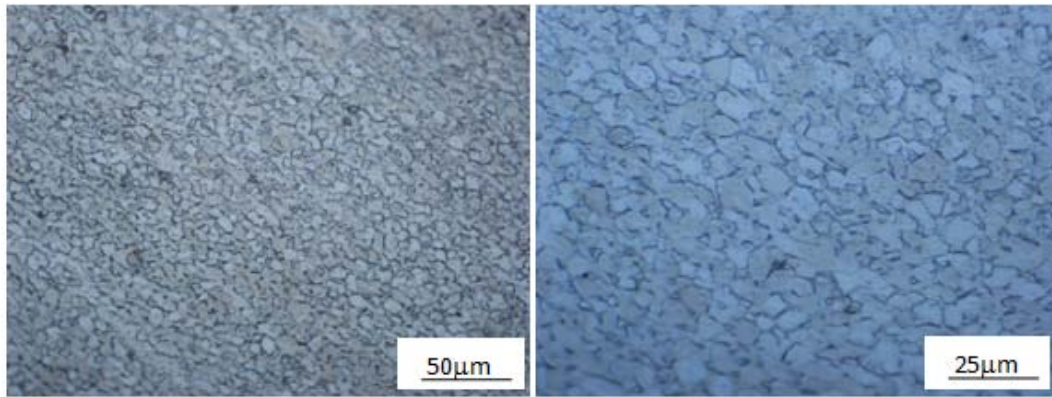
(a) In the center



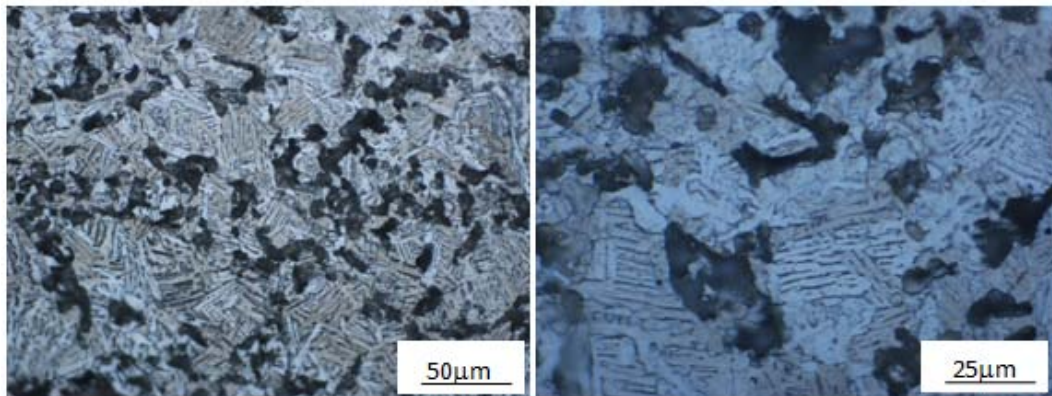
(b) Near the edge

Figure 5.5: Microstructure of different regions in a forged HDH Ti-6Al-4V part with an oxygen content of 0.52% after a solution and aging treatment.

The microstructure in the centre of an HDH Ti-6Al-4V part after recrystallization annealing only consisted of equiaxed α grains as shown in Figure 5.6(a), but the sizes of the grains, which are in the range of 3-10 μm , were larger than those found in the microstructure after a duplex annealing and solution and aging treatment. This suggests that significant grain growth occurred during the recrystallization annealing process. In contrast, the microstructure in the surface region of the part consisted of coarse α lamellae, as shown in Figure 5.6(b). This might be because the region near the surface did not experience a large amount of plastic deformation and therefore lacked a high driving force for the nucleation of equiaxed grains.



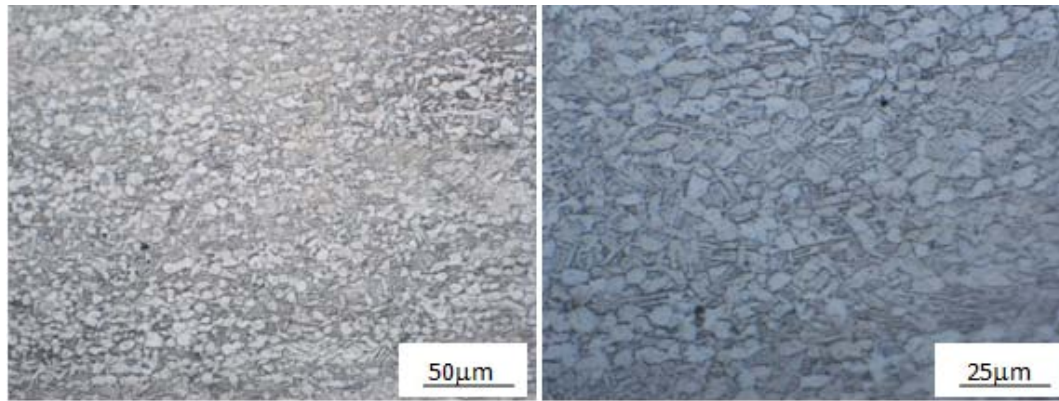
(a) In the center



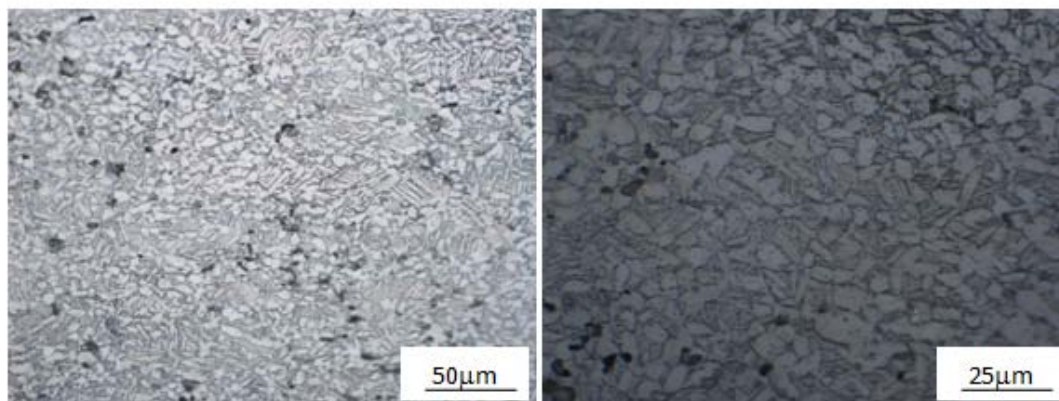
(b) Near the edge

Figure 5.6: Microstructure of different regions of a forged HDH Ti-6Al-4V part with an oxygen content of 0.52% after recrystallization annealing.

After beta annealing, the microstructures of both the centre and the surface region of the HDH Ti-6Al-4V part consisted of equiaxed α grains in an “acicular” $\alpha+\beta$ matrix, as shown in Figure 5.7. This is because during beta annealing, the part was heated to a temperature above the β transus temperature and held at this temperature for 1 hour, and through this the difference in the amounts of plastic deformation between the surface region and the centre of the part was removed, leading to a uniform microstructure.



(a) In the center



(b) Near the surface

Figure 5.7: Microstructure of different regions in a forged HDH Ti-6Al-4V part with an oxygen content of 0.52% after beta annealing.

5.4 Effect of Heat Treatment on the Mechanical Properties and Fracture Behaviour of Forged HDH Ti-6Al-4V Parts

The stress-strain curves of as-forged HDH Ti-6Al-4V parts and those after different heat treatments are shown in Figure 5.8. The average mechanical properties of the parts under different heat treatment conditions are listed in Table 5.2. From the curves and table, an HDH Ti-6Al-4V part had the lowest ductility with an average elongation to fracture of 3.3% after duplex annealing, and the mechanical properties of the HDH Ti-6Al-4V part did not change much after beta annealing, even though its ductility decreased slightly. The ductility of the forged part was improved significantly by recrystallization annealing, with its average

elongation to fracture increasing from 6.2% to 12.5%, while its ultimate tensile strength dropped from 1291.8 to 1220.6 MPa. A solution and aging treatment is normally used to increase the tensile strength of a Ti-6Al-4V alloy. From the results of this study, the ultimate tensile strength of the forged HDH Ti-6Al-4V part was clearly increased from 1291.8 MPa to 1421.7 MPa without loss in ductility.

In summary, according to the results shown in Figure 5.8 and Table 5.2, in order to get higher tensile strength with good ductility in forged HDH Ti-6Al-4V parts, a solution and aging treatment is the best condition among the heat treatments investigated in this study. If a higher ductility is required, a recrystallization anneal should be chosen, although the tensile strength of the forged part decreases by about 100 MPa after this heat treatment. This study shows that both duplex annealing and beta annealing are not favorable heat treatments for improving the mechanical properties of forged HDH Ti-6Al-4V parts.

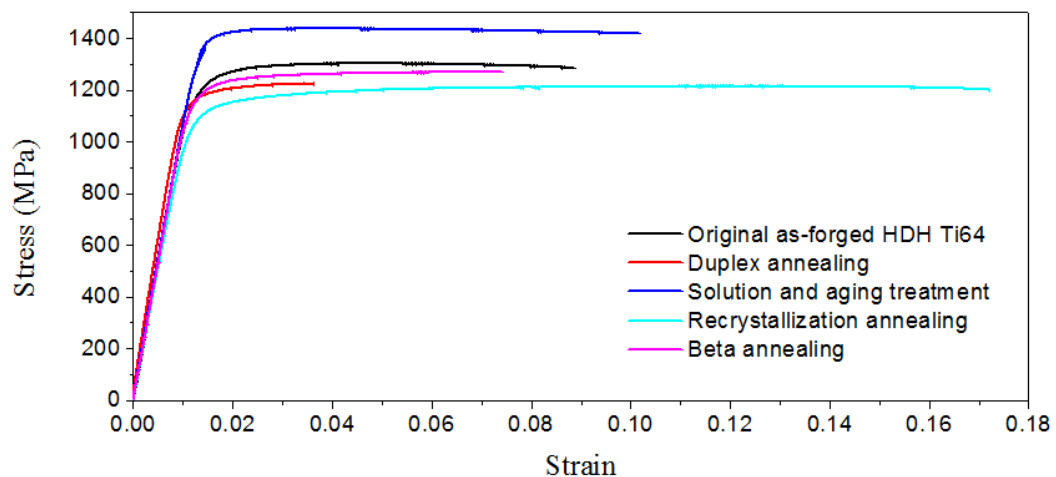


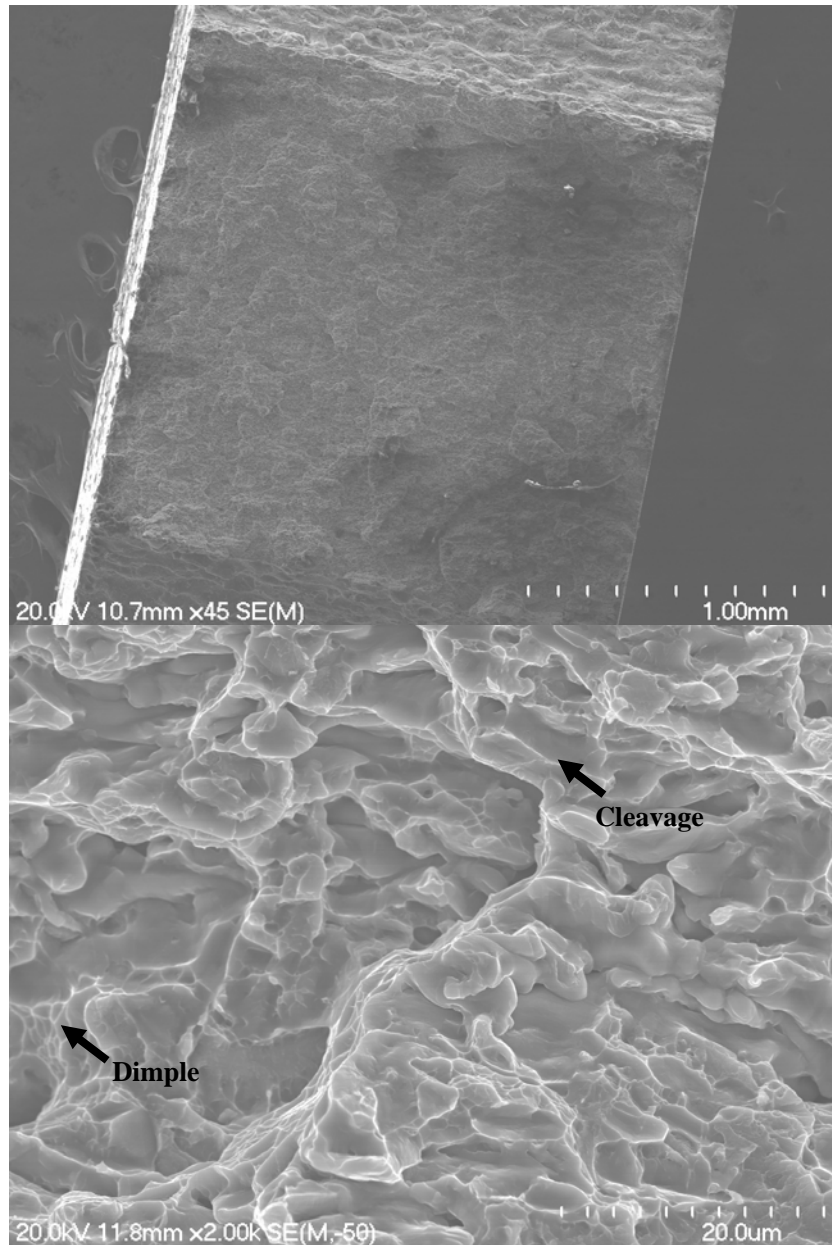
Figure 5.8: Stress-strain curves of as-forged and as-forged and heat treated HDH Ti-6Al-4V specimens with an oxygen content of 0.52%.

Table 5.2: A summary of average mechanical properties of as-forged and as-forged and heat treated HDH Ti-6Al-4V parts with an oxygen content of 0.52%.

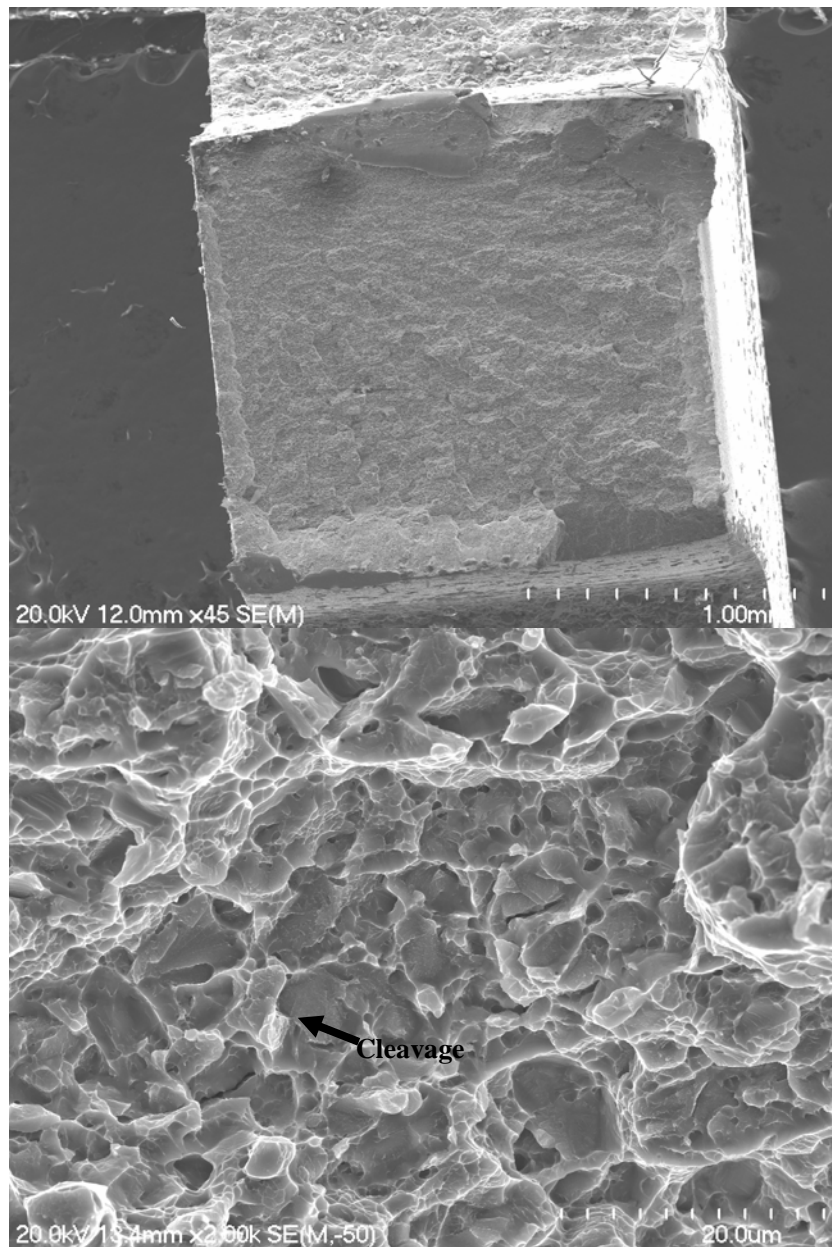
HDH Ti-6Al-4V	YS(MPa)	UTS(MPa)	Elongation to fracture (%)
As-forged	1160.6	1291.8	6.2
Duplex anneal	1206.6	1262.0	3.3
Solution and aging	1352.4	1421.7	7.2
Recrystallization	1091.5	1220.6	12.5
Beta anneal	1163.4	1264.6	4.8

As shown in Figure 5.9(a), the fracture surfaces of forged HDH Ti-6Al-4V specimens after duplex annealing show dimples formed by fracturing of equiaxed α grains and cleavage formed by fracturing of α lamellae. This means that if the volume fraction of equiaxed α grains in the microstructure is larger, the material will become more ductile. While the acicular α is detrimental to the ductility of Ti-6Al-4V, it can increase the tensile strength. As the ductility of the Ti-6Al-4V material is determined by the ease of forming cavities, the reason for the as-forged Ti-6Al-4V part to have low ductility is probably due to cleavage formed by fracturing of α lamellae. As shown in Figure 5.9(b), the fracture surfaces of forged HDH Ti-6Al-4V specimens after a solution and aging treatment show a large number of fine dimples which indicates that a large number of cavities formed by ductile fracturing of equiaxed α grains. Occasionally, cleavage planes can also be seen in the fracture surface, as arrowed in the figure. With a combination of dimples and cleavage planes, the material has good ductility and excellent tensile strength. As shown in Figure 5.9(c), the fracture surfaces of forged HDH Ti-6Al-4V specimens after recrystallization annealing show only fine dimples formed by ductile fracture of the equiaxed α grains. The ductile fracture of equiaxed α grains in the specimens subjected to recrystallization annealing are the reason for the best ductility in this material, compared with specimens subjected to other heat treatments. As shown in Figure 5.9(d), the fracture surfaces of forged HDH Ti-6Al-4V specimens after beta annealing are quite similar to those found in the specimens after duplex annealing, shown in Figure 5.9(a). The fracture surface

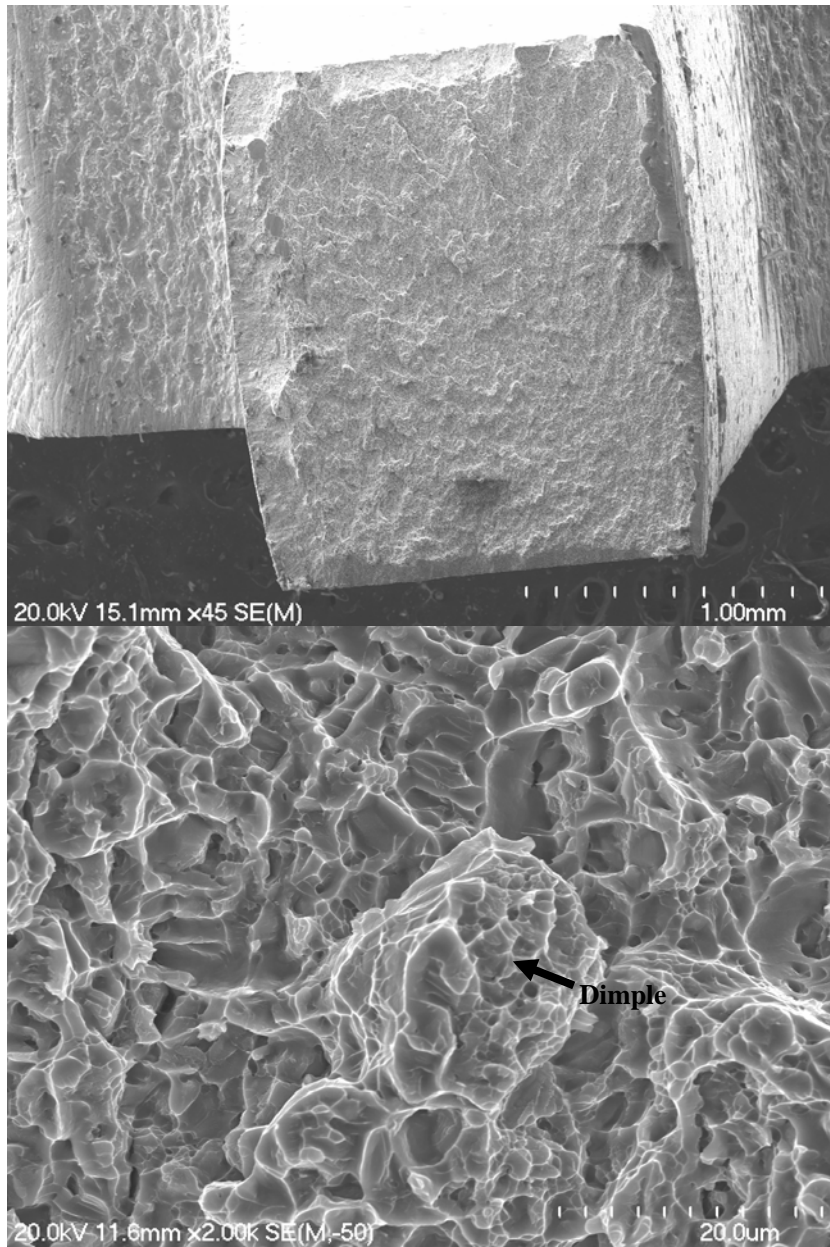
consists of coarse dimples formed by equiaxed α grains and cleavage formed by α lamellae. The reason for a lower ductility after beta annealing, compared with specimens which were given a solution and aging treatment or a recrystallization anneal, is the cleavage formed by fracturing of α lamellae.



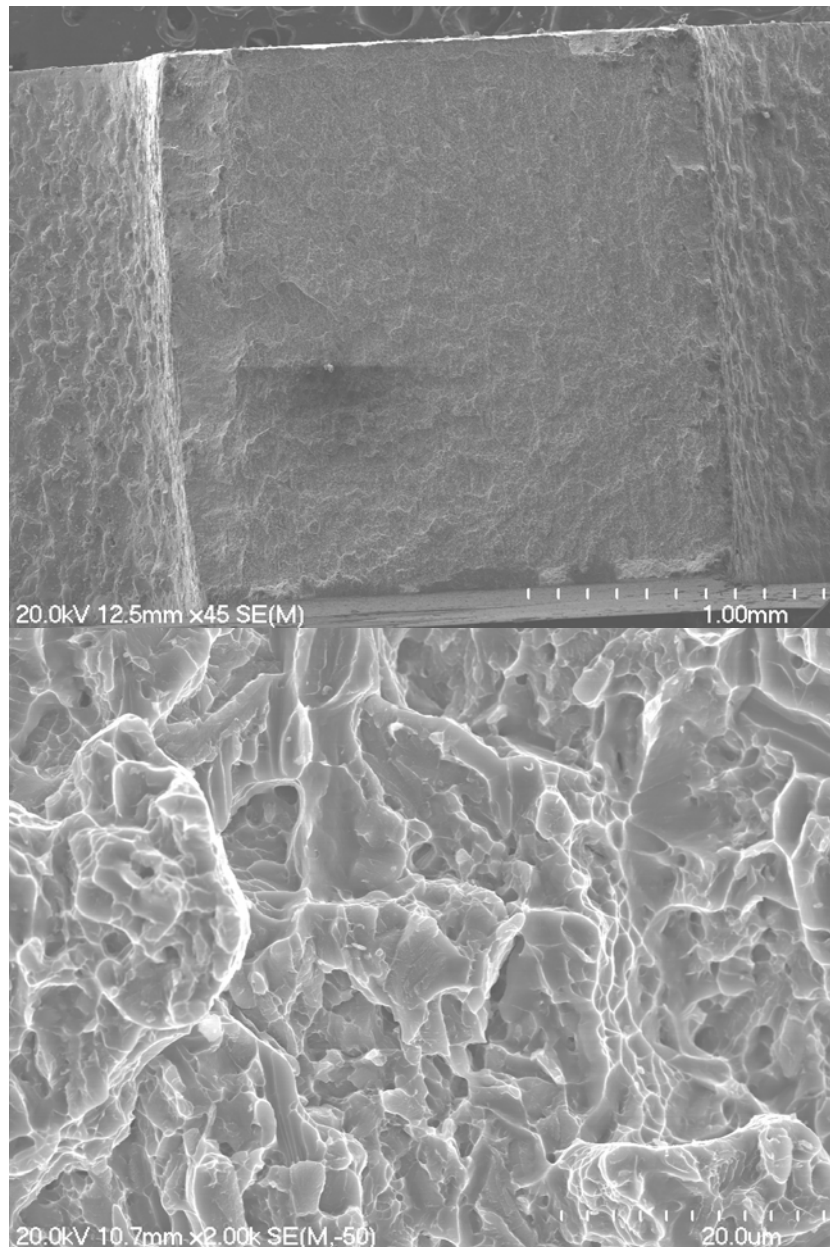
(a) Duplex annealing



(b) Solution and aging treatment



(c) Recrystallization annealing



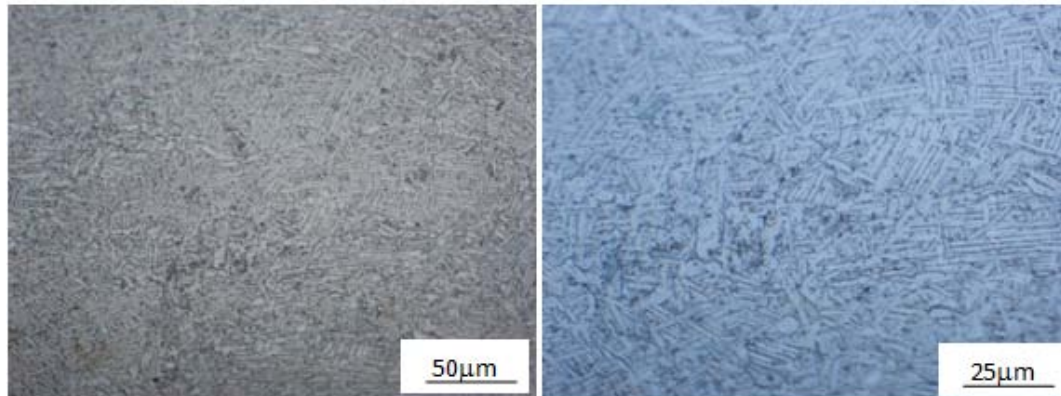
(d) Beta annealing

Figure 5.9: Fracture surfaces of forged HDH Ti-6Al-4V specimens with an oxygen content of 0.52% after different heat treatments.

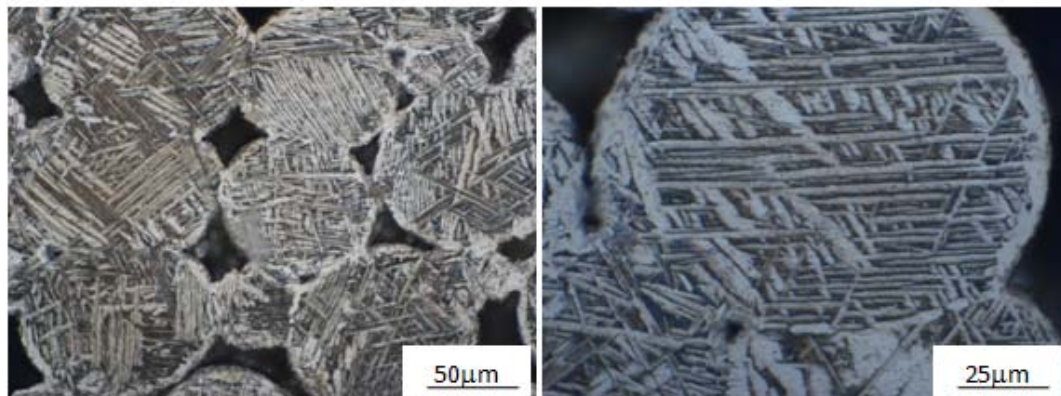
5.5 The effect of Heat Treatment on the Microstructure of Forged GA Ti-6Al-4V Parts

The microstructure of an as-forged GA Ti-6Al-4V part was shown in Figure 4.3(b), which consists of α acicular in a lamellar α/β matrix. In the center of an as-forged part, the α acicular and primary α lamellae at the grain boundaries were both

broken into shorter lengths due to the large amount of plastic deformation during powder compact forging. After duplex annealing, the microstructures in both regions were changed into one consisting of coarse α lamellae as shown in Figure 5.10. The length of the α lamellae at the centre of the part is much smaller than that in the surface region.



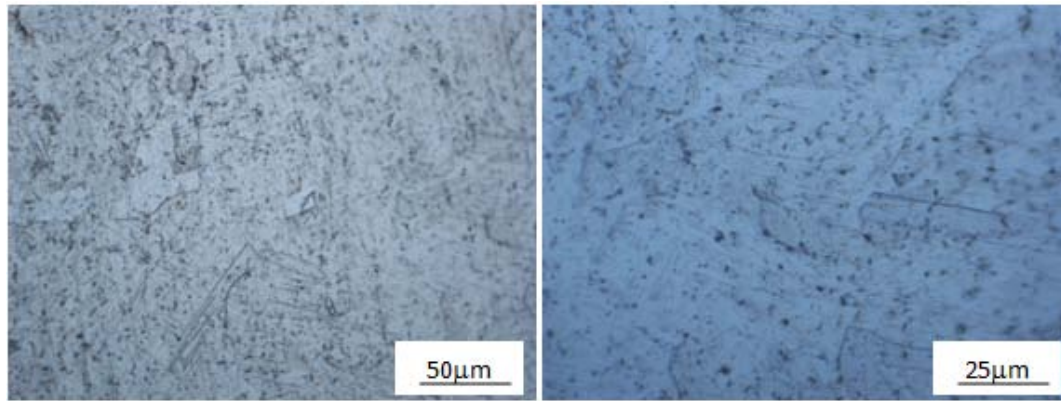
(a) In the center



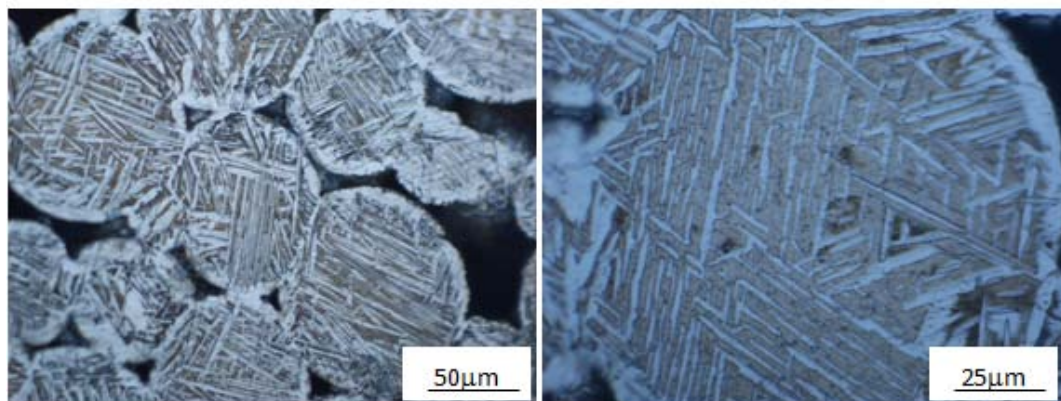
(b) Near the surface

Figure 5.10: Microstructure of different regions in a forged GA Ti-6Al-4V part with an oxygen content of 0.14% after duplex annealing.

As shown in Figure 5.11, the microstructure of a GA Ti-6Al-4V part after a solution and aging treatment was α acicular in the centre of the part, while in the surface region, there was an α lamellar microstructure with the lamellae size being smaller than those in the microstructure produced by duplex annealing.



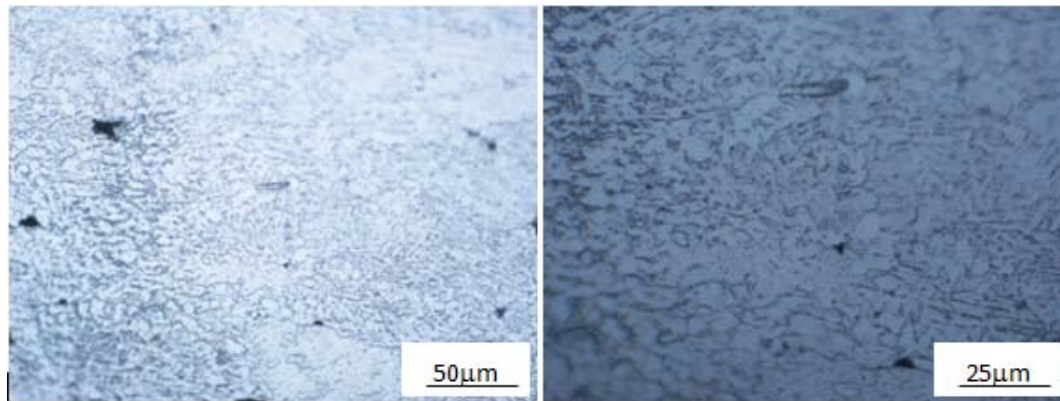
(a) In the center



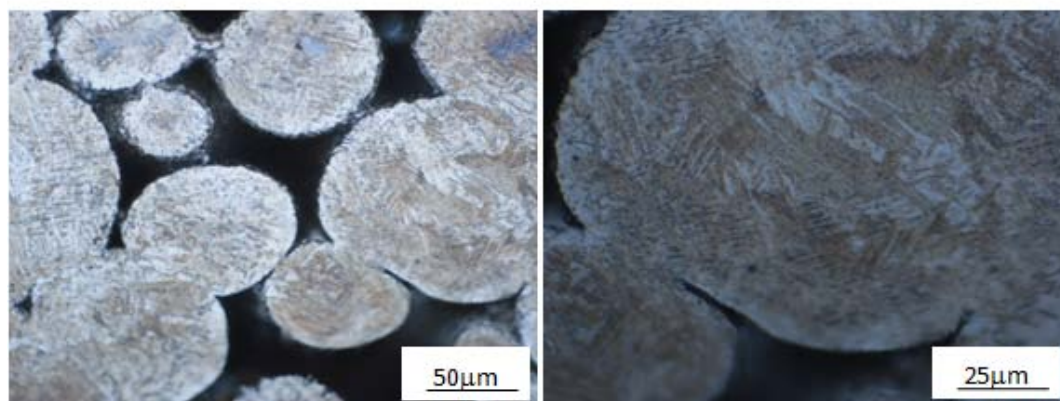
(b) Near the surface

Figure 5.11: Microstructure of different regions in a forged GA Ti-6Al-4V part with an oxygen content of 0.14% after a solution and aging treatment.

For a forged GA Ti-6Al-4V part after a recrystallization anneal, the microstructure at the centre consisted of equiaxed α grains in a matrix consisting of a fine $\alpha+\beta$ lamellar structure as shown in Figure 5.12. In the surface region with less plastic deformation, the microstructure is a fine α acicular structure, which is the same as that found in the as-forged part. This means that the equiaxed structure at the centre evolved through recrystallization driven by the large amount of plastic deformation.



(a) In the center



(b) Near the surface

Figure 5.12: Microstructure of different regions in a forged GA Ti-6Al-4V part with an oxygen content of 0.14% after recrystallization annealing.

5.6 Effect of Heat Treatment on the Mechanical Properties and Fracture Behaviour of Forged GA Ti-6Al-4V Parts

The stress-strain curves for forged GA Ti-6Al-4V parts after different heat treatments are plotted in Figure 5.13, and their average mechanical properties are summarized in Table 5.3. From the results, in contrast to the decrease in ductility in a forged HDH Ti-6Al-4V part after duplex annealing, the elongation to fracture of a forged GA Ti-6Al-4V part is increased from 9.3 to 14.3% by a duplex anneal without a decrease in tensile strength. After a solution and aging treatment, the tensile strength of the GA Ti-6Al-4V part was improved from 1063.4 to 1195.1 MPa, and its elongation to fracture remained constant at 9.9%. In Figure 5.13, the

forged GA Ti-6Al-4V part after a recrystallization anneal had the best ductility of all the specimens with an elongation to fracture of 15.1%, whereas its tensile strength dropped by 80 MPa after this heat treatment.

Based on the results of the study, duplex annealing can be used to improve the ductility of forged GA Ti-6Al-4V parts with an oxygen content of 0.14% without decreasing the tensile strength. After a solution and aging treatment, the UTS of the forged part is increased by about 140 MPa without changing the ductility, so a solution and aging treatment is a good way to improve the tensile strength of a forged part. The ductility of forged GA Ti-6Al-4V part is improved significantly after recrystallization annealing, with a small decrease in tensile strength. So recrystallization annealing is the best way to improve the ductility of a forged GA Ti-6Al-4V part.

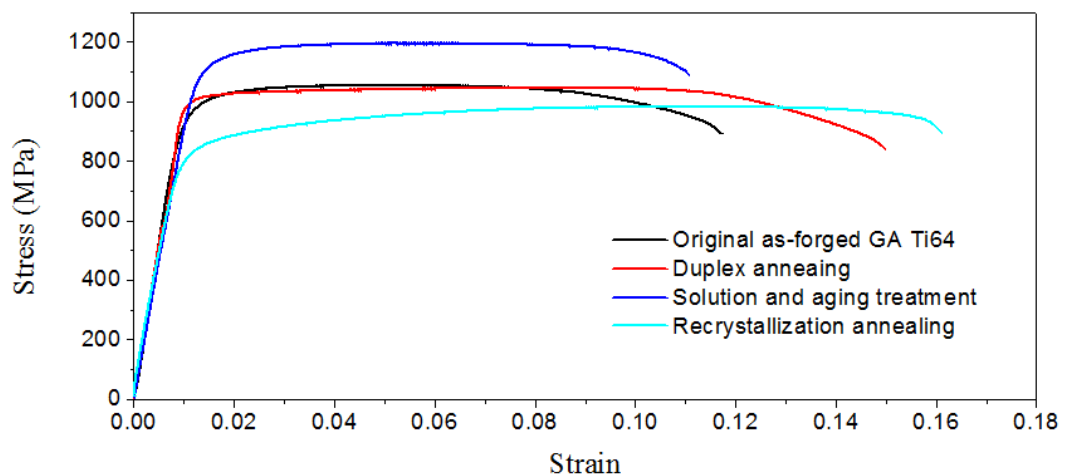
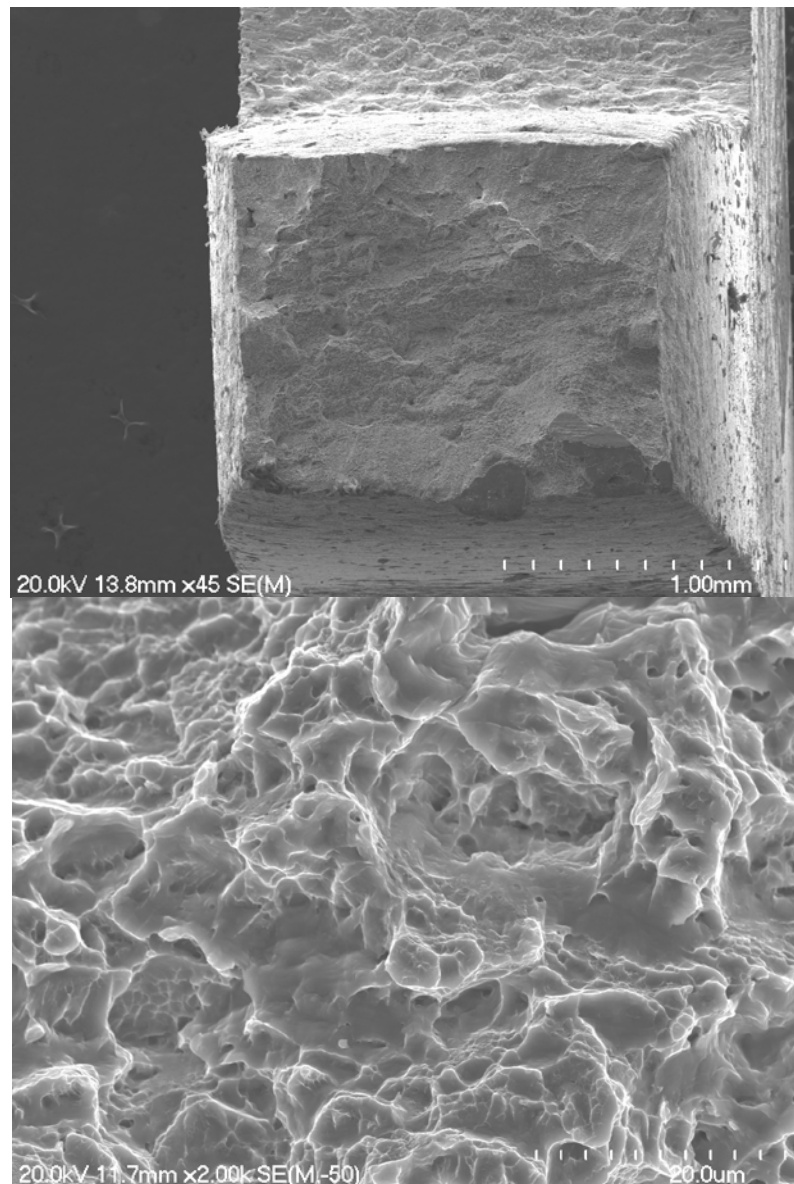


Figure 5.13: Stress-strain curves of as-forged GA Ti-6Al-4V specimens with an oxygen content of 0.14% after different heat treatments.

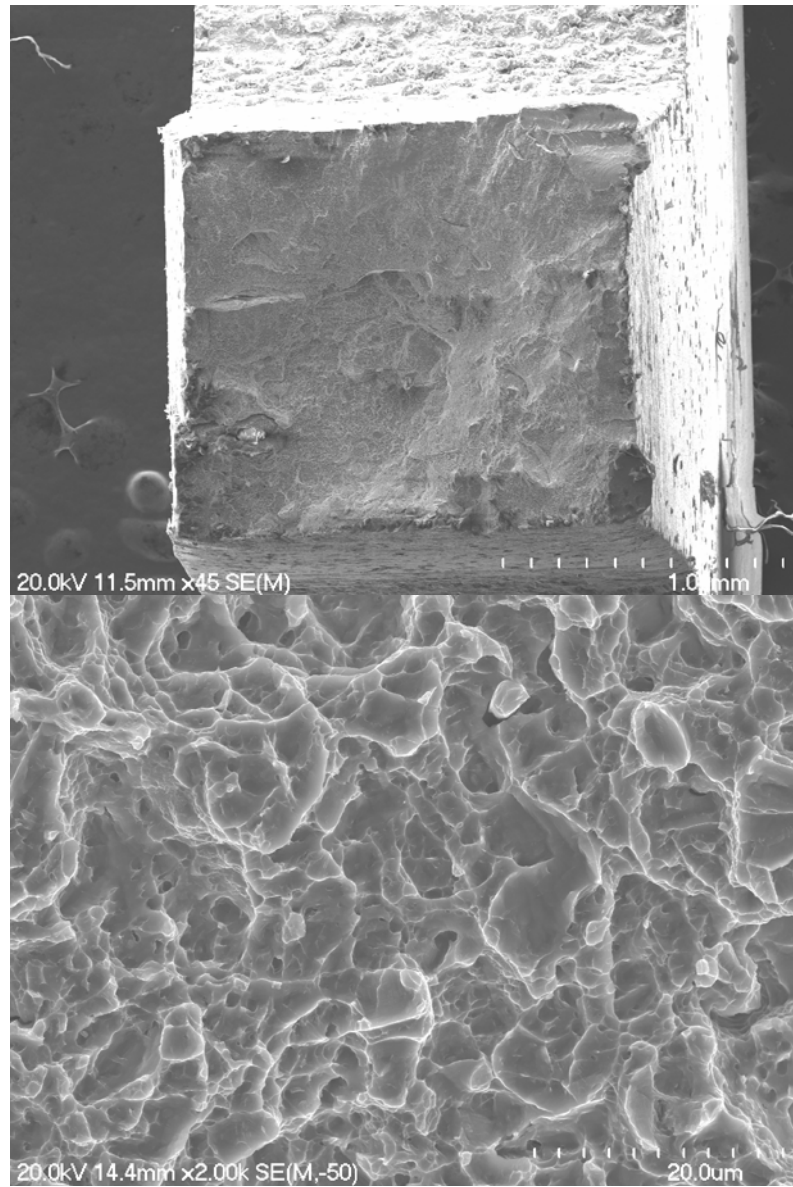
Table 5.3: Summary of the average mechanical properties of as-forged GA Ti-6Al-4V parts with an oxygen content of 0.14% after different heat treatments.

GA Ti-6Al-4V	YS(MPa)	UTS(MPa)	Elongation to fracture(%)
As-forged	955.3	1063.4	9.3
Duplex anneal	996.6	1046.2	14.3
Solution and aging	1102.6	1195.1	9.9
Recrystallization	811.4	983.1	15.1

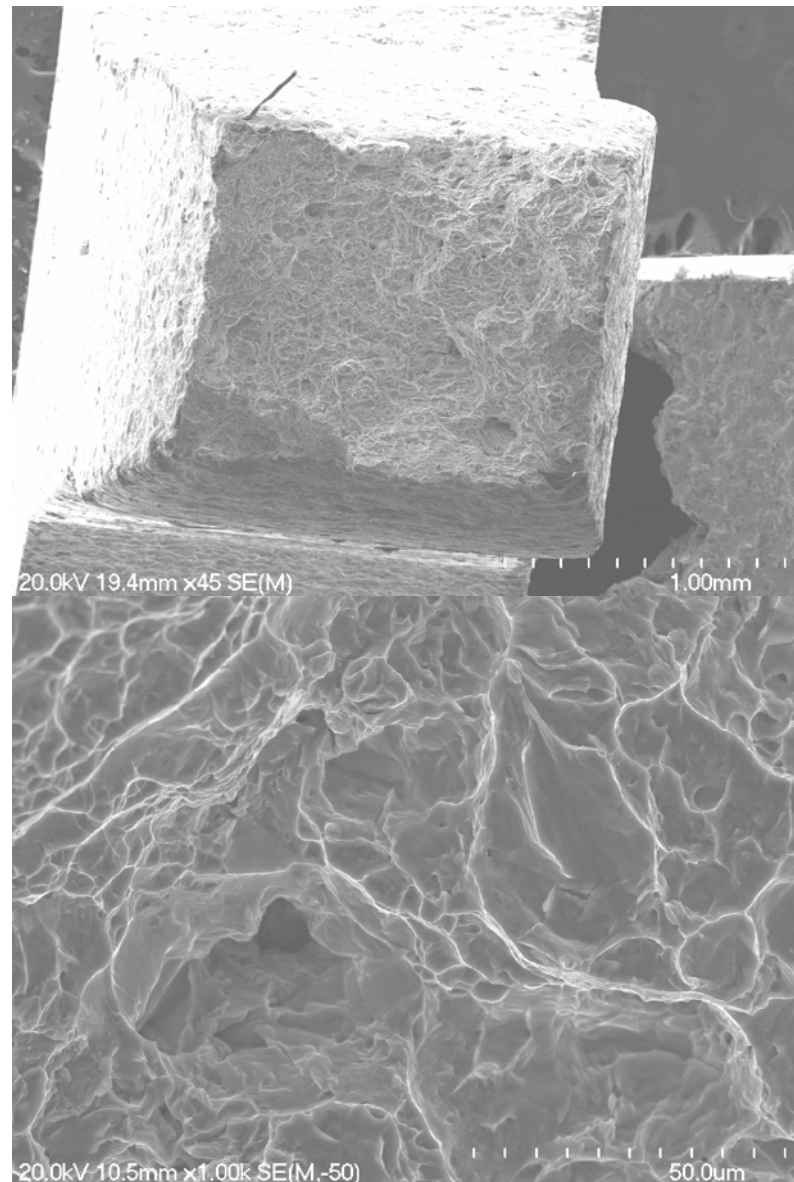
As shown in Figure 5.14(a), the fracture surfaces of forged GA Ti-6Al-4V specimens after duplex annealing showed a large number of dimples formed by ductile fracture of α lamellae with a low aspect ratio. As shown in Figure 5.14(b), the fracture surfaces of GA Ti-6Al-4V specimens after a solution and aging treatment showed fine dimples formed by fracturing of α acicular. As shown in Figure 5.14(c), the fracture surfaces of GA Ti-6Al-4V specimens, after recrystallization annealing, showed a mix of large dimples formed by the fracturing of equiaxed α grains and fine dimples formed by fracturing of fine $\alpha+\beta$ lamellar.



(a) Duplex annealing



(b) Solution and aging treatment



(c) Recrystallization annealing

Figure 5.14: Fracture surfaces of forged GA Ti-6Al-4V specimens with an oxygen content of 0.14% after different heat treatments.

5.7 Discussion

5.7.1 The effect of Heat Treatments on the Mechanical Properties of Forged HDH Ti Parts

A comparison of the mechanical properties of as-forged HDH Ti parts, an HDH Ti part after annealing and Grade 4 ingot metallurgy Ti are made in Figure 5.15.

From the figure, even though the grain growth during annealing reduced the tensile strength of a forged part by 80 MPa, the UTS and elongation to fracture of a forged HDH Ti part after an annealing treatment were both higher than those for ingot metallurgy Ti. In this study, the best elongation to fracture in a forged HDH Ti part, achieved by an annealing treatment was 25.6%, which is the same as for Grade 1 ingot metallurgy Ti. So from this study, the ductility of a forged HDH Ti part can be improved by increasing the holding time at the forging temperature or through an annealing treatment, and the property improvement can broaden the high performance applications of CP Ti.

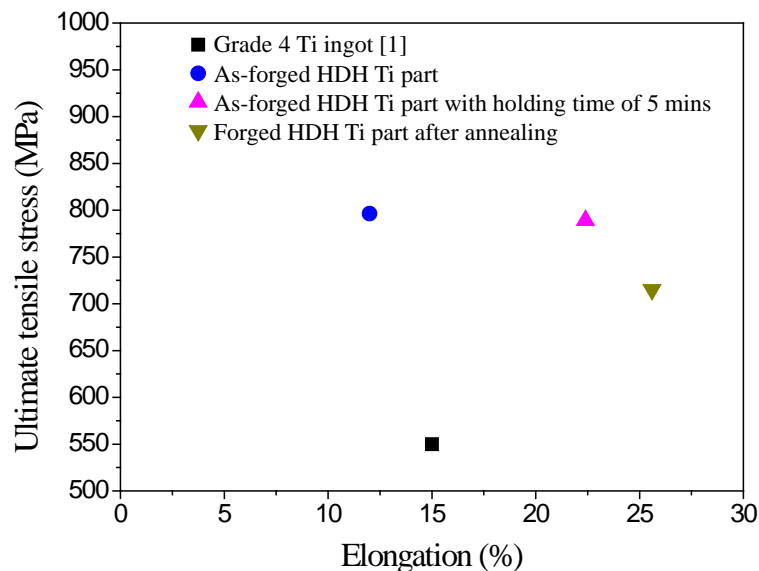


Figure 5.15: A comparison of the mechanical properties of as-forged HDH Ti parts, a forged HDH Ti part after annealing and Grade 4 ingot metallurgy Ti.

5.7.2 The Microstructural Reasons for the Effects of Different Heat Treatments on the Mechanical Properties of Forged HDH and GA Ti-6Al-4V Parts

There is a difference in the evolution of microstructure in as-forged fully consolidated HDH Ti-6Al-4V parts and GA Ti-6Al-4V parts after different heat treatments. So the effect of the microstructure in HDH Ti-6Al-4V and GA

Ti-6Al-4V parts on their mechanical properties is not the same in general.

After duplex annealing, the microstructure in an as-forged HDH Ti-6Al-4V part evolved into equiaxed grains and a small volume fraction of α lamellae due to dynamic recrystallization and a coarse α/β matrix structure. The α lamellae with a high oxygen content may reduce the ductility of an as-forged part by forming a cleavage pattern. After a solution and aging treatment, the microstructure at the centre of a forged HDH Ti-6Al-4V part consisted of equiaxed α grains with a fine acicular α . A large number of equiaxed α grains were formed by a recrystallization process during solution treatment, which enhanced the powder consolidation of a heat treated as-forged part, so its ductility is better than that of the as-forged one. On the other hand, the strength of the part is improved by a fine acicular α which formed during the aging treatment. After recrystallization annealing, the microstructure at the centre of an HDH Ti-6Al-4V part consisted of only equiaxed α grains formed by the recrystallization process, so the ductility of the part is increased significantly. This is caused by an improvement in the powder consolidation of the part and the ductile fracture of the equiaxed α grains, but its tensile strength is reduced by a coarsening of the equiaxed α grains. After beta annealing, the microstructure at the centre of the HDH Ti-6Al-4V part consisted of equiaxed α grains in a matrix of an “acicular” $\alpha+\beta$ structure, which is similar to the microstructure at the centre of the HDH Ti-6Al-4V part after duplex annealing. The ductility of the as-forged part is probably reduced by the fracturing of acicular α to form a cleavage pattern.

Due to the low interstitial element content in a GA Ti-6Al-4V part, the microstructure consists of α acicular in an α/β matrix. After duplex annealing, α acicular grow into a coarse α lamellae structure with a low aspect ratio and a low oxygen content at the centre of the part. The ductility of the part is improved by the ductile fracture of the α lamellae with a low aspect ratio. After a solution and

aging treatment, the microstructure at the centre of a GA Ti-6Al-4V part is an α acicular structure, which improves the strength. The ductility is not reduced due to the fact that the recrystallization that occurs during solution treatment enhances the powder consolidation in the as-forged part. After recrystallization annealing, the microstructure at the centre of a GA Ti-6Al-4V part consists only of equiaxed α grains formed by a recrystallization process. For the same reason, the ductility of an HDH Ti-6Al-4V part increases after recrystallization annealing.

From the microstructural evolution after heat treatment, it can be concluded that equiaxed α grains formed by recrystallization during a solution and aging treatment and recrystallization annealing can improve the ductility of HDH Ti-6Al-4V parts, whereas an α lamellae structure plays a negative role in influencing its ductility. On the other hand, the effect of duplex annealing, a solution and aging treatment and recrystallization annealing on the microstructure and mechanical properties of GA Ti-6Al-4V parts, with low oxygen content, is the same as the effects of these heat treatments on the microstructure and mechanical properties of ingot metallurgy wrought Ti-6Al-4V parts, with the same oxygen level [2].

5.7.3 The Role of Oxygen Content on the Effect of Heat Treatment

As oxygen is an α stabilizer, which increases the α transus temperature. The oxygen content in an HDH Ti-6Al-4V part (0.52%) is much higher than that in a GA Ti-6Al-4V part (0.14%), so when HDH and GA Ti-6Al-4V powder compacts are forged at 1350 °C, which is in the β phase field, the α phase precipitates earlier from the β phase in an HDH Ti-6Al-4V part compared with a GA Ti-6Al-4V part. By comparing the microstructure of as-forged HDH Ti-6Al-4V and GA Ti-6Al-4V parts, we can see that the sizes of α lamellae formed in an HDH Ti-6Al-4V part are much larger than those in a GA Ti-6Al-4V part. During duplex annealing, the coarse α lamellae partially evolves into equiaxed α grains in an

HDH Ti-6Al-4V part, while an acicular α structure in a GA Ti-6Al-4V part becomes wider to form small α lamellae with a low aspect ratio. Also after a solution and aging treatment, the equiaxed α grains in the microstructure of an HDH Ti-6Al-4V part may be caused by its higher oxygen content, which is not shown in the microstructure of a GA Ti-6Al-4V part. The effect of oxygen on the microstructure of a forged Ti-6Al-4V part is more obvious after recrystallization annealing. As a result, the equiaxed α grains in an HDH Ti-6Al-4V part were larger than in a GA Ti-6Al-4V part due to its higher oxygen content. So oxygen content changes the microstructure of a forged Ti-6Al-4V part after duplex annealing and a solution and aging treatment, while after recrystallization annealing, the oxygen content only affects the size of the equiaxed α grains, as it increases the α transus temperature.

On the other hand, with a higher oxygen content the tensile strength of a forged HDH Ti-6Al-4V part was higher than in a forged GA Ti-6Al-4V part under each of the heat treatment conditions used in this study. This is in agreement with the statement in Ref. [1]. However, with an increase in tensile strength caused by a higher oxygen content, the ductility decreases. From the respective mechanical properties of forged HDH and GA Ti-6Al-4V parts after a solution and aging treatment and recrystallization annealing, the ductility of such a heat treated HDH Ti-6Al-4V part is close to or higher than that of a forged GA Ti-6Al-4V part. This means that the oxygen content plays a much less significant role in controlling the ductility of a Ti-6Al-4V part after a solution and aging treatment and recrystallization annealing. Therefore, Ti-6Al-4V parts with a high oxygen content of up to ~0.5% produced by powder compact forging can be used for industrial applications after a solution and aging treatment or recrystallization annealing. This offers an opportunity for the wider application of Ti-6Al-4V parts with high oxygen content, due to their excellent mechanical properties.

5.7.4 The effect of Heat Treatment on the Mechanical Properties of Forged HDH and GA Ti-6Al-4V Parts

The mechanical properties of forged GA and HDH Ti-6Al-4V parts under different heat treatments in this study are summarized in Figure 5.16. The mechanical properties of ingot metallurgy Ti-6Al-4V and forged GA Ti-6Al-4V parts, shown in the figure 5.16 indicate an improvement in the ductility of these materials after duplex annealing. However, the ductility of forged HDH Ti-6Al-4V parts is reduced by duplex annealing. After a solution and aging treatment, the tensile strength of wrought Ti-6Al-4V parts increases with a decrease in ductility, whereas the tensile strengths of forged GA and HDH Ti-6Al-4V parts are improved, without sacrificing ductility, by solution and aging treatment. This may be caused by further powder consolidation by recrystallization during the solution heat treatment. After recrystallization annealing, the ductility of forged GA and HDH Ti-6Al-4V parts were both improved at the expense of their tensile strength; which agrees with the general effect of recrystallization annealing on the mechanical properties of wrought alloys. In general, the tensile strength of as-forged GA Ti-6Al-4V parts is slightly higher than that of heat treated wrought parts, and their ductility is slightly lower, but once the forged GA Ti-6Al-4V parts are heat treated, the mechanical properties are very close to those of wrought parts under the same heat treatment conditions and with the same oxygen level. This suggests that the metallurgical quality of the GA Ti-6Al-4V alloy parts produced by powder compact forging is the same as or very similar to that of corresponding wrought alloy parts. In contrast to this, the tensile strength of powder compact forged and heat treated HDH Ti-6Al-4V parts are about 250 MPa higher than those of the corresponding wrought parts under the same heat treatment conditions, and their ductility is much lower than that of the wrought alloy parts. The reason for this is that the powder compact forged HDH Ti-6Al-4V alloy parts have a much higher oxygen content (0.5%) compared with the wrought alloy parts (<0.15wt%)..

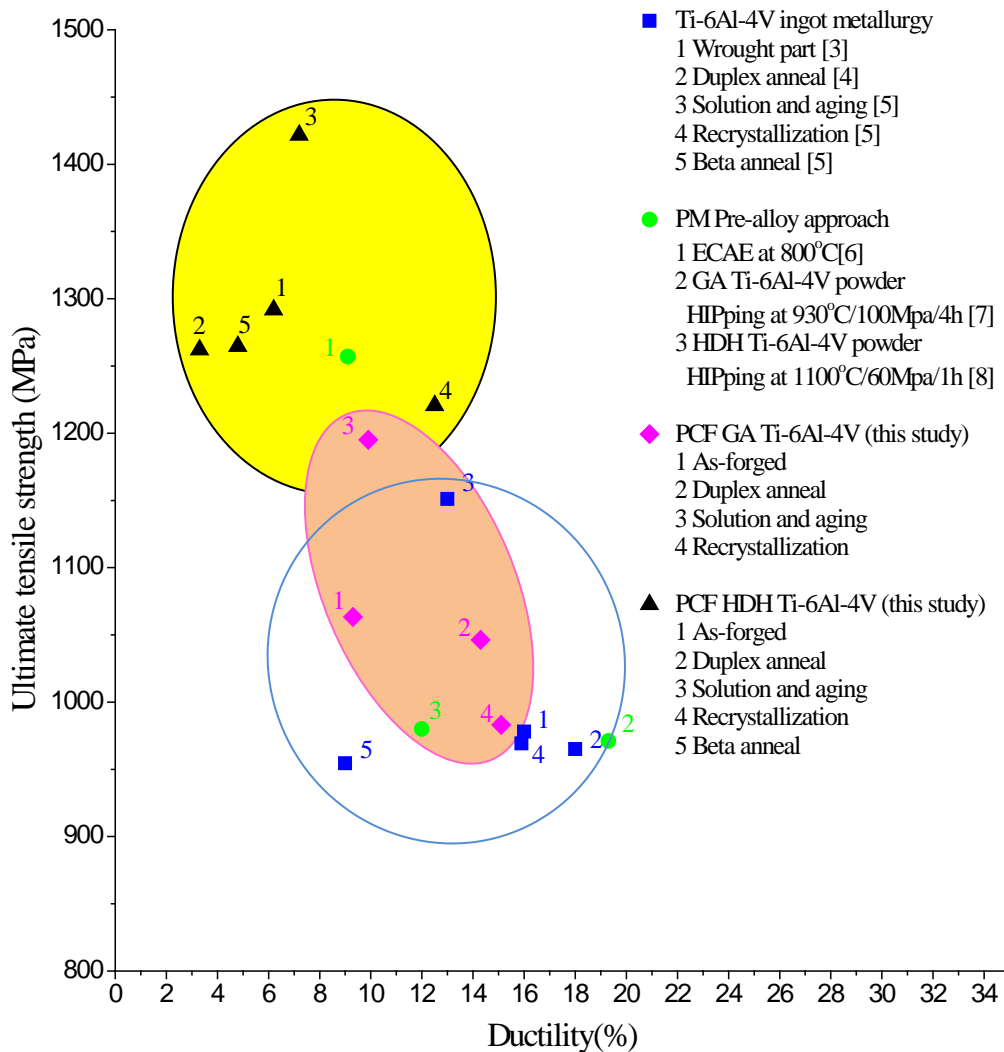


Figure 5.16: A comparison of the mechanical properties of as-forged HDH and GA Ti-6Al-4V parts made under different conditions compared with ingot metallurgy and the other pre-alloyed approaches.

As shown in Figure 5.16, the tensile strength of forged GA Ti-6Al-4V parts, after different heat treatments, is higher than that for Ti-6Al-4V parts made using other pre-alloyed approaches, except for the one made using equal channel angular extrusion. After duplex or recrystallization annealing, forged GA Ti-6Al-4V parts have a ductility close to that of the alloy shown in Ref. [7, 8]. Ti-6Al-4V parts produced by equal channel angular extrusion, using pre-alloyed powder, have a higher tensile strength and lower ductility than in those parts made using other

pre-alloyed approaches, as shown in Figure 5.16. The forged and heat treated HDH Ti-6Al-4V parts with a high oxygen content and made using pre-alloyed powder, can have at least the same mechanical properties as those parts produced by the severe deformation in equal channel angular extrusion. After recrystallization annealing, forged HDH Ti-6Al-4V parts have better ductility than those made using equal channel angular extrusion without too much of a decrease in tensile strength, while after a solution and aging treatment, forged HDH Ti-6Al-4V parts have the highest tensile strength (UTS=1421.7 MPa and YS = 1352.4 MPa) with an elongation to fracture of 7.2%, of the various alloy processing conditions shown in Figure 5.16. Its strength is improved by the formation of acicular α precipitates during the solution and aging treatment, while its ductility is improved by the formation of equiaxed α grains. Due to this bimodal microstructure, the tensile properties of forged HDH Ti-6Al-4V parts are modified by a solution and aging treatment. In summary, powder compact forging used in this study is a promising fast consolidation process for the manufacture of near-net shaped Ti and Ti-6Al-4V parts. The energy consumption during the sintering stage and the cost of manufacturing Ti and Ti-6Al-4V parts [9, 10], which limits the wider application of Ti powder metallurgy, are both decreased significantly.

5.7.5 Effect of Recrystallization on Powder Consolidation

As discussed in Chapter 4, even though full density in as-forged parts was obtained, the consolidation of the part was not complete due to the weak particle bonding, especially in the as-forged GA Ti-6Al-4V parts. This study shows that after recrystallization annealing and a solution and aging treatment, the ductility of both forged GA and HDH Ti-6Al-4V parts is improved, as shown in Figure 5.16. The recrystallization occurring during such heat treatments may enhance the degree of powder consolidation and this can be explained as follows. As shown schematically in Figure 5.17, during the recrystallization process, new grains may nucleate at the particle boundaries and grow into both particles on either sides of

the particle boundary. In this way, the weak bonding between the two particles and any interparticle boundary cavities are eliminated, leading to an improvement in the level of powder consolidation.

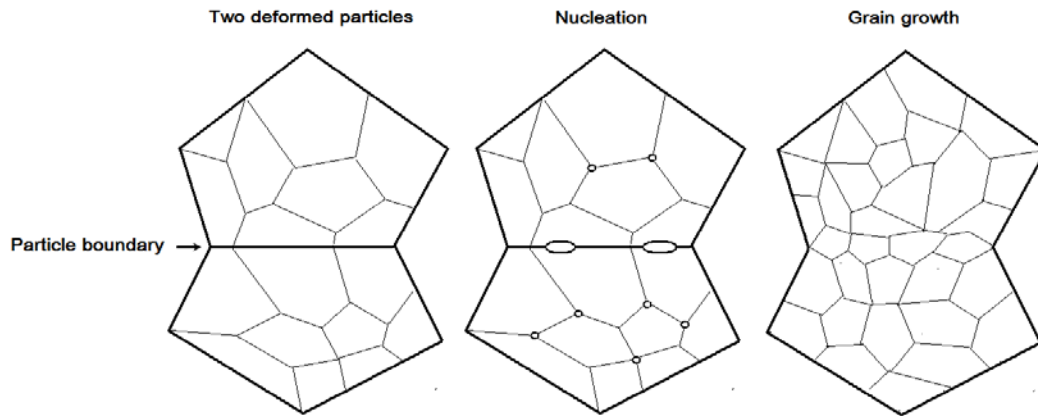


Figure 5.17: Schematic diagrams showing recrystallization at a particle boundary.

5.8 Summary

- This study shows that the ductility of forged HDH Ti parts is improved significantly after an annealing treatment due to stress relief accompanied by a coarsening of α grains.
- The oxygen content of the forged Ti-6Al-4V parts controls the microstructural evolution during heat treatment and affects their mechanical properties. As a result of this effect, the ductility of forged HDH Ti-6Al-4V parts is improved by the formation of equiaxed α grains during solution treatment and recrystallization annealing. One of the reasons for this beneficial effect might be an improvement in powder consolidation through the enhancement of particle bonding by recrystallization.

5.9 Reference

1. Rodney Boyer, G.W., E. W. Collings, *Materials Properties Handbook:*

- Titanium Alloys*. 1994: ASM International.
2. Weiss, I., R. Srinivasan, P.J. Bania, D. Eylon, S.L. Semiatin, *Advances in the Science and Technology of Titanium Alloy Processing*. 1996, California: The Minerals, Metals & Materials Society.
 3. Froes, F.H. and D. Eylon, *Titanium net shape technologies*. Los Angeles, 1984: p. 1984.
 4. Matthew J. Donachie, J., *Titanium: A Technical Guide*. 1988: ASM INTERNATIONAL.
 5. Ivasishin, O. *Cost-effective manufacturing of titanium parts with powder metallurgy approach*. 2005.
 6. Yapici, G., et al., *Microstructure and mechanical properties of severely deformed powder processed Ti-6Al-4V using equal channel angular extrusion*. Scripta materialia, 2003. **49**(10): p. 1021-1027.
 7. Zhang, K., et al., *Effect of hot-isostatic-pressing parameters on the microstructure and properties of powder Ti-6Al-4V hot-isostatically-pressed samples*. Metallurgical and Materials Transactions A, 2010. **41**(4): p. 1033-1045.
 8. Bozic, D., et al., *Influence of retained hydride particles and microstructure on mechanical properties of PM produced Ti-6Al-4V alloy*. Powder Metallurgy, 2011. **54**(1): p. 40-45.
 9. Froes, F., et al., *The technologies of titanium powder metallurgy*. JOM, 2004. **56**(11): p. 46-48.
 10. Martinez, A.M., et al., *New method for low-cost titanium production*. Key Engineering Materials, 2010. **436**: p. 41-53.

Chapter 6: Powder Compact Forging of Blended and Mechanically Alloyed Ti-6Al-4V Powders

6.1 Introduction

The microstructures and mechanical properties for Ti-6Al-4V rocker arms, produced by powder compact forging of pre-alloyed HDH and GA Ti-6Al-4V alloy powders after forging and various heat treatments, were studied in the previous chapters. In order to reduce the cost of raw Ti-6Al-4V powder, a blended elemental (BE) approach was used to produce Ti-6Al-4V rocker arms from a mixture of HDH Ti and Al-40wt%V master alloy powders. To achieve compositional homogenisation through diffusion during powder compact heating and forging, the holding time at the forging temperature (1350 °C) was increased from 0 to 10 minutes. As an alternative approach, the mixture of Ti and Al-40wt%V master alloy powders was mechanically alloyed (MA) by high energy mechanical milling (HEMM), and the MA Ti-6Al-4V powder was used as the starting powder to improve the composition homogenisation. Additionally to investigate the effect of the oxygen content of the Ti powder on the mechanical properties and microstructure of as-forged parts, made using MA Ti-6Al-4V powder, both HDH and GA Ti powders were used in this study.

6.2 Powder Compact Forging of Blend Elemental (BE) Ti-6Al-4V Powder

6.2.1 Blending of Powders

It is essential to check the compositional homogeneity of the BE Ti-6Al-4V powder produced by from HDH Ti and Al-40wt%V master alloy powders. To do this, cross sections of the powder particles were observed by optical microscope as shown in Figure 6.1. There was no agglomeration of the Al-V master alloy powder particles (bright particles in the figure), and they were generally

homogeneously distributed among the powder particles. This proves that the Ti and Al-V master alloy powder particles were blended well in producing the BE Ti-6Al-4V powder. The compositional homogeneity of the BE powder was also checked by comparing XRD patterns of three random samples of the BE powder as shown in Figure 6.2. There is no difference in the three XRD patterns, suggesting that the HDH Ti and Al-V master alloy powder particles were sufficiently blended.

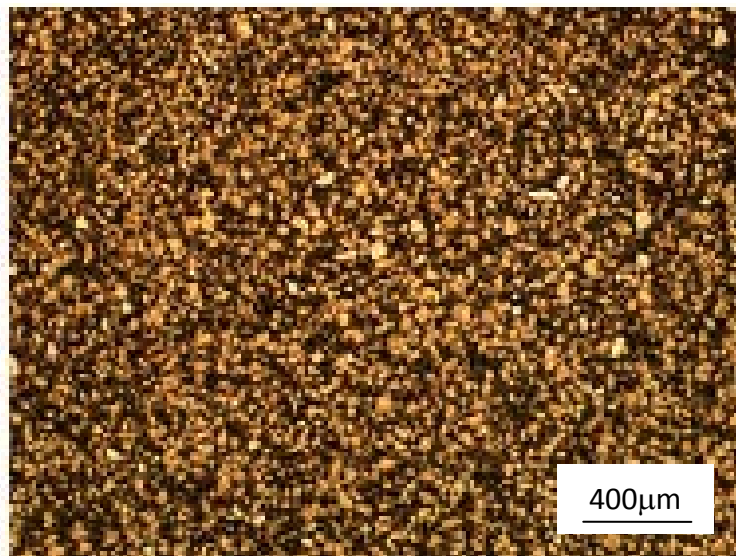


Figure 6.1: Optical microscopy image of a cross section of blended HDH Ti and Al-V master alloy powder particles.

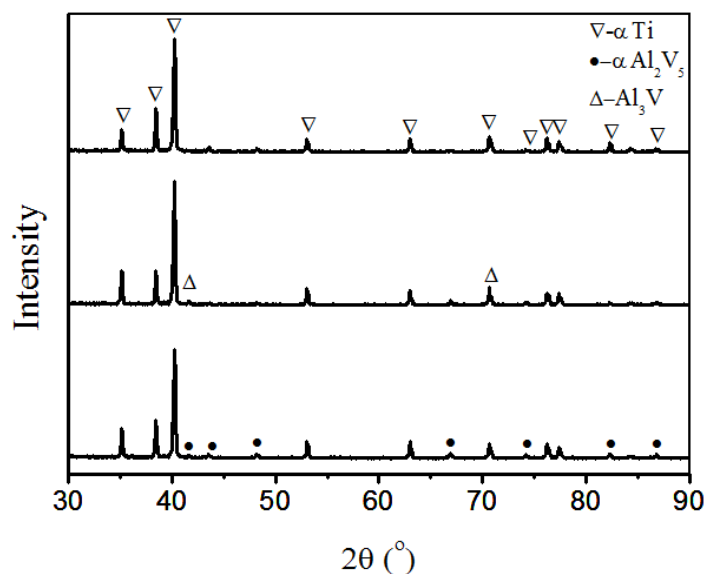


Figure 6.2: XRD patterns of three random batches of the powder mixture.

A DTA heating curve of the BE Ti-6Al-4V powder, is shown in Figure 6.3, together with the baseline curve. This shows a broad peak in the temperature range of 950 to 1150 °C, indicating that Al and V atoms diffuse into the Ti phase during heating to temperatures above 950 °C.

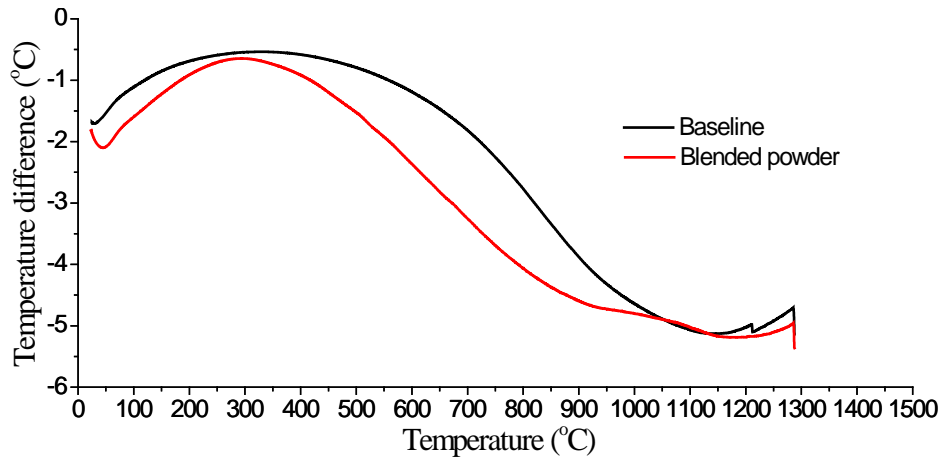


Figure 6.3: DTA heating curve of BE Ti-6Al-4V powder.

6.2.2 Phase Constituent and Element Distribution of As-forged BE Ti-6Al-4V Parts

Figure 6.4 shows a rocker arm produced by powder compact forging (PCF) of BE Ti-6Al-4V powder without any holding time at the forging temperature. There are still cold-shuts on the surface of the part, the same as those on the surface of an as-forged HDH Ti-6Al-4V part.



Figure 6.4: A rocker arm produced by PCF of BE Ti-6Al-4V powder without holding at the forging temperature.

An XRD pattern of the powder mixture, in Figure 6.5 shows Ti, α -Al₂V₅ and Al₃V peaks which are from the master alloy powder particles. An XRD pattern of the sample produced by PCF, without any holding time, shows only α -Ti peaks, suggesting that dissolution of the Al-V master alloy powder particles occurred during powder heating and forging. The amount of the β phase in the as-forged samples increased to an XRD-detectable level with increasing holding time to 5 or 10 minutes, as shown in Figure 6.5. The presence of the β -Ti phase in the forged parts suggests that more V atoms have diffused into the Ti phase during holding at 1350 °C, and assisted the stabilisation of some of the β phase during cooling after forging.

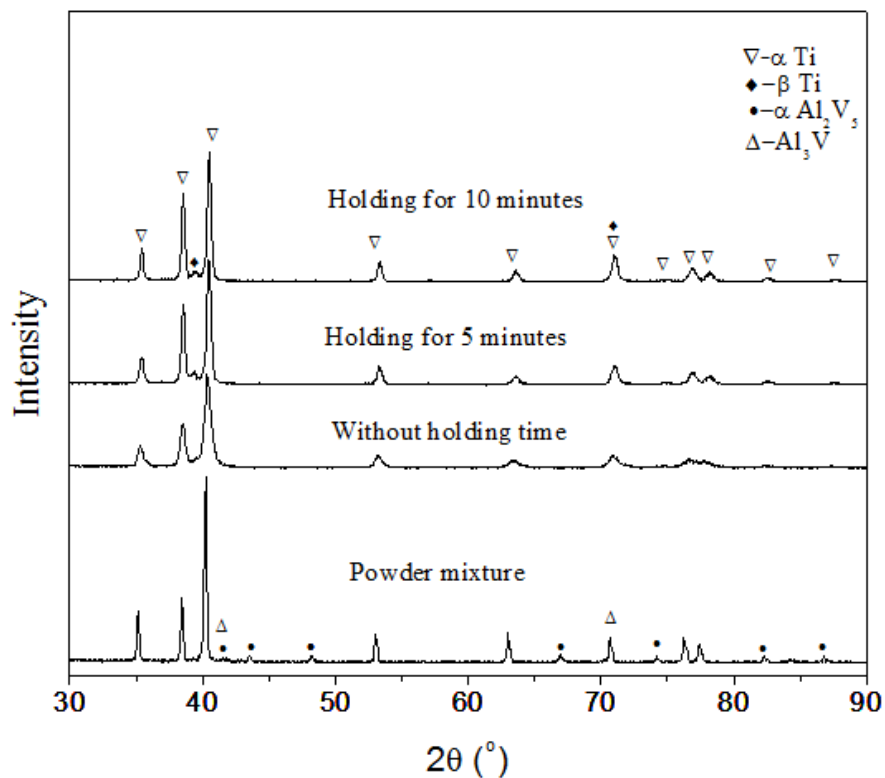


Figure 6.5: XRD patterns of a Ti-6Al-4V BE powder mixture and as-forged parts produced using PCF.

EDS elemental mapping showed Al and V rich regions in the sample produced by PCF without a holding time (Figure 6.6(a)). This means that the Al-V master alloy

powder particles were not completely dissolved during heating and forging, but Al was distributed more homogeneously than V. This is due to the fact that the diffusivity of Al in Ti is much higher than that of V at the same temperature [1], as reflected by the much lower melting point of Al than that of V. With increased holding time, to 5 minutes, at the forging temperature, EDS elemental mapping showed a more homogeneous Al distribution throughout the sample, while there were still V rich and Ti lean regions, as shown in Figure 6.6(b). The sizes of the V rich regions became much smaller with increasing holding time to 5 minutes. When the holding time was further increased to 10 minutes, EDS elemental mapping showed that the sample produced by PCF had uniform Al, Ti and V distributions, as shown in Figure 6.6(c). EDS line scanning showed that the distribution of V in the samples produced by PCF without a holding time and with a 5 minutes holding time were non-homogeneous, and became homogeneous when the holding time was increased to 10 minutes. The distribution of Al was non-homogeneous without a holding time, but became homogeneous with a 5 minute holding time. To get detailed information about the effect of holding time on elemental distribution, EDS point analysis was conducted at random points on the cross section of each of the samples, as shown in Figure 6.8. The compositions at all of the points shown in the figure were semi-quantitatively determined using the EDS point analysis, and listed in Table 6.1. The sample produced without a holding time had Al and V rich regions with a composition of Ti-63.28wt% V-11.69wt% Al (point 5 in Figure 6.8(a)), which is far away from the nominal composition of the alloy of Ti-6wt% Al-4wt% V. When the holding time was increased to 5 minutes, V rich regions with a V content of up to 52.16wt% could still be found (point 3 in Figure 6.8(b)), but there was no large difference in the Al content among the four EDS analysis points shown in Table 6.1. Finally in the sample with a 10 minutes holding time, the V rich regions also disappeared, since there were no large differences in Al, Ti and V contents among the EDS analysis points shown in Table 6.1. This confirms that a homogeneous

composition distribution in the as-forged parts can be achieved by PCF of a powder mixture with a holding time of 10 minutes at a forging temperature of 1350 °C.

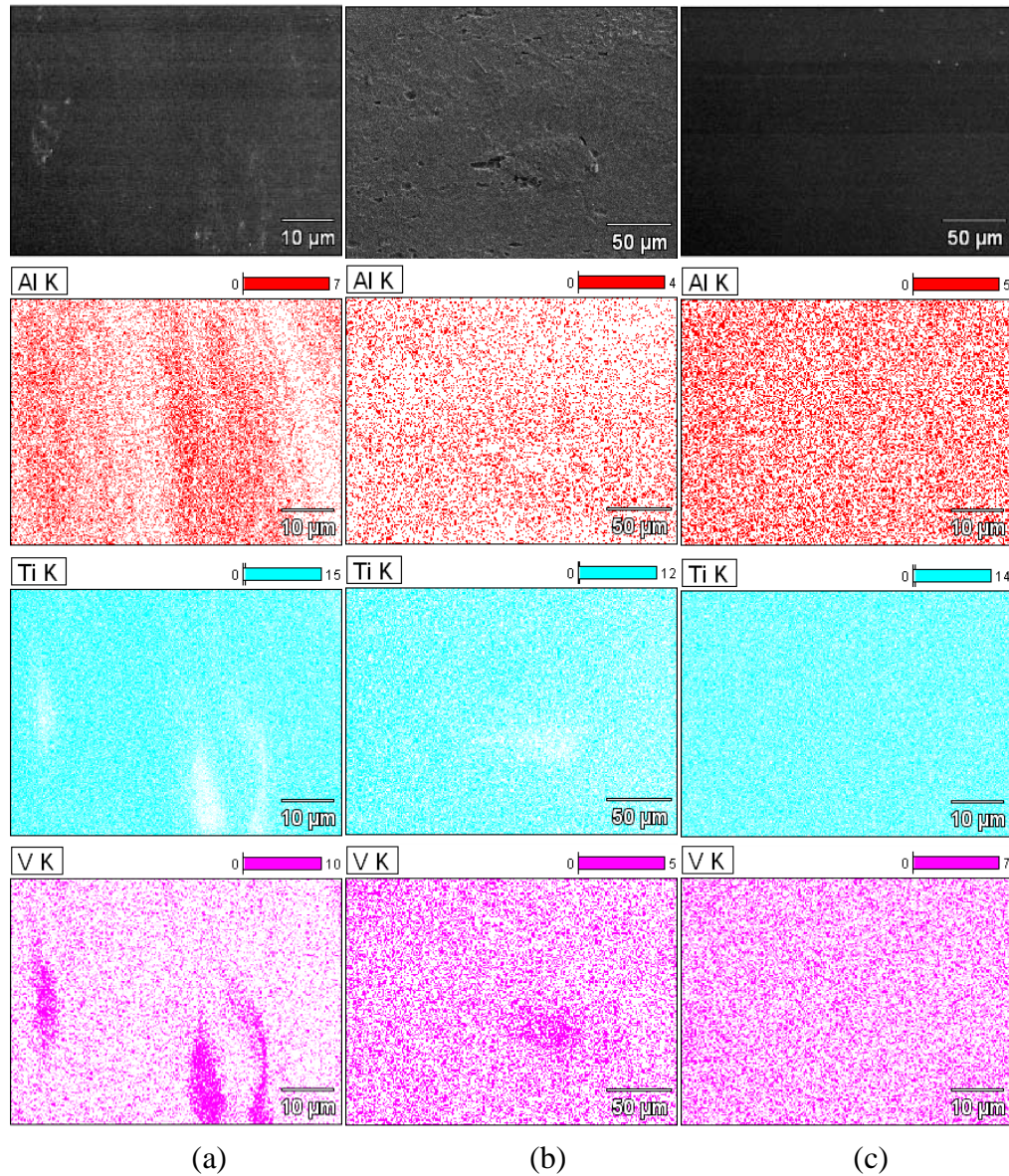
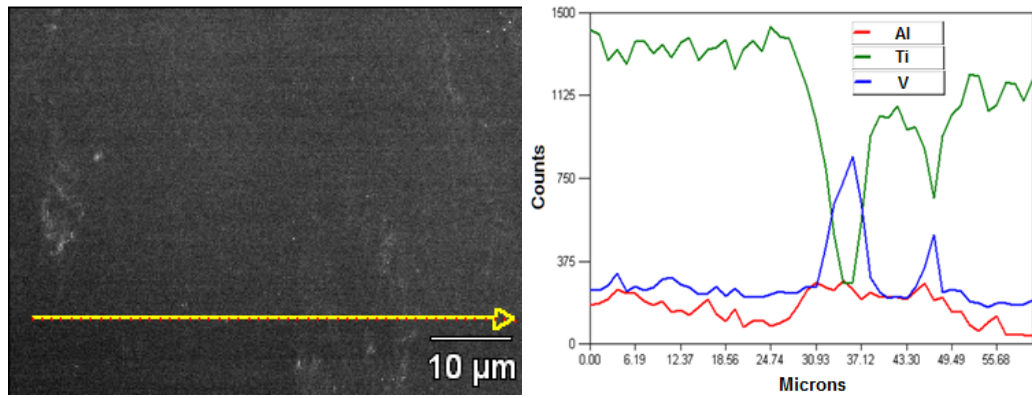
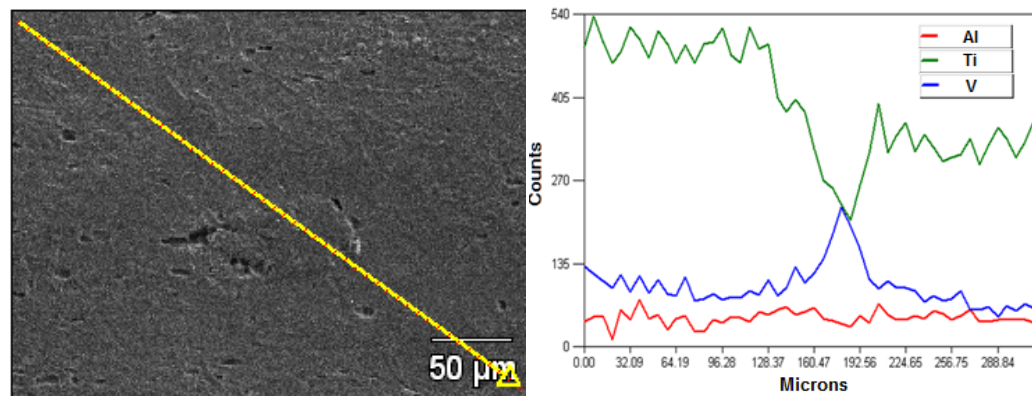


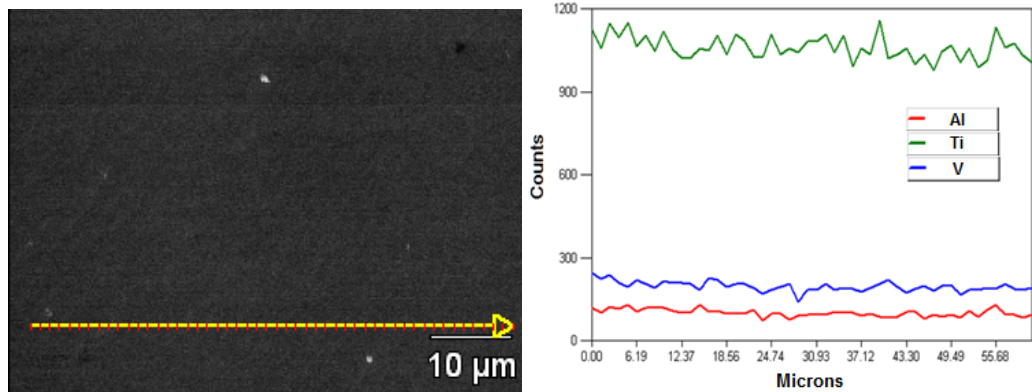
Figure 6.6: SEM images and EDS elemental mappings of cross sections of as-forged BE Ti-6Al-4V parts with different holding times at 1350 °C: (a) without holding; (b) holding time: 5 minutes; (c) holding time: 10 minutes.



(a) Without holding



(b) Holding time of 5 minutes



(c) Holding time of 10 minutes

Figure 6.7: SEM images and the results of an EDS line scan on cross sections of the as-forged BE Ti-6Al-4V parts.

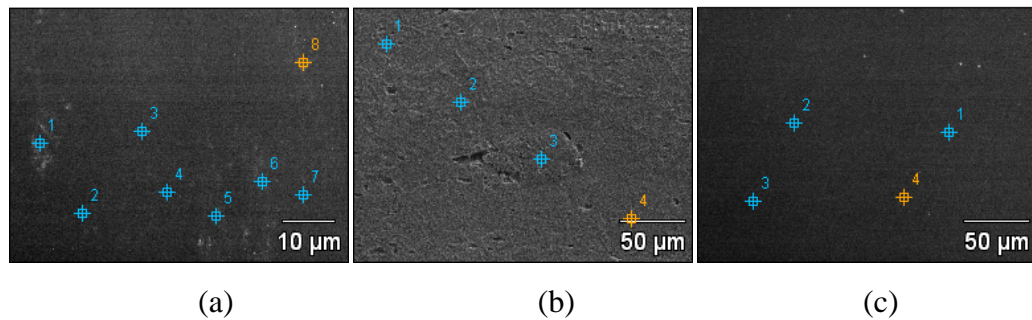


Figure 6.8: Points selected for EDS analysis on the cross sections of as-forged BE Ti-6Al-4V parts made by PCF with different holding times: (a) with no holding time; (b) holding time of 5 minutes; (c) holding time of 10 minutes.

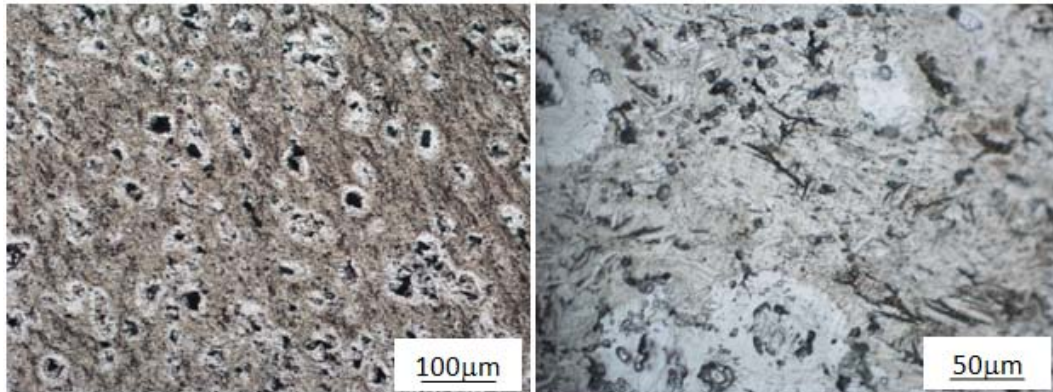
Table 6.1: Results of EDS point analysis at the points shown in Figure 6.8.

Samples (in Figure 6.8)	Point No.	Al (wt%)	Ti (wt%)	V (wt%)
(a)	1	6.88	33.11	60.01
	2	6.80	86.16	7.04
	3	2.39	95.44	2.17
	4	3.43	94.98	1.59
	5	11.69	25.03	63.28
	6	12.37	59.58	28.04
	7	3.12	95.89	0.99
	8	1.87	96.84	1.30
(b)	1	5.45	88.98	5.58
	2	4.39	92.31	3.29
	3	4.61	43.23	52.16
	4	7.87	86.66	5.48
(c)	1	4.44	91.54	4.02
	2	4.02	92.03	3.94
	3	3.99	93.06	2.95
	4	4.56	92.22	3.22

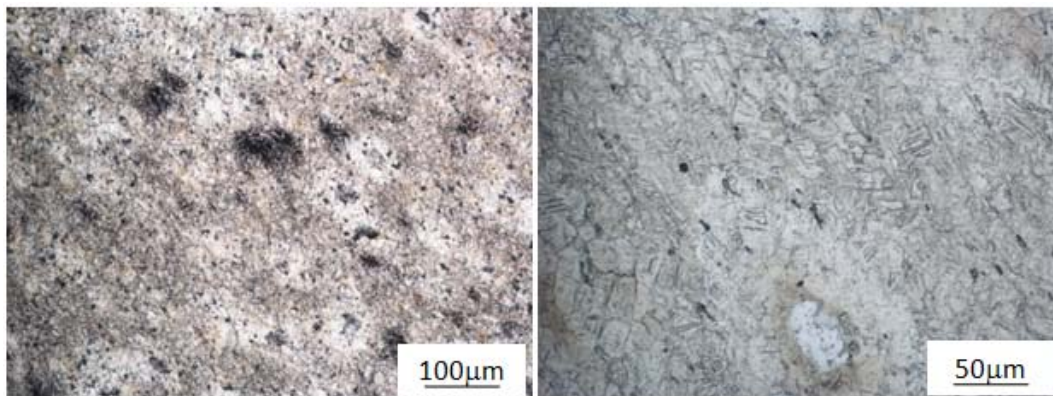
6.2.3 Microstructure of As-forged BE Ti-6Al-4V Parts

From optical microscopy images (Figure 6.9) a forged BE powder compact, with no holding time prior to forging, contained a large number of Al-40wt%V master alloy particles, with sizes in the range of 25 to 50 μm , and residual pores with sizes in the range of 1 to 10 μm . When the holding time was increased to 5 minutes, the Al-40wt%V master alloy particles and pores became smaller or disappeared as shown in Figure 6.9(b). When the holding time was further

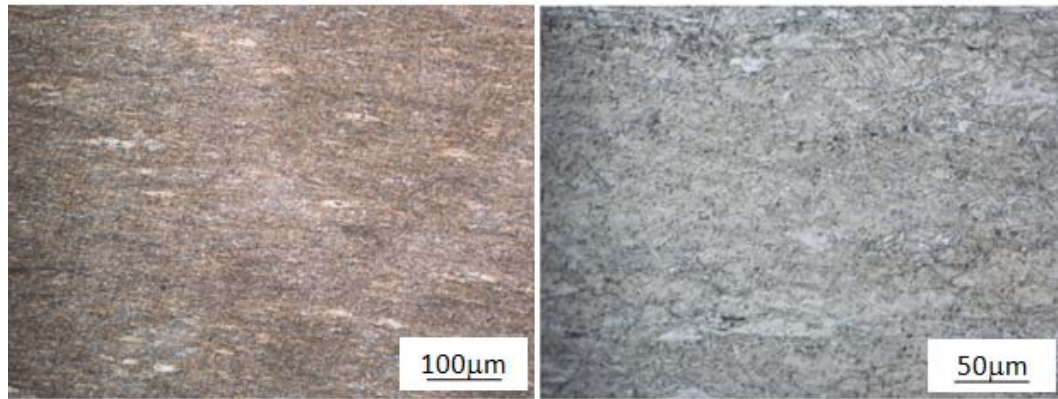
increased to 10 minutes, an uniform α/β lamellar structure formed in the as-forged part, as shown in Figure 6.9(c), and the master alloy particles and pores disappeared. This suggests that the consolidation of BE Ti-6Al-4V powder can be accomplished by forging the powder compact at 1350 °C after holding for 10 minutes.



(a) Without holding



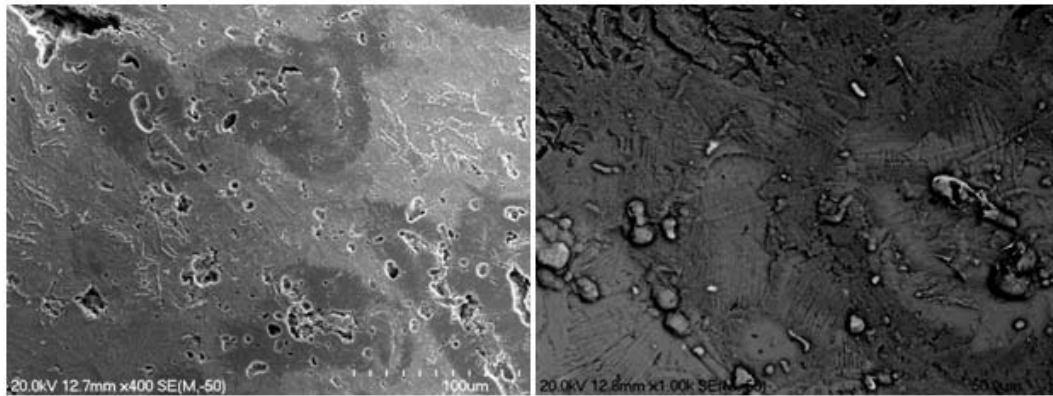
(b) Holding time of 5 minutes



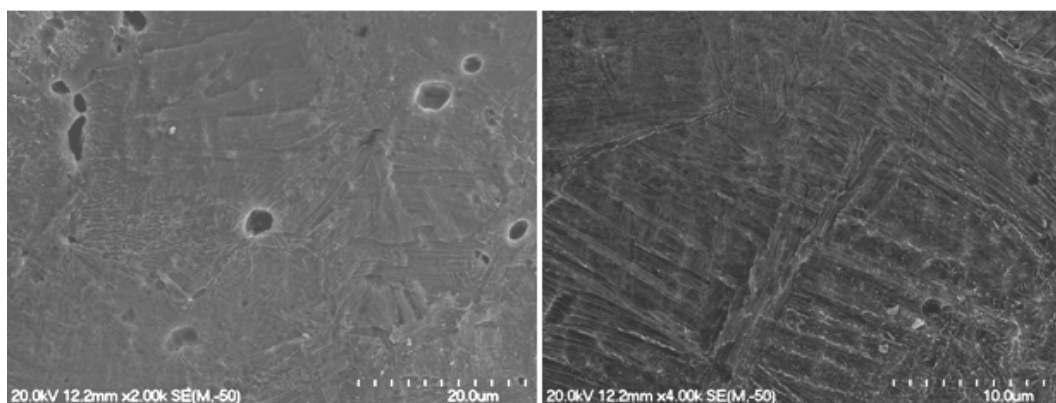
(c) Holding time of 10 minutes

Figure 6.9: Microstructure of as-forged parts made by PCF of BE Ti-6Al-4V powder with different holding times at 1350 °C.

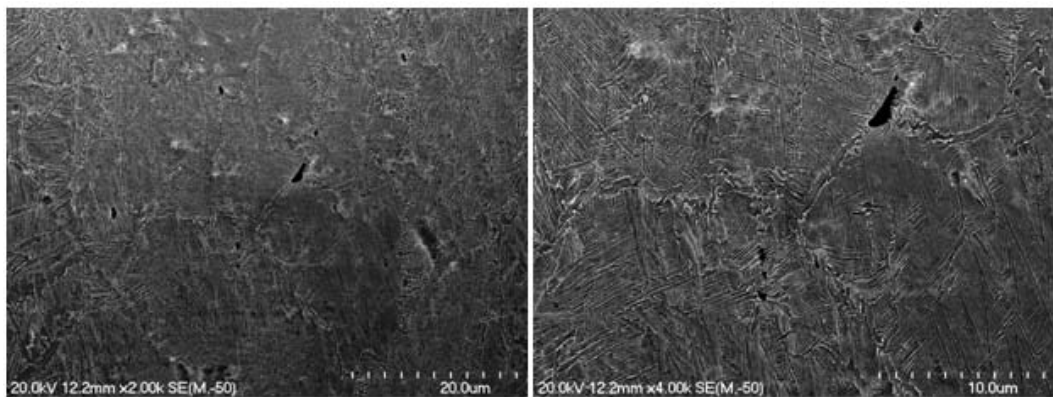
The microstructures of the samples made by forging BE powder compacts after different holding times were examined by SEM. As shown in Figure 6.10(a), the undissolved Al-V master alloy powder particles in a Ti rich matrix were visible in the microstructure of a part made without any holding time, and a lamellar structure formed around the undissolved Al-V master alloy powder particles. When the holding time was increased to 5 minutes, more regions of lamellar structure were observed in the microstructure, as shown in Figure 6.10(b), but the lamellar structure could not be seen clearly in some regions in the microstructure, indicating a non-uniform microstructure. Some primary α plates were also observed at the grain boundaries in the regions with a fine α/β lamellar structure, as shown in Figure 6.10(b). The microstructure of the sample made with a holding time of 10 minutes showed a homogeneous α/β lamellar structure, as shown in Figure 6.10(c).



(a) Without holding



(b) Holding time of 5 minutes



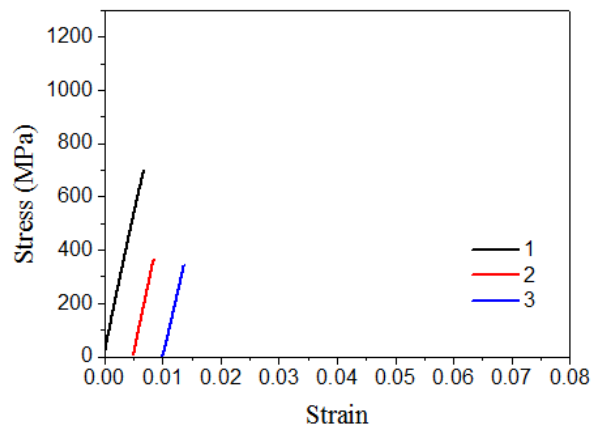
(c) Holding time of 10 minutes

Figure 6.10: SEM images of the microstructure in as-forged parts made by PCF of BE Ti-6Al-4V powder with different holding times.

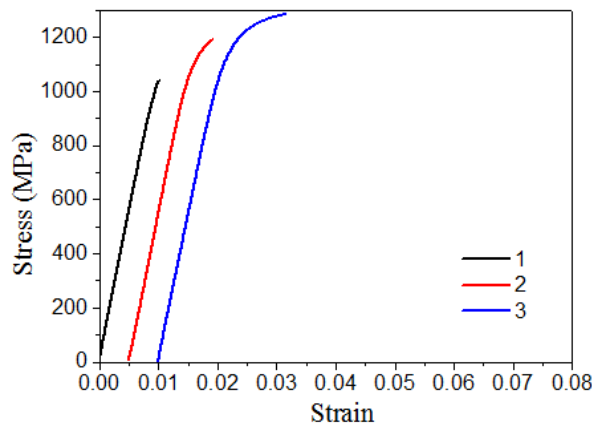
6.2.4 Mechanical Properties of an As-forged BE Ti-6Al-4V Part

The engineering stress-engineering strain curves of the tensile test specimens cut

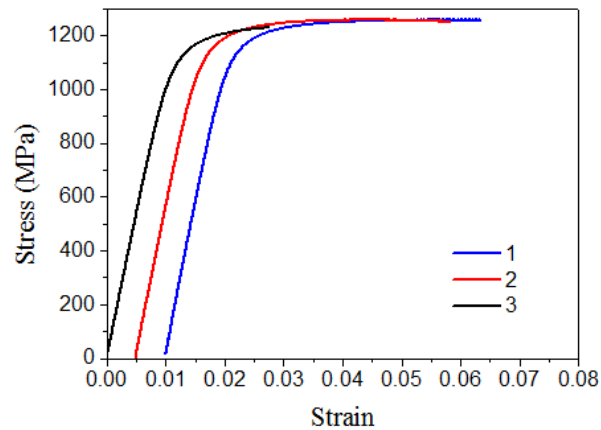
from as-forged samples are shown in Figure 6.11. The sample produced by forging without any holding time was brittle, but the samples became stronger and more ductile with increasing holding time. As shown in Table 6.2, the average yield strength, ultimate tensile strength (UTS) and elongation to fracture with a holding time of 10 minutes before forging are 1131.8 MPa, 1248.4 MPa and 3.4%, respectively. This clearly shows that with a mixture of Ti and Al-V master alloy powders as starting materials, holding the powder compact at 1350 °C for sufficient time to allow full dissolution of the Al-V master alloy powder particles and their homogenisation is essential to ensure that the consolidated Ti-6Al-4V alloy has good strength and ductility. It appears that the required holding time is 5-10 minutes.



(a) Without holding



(b) Holding time of 5 minutes



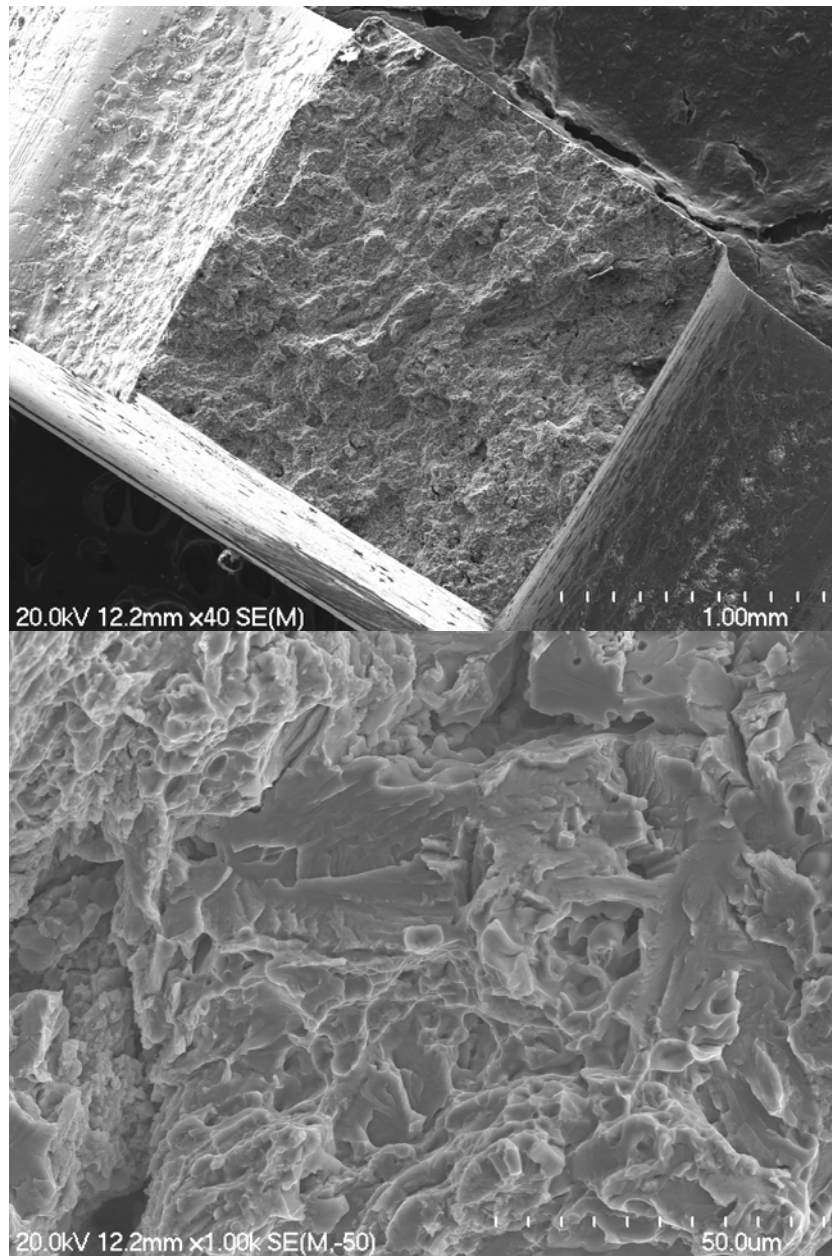
(c) Holding time of 10 minutes

Figure 6.11: Engineering stress-strain curves for specimens cut from forged compacts after different pre-forging holding times at 1350 °C.

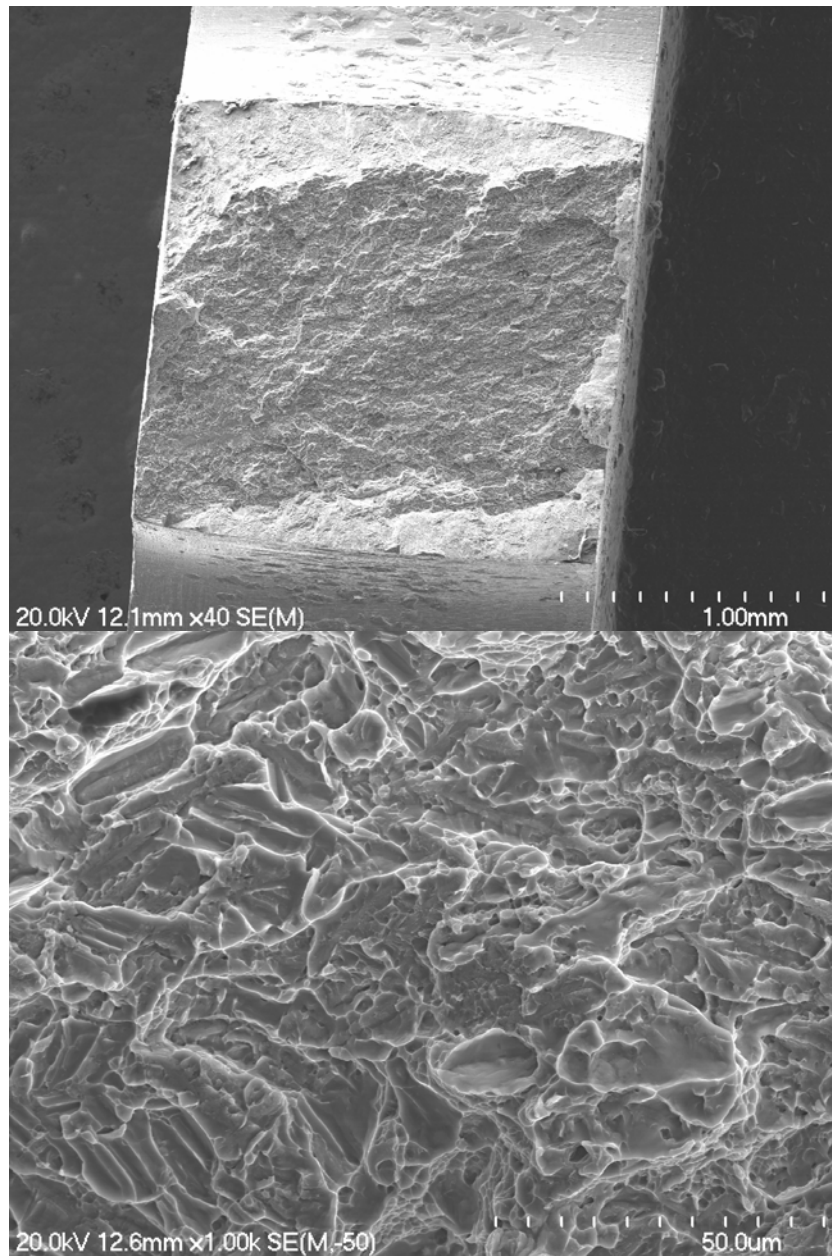
Table 6.2: Mechanical properties for specimens cut from forged compacts after a pre-forging holding time of 10 minutes at 1350 °C.

Specimen	YS(MPa)	UTS(MPa)	Elongation
1	1118.3	1228.8	1.7%
2	1139.0	1258.5	4.3%
3	1138.1	1257.9	4.3%
Average	1131.8	1248.4	3.4%

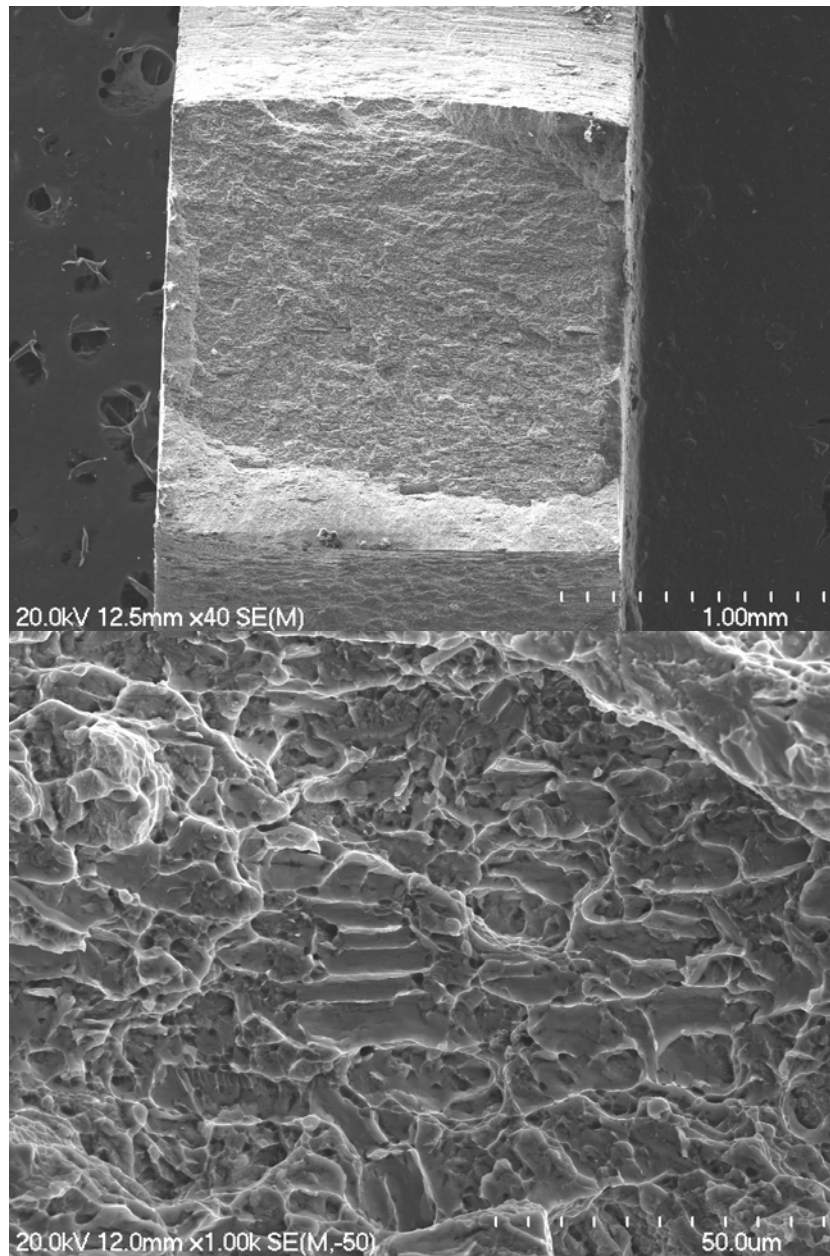
As shown in Figure 6.12(a), the fracture surfaces of tensile test specimens forged without a pre-forging holding time had a lot of flattened, smooth regions which are characteristic of brittle fracture. At low magnification, the SEM images showed that the fracture surfaces were rough (Figure 6.12(a)). This shows that debonding between the undissolved master alloy powder particles and the surrounding Ti powder particles may be the primary cause of fracture before plastic yielding. With increasing holding time at 1350 °C to 5 minutes, it was hard to find any flattened smooth regions on the fracture surfaces at high magnification, as shown in Figure 6.12(b), so the fracture mode of this specimen is probably transgranular fracture. When the holding time at 1350 °C was further increased to 10 minutes, the fracture surfaces of the tensile test specimens showed that the fracture mode was transgranular fracture.



(a) Without any holding time



(b) Holding time of 5 minutes



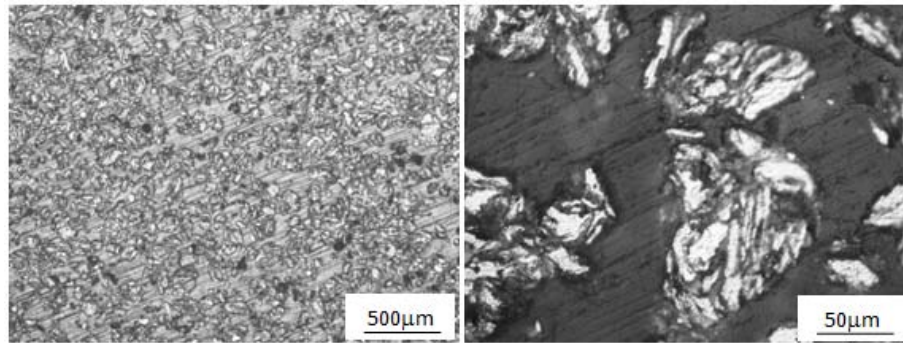
(c) Holding time of 10 minutes

Figure 6.12: Fracture surfaces of the tensile test specimens cut from samples produced by forging after different holding times at 1350 °C.

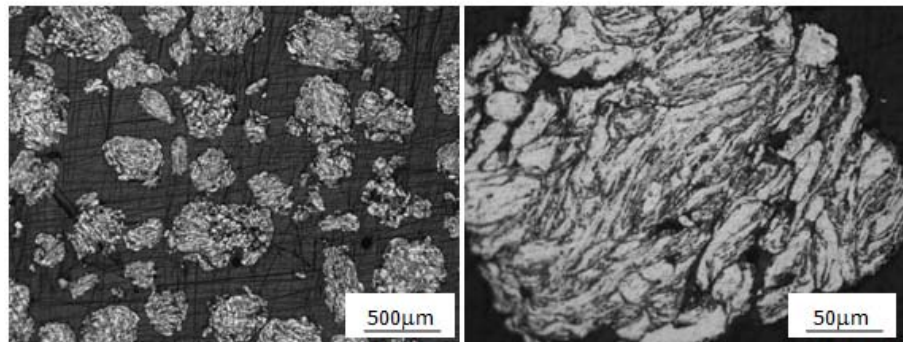
6.3 Powder Compact Forging of Mechanically Alloyed (MA) Ti-6Al-4V Powder

6.3.1 Milling of Powder Mixtures

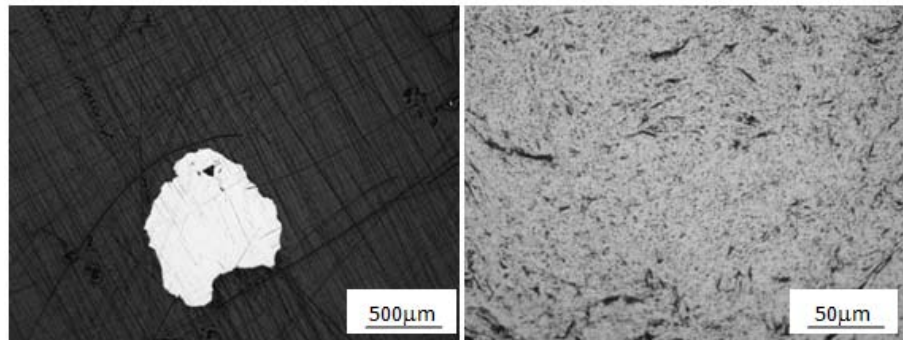
A mixture of HDH Ti and Al-V master alloy powders, with a nominal composition of Ti-6Al-4V, was milled for various times and milling speeds. Figure 6.13(a) shows that after 3 hours at a milling speed of 200 rpm, the milled powder particles consisted of several Ti and Al-40wt%V layers. With increased milling time to 6 hours, at the same milling speed of 200 rpm, the Ti/Al-40wt%V composite powder particles became larger and the Ti and Al-40wt%V layers became thinner, as shown in Figure 6.13(b). After milling for 6 hours at a higher milling speed of 400 rpm, the thickness of the Ti and Al-40wt%V layers (Figure 6.13(c)) became much smaller, and also the sizes of the Ti/Al-40wt%V composite powder particles became even larger. Granules with a maximum size of 2 mm in diameter formed, and most of the powder was stuck to the wall of the vial and the surfaces of steel balls. Only 10% of the powder could be obtained as loose powder, so it is not efficient to produce mechanical alloyed (MA) powders using this milling condition. In contrast, 95% of the powder was obtained as loose powder after milling the powder mixture at a rotational speed of 200 rpm for 6 hours. When the HDH Ti powder was replaced by GA Ti powder, after milling at 200 rpm for 6 hours, the sizes of Ti/Al-40wt%V composite powder particles became smaller, as shown in Figure 6.13(d). This might be due to the fact that GA Ti powder particles with a spherical shape have good flowability, and are therefore difficult to be captured by the milling balls during the milling process.



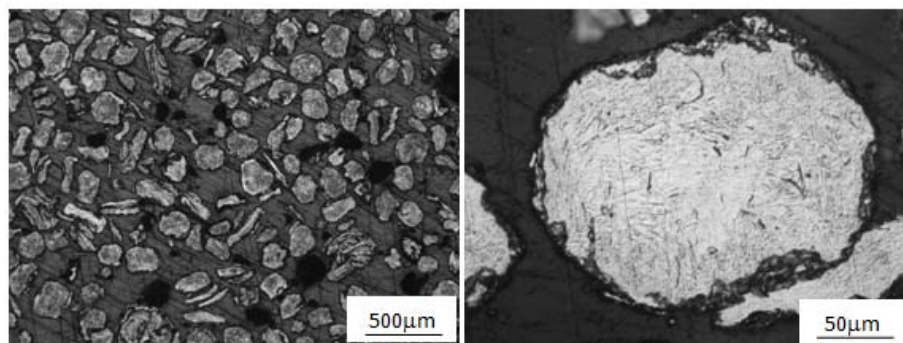
(a) HDH Ti/Al-40wt%V, 200 rpm/3hrs



(b) HDH Ti/Al-40wt%V, 200 rpm/6hrs



(c) HDH Ti/Al-40wt%V, 400 rpm/6hrs



(d) GA Ti/Al-40wt%V, 200 rpm/6hrs

Figure 6.13: Optical micrographs of powder particle cross sections produced by milling HDH or GA Ti powder with Al60V40 master alloy powder at different milling speeds and after different milling times.

As shown in Figure 6.14, compared with the XRD pattern of the powder mixture which showed Ti, Al_2V_5 and Al_3V peaks, the XRD patterns of the milled powders did not show the Al_2V_5 and Al_3V peaks. This might be due to the significant reduction in the sizes of the Al-40wt%V layers/particles which leads to a significant decrease in the XRD peak intensity of the phases in the master alloy.

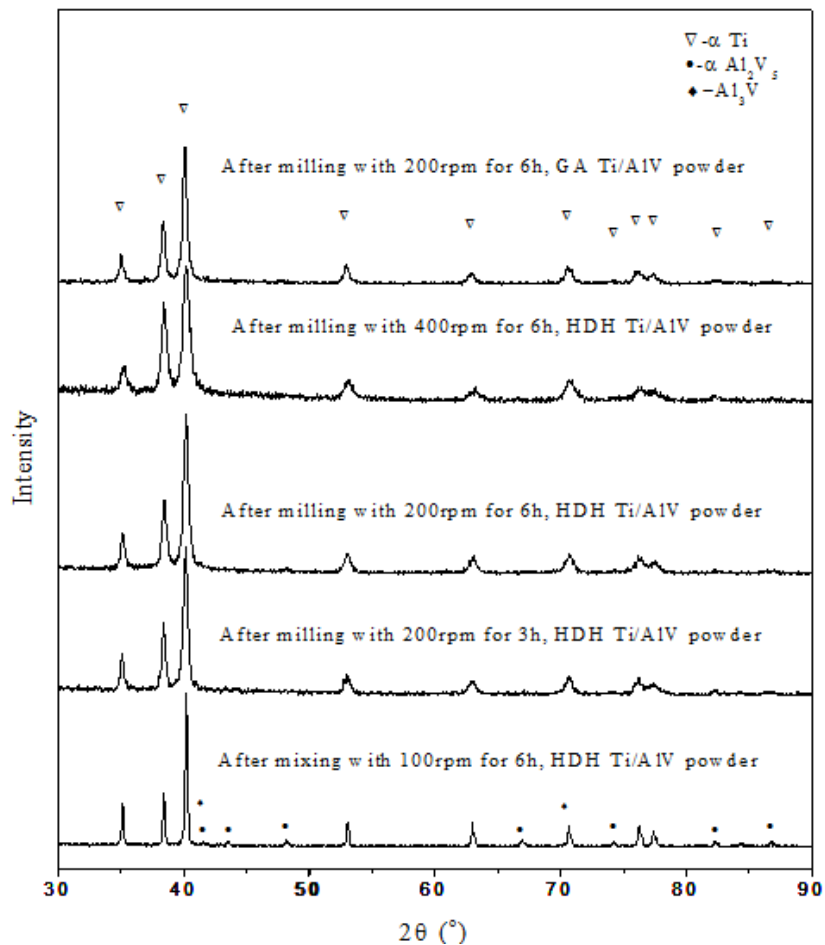


Figure 6.14: XRD patterns of composite powders made by milling powder mixtures at different milling speeds and for different times.

From the EDS mapping shown in Figure 6.15, the composite powder particles made by milling at 200 rpm for 3 and 6 hours, respectively, consisted of Ti layers and Al-40wt%V layers. When the milling speed was increased to 400 rpm, the Al-40wt%V layers became too thin to be distinguishable with EDS mapping after 6 hours of milling. However, the composite powder particles made by milling a mixture of GA Ti and Al-40wt%V master alloy powders for 6 hours at a speed of

200 rpm consisted of Ti central regions and Al-40wt% V layers. This is shown by the EDS mapping in Figure 6.16. This occurs because the GA Ti powder particles are much softer than the master alloy and HDH Ti powder particles with a much higher oxygen content. During milling, the impact of the balls cannot cause fracture of the GA Ti powder particles due to their good ductility, so the harder master alloy powder particles are cold welded onto the surface of the Ti powder particles, resulting in a covering of master alloy on the surface of the GA Ti powder particles.

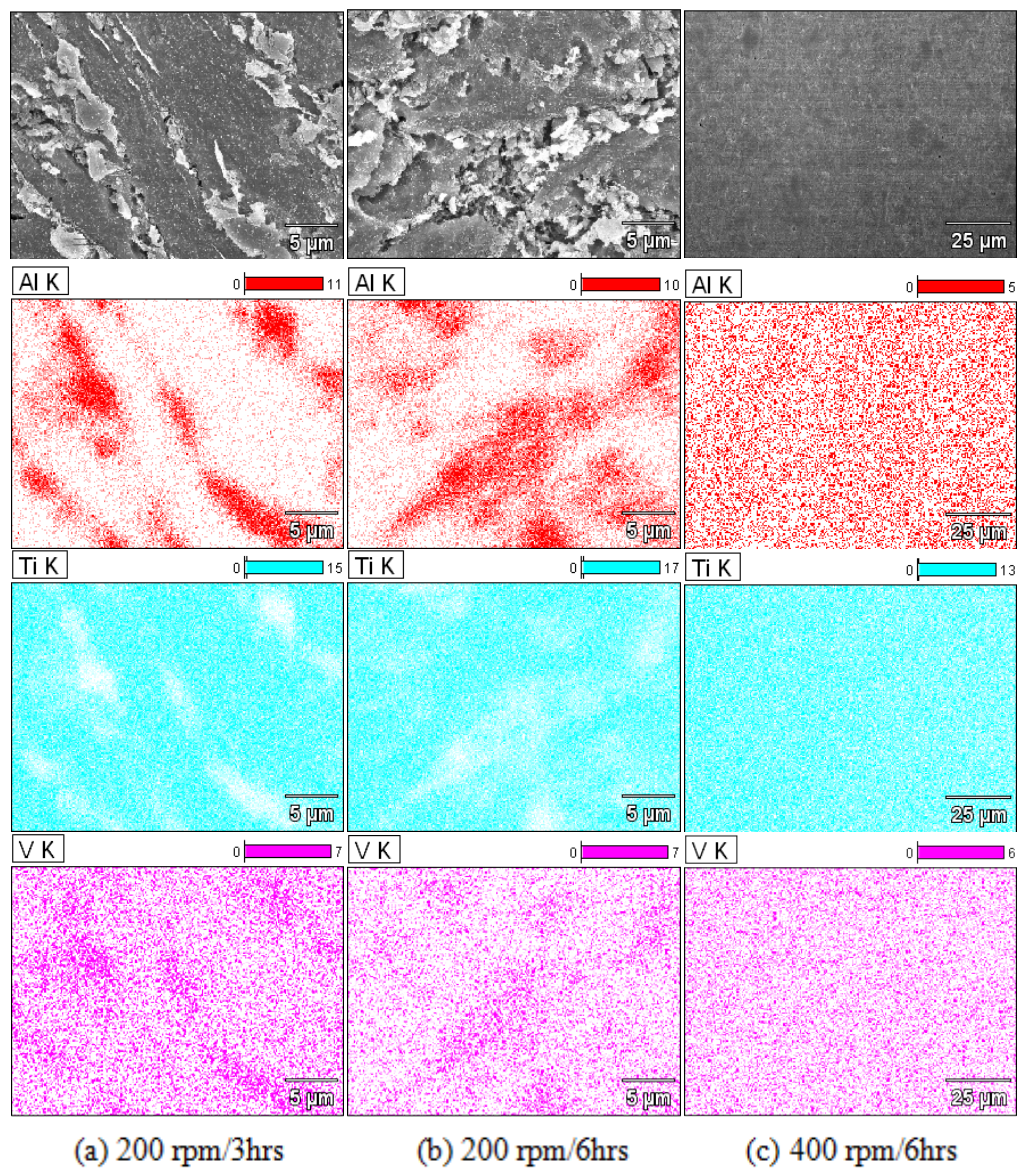


Figure 6.15: EDS mapping of composite powder particles made by milling HDH Ti and master alloy powders under different milling conditions.

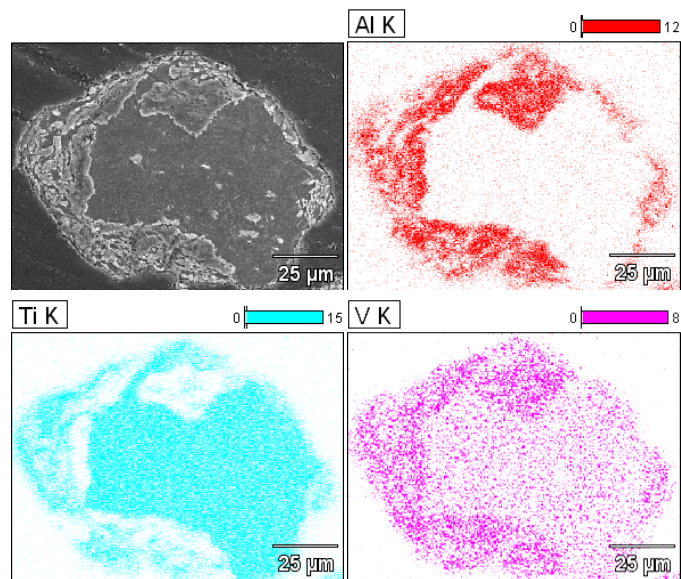


Figure 6.16: EDS mapping of a composite powder particle made by milling GA Ti and master alloy powders for 6 hours at a speed of 200 rpm.

The DTA heating curves of the composite powders (Figure 6.17) did not show any obvious peaks, suggesting that significant elemental diffusion had not occurred during heating, which is different from heating the powder mixture. Due to a combination of plastic deformation, fracturing and cold welding, the distances between master alloy particles/layers in the powder compact prepared using the composite powder are much shorter than in the one made using a powder mixture, so the diffusion of Al and V into the Ti matrix is easier. A longer milling time of 6 hours promotes the diffusion of Al and V into the Ti matrix, so before forging a more homogeneous compact exists. Therefore it is not necessary to hold the powder compact at the forging temperature in order to dissolve the master alloy powder particles during powder compact forging of composite powders.

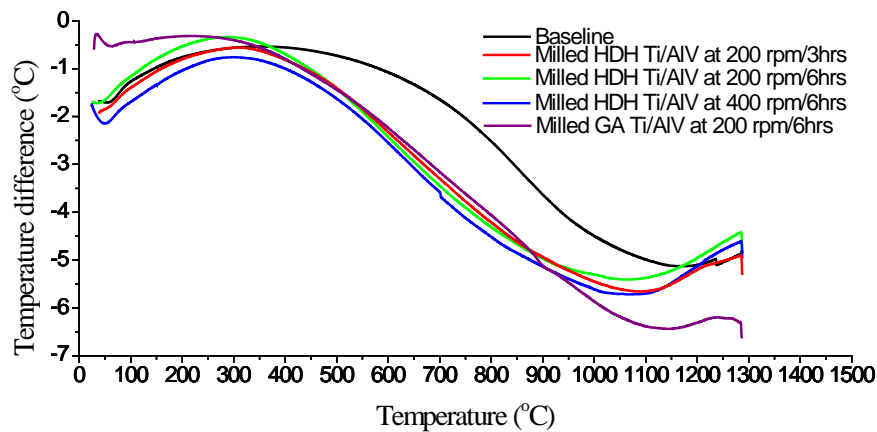


Figure 6.17: DTA curves of composite powder particles made at different milling condition using different raw powders.

6.3.2 Phase Constituency and Elemental Distribution in As-forged MA Ti-6Al-4V Parts

Rocker arms, produced by forging a compact made from mechanically alloyed (MA) powders are shown in Figure 6.18. These were made by milling HDH or GA Ti and Al-40wt% V master alloy powders for 6 hours at a speed of 200 rpm. There were a few deep cracks on the surface of the part made by forging HDH Ti/Al-40wt% V MA powder compact, as shown by the arrows in Figure 6.18(a). The surface quality of as-forged parts was improved significantly by replacing the HDH Ti/Al-40wt% V MA powder compact by a GA Ti/Al-40wt% V MA powder compact, as reflected by the absence of deep cracks on the surface of the as-forged part shown in Figure 6.18(b). The reason for the difference in surface quality of two as-forged parts might be because of the big difference in the oxygen content of the raw Ti powder used, with the HDH Ti powder having a much higher oxygen content of 0.35wt% compared with the GA Ti powder with an oxygen content of 0.11wt%. With a higher oxygen content in the MA powder, the powder compact is more brittle, so it is easier to form cracks during forging.



(a) HDH Ti/Al-40wt% V

(b) GA Ti/Al-40wt% V

Figure 6.18: Rocker arms produced by forging MA powders.

The XRD patterns of the parts made from both materials (Figure 6.19) showed peaks of the α and β Ti phases but no peaks from any of the phases in the Al-40wt%V master alloy particles/layers. This suggests that the Al-40wt%V layers in the composite powder particles were dissolved into the Ti matrix during compact heating to 1350 °C and then forging.

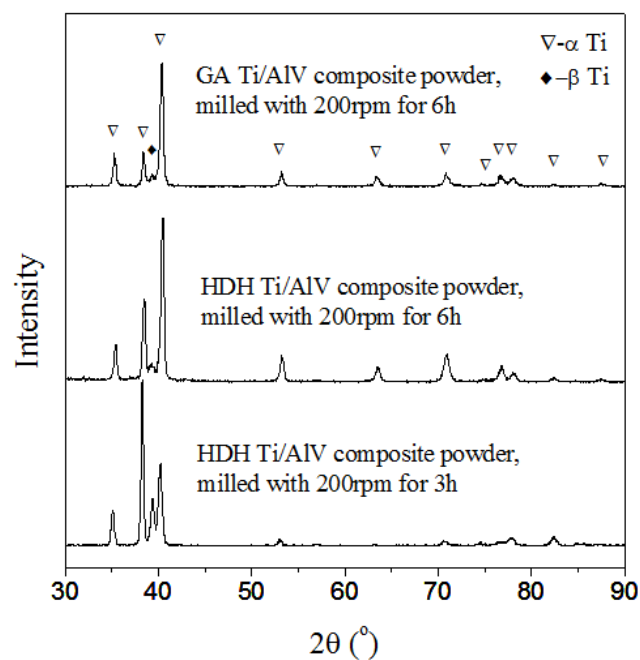


Figure 6.19: XRD patterns of as-forged parts made by PCF of HDH Ti/Al-40wt% V and GA Ti/Al-40wt% V composite powders.

The EDS elemental mapping (Figure 6.20(a) and (b)) of cross sections of the forged parts, made from HDH Ti/Al-40wt% V composite powders and milled for 3 or 6 hours at a speed of 200 rpm, showed a homogeneous distribution of Al, Ti

and V. Using EDS mapping it was hard to identify undissolved master alloy layers/particles in the samples. This proved that most of the master alloy layers/particles in the composite powders were already dissolved into the Ti matrix. On the other hand, under the same forging conditions, undissolved master alloy powder particles were observed in those forged parts made using an HDH Ti/Al-40wt%V powder mixture. This shows that milling can significantly accelerate the diffusion of Al and V from the master alloy powder particles into the Ti matrix. However, a non-uniform distribution of Al could be seen after forging compacts made from GA Ti/Al-40wt%V composite powder, as shown in Figure 6.20(c). The reason for this is that the thickness of the master alloy layers in the GA Ti/Al-40wt%V composite powder particles is much larger than that in the HDH Ti/Al-40wt%V composite powder particles. This means that the diffusion of Al and V into the Ti was not complete in the GA Ti/Al-40wt% composite powder compact, during heating to the forging temperature without holding at temperature prior to forging.

To further study the elemental distribution in forgings of compacts made from different composite powders, EDS line scanning and point analysis was carried out. The results of EDS line scanning (Figure 6.21) showed that the distribution of Al, Ti and V in the two forgings made from HDH Ti/Al-40wt%V composite powders milled under different conditions was homogeneous. Therefore there were no undissolved master alloy particles/layers in the as-forged parts. The forging made from GA Ti/Al-40wt%V composite powder had Ti rich regions. As shown in Figure 6.22, four points were selected randomly on the cross section of each of the samples to do EDS point analysis. The compositions of the points are listed in Table 6.3. From the table, there was no large difference in compositions at the four points in the HDH Ti/Al-40wt%V composite powder forgings, but there was a large difference in the Al and V contents at the four points in the GA Ti/Al-40wt%V composite powder forgings. Although undissolved master alloy

particles/layers were not observed, there still remained a non-homogeneous composition distribution in the GA Ti/Al-40wt%V composite powder forgings.

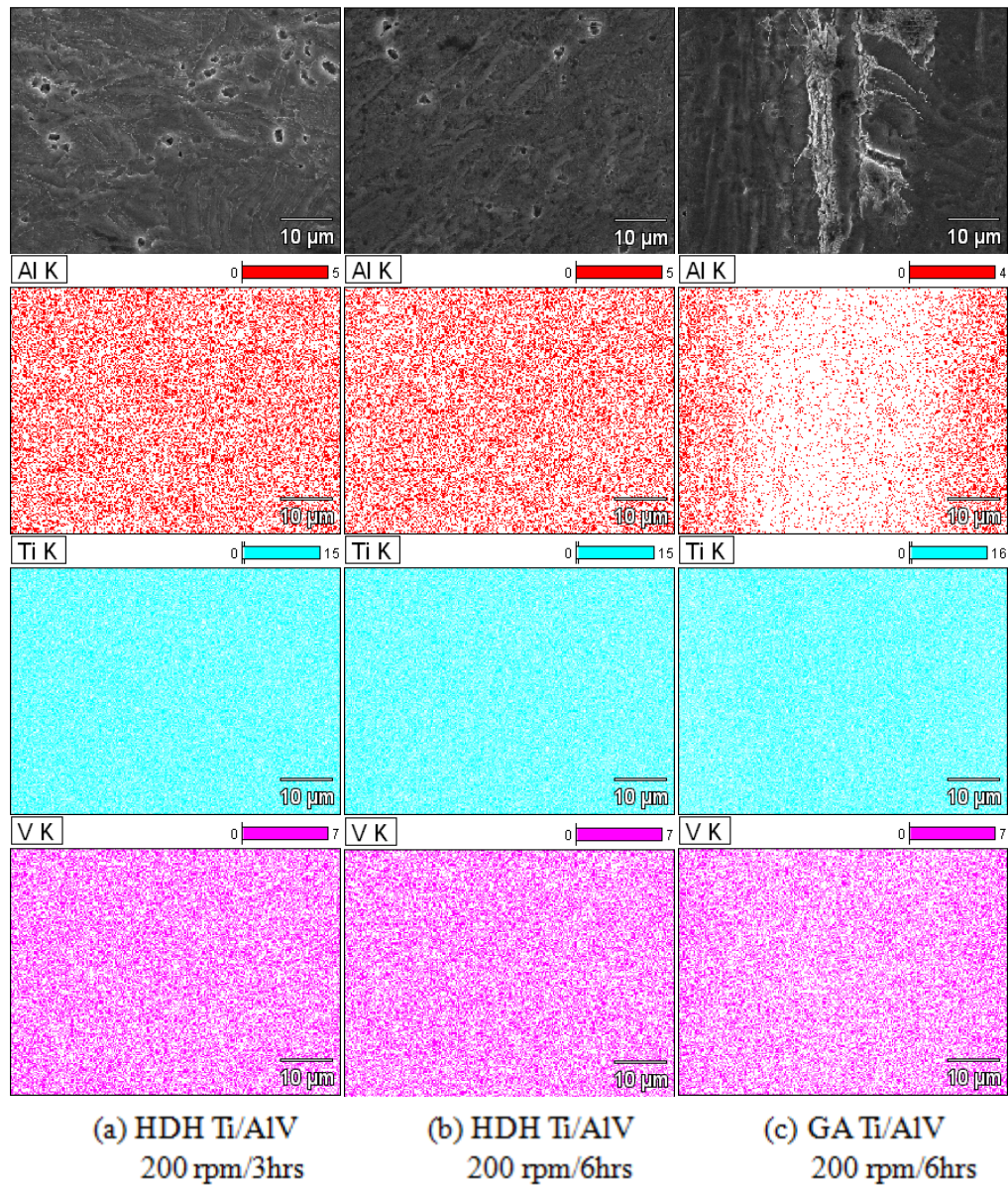
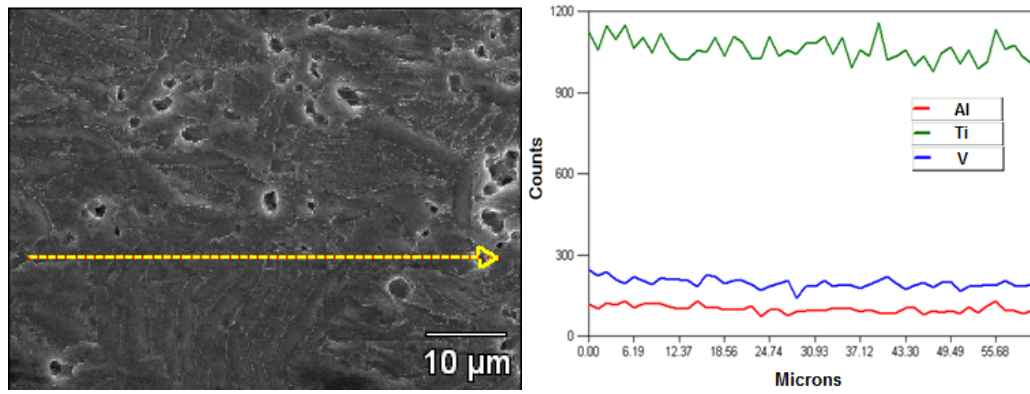
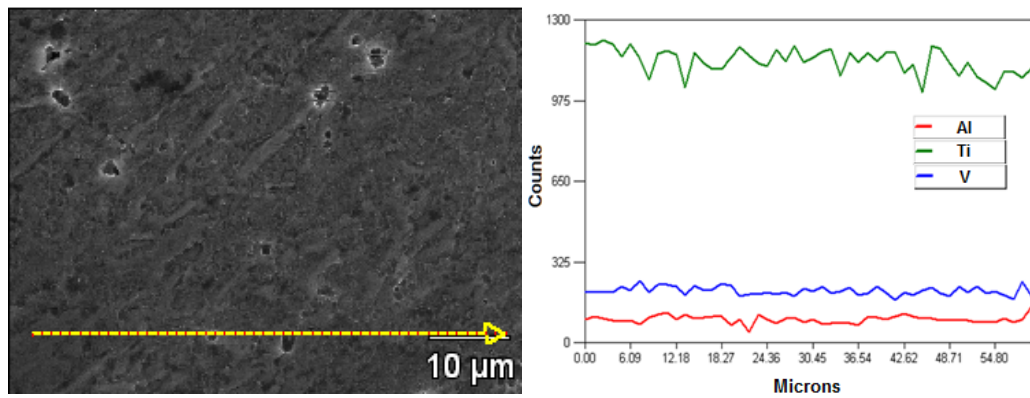


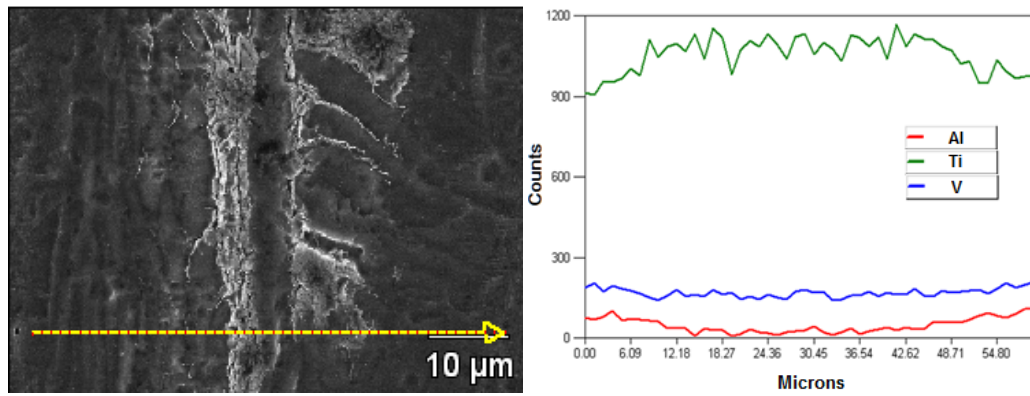
Figure 6.20: EDS mappings for as-forged parts produced by PCF of composite powders milled under different conditions.



(a) HDH Ti/Al-40wt% V, 200 rpm/3hrs



(b) HDH Ti/Al-40wt% V, 200 rpm/6hrs



(c) GA Ti/Al-40wt% V, 200 rpm/6hrs

Figure 6.21: EDS line scanning results for as-forged parts produced by PCF of composite powders milled under different conditions.

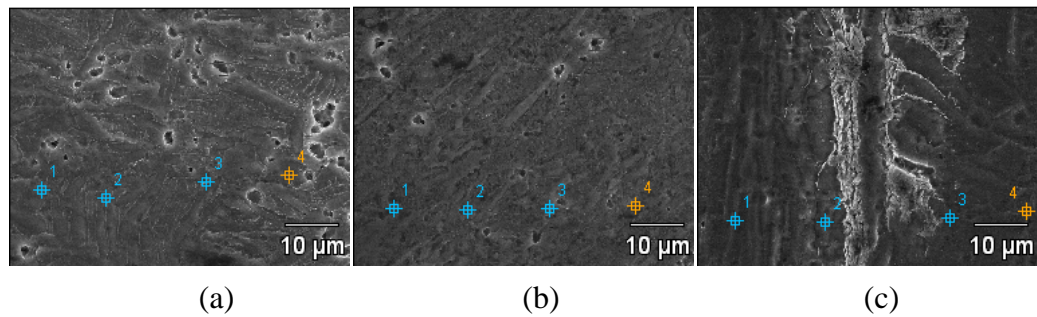


Figure 6.22: Points selected for EDS analysis on the cross sections of as-forged parts made by PCF of composite powders milled under different conditions. (a) HDH Ti/Al-40wt% V, 200 rpm/3hrs; (b) HDH Ti/Al-40wt% V, 200 rpm/6hrs; (c) GA Ti/Al-40wt% V, 200 rpm/6hrs.

Table 6.3: EDS points analysis data in Figure 6.22.

Samples (in Figure 6.22)	Point No.	Al (wt%)	Ti (wt%)	V (wt%)
(a)	1	4.93	89.71	5.36
	2	4.59	93.31	2.10
	3	5.09	90.32	4.60
	4	4.43	91.67	3.89
(b)	1	5.84	90.42	3.73
	2	4.92	91.54	3.54
	3	4.04	91.70	4.26
	4	4.00	92.05	3.95
(c)	1	5.42	91.53	3.05
	2	0	99.85	0.15
	3	1.02	98.20	0.78
	4	5.92	87.78	6.30

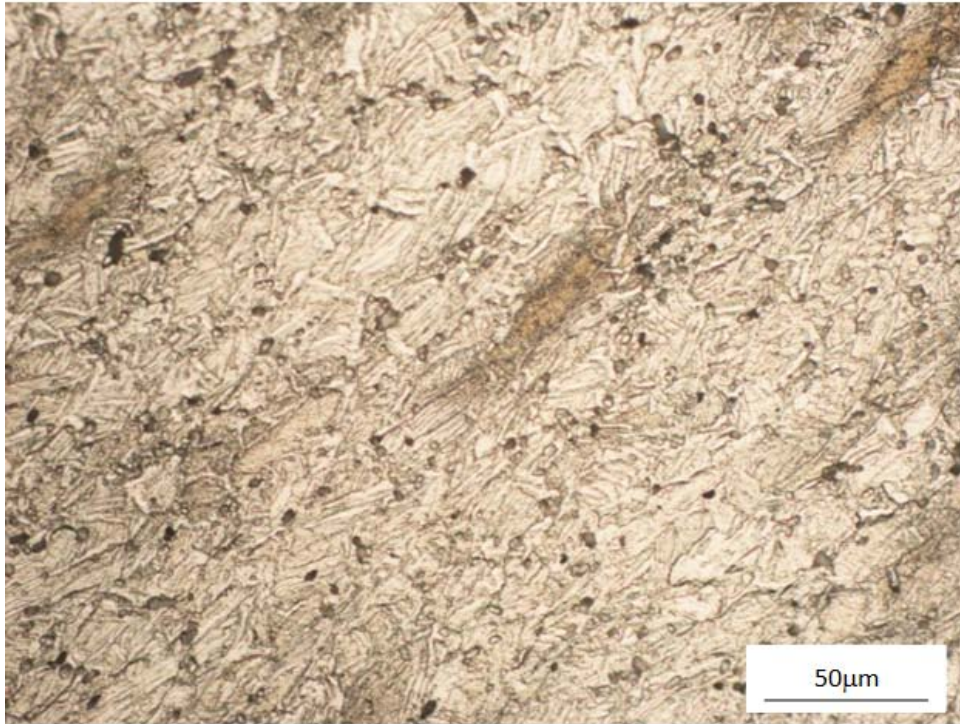
6.3.3 Microstructures of As-forged MA Ti-6Al-4V Parts

The oxygen content of as-forged MA Ti-6Al-4V parts is shown in Table 6.4. Compared with an unmilled powder mixture, the oxygen content of samples from three forged powder compacts made using mechanically milled composite powders was much higher. So a substantial amount of oxygen was absorbed by the powder particles during passivation of the milled powder particles.

Table 6.4: Oxygen content of forged samples made using a powder mixture and composite powders.

Sample	Oxygen (%)
Powder mixture of HDH Ti and Al ₆₀ V ₄₀	0.36
HDH Ti/Al-40wt% V, 200 rpm/3hrs	0.55
HDH Ti/Al-40wt% V, 200 rpm/6hrs	0.50
GA Ti/Al-40wt% V, 200 rpm/6hrs	0.29

The sample produced by forging an HDH Ti/Al-40wt%V composite powder compact, which was milled for 3 hours at a speed of 200 rpm, had an α/β lamellar structure, as shown in Figure 6.23(a). Regions with a different microstructure caused by a non-uniform composition distribution were also observed. When the composite powder milled for 6 hours at a speed of 200 rpm was used to make a part using PCF, the regions with a different microstructure disappeared, as shown in Figure 6.23(b). So, by increasing the milling time from 3 to 6 hours to produce a composite powder, the compositional distribution in an as-forged part becomes more uniform. When the HDH Ti powder was replaced by GA Ti powder using the same conditions, regions with a different microstructure appeared again, as shown in Figure 6.23(c). The sizes of such regions were much larger than in the samples made from HDH Ti/Al-40wt%V composite powder milled for 3 hours at a speed of 200 rpm, but smaller than those made by forging an HDH Ti/Al-40wt%V powder mixture (Figure 6.9(a)).



(a) HDH Ti/Al-40wt%V, 200 rpm/3hrs



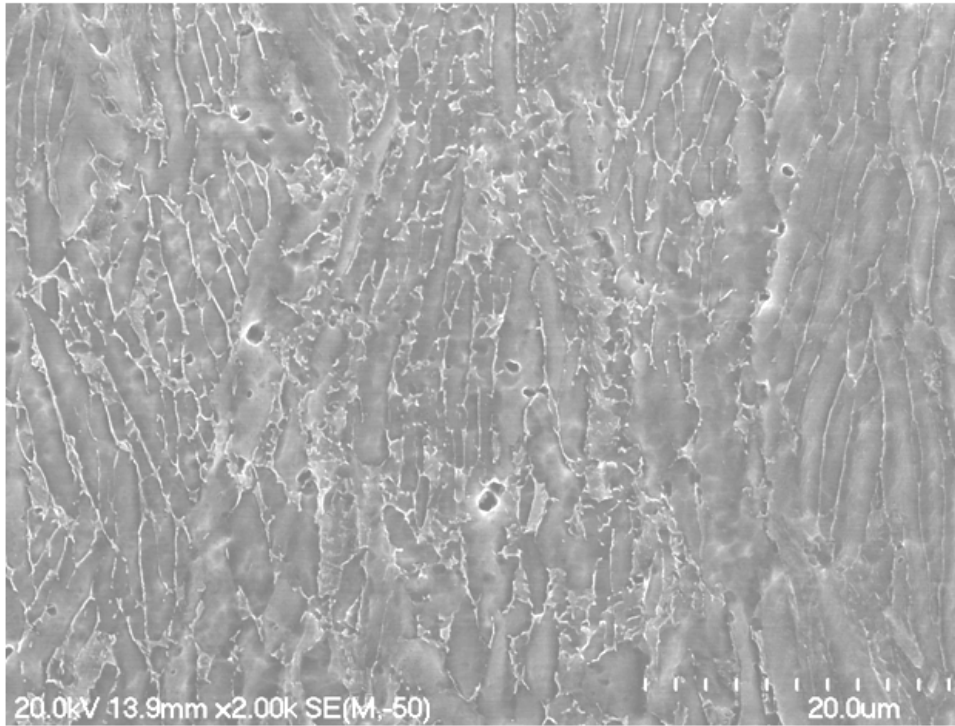
(b) HDH Ti/Al-40wt%V, 200 rpm/6hrs



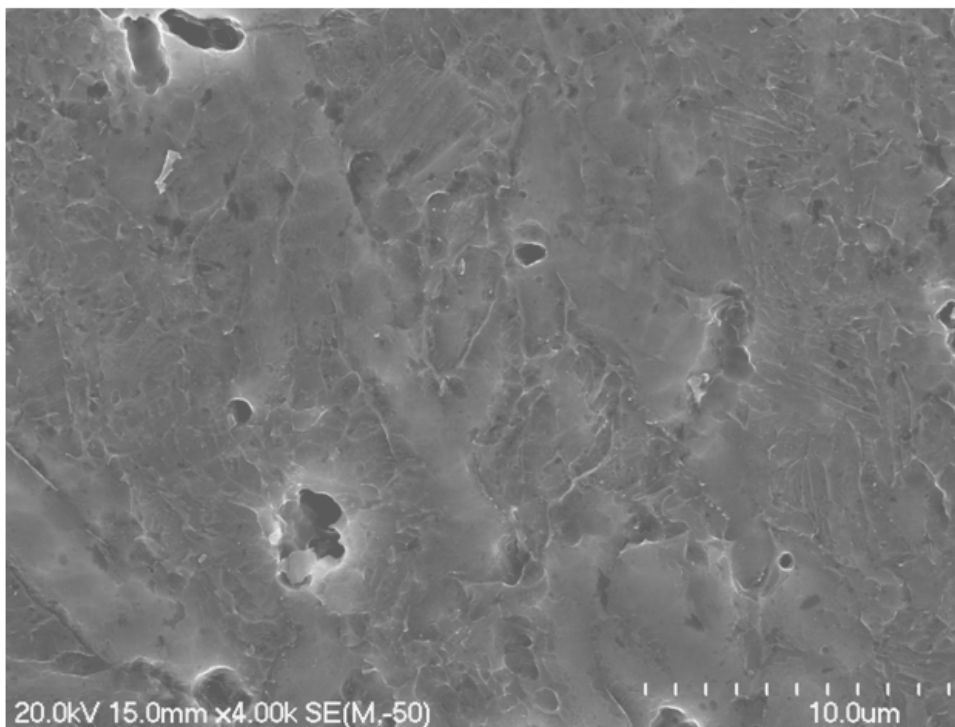
(c) GA Ti/Al-40wt%V, 200 rpm/6hrs

Figure 6.23: Optical micrographs of as-forged parts made using different composite powders.

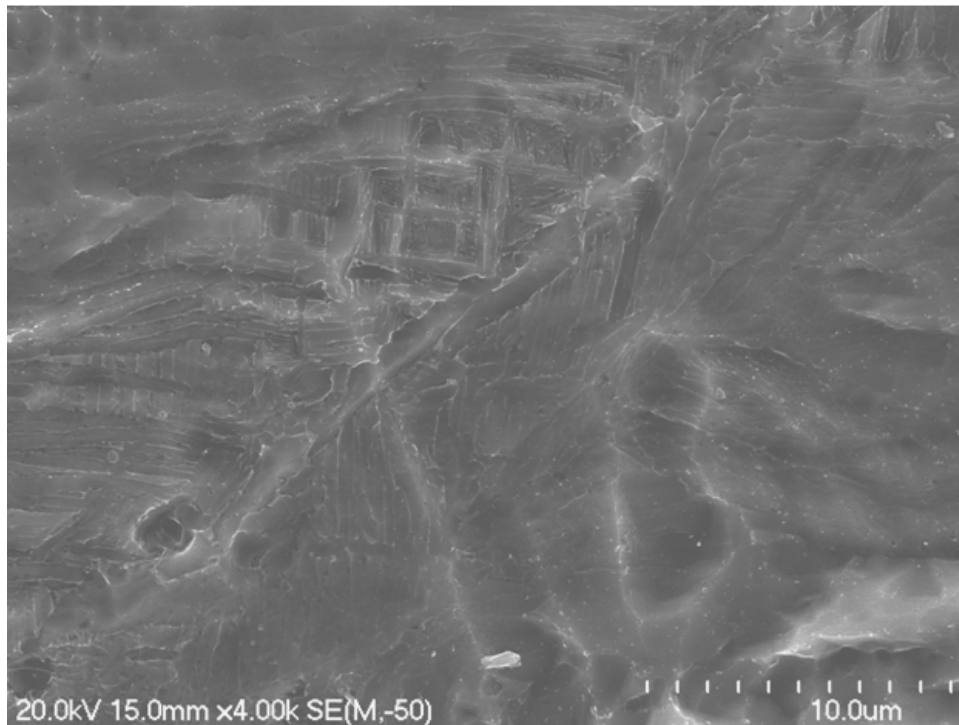
The microstructures of the samples produced using the above conditions were examined by SEM. Forgings made from HDH Ti/Al-40wt%V composite powder, which had been milled for 3 hours at a speed of 200 rpm, had a coarse α/β lamellar structure, as shown in Figure 6.24(a). While forgings made from HDH Ti/Al-40wt%V composite powder, milled for 6 hours at a speed of 200 rpm, had a fine, non-uniform α/β lamellar structure as shown in Figure 6.24(b). The forging made from GA Ti/Al-40wt%V composite powder had a fine α/β lamellar structure, as shown in Figure 6.24(c).



(a) HDH Ti/Al-40wt%V, 200 rpm/3hrs



(b) HDH Ti/Al-40wt%V, 200 rpm/6hrs



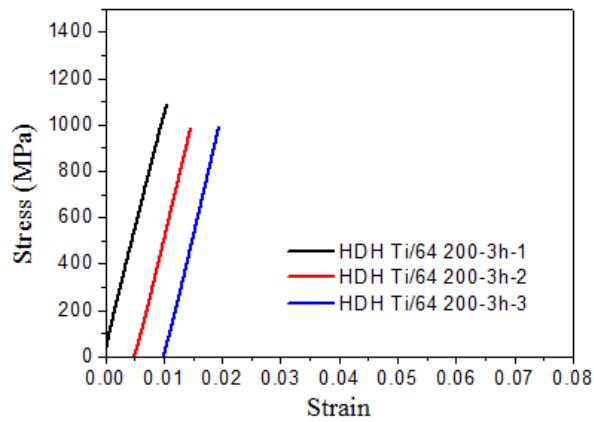
(c) GA Ti/Al-40wt%V, 200 rpm/6hrs

Figure 6.24: SEM images showing the microstructures of cross sections of as-forged parts made using different composite powders.

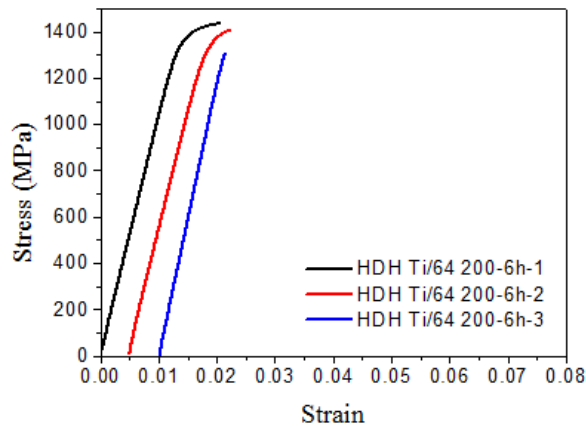
6.3.4 Mechanical Properties and Fracture Behaviour of As-forged MA Ti-6Al-4V Parts

The engineering stress-engineering strain curves in Figure 6.25(a) are for specimens taken from forgings made from HDH Ti/Al-40wt%V composite powder, milled for 3 hours at a speed of 200 rpm. The specimens fractured prematurely at a stress in the range 987-1088 MPa before reaching the yield strength of the material. With an increase in the milling time, from 3 to 6 hours, used to make the composite powder, the fracture stress increased significantly to 1383 MPa, and two out of the three specimens tested showed plastic yielding, with an elongation to fracture of 0.4%-0.7%. The forging made from GA Ti/Al-40wt%V composite powder was clearly more ductile, as shown in Figure 6.25(c). The mechanical properties of the three tensile test specimens cut from this forging are listed in Table 6.5. Their average yield strength, UTS and elongation

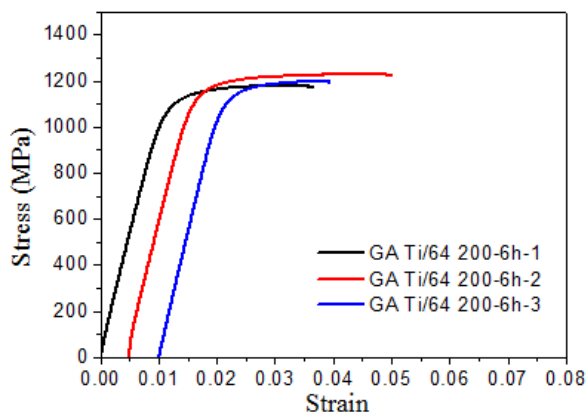
to fracture were 1123.5 MPa, 1203.3 MPa and 2.6%, respectively.



(a) HDH Ti/AlV, 200 rpm/3hrs



(b) HDH Ti/Al-40wt%V, 200 rpm/6hrs



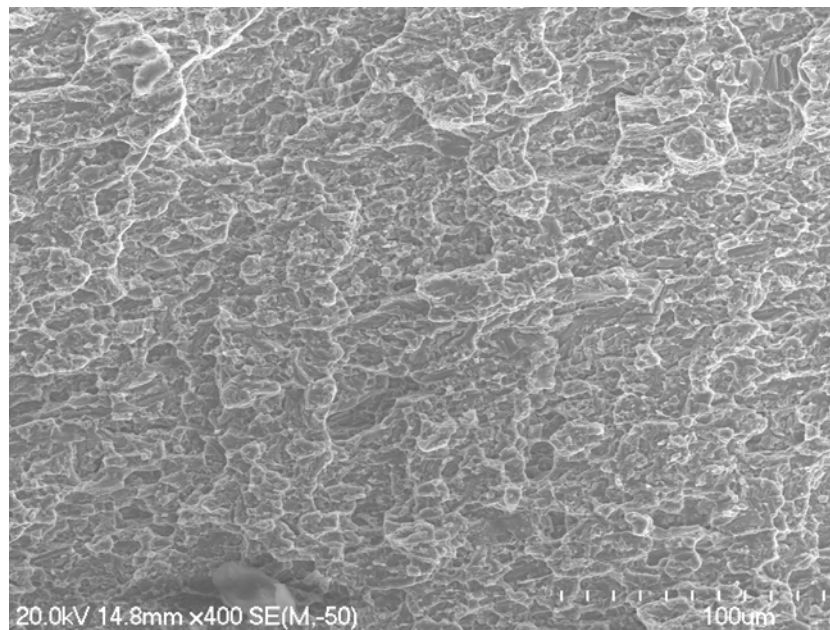
(c) GA Ti/Al-40wt%V, 200 rpm/3hrs

Figure 6.25: Engineering stress-strain curves for tensile test specimens cut from as-forged parts made using different composite powders.

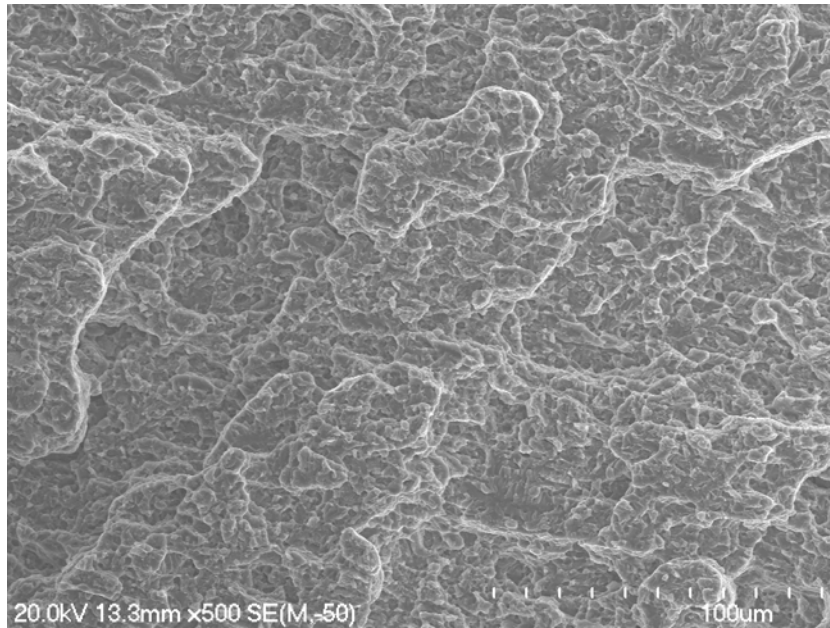
Table 6.5: Tensile properties for specimens cut from a forging made from GA Ti/Al-40wt% V composite powder, milled at a speed of 200 rpm for 6 hours.

Sample	YS(MPa)	UTS(MPa)	Elongation to fracture(%)
1	1096.5	1181	2.5
2	1147	1230	3.4
3	1127	1199	1.8
Average	1123.5	1203.3	2.6

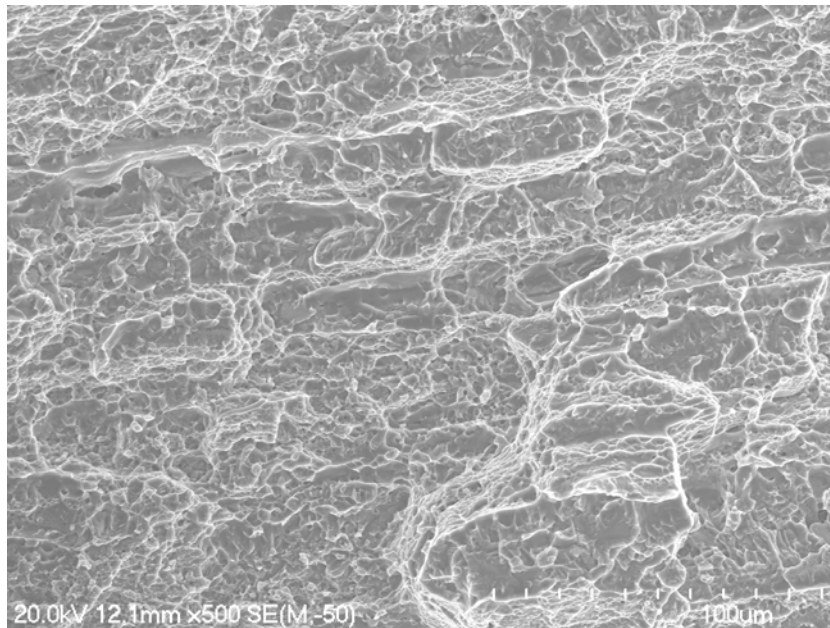
The fracture surfaces of the broken tensile test specimens from two forged parts made from HDH Ti/Al-40wt% V composite powders were flat and did not show any dimples, as shown in Figures 6.26(a) and (b). The fracture mode of both specimens was by intergranular fracture. The fracture surfaces of tensile test specimens from a forging made from GA Ti/Al-40wt% V composite powder showed some dimples and the fracture mode was transgranular fracture.



(a) HDH Ti/Al-40wt% V, 200 rpm/3hrs



(b) HDH Ti/Al-40wt% V, 200 rpm/6hrs



(c) GA Ti/Al-40wt% V, 200 rpm/3hrs

Figure 6.26: Fracture surfaces of tensile test specimens cut from as-forged parts made using different composite powders.

6.4 Discussion

6.4.1 The Effect of Undissolved Al-40wt%V Master Alloy Particles on the Microstructure, Mechanical Properties and Fracture Behaviour of BE Ti-6Al-4V Parts

As discussed in Chapter 4, powder compact forging, as a rapid consolidation process, removes pores by shear deformation, which enhances powder consolidation. With the blended elemental approach used in this study, the original pores in powder compacts and those pores formed by the Kirkendal effect, with respect to Al and V diffusion from the master alloy to the Ti matrix during heating, are removed by shear deformation during powder compact forging. As a result of this, there is good interparticle bonding, without pores at the particle boundaries, between undissolved master alloy particles and the Ti matrix in samples produced by forging without holding at temperature before forging. This is shown in Figure 6.10. However, there are plenty of residual pores in the sample, as shown by the optical images in Figure 6.9. The reason for the formation of the residual pores might be that during cooling after forging, elemental Al and V diffuse from undissolved master alloy particles into the Ti matrix, leaving pores behind. With increasing holding time to 5 minutes, fewer pores form in the as-forged part due to a smaller number of undissolved master alloy particles before forging. Finally when the holding time increases to 10 minutes, residual pores are removed completely. This might be due to the fact that in this case, there are no undissolved master alloy particles in the powder compact before forging, especially since it has been shown that there is complete dissolution of master alloy particles and a homogeneous distribution of Al, Ti and V in the sample.

Moreover, when undissolved master alloy particles are present in the forged sample, an α/β lamellar structure forms around the master alloy particles. When V diffusion into the Ti matrix is high enough, β laths form in the microstructure.

This was also observed in a Ti-6Al-4V sample produced by hot pressing of a mixture of Ti and master alloy powders at 900 °C for 4 hours [2]. When most of the master alloy particles are dissolved in the Ti, the microstructure formed consists mainly of an α/β lamellar structure. Finally, when the master alloy particles are completely dissolved, a uniform α/β lamellar structure forms in the sample. In contrast, to get a homogeneous Ti-6Al-4V compositional distribution when consolidating a Ti/Al-V master alloy powder mixture by hot pressing [2] or warm equal-channel angular pressing and vacuum sintering [3], a higher temperature of 1100 °C and a longer holding time of 2 and 4 hours, respectively have to be used. So this study shows that the holding time required to get a homogeneous composition distribution in Ti-6Al-4V parts is much shorter than the ones reported in Ref. [2, 3].

When a large number of undissolved master alloy particles are present in the sample, there is also a lot of porosity in the sample. When under tensile stress, the pores act as crack initiators, making crack nucleation easy. At the same time, the interparticle bonding between master alloy particles and the Ti matrix might be too weak to resist the tensile stress, so it is easy to form cavities along the interparticle boundaries. Such cavities also promote fracture. To prove this postulation, an examination of the morphology of the fracture surface shows that there are a lot of flattened smooth regions left by debonding between master alloy particles and the Ti matrix, and also residual pores. With easy crack nucleation at stresses lower than the yield strength of the material, the tensile test specimens fracture prematurely. When a forged sample has fewer undissolved master alloy particles and pores, the non-homogeneous distribution of Al and V are ameliorated due to their further diffusion from the master alloy to the Ti matrix. This can lead to an improvement in mechanical properties of Ti-6Al-4V forged samples made using HDH Ti and master alloy powders, as reflected by their increased yield points, figure 6.11(b). The sample still does not have good ductility, perhaps due to the presence of remaining master alloy particles in the microstructure. As most

of the master alloy particles have dissolved in Ti matrix, it is hard to find the flattened smooth regions caused by debonding between master alloy particles and Ti matrix in fracture surfaces of tensile test specimens. With a further increase in holding time to 10 minutes, all the master alloy particles are dissolved, and a homogeneous microstructure with uniform composition are achieved in the forged sample. EDS point analysis confirms that the actual composition of the samples is the nominal composition of the alloy. These factors indicate that for a Ti-6Al-4V alloy, made from a powder mixture, a holding time of 10 minutes before forging gives a forging with good mechanical properties and an average elongation to fracture of 3.4%. This is close to the elongation to fracture of a sample made by forging a pre-alloyed HDH Ti-6Al-4V powder compact (Figure 6.27). Because of a significantly higher oxygen content of 0.36%, the ductility of a sample made in this way is still substantially lower than that for a corresponding wrought alloy part or as-forged GA Ti-6Al-4V part. As a cheaper process, forging a powder compact, made using a powder mixture, with a 10 minute holding time before forging can be used to replace forging of a pre-alloyed HDH Ti-6Al-4V powder compact to make parts for many applications.

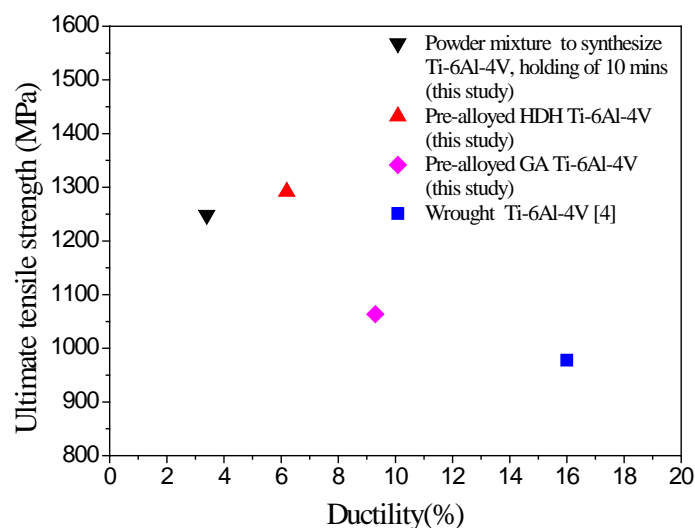


Figure 6.27: A comparison of mechanical properties of as-forged Ti-6Al-4V parts made from a powder mixture with wrought material.

6.4.2 The effect of Milling and Oxygen Content on the Mechanical Properties and Fracture Behaviour of Samples Produced by PCF of Composite Powders

To get a homogeneous microstructure and compositional distribution, without holding the powder compacts at the forging temperature or by only holding for a very short time prior to forging, Ti/Al-40wt%V composite powders produced by mechanical milling are used to reduce the elemental diffusion path. As a result of using this method, a uniform coarse or fine α/β lamellar structure without undissolved master alloy particles is obtained in forged samples, made from HDH Ti/Al-40wt%V composite powder compacts, made using powder milled for 3 or 6 hours at a speed of 200 rpm, without a pre-forging temperature hold. However, tensile testing resulted in premature fracture with a significant stress increase with increased milling time from 3 to 6 hours. The bad mechanical properties of the two as-forged parts could be attributed to their high oxygen content caused by oxygen pick up during mechanical milling.

The oxygen content of an HDH Ti/Al-40wt%V composite powder forging can be reduced by replacing HDH Ti powder by GA Ti powder. However, during mechanical milling, GA Ti powder particles are not fractured by the impact of the balls and hard master alloy powder particles are cold welded onto the surfaces of the Ti powder particles. This is because the GA Ti powder particles are much softer than the master alloy powder particles. This means that the elemental diffusion path from master alloy particles to Ti particles is not reduced by milling, and therefore there are Ti rich regions associated with an inhomogeneous composition in GA Ti/Al-40wt%V forgings. Therefore, milling a mixture of GA Ti and Al-V master alloy powders for 6 hours at a speed of 200 rpm is not suitable for producing forged Ti-6Al-4V samples with a homogeneous microstructure and composition.

6.5 Summary

This chapter has described the use of a blended elemental approach, with mechanical alloying to produce Ti-6Al-4V rocker arms by powder compact forging at 1350 °C.

- In order to get an as-forged part with a homogeneous microstructure and composition, a holding time of 5-10 minutes at the forging temperature is required for a starting mixture of Ti and Al-V master alloy powders, to remove the effect of undissolved master alloy particles on the mechanical properties of forged samples.
- A mechanical alloying approach has both a positive and negative role on Ti-6Al-4V parts produced by forging a powder compact made from an HDH Ti and Al-V master alloy powder mixture. The positive benefit is a reduction in the elemental diffusion path, leading to an improvement in the compositional homogeneity; the negative role is the high oxygen pick up.

6.6 Reference

1. Mishin, Y. and C. Herzig, *Diffusion in the Ti–Al system*. Acta materialia, 2000. 48(3): p. 589-623.
2. Bolzoni, L., et al., *Mechanical behaviour of pressed and sintered titanium alloys obtained from master alloy addition powders*. Journal of the Mechanical Behavior of Biomedical Materials, 2012.
3. Haase, C., et al., *Production of Ti-6Al-4V billet through compaction of blended elemental powders by equal-channel angular pressing*. Materials Science and Engineering: A, 2012.
4. Froes, F.H. and D. Eylon, *Titanium net shape technologies*. Los Angeles, 1984: p. 1984.

Chapter 7: Conclusions and Recommendations for Future Work

7.1 Conclusions

- Warm compaction is used to produce HDH Ti powder (O: 0.35%) and pre-alloyed HDH Ti-6Al-4V (O: 0.50%) and GA Ti-6Al-4V (O: 0.13%) compacts. It is found that with increasing temperature, the powder compact density increases. Based on the productivity rate, quality and cost of powder compaction, 250 °C, 300 °C and 550 °C are selected as the optimized conditions for compacting HDH Ti powder, and pre-alloyed HDH and GA Ti-6Al-4V powders, respectively, for future sintering and forging experiments.
- Due to an irregular shape and the rough surface of HDH powder particles, interlocking and cold welding are the main mechanisms for HDH powder compaction, while GA powder with a spherical particle shape has good flowability, and interlocking plays less of a role on powder compaction than warm welding. Warm welding is therefore the main mechanism for GA powder compaction.
- After induction sintering, an equiaxed α structure is observed in as-sintered HDH Ti powder compacts, while α acicular in an α/β matrix and a coarse α/β matrix with a primary α lamellar structure form in as-sintered GA and HDH Ti-6Al-4V powder compacts, respectively. As-sintered HDH Ti powder compact have an average elongation to fracture of 7.5%, ultimate tensile strength (UTS) of 575.4 MPa and a yield strength of 470 MPa, while as-sintered HDH and GA Ti-6Al-4V powder compacts are brittle with very little elongation to fracture.

- The microstructure in as-forged HDH Ti parts (O: 0.41%) is an equiaxed α structure, with twinned α grains due to large localized plastic deformation. The porosity distribution depths, on a cross section of the as-forged part both perpendicular to and along the forging direction, are 0.24 mm and 0.2 mm respectively. This is respectively caused by non-homogeneous deformation and a cold shut effect.
- Specimens cut from the centre of an as-forged HDH Ti part (O: 0.41%) have an average elongation to fracture of 12%, a yield strength of 661.0 MPa and UTS of 796.3 MPa due to large localized plastic deformation. The elongation to fracture can be increased to an average of 22.4% at constant stress by a 5 minute holding time at the forging temperature. An improvement in elongation to fracture of 19.5% can be achieved at a lower stress by replacing HDH Ti powder with GA Ti powder with lower oxygen content. Also, the elongation to fracture can be increased to 25.6% by an annealing heat treatment, but its UTS decreases to 715.4 MPa due to grain coarsening during the annealing process.
- An as-forged HDH Ti-6Al-4V part (O: 0.52%) has a microstructure consisting of a coarse α/β matrix with a primary α lamellar structure. The porosity distribution depths on a cross section of the as-forged part both perpendicular to and along the forging direction, are 1.85 mm and 1.8 mm, respectively. The centre of a forged part has an average elongation to fracture of 6.2%, a yield stress of 1160.6 MPa and UTS of 1291.8 MPa.
- The mechanical properties of an as-forged HDH Ti-6Al-4V part (O: 0.52%) are improved by a solution and aging treatment and recrystallization annealing. After a solution and aging treatment, an equiaxed microstructure with acicular α is obtained, and its UTS is increased to 1421.7 MPa, with an

elongation to fracture of 7.2%. The elongation to fracture can be significantly increased to 12.5% after recrystallization annealing due to a microstructure of fully equiaxed α grains. However, its UTS drops to 1220.6 MPa, but this material still offers an opportunity for industrial application for a forged HDH Ti-6Al-4V part with high oxygen content (~0.5%).

- The microstructure of an as-forged GA Ti-6Al-4V part (O: 0.14%) is an α acicular structure. The porosity distribution depth perpendicular to and along the forging direction, on a cross section are 1.25 mm and 1.2mm, respectively. This material has an average tensile elongation to fracture of 9.3%, a yield strength of 955.3 MPa and UTS of 1063.4 MPa.
- After duplex annealing, the elongation to fracture of as-forged GA Ti-6Al-4V parts (O: 0.14%) with a coarse α lamellar structure is increased to 14.3% without sacrificing tensile strength. Also the UTS can be increased to 1195.1 MPa with an elongation to fracture of 9.9% by a solution and aging treatment to give an α acicular microstructure. After recrystallization annealing, equiaxed grains with a fine α/β matrix structure are obtained, and the elongation to fracture is improved significantly to 15.1% with a small drop in tensile strength.
- As a rapid powder consolidation process for Ti and Ti-6Al-4V powders, the densification rate of powder compact forging is enhanced by pore collapse caused by material flow. Shear deformation plays an important role in influencing the degree of powder consolidation during a powder compact forging process. This is the main reason for the variation in material mechanical properties with distance, from the surface to the centre, in as-forged parts. Also, the degree of powder consolidation by powder compact forging can be improved by a recrystallization process through an

enhancement of particle bonding.

- For Ti-6Al-4V samples, produced by forging a compact made from a mixture of Ti and Al-V master alloy powders, with an increase in holding time at the forging temperature, the Al-40wt%V master alloy particles and pores become smaller. Finally the master alloy particles and pores disappear in an as-forged part when the holding time is increased to 10 minutes, and at this point, a uniform α/β lamellar structure forms. With a change in microstructure, the mechanical properties of as-forged parts improve to give a yield strength of 1131.8 MPa, a UTS of 1248.4 MPa and an elongation to fracture of 3.4%. These mechanical properties are close to those found in as-forged HDH Ti-6Al-4V parts made using pre-alloyed HDH powder, but the cost of raw powders is lower. Therefore, the undissolved master alloy particles significantly influence the mechanical properties of forged parts, and forged parts with a homogeneous composition and microstructure, achieved by adequate elemental diffusion before forging, can possess good mechanical properties.
- For an HDH Ti/Al-V compact made from a master alloy powder mixture a holding time of 5-10 minutes at the forging temperature is required to produce a part with a homogeneous composition. This holding time can be reduced to zero by processing the powder mixture using high energy mechanical milling, to turn it into a composite powder. However, the oxygen absorption during milling and powder passivation is serious, and this is the main reason for the brittleness of samples produced by forging compacts made from composite powders. The deleterious effect of high oxygen content is reduced by replacing HDH Ti powder with GA Ti powder, but this can lead to a non-homogeneous compositional distribution in the microstructure of as-forged parts.

7.2 Recommendations for Future Work

- To simulate the powder compact forging process by FEM, and analyze its stress-strain state to explain the mechanism of powder consolidation during this process.
- Apply the heat treatment conditions for an as-forged Ti-6Al-4V part on samples produced by forging powder compacts made from a powder mixture or from composite powders.
- Determine the effect of holding time at the forging temperature on samples produced by forging a Ti/Al-40wt%V master alloy composite powder compact.
- Conduct fatigue testing on as-forged parts to analyze their fatigue behaviour for potential industrial application.